

8-2017

THE ROLE OF THE EPITHELIAL-TO-MESENCHYMAL TRANSITION (EMT) IN LUNG CANCER PROGRESSION

David H. Peng

Follow this and additional works at: https://digitalcommons.library.tmc.edu/utgsbs_dissertations



Part of the [Cancer Biology Commons](#), [Laboratory and Basic Science Research Commons](#), and the [Medicine and Health Sciences Commons](#)

Recommended Citation

Peng, David H., "THE ROLE OF THE EPITHELIAL-TO-MESENCHYMAL TRANSITION (EMT) IN LUNG CANCER PROGRESSION" (2017). *The University of Texas MD Anderson Cancer Center UTHealth Graduate School of Biomedical Sciences Dissertations and Theses (Open Access)*. 784.
https://digitalcommons.library.tmc.edu/utgsbs_dissertations/784

This Dissertation (PhD) is brought to you for free and open access by the The University of Texas MD Anderson Cancer Center UTHealth Graduate School of Biomedical Sciences at DigitalCommons@TMC. It has been accepted for inclusion in The University of Texas MD Anderson Cancer Center UTHealth Graduate School of Biomedical Sciences Dissertations and Theses (Open Access) by an authorized administrator of DigitalCommons@TMC. For more information, please contact digitalcommons@library.tmc.edu.

THE ROLE OF THE EPITHELIAL-TO-MESENCHYMAL TRANSITION (EMT) IN LUNG
CANCER PROGRESSION

by

David Hwa Peng, M.S., B.S.

APPROVED:

Don L. Gibbons, M.D., Ph.D.
Advisory Professor

Jonathan M. Kurie, M.D.

Faye Johnson, M.D., Ph.D.

Randy Johnson, Ph.D.

Li Ma, Ph.D.

Yang Xia, M.D., Ph.D.

APPROVED:

Dean, The University of Texas

MD Anderson Cancer Center UTHealth Graduate School of Biomedical Sciences

THE ROLE OF THE EPITHELIAL-TO-MESENCHYMAL TRANSITION (EMT) IN LUNG
CANCER PROGRESSION

A

DISSERTATION

Presented to the Faculty of

The University of Texas MD Anderson Cancer Center

UTHealth Graduate School of Biomedical Sciences

In Partial Fulfillment

of the Requirements

for the Degree of

DOCTOR OF PHILOSOPHY

by

David H. Peng, M.S., B.S.

Houston, Texas

August 2017

DEDICATION

This dissertation is dedicated to all the teachers that told me I'd never amount to nothin', to all the people that worked beside the benches that I was pipettin' in front of, that called the ombudsman on me when I was just tryin' to make some money to feed my daughter, and all the PhD students in the struggle, you know what I'm sayin'?

It was all a dream, I used to read C.N.S. magazine, doing research that world ain't never seen. Hangin' papers on my spot, every Saturday lab attack, Mr. Freezie, Western blot. Pipette the tip box, drain the tip stocks, cell culture and I.H.C., researchin' about LOX. Way back, when I went to lab and didn't know jack, always talkin' smack. Remember bad data, always bizarre, I never thought my work would make it this far. Now I'm in the limelight 'cause my work tight. Time to get paid, publish, so my name's made. Born sinner, the opposite of a winner, remember when I used to eat cup noodles for dinner.

Peace to Don G, Rakhee B, Laura G, all the PhDs, the lab kids three. I'm movin' up like y'all thought I would. Call the cell, if y'all need me in the cell hood, it's all good.

And if you don't know, now you know...

ACKNOWLEDGEMENTS

First and foremost I would like to thank my advisor, Don Gibbons, for being patient enough to mentor and guide my development as a scientist and for understanding the work/life balance needed to be truly successful. I would like to thank all collaborators listed on my publications for contributing to my research. I would also like to thank my advisory committee as well as those in my lab who provided mentorship during my graduate studies. I would like to thank the Cancer Prevention Research Institute of Texas (CPRIT) for funding our research and providing funding for my scholarship, giving my PI one less reason to terminate my enrollment. Lastly, I would like to thank my wife and daughter who supported me throughout my graduate studies as well as my parents, whose influential careers in life science research inspired me to pursue my own.

THE ROLE OF THE EPITHELIAL-TO-MESENCHYMAL TRANSITION (EMT) IN LUNG CANCER PROGRESSION

David Hwa Peng, M.S., B.S.

Advisory Professor: Don L. Gibbons, M.D., Ph.D.

Lung cancer is the leading cause of cancer-related deaths due to conventional therapy resistance and metastatic disease, therefore understanding the mechanisms governing these biological functions is vital for improving patient survival. Approximately 30% of patients with the adenocarcinoma histologic subset of lung cancer possess an activating KRAS mutation, characterized by a lack of response to chemotherapies with a poor overall 5-year survival rate. Despite the mutational frequency, KRAS remains a challenge to pharmacologically inhibit and current drugs undergoing clinical trials that target specific downstream effector proteins of KRAS, such as MEK inhibitors, have failed to produce significant clinical benefits. Previous studies by our group on the metastatic process revealed that malignant lung cancer cells undergo an epithelial-to-mesenchymal transition (EMT) that is regulated by a double-negative feedback loop between the transcription factor Zeb1 and the microRNA-200 family (miR-200). Furthermore, these studies demonstrated that mesenchymal lung cancer cell invasion and metastasis are dependent on interaction with the extracellular matrix (ECM). In addition to metastasis, EMT has been implicated in resistance to radiation and chemotherapies as well as resistance to certain targeted drug treatments. Thus, the comprehensive objective of this study was to: (1) elucidate the detailed mechanisms of metastasis by investigating the collaborative effect of EMT and ECM on KRAS mutant lung cancer metastasis, and (2) delineate the mechanism of EMT in promoting MEK

inhibitor resistance in KRAS mutant lung cancers. Our findings reveal increased collagen deposition in mesenchymal tumor tissues due to amplification of collagen gene expression in Zeb1-driven mesenchymal lung cancer cells. Additionally, collagen fibers in the metastatic tumor tissues exhibit greater linearity and organization, correlating with direct Zeb1-upregulation of the collagen crosslinking enzyme LOXL2. Coordinated expression of LOXL2 with collagen increases insoluble collagen crosslinking and deposition in the tumor microenvironment, resulting in activated Fak/Src signaling to promote metastasis. Using functional *in vivo* shRNA screens coupled with proteomic profiling, we identified Zeb1-driven epithelial-to-mesenchymal transition (EMT) as a regulator of MAPK-dependent signaling activity and tumor maintenance in lung cancer cells. Mechanistic studies in novel cell line and animal models further demonstrated that the Ras-Raf-Mek-Erk MAPK signaling cascade in epithelial cells is activated through upregulation of the scaffold protein I17rd, which is directly repressed by Zeb1 during EMT. Translationally, we observe that poorly-differentiated, mesenchymal lung cancer cells within the heterogeneous lung tumor tissue of *in vivo* models are resistant to MEK inhibitors and identified Zeb1 and I17rd as potential biomarkers from large patient datasets. Reversion of functional EMT by genetic expression of miR-200 or treatment with the class I HDAC inhibitor mocetinostat sensitized resistant cancer cells to MEK inhibition and significantly reduced tumor growth. This study establishes the mechanisms of metastasis and MEK inhibitor resistance in KRAS mutant lung cancers, identifies multiple potential prognostic markers of metastasis and resistance, and provides pre-clinical evidence for a promising combinatorial therapy against lung cancer progression.

TABLE OF CONTENTS

APPROVAL PAGE.....	i
TITLE PAGE.....	ii
DEDICATION.....	iii
ACKNOWLEDGEMENTS	iv
ABSTRACT	v
LIST OF FIGURES	xi
LIST OF TABLES.....	xvii
CHAPTER 1: INTRODUCTION	1
KRAS Mutant Lung Cancers.....	1
Epithelial-to-Mesenchymal Transition in Lung Cancer Progression	5
Extracellular Matrix and Metastasis	7
Dissertation Objectives.....	10
CHAPTER 2: MATERIALS AND METHODS	12
Project 1: ZEB1 Induces LOXL2-Mediated Collagen Stabilization and Deposition in the Extracellular Matrix to Drive Lung Cancer Invasion and Metastasis	12
Plasmids and Reagents	12
Analysis of Human Cancer Datasets	13
Cell Culture and Transfections	13
QPCR and Western Blotting	14
Luciferase Reporter Assays	14
Chromatin Immunoprecipitation Assays	14
Migration and Invasion Assays.....	15
3D Matrigel and Matrigel/Collagen Culture	15

Syngeneic In Vivo Tumorigenesis and Metastasis Assays	15
Immunohistochemistry (IHC) and Second Harmonics Generation (SHG).....	16
Immunofluorescence (IF) Staining	16
Proliferation Assay	16
Amplex Red Assay	16
Mechanical Testing	17
Cell macerated scanning electron microscopy.....	17
Collagen Fiber Alignment Analysis	17
Statistics.....	18
 Project 2: Epithelial-mesenchymal transition promotes MEK inhibitor resistance in KRAS mutant lung cancers through suppression of IL17rd.....	 19
Mice.....	19
Cell Lines.....	20
Plasmids, Transfections, and Lentiviral Generation and Transduction	20
<i>In vivo/In vitro</i> shRNA screens and analytics.....	21
Reverse Phase Protein Array (RPPA) Preparation and Analysis	22
Protein Isolation from Cell Lines and Western Blotting Analysis	23
RNA Isolation and qPCR Analysis.....	24
Chromatin Immunoprecipitation (ChIP) and qPCR Analysis	25
Luciferase Reporter Assay	26
<i>In vitro</i> Drug Response and Cell Growth Assays	27
<i>In vivo</i> Drug Response and Tumor Growth Assays	27
Immunohistochemistry (IHC)	28
Analysis of Human Cancer Dataset and Lung Cancer Cell Line Panel	29
Statistics.....	29
 CHAPTER 3: RESULTS.....	 30
 Project 1: ZEB1 Induces LOXL2-Mediated Collagen Stabilization and Deposition in the Extracellular Matrix to Drive Lung Cancer Invasion and Metastasis	 30

Expression of collagen and ECM-associated genes correlates with EMT	30
Metastatic lung tumors have increased LOX, LOXL2, collagen deposition and linearization, correlating with their EMT status.....	50
LOX and LOXL2 are directly regulated by miR-200 and ZEB1, respectively.....	54
LOX enzymatic function is necessary for lung cancer cell migration and invasion	67
LOXL2 is necessary for collagen deposition, crosslinking and tumor cell metastasis	72
LOX and LOXL2 ectopic expression is not sufficient for epithelial cancer cell migration and invasion	84
LOXL2-mediated collagen deposition induces FAK/Src signaling <i>in vitro</i> and <i>in vivo</i>	89
Increased collagen, LOX, and LOXL2 expression predicts poor prognosis among patients with lung adenocarcinoma	94
 Project 2: Epithelial-to-Mesenchymal Transition promotes MEK inhibitor resistance in KRAS mutant lung cancers through suppression of IL17rd.....	 106
Epithelial lung cancer cells exhibit increased MAPK signaling and dependency for tumor growth	106
Activation of Mek/Erk signaling in epithelial cells is driven by the Ras-Raf-Mek-Erk signaling cascade.....	114
Regulation of MAPK pathway signaling is linked to the EMT state by differential expression of the scaffold protein IL17rd	124
Mesenchymal lung cancer cells and tumors are resistant to MEK inhibition.....	138
Mesenchymal de-differentiation of lung tumors in Kras mutant mouse models is sufficient to suppress MAPK signaling and confer resistance to MEK inhibition	143
Mocetinostat reverts EMT, derepresses IL17rd expression, and sensitizes resistant cancer cells to MEK inhibition	150
Patients with poorly differentiated lung adenocarcinomas display lower levels of phosphorylated Erk, inversely correlating with Zeb1 expression	158

CHAPTER 4: DISCUSSION	164
Project 1: ZEB1 Induces LOXL2-Mediated Collagen Stabilization and Deposition in the Extracellular Matrix to Drive Lung Cancer Invasion and Metastasis	164
Project 2: Epithelial-to-Mesenchymal Transition promotes MEK inhibitor resistance in KRAS mutant lung cancers through suppression of IL17rd.....	173
CHAPTER 5: FUTURE DIRECTIONS.....	176
Project 1: ZEB1 Induces LOXL2-Mediated Collagen Stabilization and Deposition in the Extracellular Matrix to Drive Lung Cancer Invasion and Metastasis	176
Project 2: Epithelial-to-Mesenchymal Transition promotes MEK inhibitor resistance in KRAS mutant lung cancers through suppression of IL17rd.....	177
BIBLIOGRAPHY	179
VITA.....	203

LIST OF FIGURES

Figure 1	4
Figure 2	31
Figure 3	32
Figure 4	33
Figure 5	45
Figure 6	45
Figure 7	46
Figure 8	48
Figure 9	48
Figure 10	49
Figure 11	51
Figure 12	53
Figure 13	55
Figure 14	55
Figure 16	56
Figure 15	56
Figure 17	57
Figure 18	58
Figure 19	58
Figure 20	59
Figure 21	59
Figure 22	60

Figure 23.....	62
Figure 24.....	63
Figure 25.....	64
Figure 26.....	66
Figure 27.....	68
Figure 28.....	68
Figure 29.....	69
Figure 30.....	69
Figure 31.....	69
Figure 32.....	70
Figure 33.....	70
Figure 34.....	70
Figure 35.....	71
Figure 36.....	73
Figure 37.....	73
Figure 38.....	74
Figure 39.....	74
Figure 40.....	75
Figure 41.....	75
Figure 42.....	76
Figure 43.....	76
Figure 44.....	78
Figure 45.....	79
Figure 46.....	80

Figure 47.....	81
Figure 48.....	81
Figure 49.....	82
Figure 50.....	83
Figure 51.....	85
Figure 52.....	86
Figure 53.....	86
Figure 54.....	87
Figure 55.....	87
Figure 56.....	88
Figure 57.....	90
Figure 58.....	90
Figure 59.....	91
Figure 60.....	92
Figure 61.....	93
Figure 62.....	96
Figure 63.....	97
Figure 64.....	98
Figure 65.....	98
Figure 66.....	99
Figure 67.....	100
Figure 68.....	101
Figure 69.....	102
Figure 70.....	103

Figure 71	104
Figure 72.....	105
Figure 73.....	105
Figure 74.....	108
Figure 75.....	110
Figure 76.....	111
Figure 77.....	112
Figure 78.....	113
Figure 79.....	113
Figure 80.....	115
Figure 81	116
Figure 82.....	116
Figure 83.....	117
Figure 84.....	117
Figure 85.....	119
Figure 86.....	120
Figure 87.....	121
Figure 88.....	122
Figure 89.....	122
Figure 90.....	123
Figure 91	125
Figure 92.....	127
Figure 93.....	128
Figure 94.....	128

Figure 95.....	129
Figure 96.....	130
Figure 97.....	132
Figure 98.....	133
Figure 99.....	134
Figure 100.....	135
Figure 101.....	137
Figure 102.....	139
Figure 103.....	141
Figure 104.....	141
Figure 105.....	142
Figure 106.....	142
Figure 107.....	145
Figure 108.....	146
Figure 109.....	147
Figure 110.....	147
Figure 111.....	148
Figure 112.....	149
Figure 113.....	152
Figure 114.....	152
Figure 115.....	153
Figure 116.....	154
Figure 117.....	154
Figure 118.....	155

Figure 119.....	156
Figure 120.....	157
Figure 121.....	157
Figure 122.....	160
Figure 123.....	160
Figure 124.....	161
Figure 125.....	161
Figure 126.....	162
Figure 127.....	162
Figure 128.....	163
Figure 129.....	167
Figure 130.....	169

LIST OF TABLES

Table 1.....	34
Table 2.....	109

CHAPTER 1: INTRODUCTION

KRAS Mutant Lung Cancers

Lung cancer is not only the second leading cause of estimated new cancer cases annually (with over 200,000 estimated new cases in the U.S. alone), but it is the leading cause of cancer-associated deaths in the United States (>150,000 annual deaths in the U.S.) and worldwide, surpassing the successive three cancer types combined (1). Patients with lung cancer are often diagnosed with advanced stage tumors and metastatic disease, correlating with resistance to chemotherapies and poor overall 5-year survival. Furthermore, patients who are treated for early stage disease frequently acquire resistance to first-line therapies and ultimately develop metastasis (1-5). Therefore understanding the biology orchestrating lung cancer progression, therapy resistance and metastasis is vital for improving patient survival.

Lung cancer can be separated into several different histologic forms. The majority of lung cancer patients (~85%) have non-small-cell lung cancer (NSCLC), which can be further divided into the lung adenocarcinoma, squamous cell carcinoma, and large cell subtypes (6). Approximately 30% of patients with lung adenocarcinoma possess a KRAS mutation that activates various downstream signaling pathways to promote tumor formation, tumor growth, and metastasis (7, 8). KRAS is a small GTPase protein that switches to an “on” or “off” conformational state, which is dependent upon its binding to guanosine triphosphate (GTP) or guanosine diphosphate (GDP), respectively. This conformational change leads to interactions with other

downstream effector proteins, such as Raf or PI3K, that often possess a Ras binding domain in their protein structure. KRAS bound proteins are then activated by changes in conformation or subcellular localization to other kinases, leading to activation of the proteins by phosphorylation of the serine, threonine, or tyrosine amino acid residues. Since the downstream target proteins activated by KRAS are typically kinases, this catalyzes a signaling cascade to various other kinases which ultimately drives expression of genes that regulate tumor formation, growth, survival, and metastases (7, 9, 10). In the context of cancer, KRAS mutations commonly result in a substitution of an amino acid residue, typically at codon 12, which prevents the release of bound GTP, retaining KRAS in the activated “on” state. Consequently, constant KRAS activation overstimulates various different signaling molecules responsible for tumorigenesis and malignancy (7).

Despite advancements in DNA sequencing technology that allow for the identification of KRAS mutations in lung tumors, treating KRAS mutant lung cancer patients remains a challenge due to poor response to chemotherapies as well as a lack of targetable drugs that can specifically and effectively inhibit the constitutively active oncogenic protein. Therefore, current clinical trials target the downstream effector proteins of KRAS through the use of MEK inhibitors (11, 12). The Mek 1 and 2 (Mek1/2) proteins are dual specificity kinases that are part of the mitogen activated protein kinase (MAPK) pathway. The canonical MAPK pathway is comprised of the RAF-MEK-ERK kinase cascade and is normally activated through growth factor receptor tyrosine kinase (RTK) activation of RAS to stimulate the RAS-RAF-MEK-ERK pathway. Continual stimulation of this pathway by mutant KRAS leads to high phosphorylation of the extracellular signal–regulated kinases 1 and 2 (Erk1/2), resulting

in tumor formation and growth (13, 14). Although hyperactivation of MAPK signaling by KRAS is typically simplified as a linear model of intracellular communication, in reality, the MAPK pathway is a highly complex web of interconnected kinases and regulatory proteins. While KRAS alone is sufficient to stimulate MAPK growth, numerous other cellular factors are critical at maintaining homeostasis and keeping dysregulated growth in check. Examples of tumor suppressive regulation include the feedback inhibition by the downstream Erk1/2 kinase, expression of MAPK inhibitory proteins and phosphatases, and alterations in scaffolding proteins that facilitate signaling activity (15-24). The spatial-temporal regulation of MAPK signaling determines the biological fate of the cell and each aspect of MAPK regulation can be disrupted during tumor progression.

Although MEK inhibition should theoretically reduce tumor burden in patients by suppressing MAPK-associated growth as demonstrated experimentally, recent clinical trials with MEK inhibitors have demonstrated no significant improvement in KRAS mutant NSCLC patient survival, suggesting resistance mechanisms (25, 26). Co-clinical trials utilizing MEK inhibitors with chemotherapy have shown that the acquisition of secondary mutations in tumor suppressors, such as TP53 or LKB1, contributes to resistance to a combination treatment of docetaxel with the MEK inhibitor selumetinib (27). The p53 tumor suppressor protein has countless cellular functions that are critical at preventing tumor initiation and progression (28). Although several aspects of the intricate biological functions of p53 have been elucidated, the mechanisms of how alterations in p53 function and expression promote tumor progression have yet to be fully defined (28, 29). Clinically, TP53 is one of the most commonly mutated genes in lung cancer, occurring in approximately 50% of all patients (**Figure 1**) (30, 31).

Figure 1

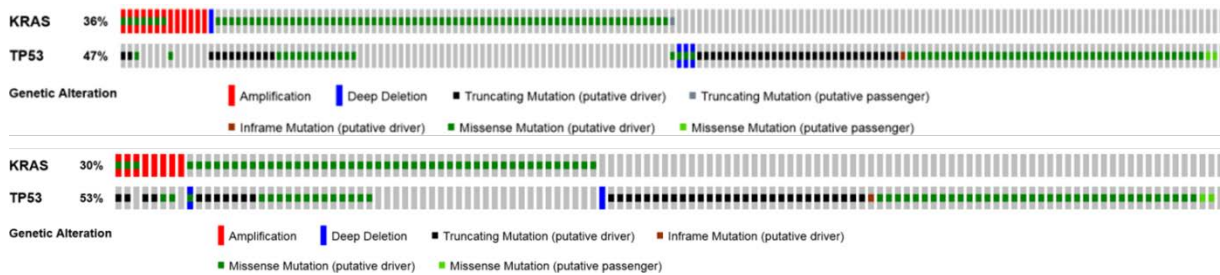


Figure 1. Top: Genetic alterations in *KRAS* and *TP53* in lung adenocarcinoma patients from TCGA dataset (Nature 2014). Bottom: Genetic alterations in *KRAS* and *TP53* in lung adenocarcinoma patients from TCGA dataset (Broad, Cell 2012). Images accessed in May 2017 with permission as described on the cbiportal.org website (<http://www.cbiportal.org/faq.jsp>) and as granted from journals of the following references:

Gao, J., B. A. Aksoy, U. Dogrusoz, G. Dresdner, B. Gross, S. O. Sumer, Y. Sun, A. Jacobsen, R. Sinha, E. Larsson, E. Cerami, C. Sander, and N. Schultz. 2013. Integrative Analysis of Complex Cancer Genomics and Clinical Profiles Using the cBioPortal. *Science Signaling* 6: pl1-pl1.

Cerami, E., J. Gao, U. Dogrusoz, B. E. Gross, S. O. Sumer, B. A. Aksoy, A. Jacobsen, C. J. Byrne, M. L. Heuer, E. Larsson, Y. Antipin, B. Reva, A. P. Goldberg, C. Sander, and N. Schultz. 2012. The cBio Cancer Genomics Portal: An Open Platform for Exploring Multidimensional Cancer Genomics Data: Figure 1. *Cancer Discovery* 2: 401-404.

Since rescued expression of a somatically mutated tumor suppressor is not a feasible therapeutic option against lung cancer, understanding the precise mechanisms of p53 mutations on lung tumor progression is vital for identification of novel biomarkers and therapeutic targets to overcome drug resistance.

Epithelial-to-Mesenchymal Transition in Lung Cancer Progression

Previous work by our group utilizing the spontaneous mutant *Kras*^{LA1-G12D/+} (Kras) and double-mutant *Kras*^{LA1-G12D/+}; *p53*^{R172HΔg/+} (KP) murine models of lung adenocarcinoma demonstrated that co-mutation of p53 with KRAS increased tumor formation, displayed more advanced grade lung adenocarcinomas, and produced metastasis (32). Further studies on the metastatic process using syngeneic tumor models with cell lines derived from the primary and metastatic tumor tissues of the KP mice revealed that malignant murine lung cancer cells had undergone an epithelial-to-mesenchymal transition (EMT) (33). EMT is a biological process essential for human development that is involved in tissue expansion and wound repair (34). During EMT, polarized, well-differentiated epithelial cells alter various genetic and biochemical properties to adopt a more de-differentiated, mesenchymal phenotype. Although the terminology suggests a binary transformation, EMT is actually a complex process with varying degrees of differentiation states at the molecular level that are regulated by a multitude of factors including extrinsic stimuli, transcription factors, and microRNAs (34-37). From a tumor progression standpoint, EMT is a proposed model of metastasis whereby epithelial cancer cells lose their cell-cell adherence junctions and become more motile and invasive, resulting in primary tumor dissemination and colonization of distant organs (34). In addition to metastasis, EMT has also been implicated as a model for resistance to chemotherapies, radiation, and targeted drug therapies (38-43). Although a functional role for EMT in the development of therapy resistance is frequently observed, the mechanism(s) by which EMT promotes resistance are poorly understood in most cases.

Prior studies by our group and others using cell line models and genetically-engineered murine models demonstrate that EMT is regulated by a double-negative feedback loop between the miR-200 family of microRNAs and the Zeb1 transcription factor, where high Zeb1 expression promotes the mesenchymal phenotype while high miR-200 expression reverses EMT and promotes a mesenchymal-to-epithelial transition (MET) state in lung cancer cells (33, 44). MicroRNAs are small, non-coding RNAs which, in their mature form, regulate gene expression by typically binding to the 3'-untranslated region (3'-UTR) of a target mRNA through complementary nucleotide base pairing. Once bound to the mRNA 3'-UTR, microRNAs hinder translation and/or cause mRNA instability and degradation. The miR-200 family consists of five members: miR-200a, miR-200b, miR-200c, miR-141, and miR-429. MiR-200a, miR-200b, and miR-429 are clustered on the same loci of chromosome 1 in humans while miR-200c and miR-141 are clustered on the same loci of chromosome 12. All five miR-200 family members bind to the Zeb1 3'-UTR which results in downregulation of Zeb1 expression (45-47). Conversely, Zeb1 directly suppresses miR-200 expression by binding onto the E-box recognition sites on the promoter region of miR-200 and other epithelial-related genes, inhibiting transcription (46-49). Besides transcriptional repression by direct promoter hindrance, Zeb1 has been reported to epigenetically silence miR-200 expression as well (50). Numerous studies by our group and others have demonstrated that increased Zeb1 expression in cancer cells leads to greater metastatic propensities, enhanced resistance to first-line radiation/chemotherapies, and significantly reduced patient survival (38, 45, 48-60). Despite the importance of Zeb1 and miR-200 in regulating EMT-induced cancer progression, direct silencing of Zeb1 or direct administration of miR-200 presents numerous challenges pharmacologically due to the

complicated delivery methods as well as the pleiotropic downstream targets of these two genes. EMT also transpires in only a subset of cells within the heterogeneous primary tumor tissue (61), which consists of predominantly epithelial cancer cells that exhibit distinct responses to treatment. Thus, insights into the downstream targets regulated Zeb1/miR-200 to produce functionally relevant phenotypic changes are necessary to uncover the contrasting sensitivities to specific targeted therapies between epithelial and mesenchymal lung cancer cells as well as define prognostic and therapeutic markers against metastasis.

Extracellular Matrix and Metastasis

While the cell-intrinsic effects of Zeb1/miR-200 are critical at regulating EMT, findings by our group and others have demonstrated that tumor cell-extracellular matrix (ECM) interactions play a crucial role in modulating cell behavior, including EMT, invasion, and metastasis (33, 58, 62-66). For instance, *in vitro* three dimensional (3D) culture of our metastatic, mesenchymal murine lung cancer cell line in laminin-rich Matrigel basement membrane caused the cells to form highly polarized, epithelial organoids that only became invasive upon forced induction of EMT by stimulating the cell structures with transforming growth factor beta (TGF- β) (33). However, replicating the 3D culture conditions of the mesenchymal murine lung cancer cells in an ECM-free polyethylene glycol (PEG) hydrogel did not produce invasive structures following TGF- β treatment, signifying that, both, ECM interaction and modification, is necessary for invasion and metastasis (65). Several reports have also suggested that there exists a reciprocal dynamic interplay between EMT and the structural/compositional properties of ECM that determines the invasiveness of cancer cells (67). Proteomic analyses of

our epithelial and mesenchymal lung cancer cell lines uncovered several upregulated ECM-associated proteins in mesenchymal cells that could potentially drive metastasis (68). A major component of the ECM that has been implicated in promoting EMT and driving cancer cell invasion is collagen, which represents the majority of interstitial ECM proteins in mammalian tissues (63, 66, 69). There are 29 different collagen isoforms encoded by 44 genes that are localized in different components of tissue architecture, each contributing to various cellular functions (70). Mature fibrillar collagen molecules are comprised of three individual collagen fibrils that form a triple-helical structure, with collagen type I being the most abundant fibrillar collagen isoform in mammals (63, 71).

Collagen type I has been implicated in tumor progression as well as promoting metastasis (62, 72-74). Collagen binding to cancer cells through various receptors regulates different cancer cell behaviors including cell adhesion, tumor growth, invasion and metastasis, and drug resistance. The maturation process for collagen type I fibers is extensive and requires multiple tiers of post-translational modifications (71). Collagen type I consists of two isoforms expressed by the genes COL1A1 and COL1A2 that synthesize the $\alpha 1$ and $\alpha 2$ chains in the endoplasmic reticulum, respectively. Two $\alpha 1$ and one $\alpha 2$ chains form intramolecular covalent bonds that result in the triple-helical structure of an immature procollagen molecule. To form the intramolecular covalent bonds, the lysine and proline amino acid residues in each chain are hydroxylated by various enzymes of the lysyl hydroxylase family to stabilize the helical structure. The procollagen molecules are then secreted into the extracellular space where the N- and C-terminus propeptides are cleaved off by metalloproteinase to form an individual mature collagen fiber. However, individual mature collagen fibers are still soluble and are prone to degradation by various enzymes. In order to obtain insoluble collagen

deposition in the microenvironment, the mature triple-helix collagen fibers must endure further crosslinking through extracellular, intermolecular covalent bonds. This process is facilitated by the lysyl oxidase (LOX) family of enzymes. The LOX family possesses a conserved catalytic region that deaminates the lysine amino acid residues on proteins including collagen. Once deaminated, the lysine residues form covalent bonds with the aminated ϵ -amine group of other lysine residues on collagen to spontaneously form inter-collagen crosslinks (71). The crosslinked collagen becomes insoluble and stabilizes in the tumor microenvironment, activating various collagen binding receptors that promote invasion and metastasis (58, 63).

Though the presence of collagen is correlated with tumor progression, numerous studies have shown that collagen requires LOX crosslinking to increase matrix stiffness and promote cancer cell invasiveness and malignancy (33, 65, 75-78). LOX enzymes are developmentally necessary for insoluble collagen maturation and deposition in tissues (66, 79). There are five LOX isoforms with a conserved catalytic domain at the C-terminus end of the protein while the N-terminus regions are variable, giving rise to differential localization, protein targets, and functional regulation (80). Upregulation of the LOX and LOXL2 isoforms has been shown to promote invasion and metastasis in certain cancer types (80) but due to the N-terminus posttranslational modifications as well as the non-specific nature of the lysine deamination process, LOX and LOXL2 also have non-ECM, intracellular roles in promoting metastasis (81-86). Although LOX has been reported to promote fibrosis-mediated breast cancer metastasis, there has been little work establishing their role in lung cancer systems. Furthermore, the relationship between EMT, the LOX family, and the ECM in regulating lung cancer metastasis is still poorly understood.

Dissertation Objectives

This dissertation is sectioned into two projects that describe the role of EMT on KRAS mutant lung cancer progression. The first project aims to determine the cooperative mechanisms of EMT and ECM on lung cancer invasion and metastasis. The second study aims to identify differences in therapeutic vulnerabilities between epithelial and mesenchymal KRAS mutant lung cancer cells as well as delineate the mechanisms behind MEK inhibitor resistance.

First, we demonstrate that mesenchymal lung cancer cells drive invasion and metastasis by increasing collagen deposition, crosslinking, and stabilization in their surrounding microenvironment due to an increase in Zeb1-driven LOXL2 expression. The increase in collagen deposition results in the activation of focal adhesion signaling, which we have previously demonstrated to be involved in lung cancer invasion and metastasis (58). Functional *in vitro* and *in vivo* assays establish LOXL2 as a potential therapeutic target for the prevention of lung cancer metastasis. Pathological analyses of our KP murine model as well as human lung cancer patient tissues define collagen type I and type III as promising prognostic markers.

Next, we sought to understand the differences in therapeutic vulnerabilities between epithelial and mesenchymal lung tumors through the use of *in vivo* short hairpin RNA (shRNA) library screens and identified greater dependency on MAPK signaling molecules for tumor initiation and maintenance in epithelial cells. Proteomic profiling and in-depth mechanistic analyses in murine and human cell line and multiple animal models revealed higher MAPK signaling proteins in epithelial cells and demonstrated that MAPK pathway activation is dependent on the scaffold protein I17rd (Sef1/I17rlm/Hh18), which is directly repressed by Zeb1 during EMT. Therapeutically,

both *in vitro* and in multiple genetic animal models, epithelial lung cancer cells (low Zeb1, high IL17rd) are very responsive to MEK inhibition while mesenchymal cells (high Zeb1, low IL17rd) are resistant. Moreover we demonstrate that suppression of Zeb1 function through genetic induction of miR-200 or inhibition of class I histone deacetylases (HDAC) with mocetinostat sensitized mesenchymal lung cancer cells to MEK inhibitors. Histologic and bioinformatics analyses of large human patient sample sets revealed an inverse correlation of Zeb1 and activated MAPK (p-Erk) or ZEB1 and IL17RD expression, respectively. Our study identifies distinct well- and de-differentiated subpopulations of lung cancer cells with differential sensitivities to MEK inhibition, defines Zeb1 and IL17rd as the causative mechanism and potential biomarkers that predict sensitivity to treatment, and presents a prospective combinatorial therapeutic strategy to overcome resistance.

CHAPTER 2: MATERIALS AND METHODS

Project 1: ZEB1 Induces LOXL2-Mediated Collagen Stabilization and Deposition in the Extracellular Matrix to Drive Lung Cancer Invasion and Metastasis

Contents of this chapter are derived from the publication Peng DH, Ungewiss C, Tong P, Byers LA, Wang J, Canales JR, Villalobos PA, Uraoka N, Mino B, Behrens C, Wistuba II, Han RI, Wanna CA, Fahrenholtz M, Grande-Allen KJ, Creighton CJ, Gibbons DL. "ZEB1 induces LOXL2-mediated collagen stabilization and deposition in the extracellular matrix to drive lung cancer invasion and metastasis." *Oncogene*. 2016 Oct 03. PubMed PMID: 27694892 with approval from Nature Publishing Group.

Plasmids and Reagents

Mouse LOX shRNA constructs were purchased from Thermo Fisher Scientific (Cat#: RMM4534-EG16948, Grand Island, NY). Mouse LOXL2 shRNA constructs were cloned the pLKO.1 lentiviral vector. Murine LOX and LOXL2 isoforms were cloned and expressed using the Doxycycline inducible pTRIPz-GFP lentiviral vector. Viral vectors were the psPAX2 packaging and pMD2.G envelope vectors. Luciferase 3'-UTR reporter constructs were made by reverse-transcription PCR (RT-PCR) and PCR amplification of ~2.9 kb and ~2.6 kb of mouse LOX and LOXL2 3'-UTR mRNA, respectively. The promoter region for LOXL2 was PCR amplified from mouse genomic DNA ~1.3 kb upstream of the transcriptional start site. Site directed mutagenesis of binding sites were performed using the QuikChange II XL Site-Directed Mutagenesis Kit (Agilent, Santa Clara, CA, USA).

Analysis of Human Cancer Datasets

Level 3 gene expression data from the TCGA pan-cancer data sets were used (87, 88). EMT score was calculated based on the EMT signature previously published (40, 53). Pearson correlation was used to quantify the association between EMT and collagen expression. To investigate if collagen family genes were enriched with strong correlations with EMT, we compared the correlations between EMT score and collagen family genes and correlations between EMT score and non-collagen family genes using the Kolmogorov–Smirnov test. For analysis of collagen-associated mRNA expression and lung cancer patient survival, we examined a previously-assembled compendium dataset (89) of 11 published expression profiling datasets for human lung adenocarcinomas ($n = 1,492$ tumors), with the addition of another dataset from Sato et al (90), patients represented in both Shedden and Chitale datasets ($n=88$ patients) were first removed from the Shedden dataset, and one patient from the Bild dataset thought to potentially represent SQCC was also removed (leaving $n = 1,586$ tumors in total).

Cell Culture and Transfections

All lung cancer cell lines were cultured in RPMI 1640 supplemented with 10% fetal bovine serum (FBS). HEK-293 cells were cultured in DMEM supplemented with 10% FBS. Lentiviral vectors were co-transfected in HEK-293 cell with Lipofectamine LTX (Thermo). Luciferase reporter assays used Lipofectamine 2000 (Thermo) as the transfection reagent. Murine cell lines were previously generated by our lab (33) and

human cell lines were obtained through ATCC. All cell lines were verified to be mycoplasma negative monthly.

QPCR and Western Blotting

Total RNA was isolated from cells by TRIzol (Thermo) according to manufacturer protocol and cDNA was generated using iSCRIPT reagents (Bio-Rad, Hercules, CA). QPCR assays were performed using SYBR Green PCR Master Mix (Thermo) and normalized to the L32 gene. Cell lysates were prepared according to the RIPA buffer protocol (CS9806), separated by SDS-PAGE, transferred to nitrocellulose membranes, and probed with listed antibodies.

Luciferase Reporter Assays

Luciferase reporter assays were carried out by transfection of 500 ng of the reporter constructs in specified cell lines with 50 nM miR-200a/b/c precursors where appropriate (Thermo). Assays were carried out using Dual-Luciferase Reporter Assay kit (Promega, Madison, WI).

Chromatin Immunoprecipitation Assays

Chromatin immunoprecipitation assays were performed as previously described (48, 91). Immunoprecipitation was carried out using an anti-ZEB1 antibody or mock IgG control (Santa Cruz, Dallas, TX). Promoter segment enrichment was analyzed by qPCR using primers flanking the potential ZEB1 binding sites along the LOXL2 promoter.

Migration and Invasion Assays

Migration/invasion assays were performed using 8 μ m Transwell inserts pre-coated with Matrigel or 100 μ l of 0.2 mg/ml collagen type I (BD Biosciences, San Jose, CA). Assays progressed at 37°C for 8 hrs for human cell lines and 20 hrs for murine cell lines following a published protocol (33). BAPN and D-Penicillamine were purchased from Sigma (St. Louis, MO). Inserts were stained with crystal violet and cells were imaged by bright field microscopy and counted using ImageJ software.

3D Matrigel and Matrigel/Collagen Culture

Glass 8-well chamber slides (Thermo) were coated with 100 μ l Matrigel or Matrigel/collagen type I mix at 1.5 mg/ml final collagen concentration. Cells were seeded in the matrices and cultured for 7 days with indicated daily treatments. Collagen gels for SEM analysis were 2 mg/ml of pure collagen with cells encapsulated and treated with TGF- β for 7 days.

Syngeneic In Vivo Tumorigenesis and Metastasis Assays

Cells were subcutaneously injected in the right flanks of male, syngeneic 129/sv mice at 3 months of age and allowed to form tumors for 5 to 6 weeks. After euthanasia, tumors were measured and lung metastatic nodules were quantified. For *in vivo* inhibitor treatments, mice received 100 mg/kg BAPN or 150 mg/kg D-Pen in H₂O or PBS, respectively, by daily intraperitoneal injection. Lung tissues and primary tumor tissues were formalin fixed, paraffin embedded, and sectioned for further analysis. All animal experiments were reviewed and approved by the Institutional Animal Care and Use Committee at The University of Texas MD Anderson Cancer Center.

Immunohistochemistry (IHC) and Second Harmonics Generation (SHG)

Paraffin embedded tissue sections were rehydrated, blocked with goat serum, and probed with listed antibodies. Tissues were subsequently washed and probed with HRP-conjugated secondary antibodies and signal was attained by developing with a DAB reagent. For SHG microscopy, tissues stained by H&E were visualized using a Zeiss LSM 7 MP Multiphoton Microscope at an excitation wavelength of 800 nm and collagen fiber signals were detected at 380-430 nm using bandpass filters. Collagen linearity was calculated as a ratio of the total length versus the end-to-end length of the individual collagen fiber as previously described (62).

Immunofluorescence (IF) Staining

IF stains were performed as previously described (58), stained with listed antibodies and visualized by fluorescence microscopy.

Proliferation Assay

Cells were seeded in 96-well plates at 500 cells/well and treated with BAPN or D-Pen at specified concentrations. Proliferation was measured following the WST-1 (Roche, Basel, Switzerland) protocol and absorbance was measured at 450 nm after 2 hours.

Amplex Red Assay

LOX family enzyme activity from cell culture media with indicated treatments was measured using the Amplex Red protocol (Thermo) and 2mM benzylamine (Sigma).

Mechanical Testing

A bioindenter (BHT, Anton Paar, Ashland, VA) was used to test the local mechanical properties of tumor tissues approximately 1 cm wide under hydrated conditions and carried out using a 500 μm diameter flat punch indentation tip with a constant loading rate up to a maximum load of 60 μN . Instrumentation software analysis of the resulting unloading curve by the Oliver & Pharr method was used to calculate the indentation modulus (92).

Cell macerated scanning electron microscopy

A modification of the NaOH cell-maceration technique reported by Rossi was used (93). This technique dissolves the cellular elements, fixed, and dehydrated, leaving behind the collagen matrix, network, allowing three-dimensional imaging using SEM. Dehydrated specimens were critical point dried (Critical Point Dyer 850, Electron Microscopy Science, Hatfield, PA), mounted on aluminum mount (Electron Microscopy Science, Hatfield, PA), sputter coated with 15 nm gold palladium in a Denton Desk V sputter (Moorestown, NJ), and viewed in a FEI Quanta 400 ESEM FEG (Hillsboro, Oregon).

Collagen Fiber Alignment Analysis

A custom-written MATLAB program was used to analyze the alignment of the collagen fibers within the SEM images. The program imported the SEM .tiff files, enhanced the grayscale contrast, applied a filter and a mask to reduce white noise and detect the fiber edges, respectively (94). The program then developed a high-resolution histogram (with 0.5 degree bins) of the fiber directions and set the mean fiber direction at 0

degrees. After preparing this histogram for each SEM image, the distributions from multiple pictures taken from each gel were compiled to obtain an accurate representation of the alignment of each gel. The compiled histogram data from each gel was averaged across all gels within a treatment group and then fit to a normal distribution. Because the compiled data sets were extremely large, before performing a statistical analysis the data was subsampled to retain only one out of every hundred points within each 0.5 degree bin.

Statistics

Statistical analysis was performed with unpaired student's t-test or otherwise stated.

Project 2: Epithelial-mesenchymal transition promotes MEK inhibitor resistance in KRAS mutant lung cancers through suppression of IL17rd

Mice

All animal experiments were reviewed and approved by the Institutional Animal Care and Use Committee (IACUC) at The University of Texas MD Anderson Cancer Center. The *miR-141/200c^{fl/+}* mice contained a cassette (95, 96) bearing a LacZ reporter gene and loxP sites flanking the *Mirc13^{tm1Mtm}* allele on chromosome 6 that targeted the *Mir141* and *Mir200c* genes. Mice were purchased from the Mutant Mouse Resource & Research Centers (MMRRC) and were initially of the C57BL/6 background upon receipt. Subsequently, *miR-141/200c^{fl/+}* mice were bred with the 129/sv mice and backcrossed for at least 3 generations to obtain a background >50% genetically related to the 129/sv background. The *miR-141/200c^{fl/+}* mice were then crossed with the *Kras^{LSL-G12D}* mice to generate the *Kras^{LSL-G12D};miR-141/200c^{fl/+}* mouse model. Male and female *Kras^{LSL-G12D}*, *Kras^{LSL-G12D};p53^{fl/+}*, and *Kras^{LSL-G12D};miR-141/200c^{fl/+}* adeno-Cre inducible mouse models (129/sv background) of lung adenocarcinoma were infected with virus by intratracheal intubation at 3 months of age. Experiments with the inducible mice were performed 3 months post-infection when tumors properly formed and could be visualized by micro-CT imaging. For experiments with the syngeneic tumor xenograft assays, male wild-type 129/sv mice ages 3 months and up were used. For experiments with the spontaneous *Kras^{LA1-G12D}* and *Kras^{LA1-G12D/+};p53^{R172HΔg/+}* mouse models of lung adenocarcinoma (129/sv background), male mice between the ages of 6 to 8 months were used. For drug treatment experiments, mice were randomly assigned to either treatment or solvent vehicle control groups. For the inducible mouse

models, an even number of male and female mice were randomly assigned to receive either treatment or vehicle control. Inducible mice that required administration of adenovirus were housed specifically in suites designated for biohazardous handling as approved by the IACUC protocol. Two weeks post-infection, mice were returned to the regular housing suite. All mice were immunocompetent and assessed for health daily by the Department of Veterinary Medicine and Surgery (DVMS). All mice were genotyped to determine the mutational status by tail snips 2 weeks after birth.

Cell Lines

BEAS2B cell lines as well as human and murine lung cancer cell lines were cultured in RPMI 1640 (Gibco, Thermo Fisher Scientific, Grand Island, NY, USA) supplemented with 10% fetal bovine serum (FBS, Gibco). 293T cells were cultured in DMEM (Gibco) supplemented with 10% FBS. All human cell lines were obtained through ATCC (Manassas, VA, USA). Murine cell lines and manipulated cell lines were derived as previously described (33, 41, 53, 55, 56, 58, 89). BEAS2B cell lines were generously provided by Dr. Yanan Yang and generated as previously published (59). All cells were cultured at 37°C in a humidified incubator at 5% CO₂ and verified on a monthly basis to be mycoplasma negative using LookOut Mycoplasma PCR Detection Kit (Sigma-Aldrich, St Louis, MO, USA). Cell lines with inducible Zeb1 or miR-200 expression were treated with a final concentration of 2 µg/mL Doxycycline (Dox) from Sigma-Aldrich.

Plasmids, Transfections, and Lentiviral Generation and Transduction

All shRNAs used in the experiment were expressed in the pLKO.1-puro vector with a scramble sequence as the non-targeting control. All cDNAs expressing the open

reading frame (ORF) of indicated proteins were cloned into the pLenti-puro vector using primers listed in Supplementary Table S6. For transient shRNA or cDNA expression, vectors were transfected using the Lipofectamine LTX transfection reagent (Thermo Fisher Scientific). Transfection of siRNAs was performed using the Dharmafect reagent (GE Dharmacon, Lafayette, CO). For lentiviral transductions, viruses were first generated by co-transfecting packaging vector psPAX2, envelope vector pMD2.G, and the pLenti-puro expression vector into 293T cells using Lipofectamine LTX. Transfection media was removed and 293T cells were cultured in RPMI 1640 supplemented with FBS for 48hrs. Viruses were then syringe filtered through a 0.45 μ m nylon filter and Polybrene (Santa Cruz, Dallas, TX) was added to a final concentration of 8 μ g/mL. Media containing lentiviruses were then added to cells, infected for 48hrs, and replaced with fresh media for further experiments.

***In vivo/In vitro* shRNA screens and analytics**

Murine lung cancer cell lines (393P and 344P) were infected at a multiplicity-of-infection (MOI) of 0.3 with a pooled shRNA lentiviral library targeting 191 genes associated with FDA-approved target therapies (10 shRNA/gene, for target list see TableS1b). In parallel *in vivo* and *in vitro* screens were executed in at 1000X coverage and the shRNA-coupled barcodes were detected deploying high-throughput sequencing technology (for detailed procedures and primer sequences see the following reference) (97). *In-vivo* and *in vitro* screens were carried out in triplicate, and duplicate respectively. Raw counts for the screen endpoints and a reference population, isolated after transduction, were normalized using the variance stabilizing transformation in R with the DESeq2 in R. The normalized counts we divided by the

reference to estimate a fold change in barcode abundance. Four independent shRNA targeting essential genes (Rpl30, Psma1) or Luciferase (LUC) were cloned with 5 unique barcodes each and incorporated in the library as positive and negative controls (20 reagents/control, see TableS1A). One LUC hairpin showed apparent off-target effect, and this trend has been observed over a wide-spectrum of in-vitro and in-vivo screens (data not shown). One hairpin for PSMA1 did not show robust drop out, however as the trend was consistent across the 5 barcodes, this result was not reflective of poor screen performance. The separation of positive and negative controls was evaluated by the robust strictly standardized mean (SSMD*, Table S1A), excluding the hairpins mentioned above. Fold change distribution was converted to percentiles, and biological replicates were collapsed for RSA analysis. The RSA logP-values and ranks are provided in Table S1B.

Reverse Phase Protein Array (RPPA) Preparation and Analysis

Cultured cells described above were washed with PBS and proteins were extracted by the addition of lysis buffer (1% Triton X-100, 50 mM HEPES [pH 7.4], 150 mM NaCl, 1.5 mM MgCl₂, 1 mM EGTA, 100 mM NaF, 10 mM NaPPi, 10% glycerol, 1 mM phenylmethylsulfonyl fluoride, 1 mM Na₃VO₄, and protease and phosphoprotease inhibitors from Roche, Basel, Switzerland), incubated on ice for 20 minutes, spun down at 14,000 rpm for 10 minutes, and collected for supernatant. Protein concentration was measured using the Pierce BCA Protein Assay Kit (Thermo Fisher Scientific) and protein samples were prepared to a final concentration of 1 µg/µl mixed with 4x SDS sample buffer (40% glycerol, 8% SDS, 0.25M Tris-HCl pH 6.8, 10% 2-mercaptoethanol) to produce a 1x SDS sample buffer solution. Protein samples were

then boiled at 100°C for 5 minutes and stored at -80°C for RPPA processing described here: (<https://www.mdanderson.org/research/research-resources/core-facilities/functional-proteomics-rppa-core/rppa-process.html>). For analysis of RPPA data, a linear mixed model was applied to compare protein levels on a protein-by-protein base between epithelial and mesenchymal groups; the model includes cell line effects as a random effect factor. The resulting p-values were modeled by a Beta-Uniform Model (BUM). To select protein markers differentially regulated in epithelial and mesenchymal phenotypes, we used False Discovery Rate (FDR) of 0.05 as cutoff. The heatmap was generated based on mean adjusted expression level by each cell line. The Pearson correlation was used for distance matrix calculation and Ward method was applied as linkage rule for the hierarchical clustering.

Protein Isolation from Cell Lines and Western Blotting Analysis

Cultured cells were washed with PBS and proteins were extracted from cell lysates using 1x RIPA buffer (Cell Signaling, Danvers, MA) with protease and phosphoprotease inhibitors, scraped off the plate with cell scrapers, and transferred into 1.5 mL centrifuge tubes. Cell lysates were then sonicated on ice using Vibra-Cell VCX130 Sonicator (Sonics & Materials, Inc., Newtown, CT) at 30% amplitude with 2-second sonication and pulse intervals and 1-second rest intervals for 10 cycles. Lysates were then centrifuged at 14,000 rpm for 10 minutes and supernatant was collected for protein concentration estimation using the Pierce BCA Protein Assay Kit. For Western blotting analysis, protein samples were mixed with 5x SDS Sample Buffer (0.3M Tris-Base, 10% SDS, 50% Glycerol, 5% 2-mercaptoethanol, and 0.025% w/v Bromophenol Blue) to obtain a final 1x concentration of SDS Sample Buffer. Samples

were boiled at 100°C for 10 minutes, incubated on ice for 10 minutes, loaded onto a 10% SDS polyacrylamide gel, separated by SDS-PAGE, and transferred to a nitrocellulose membrane at 100 volts for 2 hours. Membranes containing the transferred proteins were then washed with TBS (20mM Tris-Base, 150mM NaCl, pH 7.6) added with 0.1% Tween-20 (TBST) and blocked with 5% w/v fat free dry milk (Bio-Rad, Hercules, CA) dissolved in TBST. Membranes were then probed with listed primary antibodies diluted in 1% w/v bovine serum albumin (BSA) dissolved in TBST overnight at 4°C. Next, antibodies were removed, membranes were washed three times with TBST, and horse radish peroxidase (HRP) conjugated secondary antibodies diluted in blocking solution were added to the membranes and incubated at room temperature for 1 hour. Following the addition of secondary antibodies, membranes were washed three times with TBST and HRP-induced chemiluminescence signal was produced using Pierce ECL Western Blotting Substrate (Thermo Fisher Scientific). ECL signal from antibody probed protein was detected using autoradiography film (BioExpress, Kaysville, UT) and developer.

RNA Isolation and qPCR Analysis

Cultured cells were washed with PBS and total RNA was isolated using TRIzol Reagent (Thermo Fisher Scientific). Chloroform was added to the TRIzol solution at a 1:5 v/v ratio, mixed, and centrifuged at 12,000 rpm for 15 minutes at 4°C. The clear, upper liquid phase of the separated solution was collected and equal volumes of 100% isopropanol was added, mixed, and centrifuged at max speed for 10 minutes. Precipitated RNA was washed twice by adding 75% ethanol and centrifuged at max speed for 5 minutes. RNA was air dried on ice for 20 minutes, resuspended in nuclease

free water, and RNA concentration was measured using 260/280 nm spectrophotometry. For qPCR analysis of mRNA expression levels, cDNA was first generated from 2 µg of purified mRNA using qSCRIPT reverse transcriptase mix (Quanta Biosciences, Beverly, MA). QPCR assays were performed using SYBR Green PCR Master Mix (Thermo Fisher Scientific) along with primers listed in Supplementary Table S6 and normalized to the L32 gene. For qPCR analysis of microRNA expression levels, reverse transcription was first performed on purified RNA using the TaqMan MicroRNA RT Kit (Applied Biosystems, Foster City, CA) and primers specific for the microRNA. QPCR assays were performed using the TaqMan Universal qPCR Master Mix (Applied Biosystems) along with labeled primer probes specific to the microRNA listed in Supplementary Table S6 and normalized to miR-16. All qPCR reactions were performed using the 7500 Fast Real-Time PCR System (Applied Biosystems).

Chromatin Immunoprecipitation (ChIP) and qPCR Analysis

Zeb1 ChIP was performed following previously reported protocol (48). Briefly, an equal number of epithelial and mesenchymal human lung cancer cell lines were washed with PBS, trypsinized, resuspended in 15 mL conical tubes, crosslinked with 1% formaldehyde at room temperature for 10 minutes, washed with PBS, and incubated in lysis buffer (50 mM Tris-HCl, pH 8.1, 1% SDS, 10 mM EDTA, and protease/phosphatase inhibitor cocktail) on ice for 10 minutes. Cells were then sonicated on ice using 50% amplitude with 10-second pulse intervals and 10-second rest intervals for 20 cycles. Samples were then centrifuged at 14,000 rpm for 5 minutes, supernatant was collected, and immunoprecipitated with 2 µg of Zeb1 antibody or rabbit IgG (Santa Cruz) and rotated at 4°C overnight. Pre-cleared protein A/G agarose

beads (Santa Cruz) were added to each sample and rotated at 4°C for 2 hours. Beads were then centrifuged down at 3,000 g for 2 minutes at 4°C, sequentially washed with Wash Buffer 1 (0.1% SDS, 1% Triton X-100, 2 mM EDTA, 20 mM Tris-HCl pH 8.1, 150 mM NaCl), Wash Buffer 2 (0.1% SDS, 1% Triton X-100, 2 mM EDTA, 20 mM Tris-HCl pH 8.1, 500 mM NaCl), Wash Buffer 3 (0.25 M LiCl, 1% NP-40, 1% deoxycholate, 1 mM EDTA, 10 mM Tris-HCl pH 8.1), and Tris-EDTA (1 mM EDTA, 10 mM Tris-HCl pH 8.1). Immunoprecipitated DNA was eluted using Elution Buffer (1% SDS, 0.1 M NaHCO₃) and incubated at 65°C overnight. DNA was purified using QIAquick PCR Purification Kit (Qiagen, Valencia, CA) and 50 ng of eluted DNA was used for each qPCR reaction using primers, listed in Supplementary Table S6, flanking potential Zeb1 promoter binding sites to quantify relative ChIP signal.

Luciferase Reporter Assay

IL17RD promoter region was cloned from the extracted genomic DNA of H441 cells and inserted into the pGL3-promoter vector (Promega, Madison, WI, USA). Mutations of Zeb1 binding sites were carried out using the QuikChange II XL Site-Directed Mutagenesis Kit (Agilent, Santa Clara, CA, USA). Luciferase reporter assays were carried out by co-transfection of 500 ng of the reporter pGL3 constructs with 50 ng of the pRL-TK renilla luciferase vector (Promega) in H441 cells with inducible GFP or Zeb1 using Lipofectamine 2000 (Thermo Fisher Scientific). Assays were carried out using Dual-Luciferase Reporter Assay System (Promega) where renilla signal was used as an internal control. Relative luciferin signal was normalized to signal from the empty pGL3 promoter vector control. Primers used to clone the IL17RD promoter region and generate the Zeb1 mutants are listed in the STAR Methods.

***In vitro* Drug Response and Cell Growth Assays**

Cells were seeded in 96-well plates at 1,000 cells per well and each row was treated with the indicated concentrations of drug inhibitors where the first row is the solvent control that does not contain any drug. After 72hrs of drug inhibitor treatments, media was removed and WST-1 (Roche) colorimetric cell proliferation reagent was added to each well, incubated at 37°C for 2 hrs and color intensity measured at 450 nm with 690 nm reading subtracted for background. Percent surviving fraction of cells were normalized against cells treated with solvent control only.

***In vivo* Drug Response and Tumor Growth Assays**

For *in vivo* tumor growth assays with transplantation of mouse lung cancer cell lines into syngeneic wild-type mice, cells were injected subcutaneously into the right flanks of male 129/sv mice at 3 months of age and allowed to form tumors for 3 to 4 weeks when tumor volumes were approximately 150 to 200 mm³ measured using digital calipers. For induced mouse models of lung adenocarcinoma, adenovirus-expressing *Cre* recombinase was administered into mice lungs at 3 months of age by intratracheal intubation at a viral titer of 2.5×10^7 viruses per mouse. After 3 months post-induction, mice lungs were visualized by micro-CT scans to validate tumor formation and measure tumor areas. For spontaneous mouse models of lung adenocarcinoma, mice approximately 7 months of age were scanned by micro-CT to validate lung tumor formation and measure tumor areas. Selumetinib and mocetinostat were administered daily by oral gavage at a dosage of 25 mg/kg mouse weight and 80 mg/kg mouse weight, respectively. Tumor sizes were measured weekly after treatment began.

Selumetinib was dissolved at 5 mg/mL in solvent (4% DMSO, 30% PEG 300, 5% Tween 80) and mocetinostat was dissolved at 25 mg/mL in solvent (30% PEG 400, 0.5% Tween 80, 5% propylene glycol). Control mice received solvent at a volume equal to the drug dosage using calculations at the indicated drug concentrations. Mice weights were measured weekly to adjust total dosage and assess drug combinations on mice health. After euthanasia, syngeneic primary tumors and/or mice lungs were formalin fixed, paraffin embedded, and sectioned for histological analysis.

Immunohistochemistry (IHC)

Paraffin-embedded tissue sections were rehydrated and antigen retrieval was performed using citrate buffer, pH 6.0 (Dako Agilent Technologies, Santa Clara, CA) and boiled for 25 minutes. Endogenous peroxidases were blocked with 3% H₂O₂ in TBS and slides were further blocked with 5% goat serum in TBST. Tissues were probed with indicated primary antibodies diluted in goat serum overnight at 4°C. Antibody dilutions are as follows: Zeb1 (1:200), E-cadherin (1:300), Vimentin (1:150), p-Erk (1:250), p-Mek (1:100). Slides were then washed three times with TBST and incubated with streptavidin conjugated secondary antibodies targeting rabbit IgG diluted in goat serum for 1hr at room temperature. Slides were washed again and incubated with biotinylated HRP in goat serum for 30 minutes at room temperature. After washing, signal was attained by developing with DAB reagent (Dako) for 5 minutes at room temperature. Slides were washed with ddH₂O to stop the reaction and then stained with Harris Hematoxylin (Thermo Fisher Scientific) for 1 minute and rinsed with warm tap water for 5 minutes. Slides were dunked eight times in 0.25% HCl in

70% ethanol and rinsed with tap water again for 5 minutes. Slides were dehydrated and mounted for further analysis by bright field microscopy.

Analysis of Human Cancer Dataset and Lung Cancer Cell Line Panel

EMT score was calculated based on the EMT signature previously published (40, 53). Gene expression data from the PROSPECT lung adenocarcinoma dataset as well as a panel of 77 human lung cancer cell lines were used. Spearman correlation was used to quantify the association between EMT score/Zeb1 with IL17RD expression.

Statistics

Unless specified in the above methods, figures, or in-text, all assays were performed using technical triplicates with three experimental replicates for each assay so that a significance p-value less than 0.05 indicates statistical significance using student's t-test.

CHAPTER 3: RESULTS

Project 1: ZEB1 Induces LOXL2-Mediated Collagen Stabilization and Deposition in the Extracellular Matrix to Drive Lung Cancer Invasion and Metastasis

Contents of this chapter are derived from the publication Peng DH, Ungewiss C, Tong P, Byers LA, Wang J, Canales JR, Villalobos PA, Uraoka N, Mino B, Behrens C, Wistuba II, Han RI, Wanna CA, Fahrenholtz M, Grande-Allen KJ, Creighton CJ, Gibbons DL. "ZEB1 induces LOXL2-mediated collagen stabilization and deposition in the extracellular matrix to drive lung cancer invasion and metastasis." *Oncogene*. 2016 Oct 03. PubMed PMID: 27694892 with approval from Nature Publishing Group.

Expression of collagen and ECM-associated genes correlates with EMT

To determine if EMT alters the expression of ECM-associated genes, we correlated gene expression patterns of patient tumor samples across multiple tumor types from the TCGA dataset to our previously reported 76-gene EMT signature score (40). The analysis revealed numerous ECM genes that have significant positive correlation with EMT ($r > 0.5$) in at least six different epithelial tumor types (**Figure 2-5 and Table 1**).

Figure 2

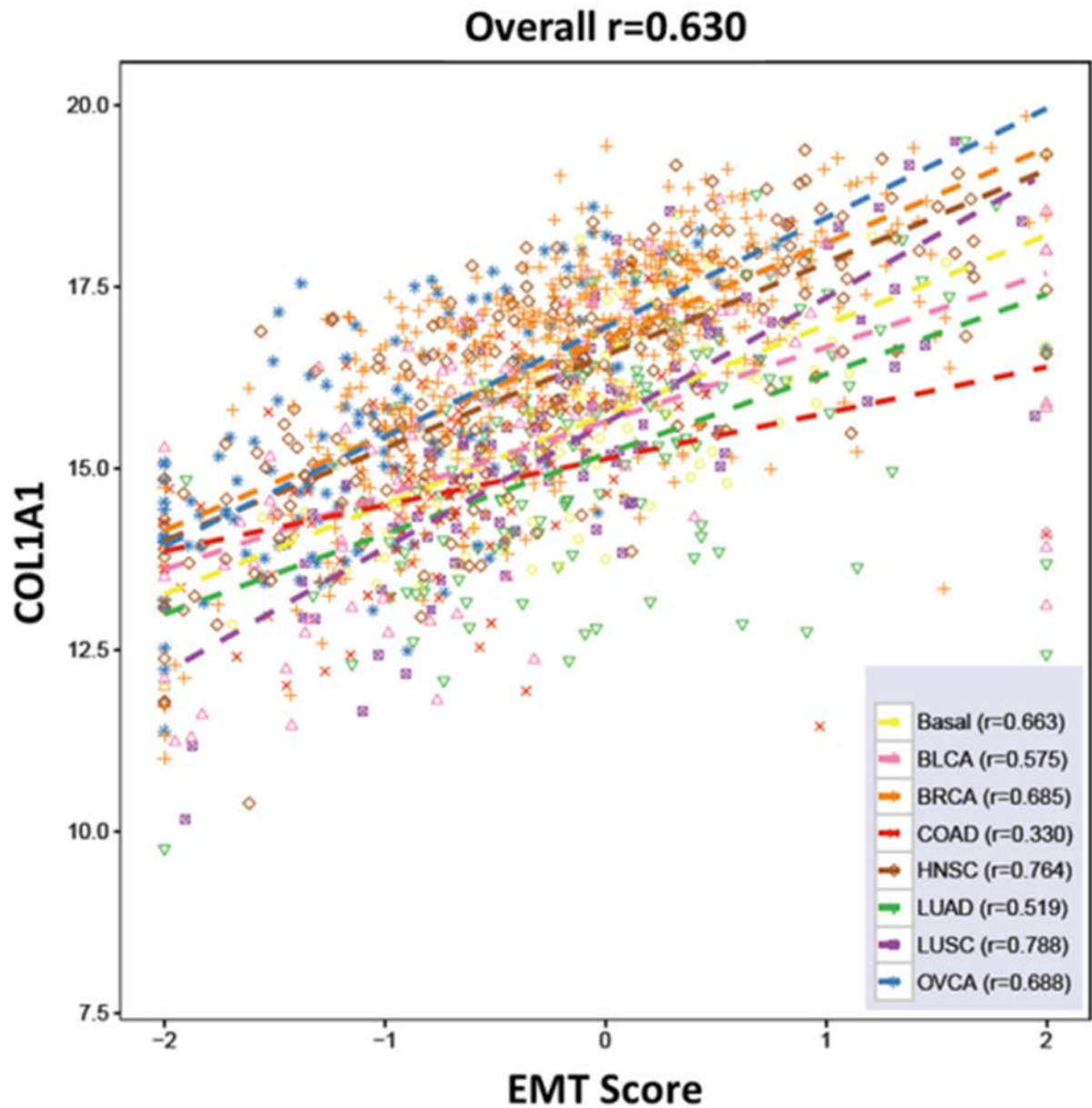


Figure 2. Representative plot correlating gene expression of collagen 1A1 to EMT scores of human tumors from TCGA datasets (BASAL: Basal-like breast cancer; BLCA: Bladder Urothelial Carcinoma; BRCA: Breast invasive carcinoma; COAD: Colon adenocarcinoma; HNSC: Head and Neck squamous cell carcinoma; LUAD: Lung adenocarcinoma; LUSC: Lung squamous cell carcinoma; OVCA: Ovarian carcinoma).

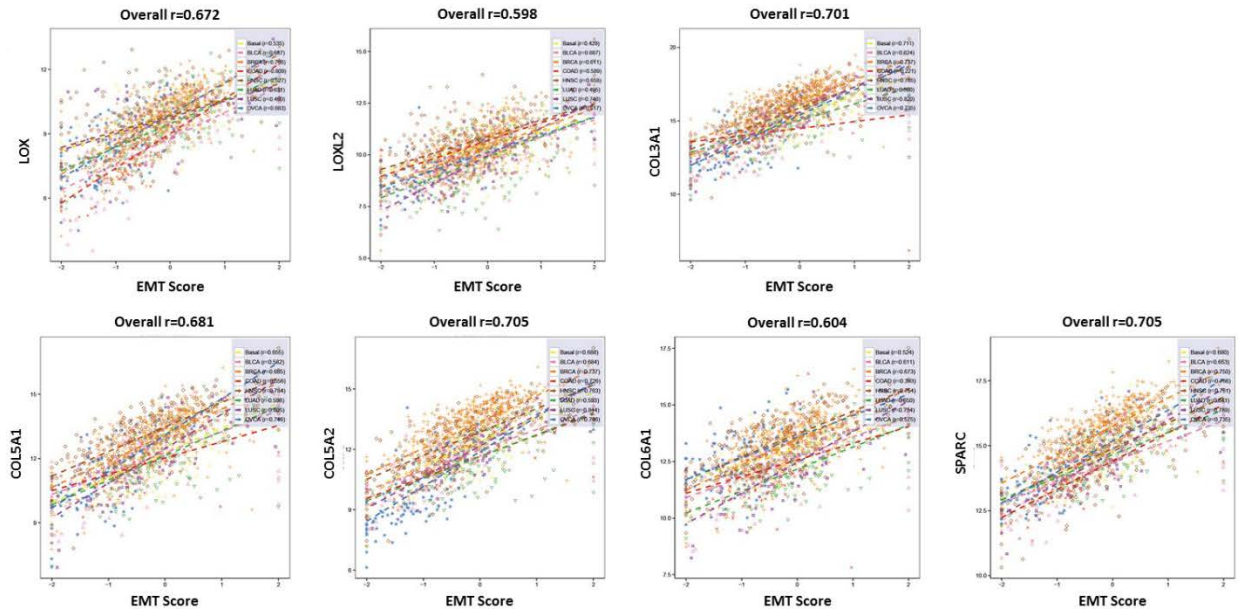


Figure 3. Correlation plots for expression of representative genes and EMT scores of human tumors from TCGA datasets (BASAL: Basal-like breast cancer; BLCA: Bladder Urothelial Carcinoma; BRCA: Breast invasive carcinoma; COAD: Colon adenocarcinoma; HNSC: Head and Neck squamous cell carcinoma; LUAD: Lung adenocarcinoma; LUSC: Lung squamous cell carcinoma; OVCA: Ovarian carcinoma).

Kolmogorov-Smirnov test p value: 8.60e-11

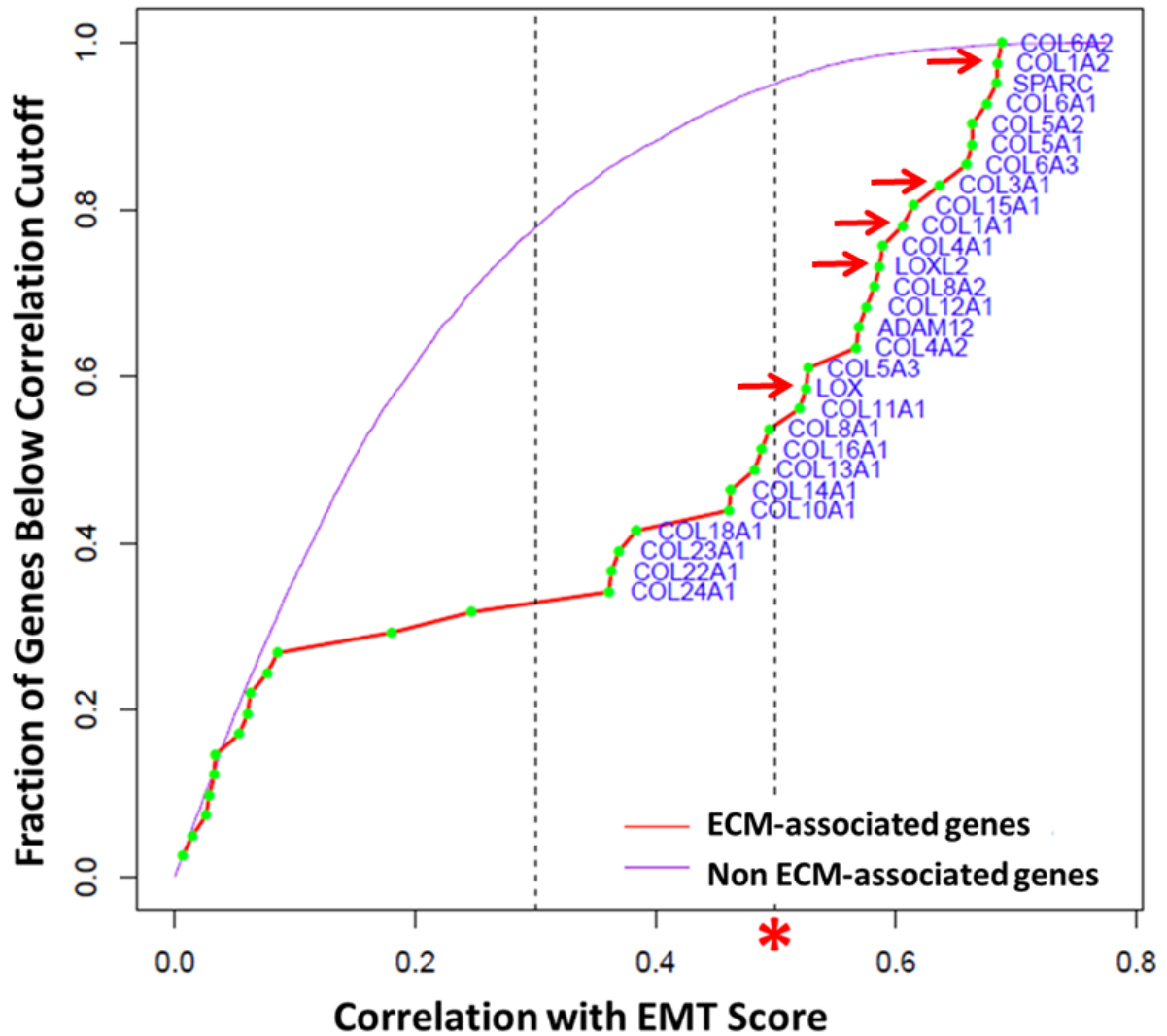


Figure 4. Graph showing the fraction of genes from TCGA dataset analysis below the correlation value to EMT score. Purple line represents genes that are not associated with the ECM but still correlated with EMT gene signatures. ECM-related genes are represented by the red line with collagen-associated genes specifically denoted by green points. Collagen genes above a high correlation cutoff ($r > 0.5$), as indicated by the red asterisks, were selected for further validation. Red arrows indicate qPCR validated collagen-associated genes that were consistently downregulated by miR-200, upregulated by Zeb1, and selected for further analyses.

Table 1. List of ECM-associated genes with strong, positive correlation ($r>0.5$) to 76-gene EMT signature score of human tumors from TCGA datasets (BASAL: Basal-like breast cancer; BCLA: Bladder Urothelial Carcinoma; BRCA: Breast invasive carcinoma; COAD: Colon adenocarcinoma; HNSC: Head and Neck squamous cell carcinoma; LUAD: Lung adenocarcinoma; LUSC: Lung squamous cell carcinoma; OVCA: Ovarian carcinoma). Spearman's correlation and p-value significance are provided for each gene.

Gene	Correlation	P-value			
OLFML2B	0.77508867	0	LOXL3	0.68641251	0
BNC2	0.75144666	0	COL1A2	0.68476766	0
ZEB1	0.74211264	0	SPARC	0.68381357	0
TIMP2	0.74029499	0	ANXA6	0.68346918	0
VIM	0.73904264	0	PMP22	0.68069249	0
FN1	0.72825134	0	SH2B3	0.68030065	0
NID2	0.7237854	0	ANGPTL2	0.67999649	0
ZEB2	0.72032535	0	MSRB3	0.67685026	0
CALD1	0.71446639	0	COL6A1	0.67548305	0
RECK	0.70482075	0	ADAM19	0.6747945	0
FBN1	0.70115155	0	VCAN	0.67221469	0
ZNF521	0.69907582	0	OLFML1	0.67184317	0
LAMA4	0.69839197	0	EMILIN1	0.67138064	0
FMNL3	0.69755876	0	ARSB	0.67089987	0
AXL	0.69564199	0	NAV3	0.67039979	0
ST3GAL2	0.69548142	0	CNRIP1	0.66638559	0
PDGFRB	0.69419038	0	BICC1	0.66526175	0
CDH11	0.68852288	0	DACT1	0.66516554	0
COL6A2	0.68809068	0	GPC6	0.66489744	0
			COL5A2	0.66363698	0

COL5A1	0.66338205	0
AEBP1	0.66304922	0
RASGRF2	0.66253018	0
GLT8D2	0.66240907	0
HLX	0.66164494	0
SIRPA	0.66119581	0
COL6A3	0.65892982	0
MMP2	0.65889674	0
IGDCC4	0.65876848	0
WIPF1	0.65860069	0
ENOX1	0.65831566	0
GPR124	0.65746105	0
DAB2	0.65628326	0
THBS2	0.65404242	0
KIAA1462	0.65379381	0
GNG2	0.65211636	0
TGFB1I1	0.65085971	0
ADAMTS2	0.64958316	0
FAM26E	0.64890295	0
TGFB3	0.64839858	0
ZCCHC24	0.64616239	0
ADAMTS12	0.64516515	0
FMOD	0.64411747	0

CD248	0.64290082	0
PLXDC2	0.64143974	0
UNC5C	0.64064163	0
POSTN	0.63946182	0
PLEKHO2	0.63919276	0
KIAA1949	0.63841105	0
COL3A1	0.63651347	0
TSHZ3	0.63629818	0
STARD13	0.63616955	0
CSGALNACT2	0.63560212	0
FSTL1	0.6347633	0
APBB2	0.63197225	0
GFPT2	0.63002586	0
LRRC32	0.62860966	0
DCHS1	0.62855691	0
GLIPR1	0.62822223	0
ENTPD1	0.62470949	0
CHN1	0.6246143	0
RASA3	0.62393159	0
ITGA4	0.62382507	0
SGCD	0.62344533	0
FAP	0.62286049	0
FLI1	0.62256676	0

EMP3	0.62149209	0
ETS1	0.62135446	0
PCOLCE	0.61920804	0
C13orf18	0.61894071	0
GAS7	0.61809719	0
INHBA	0.61721075	0
CXCL12	0.61670548	0
ECM2	0.61474174	0
COL15A1	0.61469936	0
BGN	0.61459953	0
SULF1	0.61367607	0
FGD5	0.61225814	0
STARD8	0.61202985	0
AKAP2	0.61179793	0
TRPV2	0.61135787	0
SCARF2	0.61127639	0
FAM101B	0.61089855	0
MMP16	0.60876548	0
LHFPL2	0.60732466	0
THY1	0.6067692	0
EDNRA	0.60675019	0
PDZRN3	0.6064567	0
ASAM	0.60643947	0

NAP1L3	0.60616964	0
COL1A1	0.60560262	0
PALM2.AKAP2	0.60447824	0
PCDHGA12	0.6041466	0
ISLR	0.60411733	0
ENPP2	0.60398382	0
ACTA2	0.60315228	0
PCDH18	0.60262364	0
RHOJ	0.60209399	0
GNAI2	0.60162085	0
SYDE1	0.60060704	0
CPXM1	0.60044688	0
PPAPDC3	0.59908974	0
VCAM1	0.5988555	0
FPR3	0.59857547	0
DDR2	0.59836227	0
ANTXR1	0.59832674	0
F2R	0.59765524	0
CEP170	0.59703612	0
TIMP3	0.59563893	0
ARHGAP31	0.59405935	0
CTSK	0.59319061	0
DOCK10	0.59295261	0

ZNF423	0.59242547	0
HTRA1	0.59169298	0
CRISPLD2	0.59162205	0
EMILIN2	0.59116507	0
PRKG1	0.59066862	0
SERPING1	0.59062266	0
ZNF469	0.58953083	0
COL4A1	0.58892143	0
PRRX1	0.58657604	0
LOXL2	0.58642912	0
VGLL3	0.58603346	0
HRH2	0.5859803	0
SGIP1	0.58589894	0
FIBIN	0.58499253	0
CCDC80	0.58434576	0
HEG1	0.58380878	0
FILIP1L	0.58335161	0
HIC1	0.58316725	0
IFFO1	0.58272338	0
COL8A2	0.58229285	0
NLRP3	0.58221179	0
FAM180A	0.58127719	0
DACT3	0.58071685	0

SSPN	0.5807097	0
MRC2	0.58058602	0
LILRB2	0.58038402	0
LIX1L	0.58034509	0
VASH1	0.58031565	0
COLEC12	0.57852232	0
TNS3	0.57755578	0
KCTD12	0.57751447	0
CSF1R	0.57748032	0
BMP2K	0.57736826	0
PTGIR	0.57713461	0
LRRC8C	0.57707852	0
STK10	0.57636374	0
KCNMB1	0.57632911	0
PDGFC	0.57578105	0
COL12A1	0.57540518	0
NEXN	0.57527429	0
FAM38B	0.57508039	0
FCGR2A	0.57480353	0
ZFPM2	0.57406712	0
MMP14	0.5737316	0
EPB41L2	0.57295245	0
TLR4	0.57252759	0

FLJ10357	0.5721361	0
CCDC88A	0.57193816	0
MRVI1	0.57161564	0
ENG	0.57068932	0
LRRC15	0.57018244	0
GAS1	0.56949604	0
ADAM12	0.5690462	0
IGSF21	0.56879705	0
CD300C	0.5677861	0
COL4A2	0.56701767	0
FBLN2	0.56684995	0
MXRA5	0.56673473	0
CD93	0.56637394	0
TMEM26	0.56621647	0
LZTS1	0.56492096	0
EFEMP2	0.56477457	0
BTBD19	0.56468529	0
CMTM3	0.56462085	0
FNDC1	0.56424922	0
CMKLR1	0.56413466	0
C10orf72	0.56396836	0
TNFSF4	0.56344551	0
PDE1B	0.56255144	0

SLAMF8	0.56189811	0
CDK14	0.56107461	0
EBF1	0.56101757	0
TGFBI	0.56041968	0
CD209	0.56023633	0
C3AR1	0.55989301	0
PRR16	0.55983782	0
ISM1	0.55911821	0
PREX1	0.55874676	0
THBS1	0.55859721	0
GYPC	0.5585835	0
LRRC25	0.55847901	0
CD163	0.55790287	0
ANTXR2	0.55715334	0
ITGB3	0.55687892	0
PLXNC1	0.55521357	0
WISP1	0.55499554	0
GXYLT2	0.55496526	0
SIRPB1	0.55485654	0
ROR1	0.55471385	0
TMEM200A	0.55411464	0
ITGA1	0.55386978	0
ARHGEF6	0.55359828	0

DSE	0.55321348	0
LAMB1	0.55305099	0
ADAMTS6	0.55302978	0
MPP1	0.55270892	0
EVC	0.55245465	0
C5AR1	0.55187613	0
MYLK	0.55159366	0
DOCK2	0.55113667	0
LILRA6	0.55086905	0
CTHRC1	0.55080414	0
SYT11	0.55074656	0
CYTH4	0.54998791	0
CD4	0.54818076	0
PKD2	0.54805273	0
NRP2	0.54762161	0
SEMA6B	0.54723734	0
ITGA5	0.54721087	0
TMEM169	0.54689485	0
MYADM	0.54620367	0
CD86	0.54605186	0
MAN1A1	0.54539591	0
STX2	0.54521555	0
PIK3CG	0.54421985	0

CYSLTR2	0.54414433	0
ODZ3	0.54376811	0
JAM3	0.54337281	0
FCGR2C	0.54293352	0
MITF	0.54291993	0
IL7R	0.54270399	0
DCLK2	0.54243618	0
RAB3IL1	0.54178822	0
CCR1	0.54178447	0
KIAA1755	0.5416801	0
TNFAIP6	0.54152846	0
CLIC4	0.54149622	0
CD14	0.54117471	0
LRRC17	0.54110479	0
LPAR4	0.54109895	0
PRICKLE1	0.54098701	0
RUSC2	0.54091918	0
ZYX	0.54087973	0
S1PR3	0.54079324	0
STAB1	0.54059643	0
RAB8B	0.53999609	0
LHFP	0.53993905	0
C14orf49	0.53897834	0

PTRF	0.53881031	0
NCKAP1L	0.53860348	0
MRGPRF	0.53845203	0
QKI	0.53777444	0
MPEG1	0.53757906	0
HAS2	0.53739011	0
LILRB3	0.5373593	0
NETO1	0.53734452	0
ACVRL1	0.5372687	0
CCIN	0.53690666	0
APLNR	0.53663915	0
XYLT1	0.53661847	0
MFRP	0.5361926	0
MAFB	0.53607529	0
CTGF	0.53598762	0
MAGEL2	0.53456384	0
RUNX1T1	0.53435534	0
LCP1	0.5330044	0
C9orf110	0.53293681	0
ALPK2	0.53286964	0
ADAMTS5	0.53282857	0
ENPP1	0.53270561	0
TMEM204	0.53236228	0

SLCO2B1	0.53222394	0
BHLHE41	0.53176594	0
DOK5	0.53115624	0
FCGR3A	0.53109282	0
PDGFRA	0.53062427	0
SAMHD1	0.53041106	0
RASGRP4	0.52972591	0
LRCH1	0.52966404	0
LCP2	0.52961135	0
ITGAM	0.52892733	0
GLIPR2	0.52853382	0
CYBB	0.52829826	0
SPON1	0.52819175	0
CD80	0.52791029	0
ITGA11	0.52754319	0
COL5A3	0.52711254	0
MYL9	0.52709389	0
SLC8A1	0.5270471	0
ABCA6	0.52675033	0
LAIR1	0.52672267	0
LOC399959	0.52671146	0
DENND2A	0.52615231	0
FAM70B	0.52585912	0

DOCK11	0.5258348	0
RCSD1	0.52574283	0
LOX	0.52544659	0
PLXDC1	0.52497023	0
SLA	0.52480561	0
GIMAP4	0.52470005	0
KIRREL	0.52446818	0
HEPH	0.52431315	0
LRP1	0.5242638	0
PIK3R5	0.5241642	0
NLRC4	0.52386314	0
CD84	0.52382308	0
KLHL4	0.52376455	0
CSF2RB	0.52342629	0
GPR176	0.52333796	0
PABPC5	0.52325284	0
GAL3ST4	0.52321702	0
FERMT2	0.5230962	0
LAPTM5	0.5230915	0
RNASE6	0.52297437	0
MRAS	0.52276397	0
PDCD1LG2	0.52269757	0
IL16	0.52245182	0

F13A1	0.52235103	0
SIGLEC9	0.52195907	0
PILRA	0.52149361	0
JPH2	0.52141839	0
C13orf33	0.52104062	0
NCF2	0.52093148	0
C1R	0.52080357	0
SIRPB2	0.52070153	0
SLC7A7	0.52005929	0
CACNA1C	0.5199663	0
COL11A1	0.51975435	0
CSMD2	0.51941365	0
LGALS1	0.51889056	0
CORIN	0.51799816	0
PCDH12	0.51789659	0
ACTN1	0.51772529	0
PDLIM7	0.51658159	0
GIMAP8	0.51657283	0
FAM78A	0.51655948	0
SHANK1	0.51618922	0
TAGLN	0.51563263	0
SSC5D	0.51539308	0
GJD3	0.51508814	0

NOX4	0.5148434	0
CLIP3	0.51458275	0
ADARB1	0.51452833	0
CXorf36	0.51439327	0
CAMK1G	0.51391006	0
CD200	0.51384175	0
C1QTNF1	0.51362574	0
PHLDB1	0.51356649	0
FYB	0.51353884	0
TLN1	0.51309967	0
GPR84	0.51305586	0
FAT4	0.51279157	0
PIK3R6	0.5119378	0
FPR1	0.51186574	0
CCR8	0.51130164	0
LILRB1	0.51055831	0
GPR68	0.51050574	0
CILP	0.51047117	0
TBC1D1	0.51029801	0
MAP3K3	0.51025289	0
MXRA8	0.50993842	0
VEGFC	0.50955409	0
ASPN	0.50946003	0

NFAM1	0.50925368	0
TMEM119	0.50892472	0
HTRA3	0.50889629	0
CLEC11A	0.50842279	0
GPX8	0.50831175	0
SLIT2	0.50794894	0
GAB3	0.50793862	0
AP1S2	0.50754285	0
ADAMTSL1	0.50706649	0
BACE1	0.50657123	0
ITGAV	0.50613737	0
ADAMTS9	0.50594002	0
GAS6	0.50592047	0
FHL3	0.50578779	0
FGFR1	0.50571179	0
LPXN	0.50532377	0
ELTD1	0.50523078	0
LIMS1	0.50510842	0
LATS2	0.5050326	0
OSCAR	0.50488865	0
GNA12	0.50487685	0
SELPLG	0.50440782	0
SLC1A3	0.50429708	0

SGK269	0.5042789	0
SPI1	0.50416362	0
JAZF1	0.50413489	0
MFGE8	0.50385022	0
KCNK13	0.50384933	0
SLC36A1	0.50378346	0
CYR61	0.50367254	0

Focusing this analysis on lung adenocarcinoma and squamous cell carcinoma samples with a high correlation cutoff, we delineated multiple collagen family and ECM-associated genes that showed strong correlation with EMT (**Figure 4**). To validate which specific collagen genes are differentially regulated by miR-200 and ZEB1, we performed qPCR assays of each collagen and collagen-associated gene from Figure 4 in a panel of human and murine epithelial and mesenchymal lung cancer cell lines with overexpression of ZEB1 or miR-200, respectively. Expression of miR-200 in mesenchymal murine and human lung cancer cells (H157 and 344SQ) consistently showed a decrease in mRNA levels for collagen type I, type III, as well as the collagen crosslinking enzymes LOX and LOXL2, which are indicated by red arrows in Figure 4 (**Figure 5**).

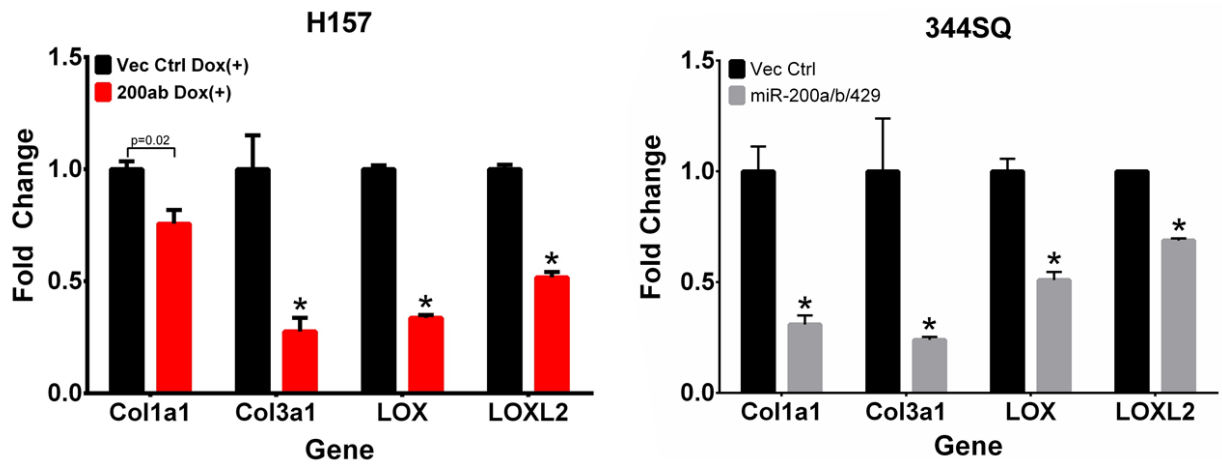


Figure 5. qPCR analysis for relative expression of COL1A1, COL3A1, LOX, and LOXL2 in human H157 and murine 344SQ mesenchymal lung cancer cell lines with inducible and stable miR-200 expression, respectively. Asterisks (*) for qPCR data indicate significance value of $p < 0.01$.

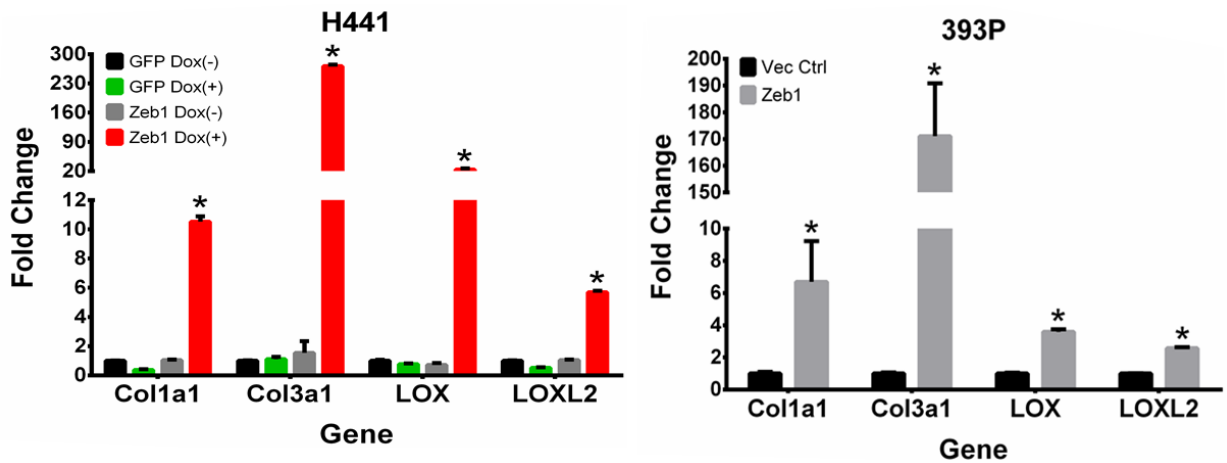


Figure 6. qPCR analysis for relative expression of COL1A1, COL3A1, LOX, and LOXL2 in human H441 and murine 393P epithelial lung cancer cell lines with inducible and stable Zeb1 expression, respectively. Asterisks (*) for qPCR data indicate significance value of $p < 0.01$.

Conversely, ZEB1 expression in epithelial cells (H441 and 393P) consistently displayed an increase in mRNA levels for these genes (**Figure 6**). Further induction of EMT in the metastatic 344SQ murine lung cancer cell line by TGF- β (33) drastically increased expression of the same collagen-associated genes as well (**Figure 7**).

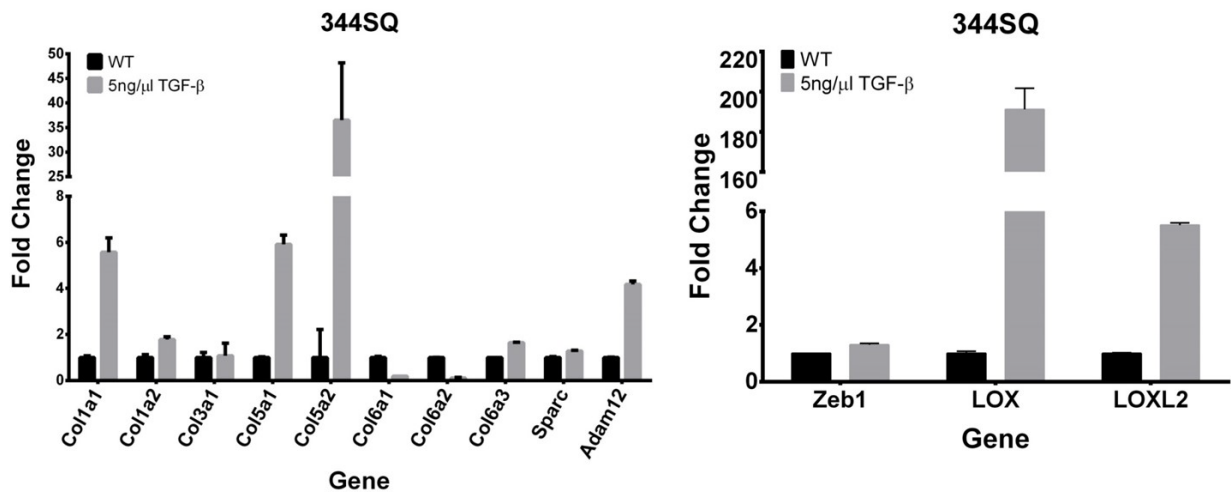


Figure 7. qPCR analysis for relative expression of collagen-associated genes in 344SQ cells treated with TGF- β for 7 days.

This relationship between ECM-associated gene expression and EMT is consistent with results from 3D culture experiments, which demonstrate that Zeb1-mediated mesenchymal lung cancer cell invasion is not only dependent upon extrinsic collagen interaction (33) (**Figure 8**), but requires additional crosslinking, maturation, and deposition of collagen fibers when cultured under low collagen concentrations (62) (**Figure 9**). Although several other collagen genes were correlated with EMT, expression of these genes either showed inconsistent correlation between miR-200 and ZEB1 or had undetectable qPCR signals due to low basal levels of expression in the lung cancer cell lines tested (**Figure 7 and Figure 10**).

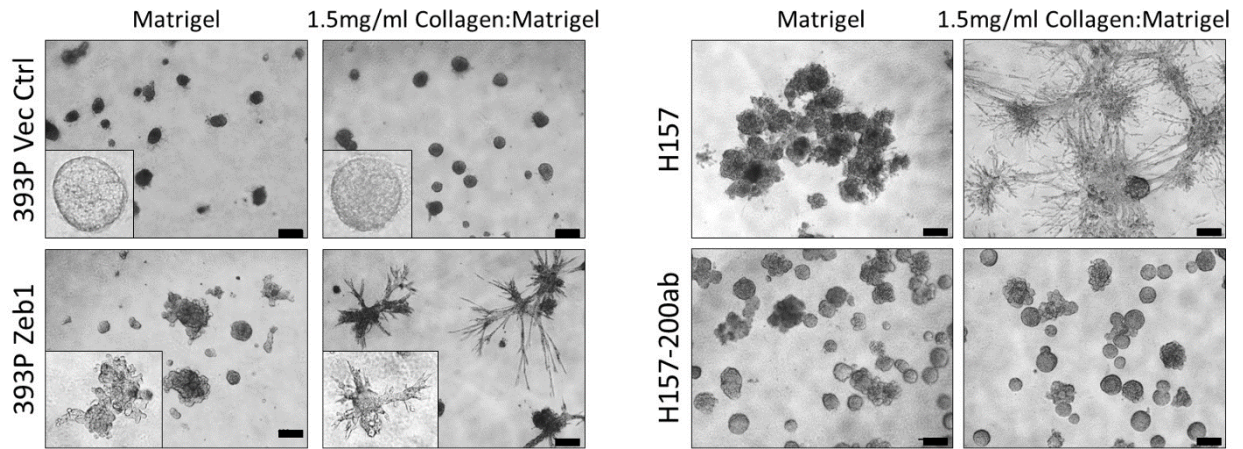


Figure 8. Left: Three-dimensional culture of 393P cells with constitutive Zeb1 or vector control expression in pure Matrigel or a 1:1 mixture of Matrigel and collagen. Right: Three-dimensional culture of H157 cells with inducible miR-200a/b or vector control in pure Matrigel or a 1:1 mixture of Matrigel and 1.5mg/ml collagen. Bright field microscopy images were captured at 4x magnification, scale bars represent 200 μm.

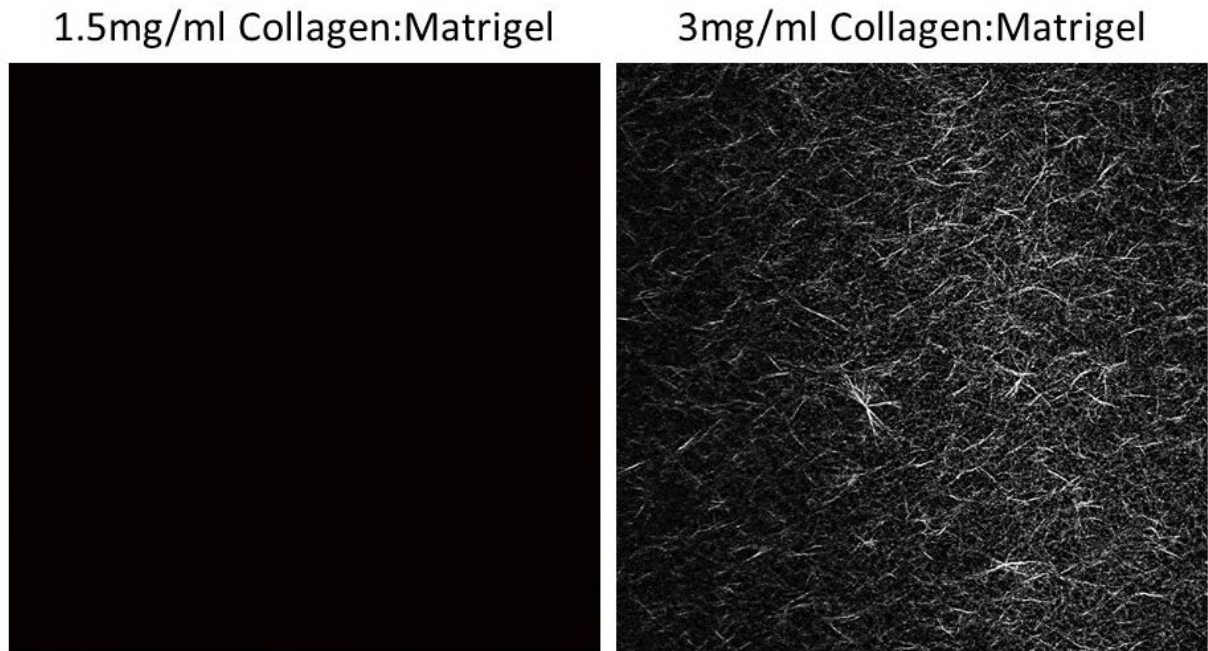


Figure 9. Second harmonic generation (SHG) images of Matrigel/collagen mixtures at 1.5 mg/ml or 3 mg/ml final collagen concentration. Linear fibers at 3 mg/ml concentration indicate crosslinked, mature collagen fibers. Lower concentrations of collagen do not exhibit this crosslinking.

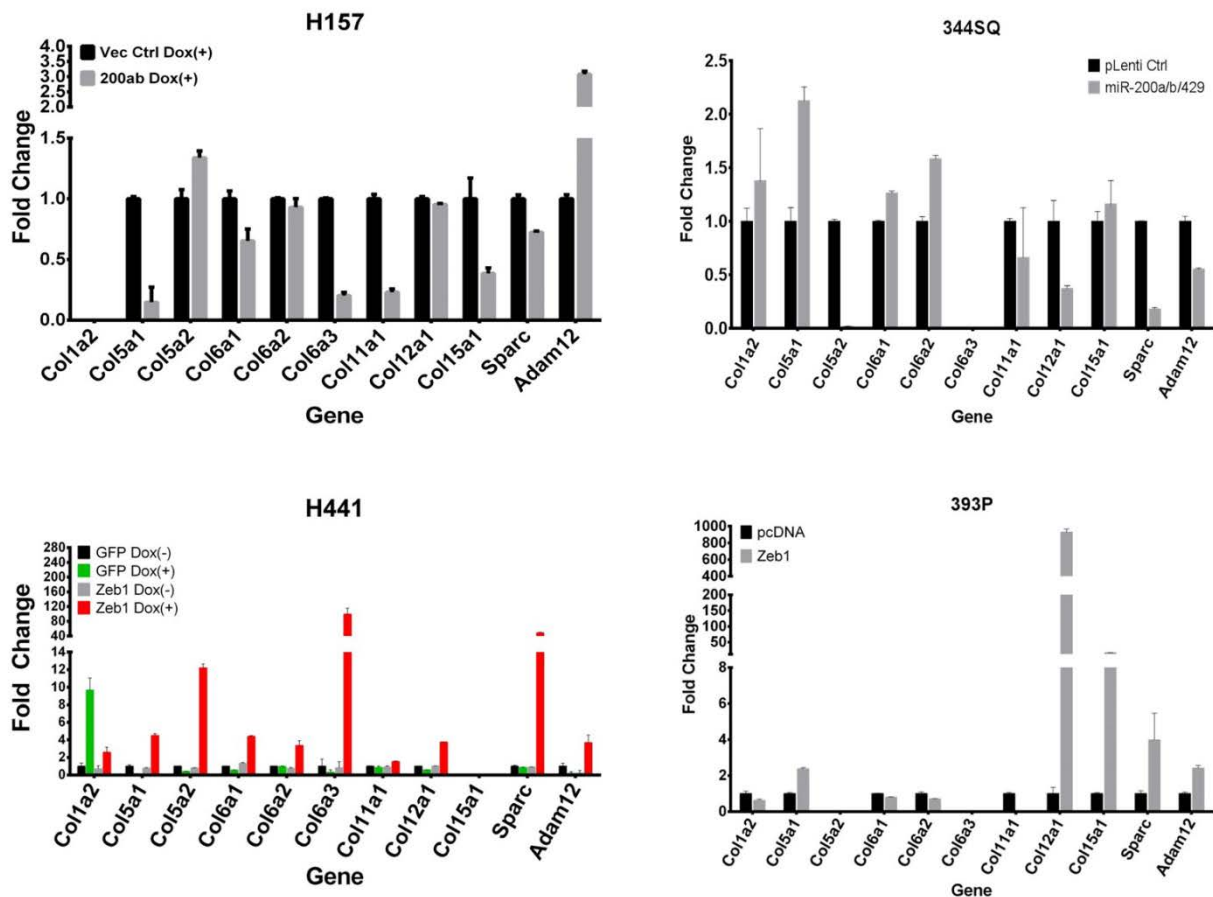


Figure 10. Top: qPCR analysis for relative expression of collagen-associated genes identified from TCGA dataset analysis in Figure 1B in mesenchymal human H157 and murine 344SQ cells with inducible or stable miR-200 expression, respectively. Bottom: qPCR analysis for relative expression of collagen-associated genes in epithelial human H441 and murine 393P cells with inducible or stable Zeb1 expression, respectively.

Metastatic lung tumors have increased LOX, LOXL2, collagen deposition and linearization, correlating with their EMT status

Once we confirmed the correlation between EMT and collagen-associated gene expression *in vitro*, we next sought to verify this correlation *in vivo*. Analysis of primary lung tumors in KP mice capable of metastasis compared to non-metastatic *Kras*^{G12D} mice revealed greater tumor areas presenting EMT patterns (based on Zeb1, E-cadherin, and Vimentin levels), which correlated with increased total collagen, collagen type I/type III deposition, and LOX/LOXL2 expression (**Figure 11**).

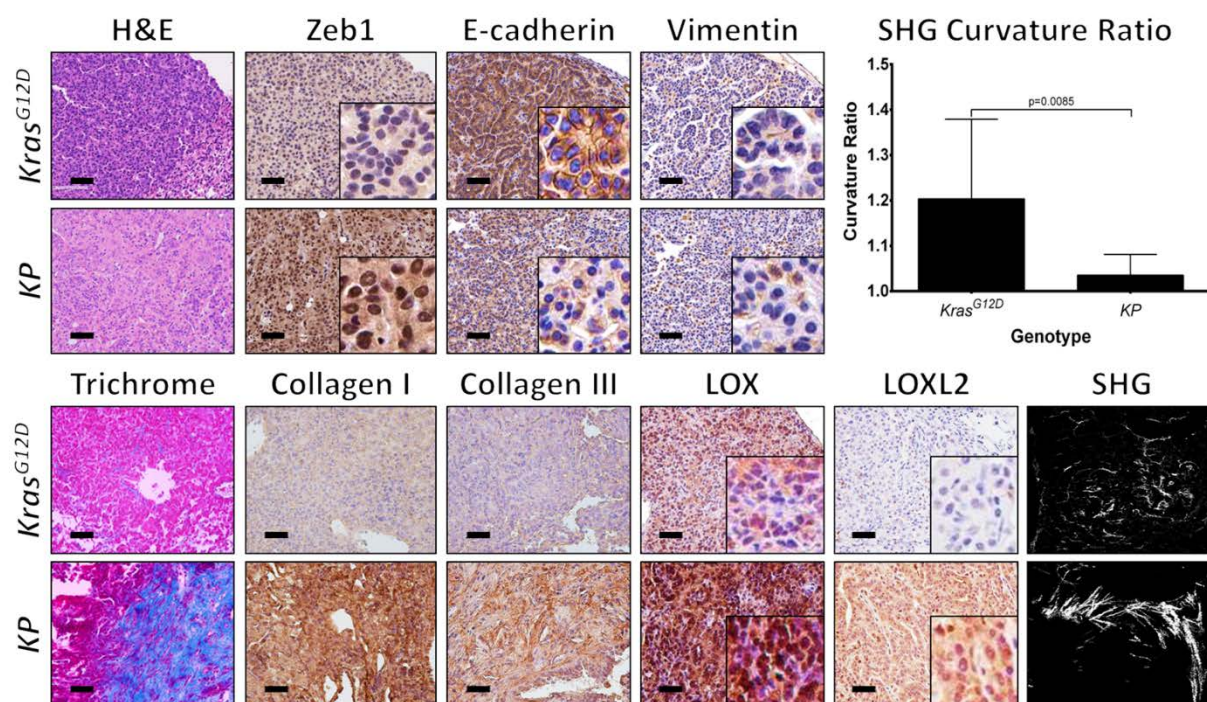


Figure 11. Hematoxylin and eosin (H&E), Masson's trichrome, Zeb1, E-cadherin, Vimentin, collagen type I/type III, LOX, and LOXL2 immunohistochemical (IHC) stains, and second harmonics generation (SHG) microscopy of lung tumor tissues from non-metastatic *Kras*^{G12D} and metastatic *Kras*^{G12D};p53^{R172H} (KP) mice (n=5 tissues per group). Upper right corner: Quantification of curvature ratio for individual collagen fibers (n=50 collagen fibers per sample) imaged by SHG microscopy of tumor tissues. Microscopy images were captured at 20x magnification, scale bars represent 50 μ m.

Second harmonics generation (SHG) microscopy of collagen fibers in the tumor tissues confirmed the increase in collagen density and revealed increased collagen fiber linearization in the KP tumors (**Figure 11**). To validate that mesenchymal lung cancer cells were directly responsible for collagen deposition and fibrillar organization in primary tumors, we analyzed syngeneic tumors generated by subcutaneous injection of the non-metastatic 393P (epithelial) and highly metastatic 344SQ (mesenchymal) murine lung cancer cell lines in syngeneic wild type mice (33). Tissue stains confirmed the mesenchymal phenotype of 344SQ tumors (high nuclear Zeb1, low/mislocalized E-cadherin, and high cytoplasmic vimentin) compared to 393P tumors (low/absent nuclear Zeb1, high/membranous E-cadherin, absent vimentin), correlating with an increase in collagen type I, type III, and LOXL2 expression but no change in LOX levels (**Figure 12**). SHG analysis also showed increased linear collagen fibers in the mesenchymal 344SQ tumors (**Figure 12**). Previous studies have shown that the collagen fiber linearization is dependent on collagen crosslinking by LOX enzymes (62, 98, 99). Our findings suggest that up-regulation of collagen and LOX/LOXL2 in mesenchymal lung cancer cells results in increased collagen deposition and organization in the tumor microenvironment. Because secreted LOX and LOXL2 are potential therapeutic targets (80) that have been implicated as drivers of metastasis in various cancer types (77, 78, 98-100), we sought to further test their mechanistic role in metastasis.

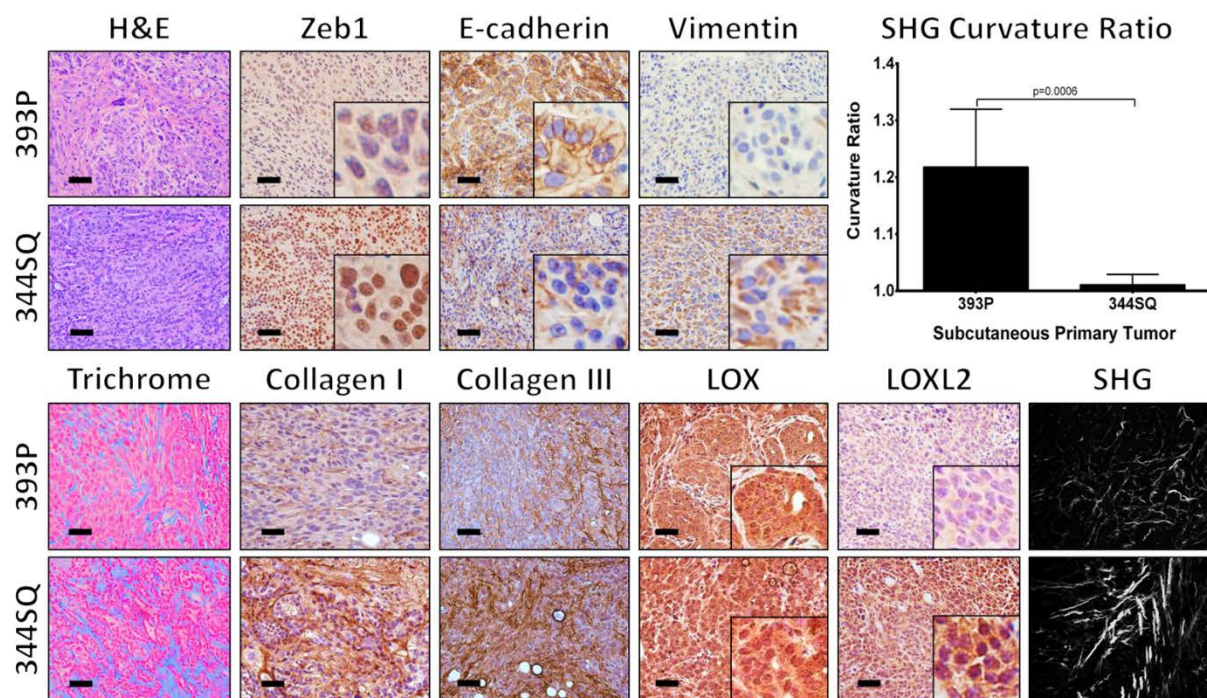


Figure 12. Staining and SHG microscopy of primary syngeneic tumor tissues generated by subcutaneous injection of non-metastatic 393P and metastatic 344SQ murine lung cancer cell lines in syngeneic mice (n=10 tumors per group). Upper right corner: Quantification of curvature ratio for individual collagen fibers (n=50 collagen fibers per sample) imaged by SHG microscopy of tumor tissues. Microscopy images were captured at 20x magnification, scale bars represent 50 μ m.

LOX and LOXL2 are directly regulated by miR-200 and ZEB1, respectively

Since our previous studies have shown that the ZEB1/miR-200 axis is critical in regulating EMT and metastasis (33, 48), we wanted to determine if LOX and LOXL2 expression were regulated by this EMT program. We first evaluated the protein levels of LOX and LOXL2 in the panel of murine and human lung cancer cell lines that we previously characterized (33, 48, 53, 89, 91) and observed higher levels of LOX and LOXL2 in mesenchymal cell lines with higher mesenchymal marker expression (**Figure 13 – 16**). Snail1 does not associate with the EMT status or LOX/LOXL2 expression in these cells, which is consistent with our previous findings (33, 48) that EMT in this system is Zeb1-dependent (**Figure 13**). Although collagen I mRNA levels were higher in mesenchymal cells, collagen III expression did not significantly change between cell lines (**Figure 14**). Analyzing the conditioned media from our murine cell line panel revealed increased secreted LOXL2 protein from mesenchymal cells (**Figure 13**) and demonstrated active LOXL2 enzymatic function by Amplex Red assays (101) (**Figure 17**). Interestingly, we were unable to detect secreted LOX in the conditioned media from any of the cell lines (**Figure 13**). Additional analysis of miR-200 and LOX/LOXL2 gene expression confirmed lower miR-200c levels in mesenchymal cell lines and showed a strong, inverse correlation to LOX and LOXL2 mRNA levels (**Figure 18**). Forced expression of ZEB1 in epithelial murine and human cell lines induced EMT at the molecular level and led to an increase in LOX and LOXL2 protein levels (**Figure 18 – 21**). Ectopic miR-200 expression or siRNA-mediated Zeb1 knockdown in mesenchymal cells had the contrasting effect (**Figure 19, Figure 20, and Figure 22**).

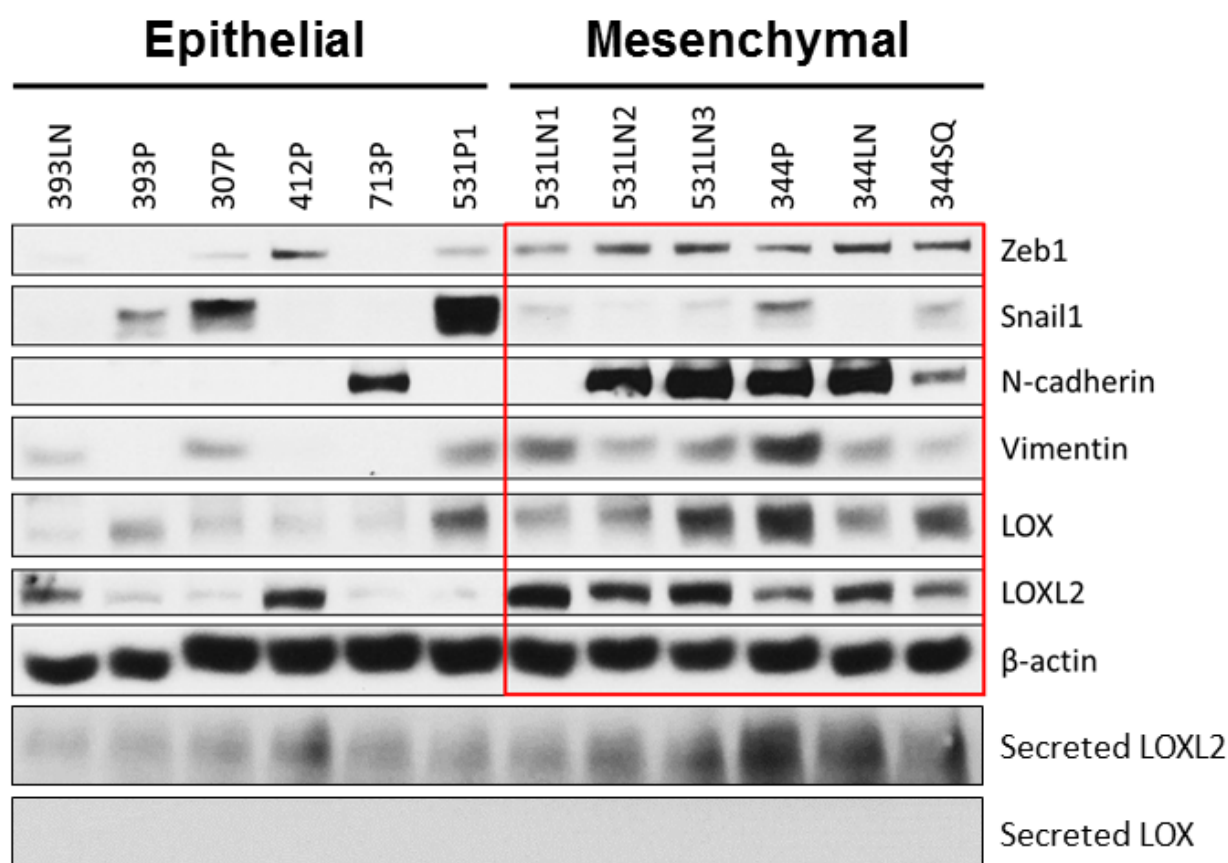


Figure 13. Top: Western blot analysis of Zeb1, Snail1, N-cadherin, Vimentin, LOX, LOXL2, and β -actin (loading control) in a panel of epithelial or mesenchymal murine KP lung cancer cell lines. Bottom: Western blot of secreted LOX and LOXL2 in conditioned media of murine panel cell lines.

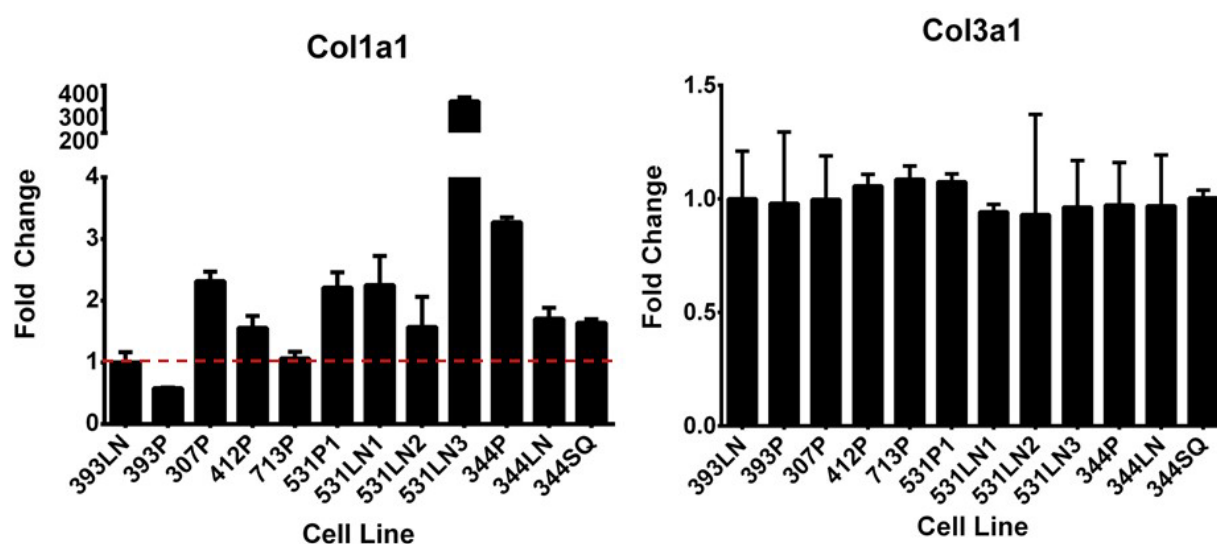


Figure 14. qPCR analysis of relative expression of collagen genes Col1a1 and Col3a1 in murine lung cancer cell line panel.

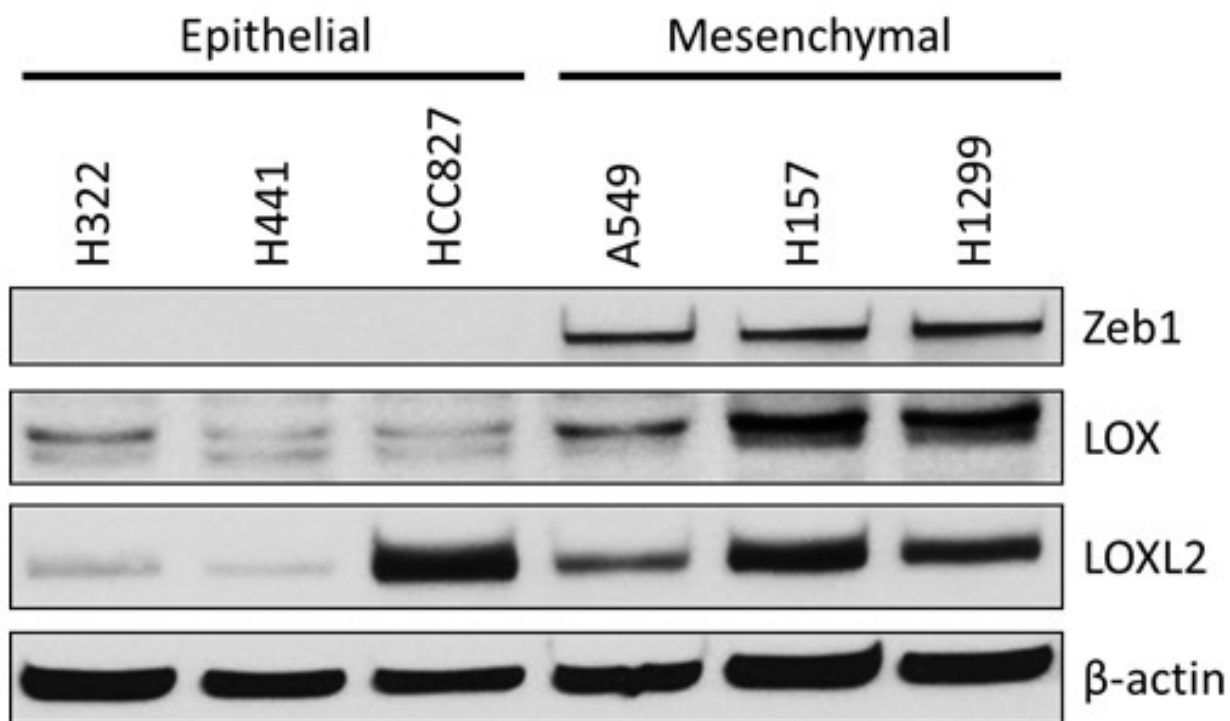


Figure 15. Western blot analysis of Zeb1, LOX, LOXL2, and β-actin in a panel of epithelial or mesenchymal human lung cancer cell lines.

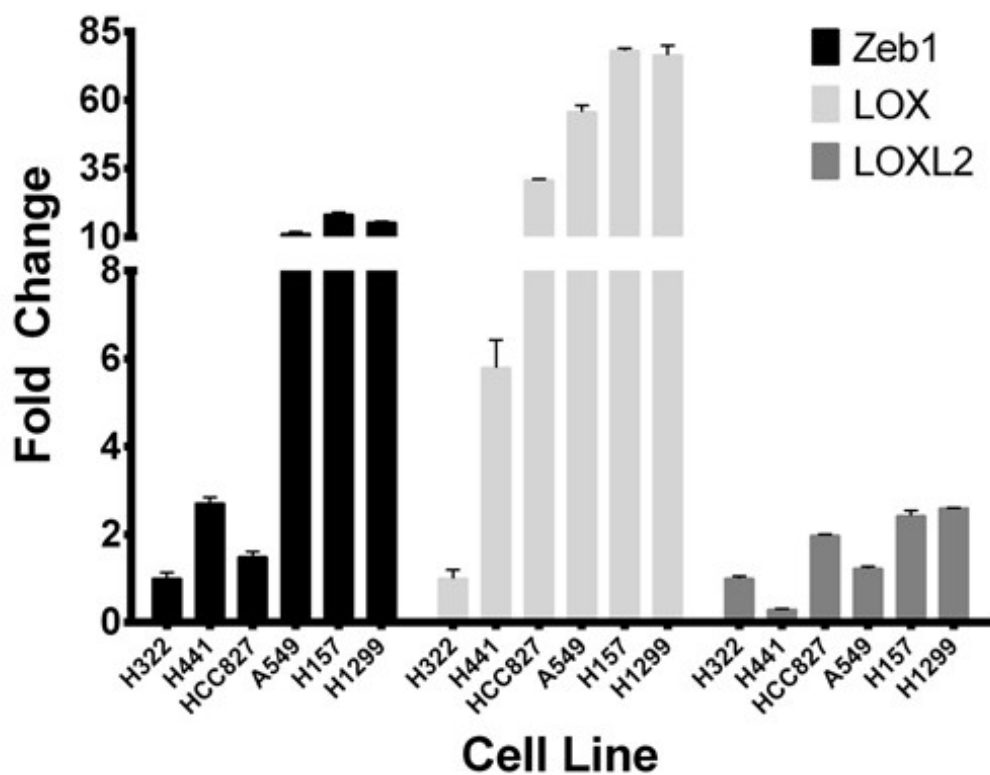


Figure 16. qPCR analysis of relative Zeb1, LOX, and LOXL2 expression in the panel of epithelial or mesenchymal human lung cancer cell lines from Figure 15.

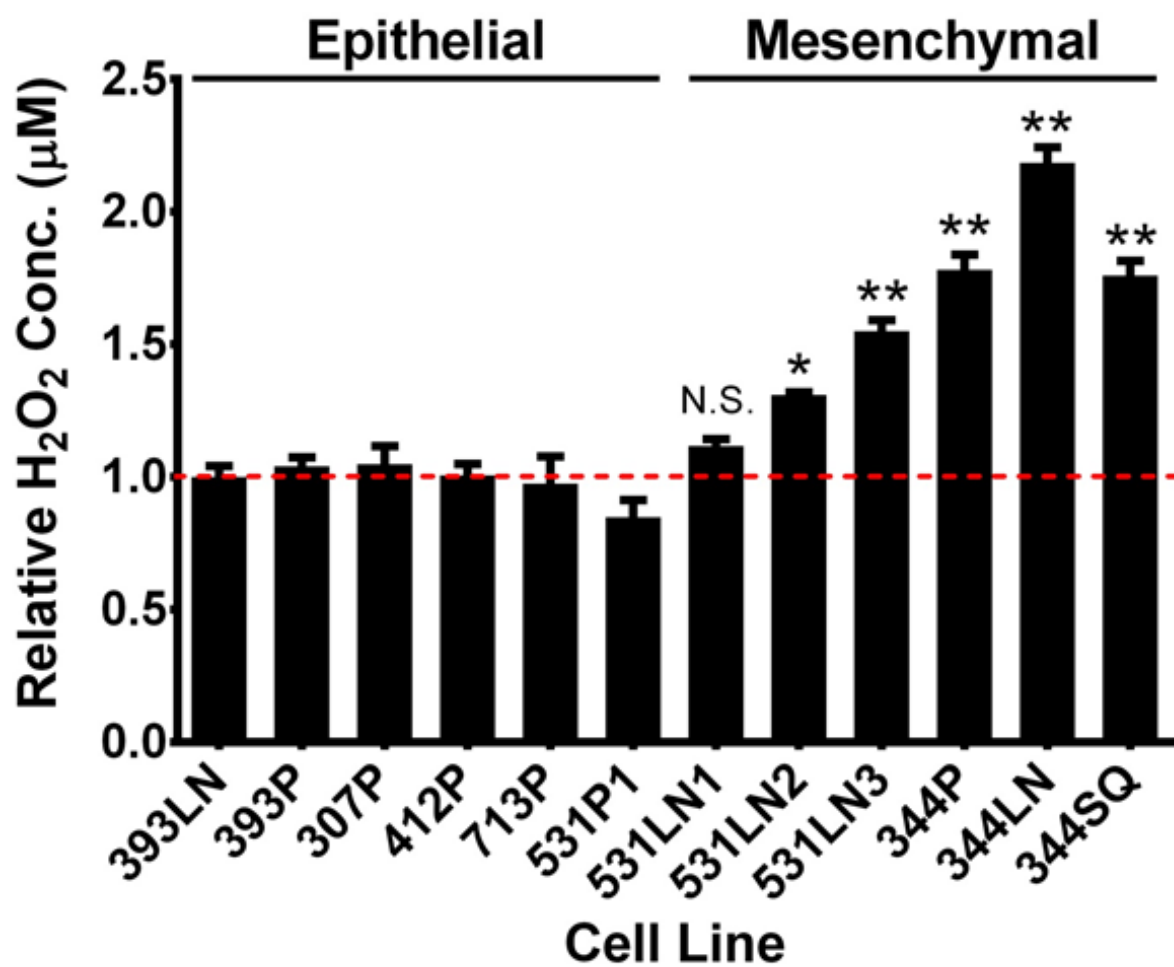


Figure 17. Amplex Red assay to determine LOX/LOXL2 enzymatic activity in conditioned media of murine cell line panel. (*): $p < 0.05$ and (**): $p < 0.01$.

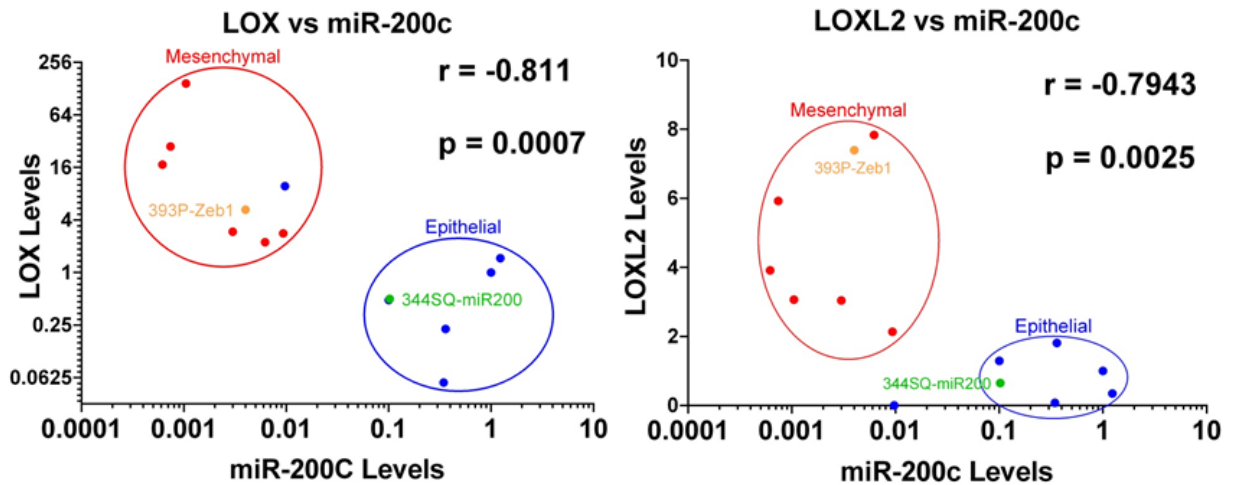


Figure 18. Cluster plots of normalized miR-200c and LOX or LOXL2 mRNA levels in epithelial and mesenchymal murine lung cancer cell lines. 393P-Zeb1 and 344SQ-miR200 cells have also been included in the analysis. Data points represent mean \pm SD ($n = 3$ samples). Spearman's rank correlation used for co-expression analysis.

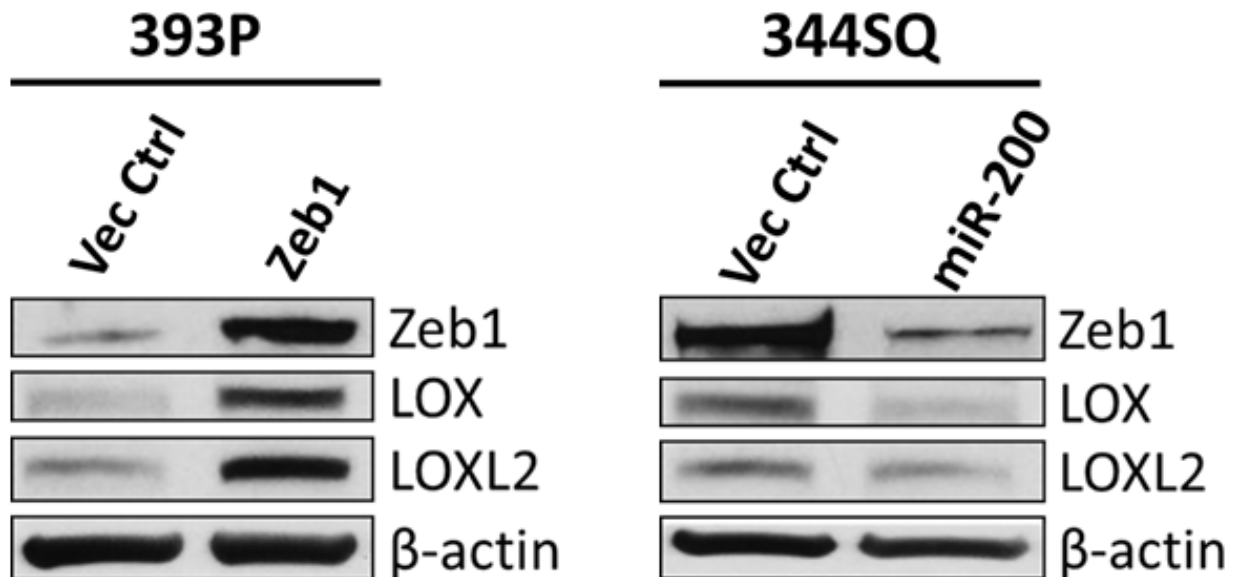


Figure 19. Western blot analysis of Zeb1, LOX, LOXL2, and β -actin in epithelial 393P and mesenchymal 344SQ cell lines with constitutive Zeb1 or miR-200a/b/429 expression, respectively.

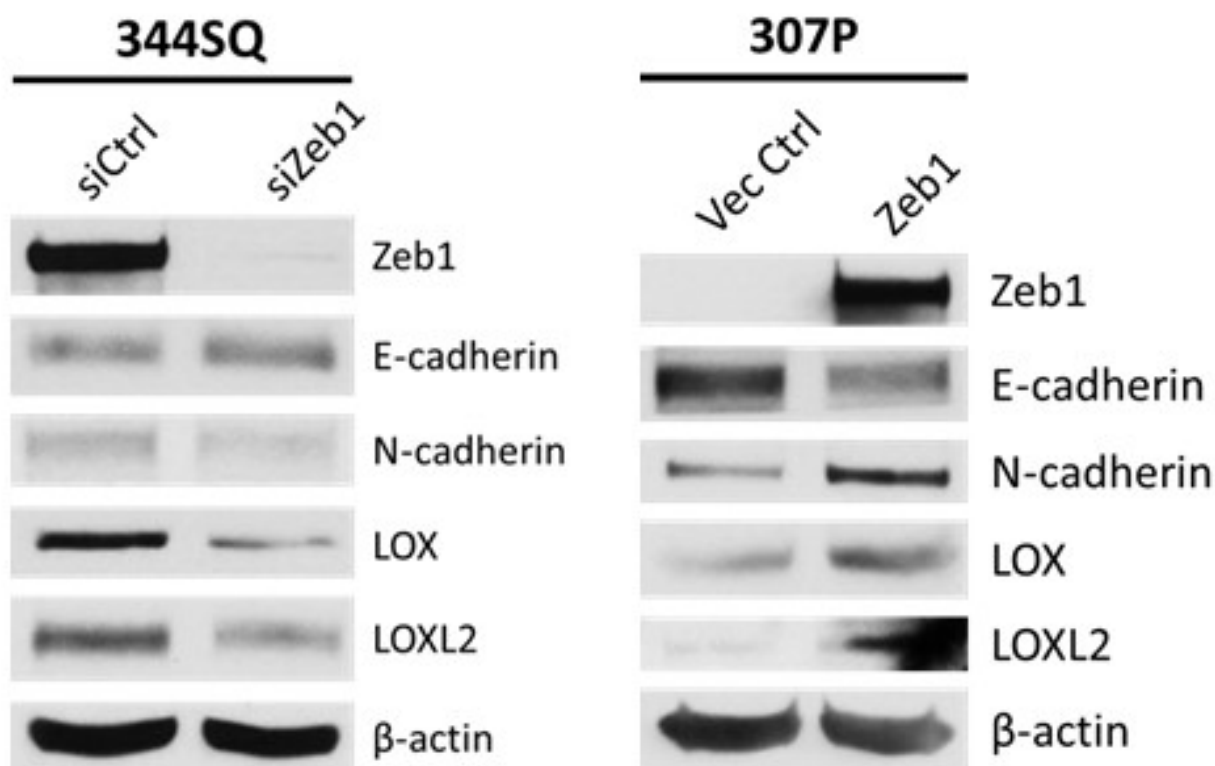


Figure 20. Left: Western blot analysis of Zeb1, E-cadherin, N-cadherin, LOX, LOXL2, and β-actin in 344SQ cells after 48hrs of Zeb1 knockdown by siRNA. Right: Western blot of EMT markers and LOX/LOXL2 in 307P cells after transient overexpression of Zeb1.

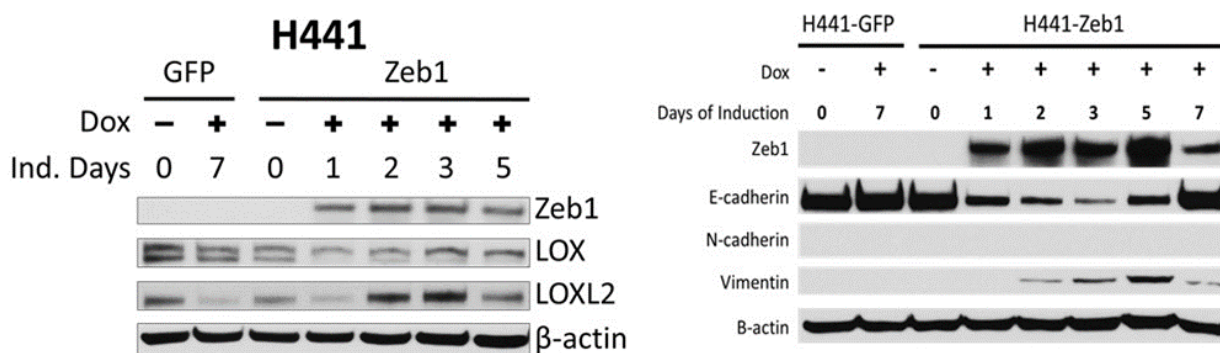


Figure 21. Left: Western blot analysis of Zeb1, LOX, LOXL2, and β-actin in epithelial H441 cells with doxycycline inducible Zeb1 over a 5-day time course. Right: Western blot of Zeb1, E-cadherin, N-cadherin, Vimentin, and β-actin in H441 cells with doxycycline inducible Zeb1.

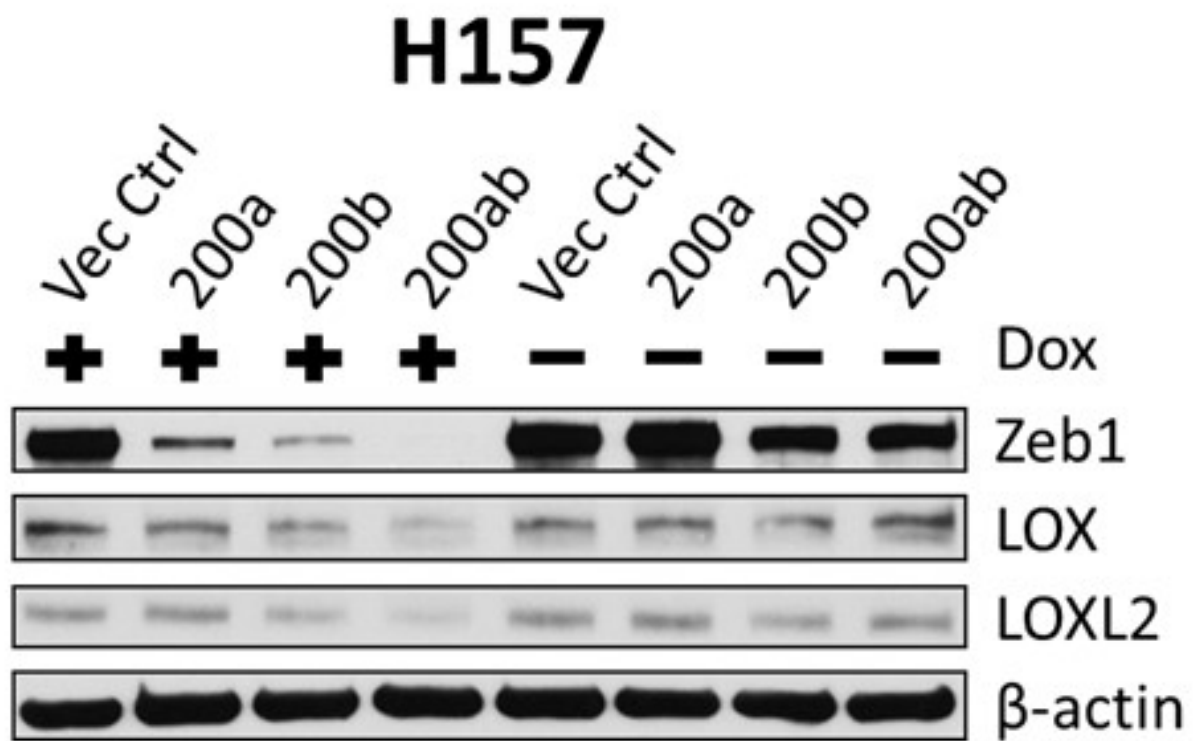


Figure 22. Western blot analysis of Zeb1, LOX, and LOXL2, and β -actin in mesenchymal H157 cells with doxycycline inducible miR-200.

Due to the strong correlation between LOX, LOXL2, and the ZEB1/miR-200 axis, we proceeded to test whether these two enzymes were directly regulated by ZEB1 or miR-200. Evaluating potential microRNA binding sites in the 3'-untranslated region (UTR) of LOX using the TargetScan (www.targetscan.org) algorithm revealed one potential miR-200a and two potential miR-200b/c/429 seed sequences. Luciferase reporter assays with a cloned LOX 3'-UTR showed significant repression in luciferin signal in the presence of miR-200b/c but no repression with miR-200a (**Figure 23**), which was further validated through introduction of miR-200b/c binding site mutations for each site individually or in combination. These findings were consistent with algorithm predictions that showed the first miR-200b site as having strong sequence binding while the miR-200a and second miR-200b sites had weaker complementation (**Figure 24**). Although LOXL2 has no predicted miR-200 binding sites, which we verified by 3'-UTR luciferase reporter assays (**Figure 24 – 25**), the promoter region contains several ZEB1 and ETS1 regulatory sites predicted by the JASPER transcription factor binding database (<http://jaspar.genereg.net/>), which are known to drive transcriptional activity in certain contexts (60, 102, 103).

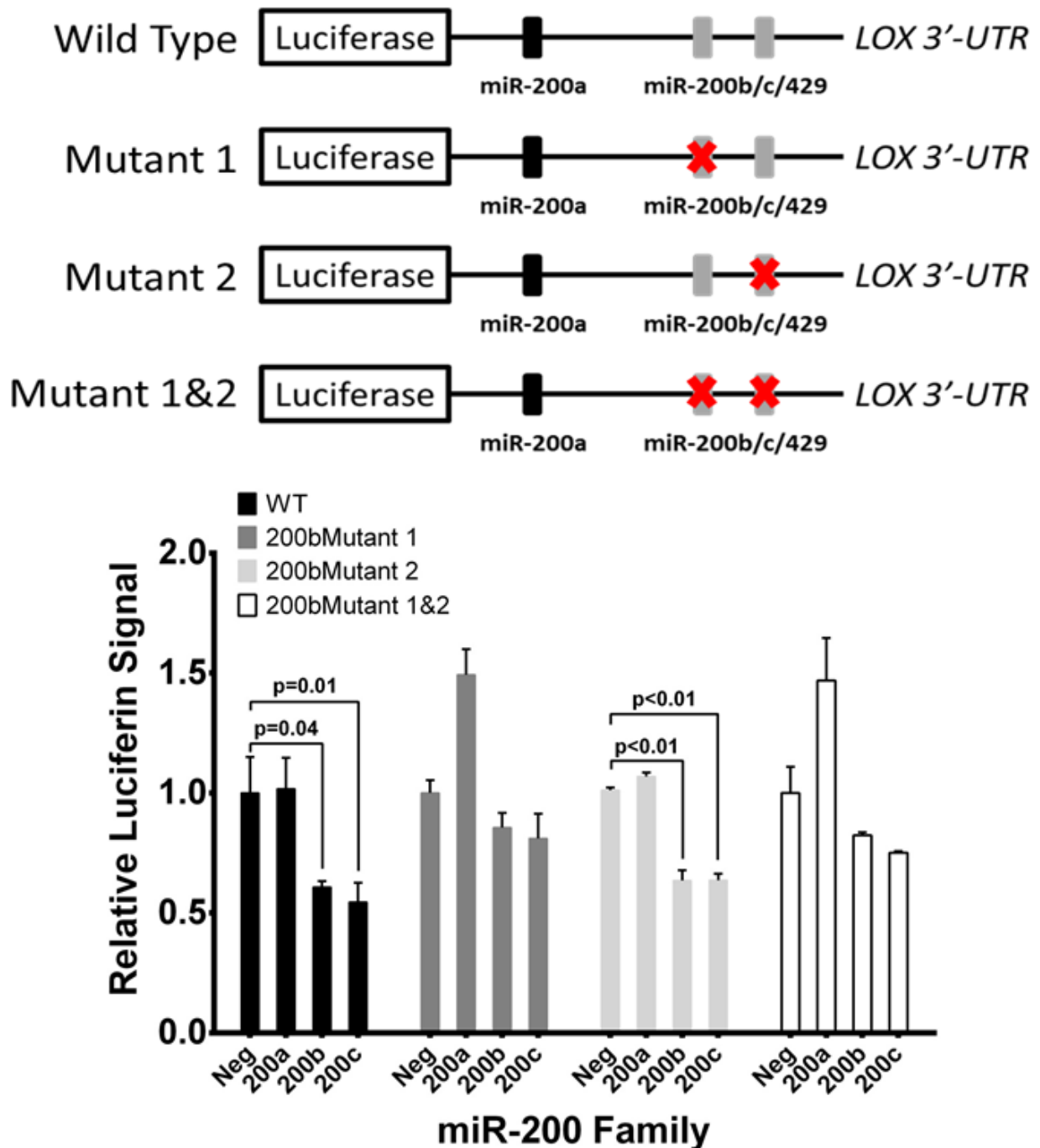


Figure 23. Top: Schematic of luciferase reporter constructs for wild-type (WT) mouse LOX-3'UTR and mutated potential miR-200b/c binding sites. Bottom: Relative luciferase activity of LOX-3'UTR reporter constructs above, co-transfected with non-targeting control miRNA, miR-200a, miR-200b, or miR-200c precursors in 344SQ cells. Three experimental replicates were performed with three technical replicates per experiment.

TargetScan prediction of miRNA sites on 3'-UTR region of LOX

miRNA	conserved sites				poorly conserved sites				Total Context score	Aggregate P _{CT}
	Total	8mer	7mer-m8	7mer-1A	Total	8mer	7mer-m8	7mer-1A		
miR-29abcd	3	0	3	0	0	0	0	0	-0.54	> 0.99
miR-145	1	0	1	0	1	1	0	0	-0.34	0.73
miR-218/218a	1	0	1	0	1	0	1	0	-0.33	0.46
miR-183	0	0	0	0	2	1	0	1	-0.27	< 0.1
miR-24/24ab/24-3p	1	1	0	0	1	0	0	1	-0.27	0.85
miR-200bc/429/548a	2	2	0	0	3	1	0	2	-0.25	0.62
miR-1ab/206/613	0	0	0	0	1	0	1	0	-0.22	< 0.1
miR-30abcdef/30abe-5p/384-5p	1	1	0	0	1	0	0	1	-0.22	0.94
miR-141/200a	0	0	0	0	1	0	1	0	-0.21	0.17

TargetScan prediction of miRNA sites on 3'-UTR region of Col1a1

miRNA family	Conserved sites				Poorly conserved sites				6mer sites	Cumulative weighted context++ score	Total context++ score	Aggregate P _{CT}
	Total	8mer	7mer-m8	7mer-A1	Total	8mer	7mer-m8	7mer-A1				
miR-29-3p	3	1	0	2	0	0	0	0	0	-2.72	-2.76	> 0.99
let-7-5p/98-5p	1	0	1	0	0	0	0	0	0	-0.28	-0.29	0.89
miR-196-5p	1	0	1	0	0	0	0	0	0	-0.22	-0.22	0.83
miR-218-5p	1	1	0	0	0	0	0	0	0	-0.26	-0.26	0.77
miR-133a-3p.2/133b	1	0	0	1	0	0	0	0	1	-0.21	-0.22	0.67
miR-338-3p	1	0	0	1	0	0	0	0	0	-0.26	-0.26	0.31
miR-143-3p	1	0	1	0	0	0	0	0	1	-0.24	-0.24	0.25
miR-24-3p	0	0	0	0	1	0	1	0	0	0.00	-0.02	0.24
miR-34-5p/449-5p	0	0	0	0	1	0	0	1	1	-0.12	-0.12	0.23
miR-146-5p	0	0	0	0	1	0	0	1	0	-0.01	-0.01	0.12
miR-96-5p/1271-5p	0	0	0	0	1	0	0	1	0	-0.01	-0.01	< 0.1

TargetScan prediction of miRNA sites on 3'-UTR region of Col3a1

miRNA family	Conserved sites				Poorly conserved sites				6mer sites	Cumulative weighted context++ score	Total context++ score	Aggregate P _{CT}
	Total	8mer	7mer-m8	7mer-A1	Total	8mer	7mer-m8	7mer-A1				
miR-29-3p	2	2	0	0	0	0	0	0	1	-1.06	-1.71	> 0.99
let-7-5p/98-5p	1	1	0	0	0	0	0	0	0	-0.17	-0.49	0.95
miR-196-5p	1	0	1	0	0	0	0	0	0	-0.13	-0.37	0.81
miR-128-3p	1	0	1	0	0	0	0	0	1	-0.07	-0.20	0.22
miR-129-5p	0	0	0	0	1	0	0	1	0	-0.05	-0.05	< 0.1
miR-33-5p	0	0	0	0	1	0	0	1	1	-0.03	-0.07	< 0.1
miR-192-5p/215-5p	0	0	0	0	1	0	0	1	0	-0.08	-0.23	< 0.1

TargetScan prediction of miRNA sites on 3'-UTR region of LOXL2

miRNA family	Conserved sites				Poorly conserved sites				6mer sites	Cumulative weighted context++ score	Total context++ score	Aggregate P _{CT}
	Total	8mer	7mer-m8	7mer-A1	Total	8mer	7mer-m8	7mer-A1				
miR-29-3p	2	0	1	1	0	0	0	0	0	-0.57	-0.58	0.96
miR-192-5p/215-5p	0	0	0	0	1	0	1	0	0	-0.22	-0.22	0.14
miR-7-5p	0	0	0	0	2	0	0	2	1	-0.20	-0.20	0.10
miR-425-5p	1	0	1	0	0	0	0	0	1	-0.12	-0.12	< 0.1

Figure 24. TargetScan prediction of strongest potential microRNA binding sites on LOX, Col1a1, Col3a1, and LOXL2 3'-UTR.

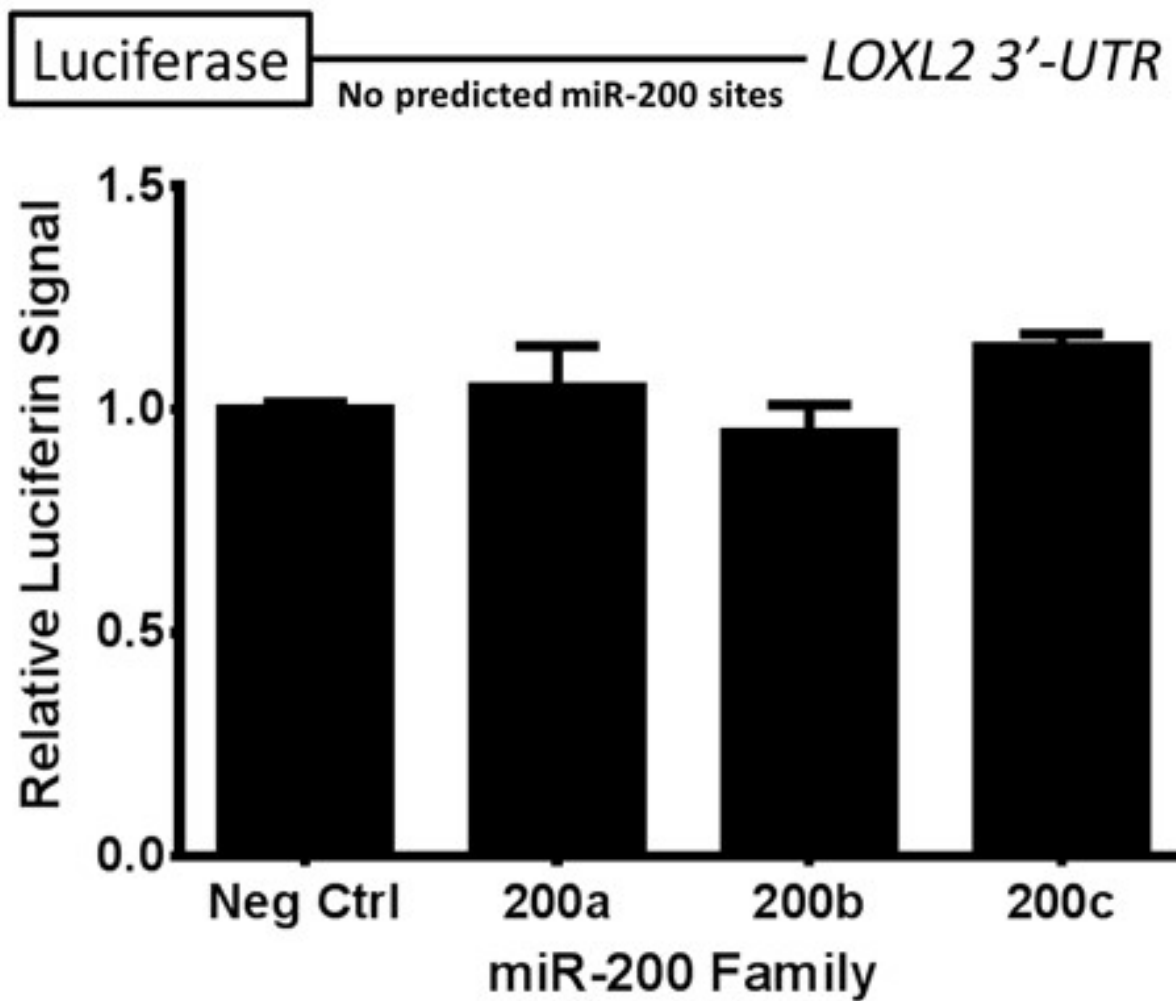


Figure 25. Top: Schematic of LOXL2 3'-UTR showing no predicted miR-200 binding sites. Bottom: LOXL2 3'-UTR luciferase reporter assay following co-expression with miR-200a, 200b, or 200c.

Luciferase reporter assays with the wild-type LOXL2 promoter region confirmed transcriptional regulation by ZEB1, which was verified by introduction of mutations into each of the ZEB1 binding sites individually and in combination. We further confirmed direct binding of ZEB1 to the endogenous LOXL2 promoter region by ZEB1 chromatin immunoprecipitation (ChIP) assays in multiple epithelial and mesenchymal cell lines (**Figure 26**). The collagen I (COL1A1) and collagen III (COL3A1) genes did not show any predicted miR-200 binding sites in their 3'-UTR (**Figure 24**) nor any potential Zeb1 binding sites in their promoters (data not shown), suggesting an indirect mechanism of regulation.

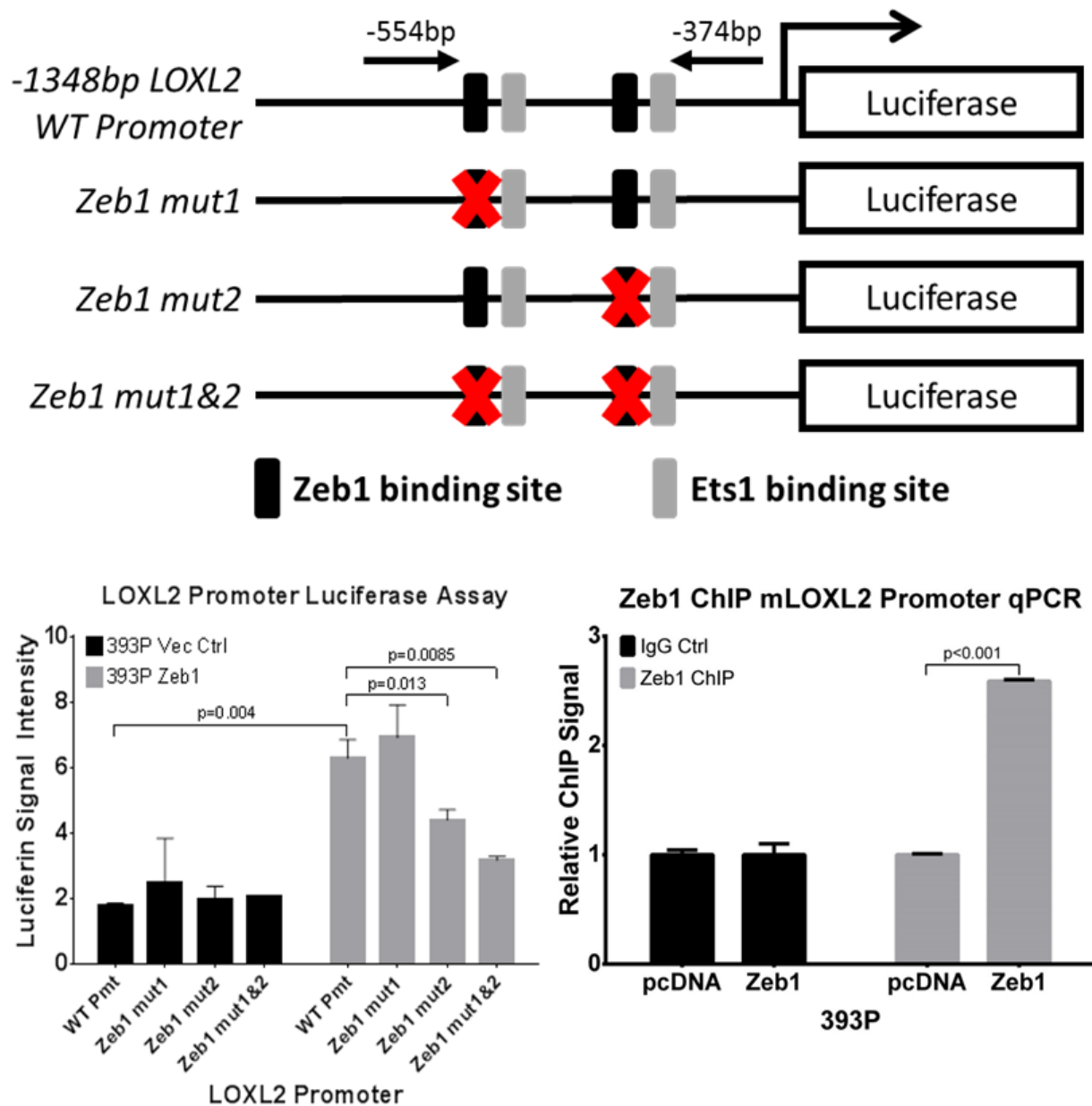


Figure 26. Top: Schematic of luciferase reporter constructs for mouse LOXL2 promoter region containing predicted Zeb1 and Ets1 binding sites. Mutations of potential Zeb1 binding sites indicated with red X and location of qPCR primers to amplify the region containing potential Zeb1 binding sites indicated by black arrows. Bottom-Left: Relative luciferase activity of LOXL2 reporter constructs above transfected into epithelial 393P cells with vector control or Zeb1 expression. Bottom-Right: Fold enrichment by qPCR analysis of LOXL2 promoter segments containing potential Zeb1 binding sites after chromatin immunoprecipitation in 393P-pcDNA vector control and 393P-Zeb1 cells, using Zeb1 antibody or mock IgG control antibody.

LOX enzymatic function is necessary for lung cancer cell migration and invasion

We next wanted to assess the functional relevance of LOX and LOXL2 in promoting lung cancer cell migration and invasion. Inhibition of pan-LOX enzymatic activity with β -aminopropionitrile (BAPN) significantly reduced enzymatic activity in conditioned media (**Figure 27**) as well as Transwell migration and collagen invasion of mesenchymal murine 344SQ, 393P-ZEB1, and human H157 cells, but with no significant change in invasion through laminin-rich Matrigel (**Figure 28**). BAPN treatment of 393P-ZEB1 cells significantly reduced formation of invasive structures in 3D Matrigel/collagen I (**Figure 29**) and reduced invasion of 344SQ cells through Matrigel alone upon TGF- β induction (**Figure 30**). Because LOX enzymes require copper as a co-factor, we also utilized the copper chelator D-Penicillamine (D-Pen) to inhibit LOX enzyme function and observed a significant reduction in 393P-ZEB1 2D migration/invasion in Transwell assays or 3D Matrigel/collagen I assays (**Figure 31**). We observed no adverse effects of the inhibitors on cell proliferation and viability (**Figure 32**). We next evaluated the effects of BAPN and D-Pen treatment on metastasis of 344SQ cells in syngeneic mice *in vivo*. Mice that received either inhibitor did not show a significant change in tumor size or metastatic lesions (**Figure 33 – 34**). Interestingly, analysis of collagen fibers by SHG revealed increased linearized collagen in primary tumor tissues (**Figure 35**), which suggests that the inhibitors either do not effectively reach the primary tumors or produced off-target effects. These results are consistent with several studies corroborating the inconsistency and ineffectiveness of chemical LOX inhibitors *in vivo* (80, 98, 104-107).

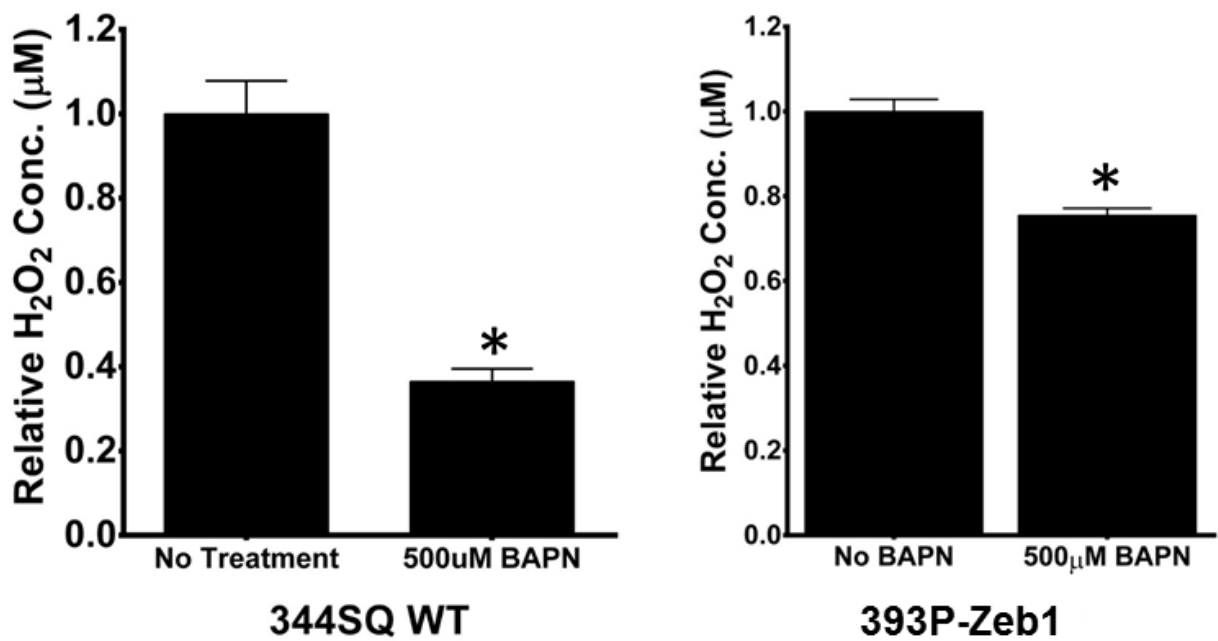


Figure 27. Amplex Red assay to determine LOX/LOXL2 enzymatic activity in conditioned media of 344SQ and 393P-Zeb1 cells with or without 500 μM BAPN treatment.

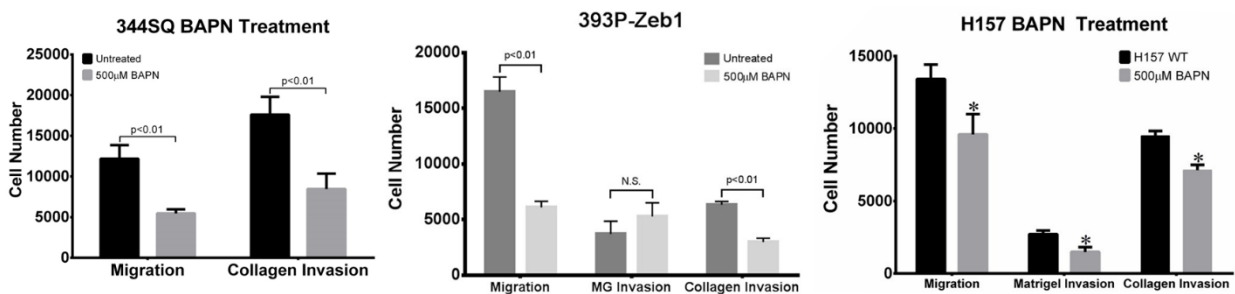


Figure 28. Left: Transwell migration and invasion through collagen for 344SQ cells treated with 500 μM BAPN. Middle: Transwell migration and invasion through Matrigel and collagen for 393P-Zeb1 cells treated with 500 μM BAPN compared to untreated H₂O control. Asterisks (*) indicate significance value of $p < 0.01$. Right: Transwell migration and invasion through Matrigel and collagen for H157 cells treated with 500 μM BAPN.

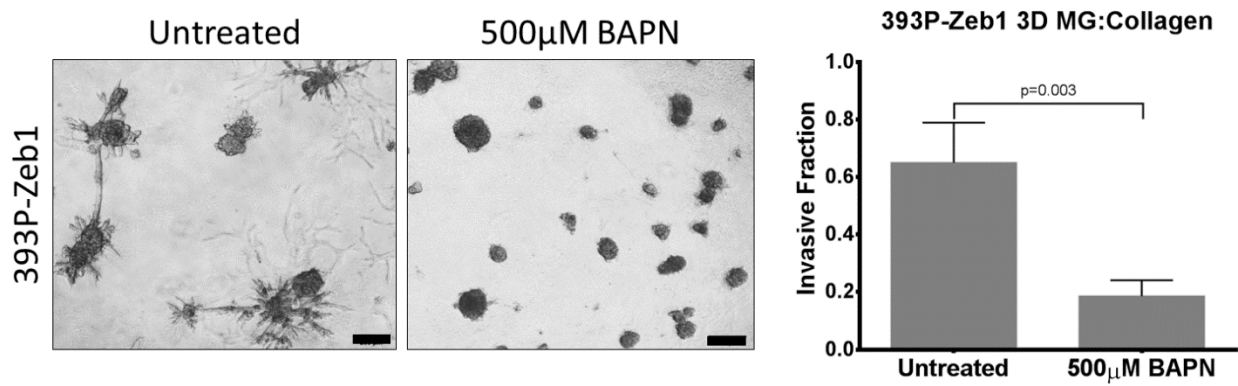


Figure 29. 393P cells with constitutive Zeb1 expression cultured in a 3D matrix consisting of 1.5 mg/ml collagen/Matrigel mixture for 7 days, treated with 500 µM BAPN.

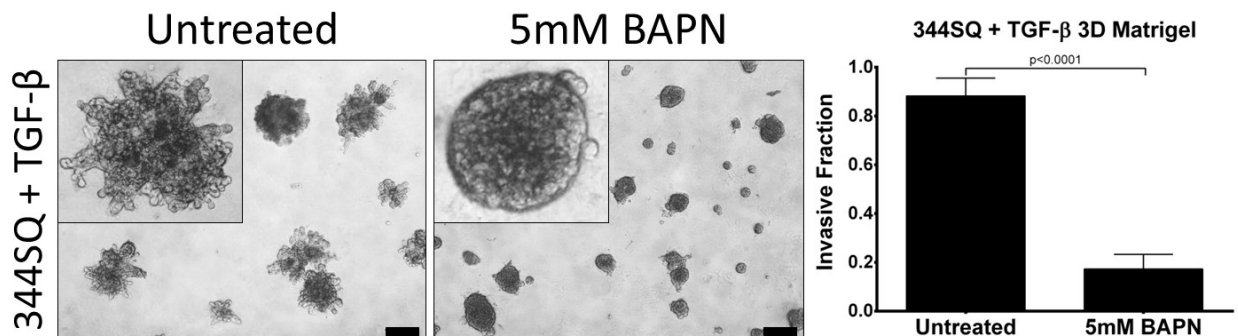


Figure 30. Left: Bright field microscopy images of three-dimensional culture of 344SQ cells co-treated with 5 ng/ml TGF-β and 5 mM BAPN. Right: Quantification of fraction of 3D structures that displayed invasive phenotype (n=50 structures per treatment group). Microscopy images were captured at 4x magnification, scale bars represent 200 µm.

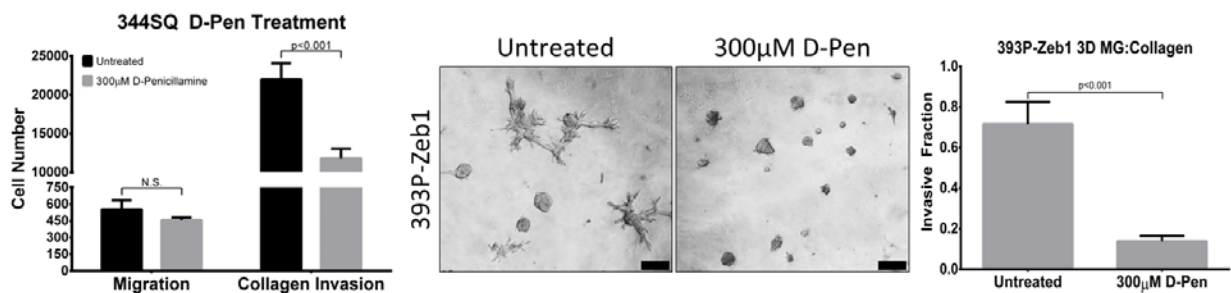


Figure 31. Left: Transwell migration and invasion through collagen for 344SQ cells treated with 300 µM D-Penicillamine (D-Pen). Right: 393P cells with constitutive Zeb1 expression cultured in a 3D matrix consisting of 1.5 mg/ml collagen/Matrigel mixture for 7 days, treated with 300 µM D-Pen. Quantification of fraction of invasive structures in 3D culture assays to the right (n = 50 structures counted per condition). Microscopy images were captured at 4x magnification, scale bars represent 200 µm.

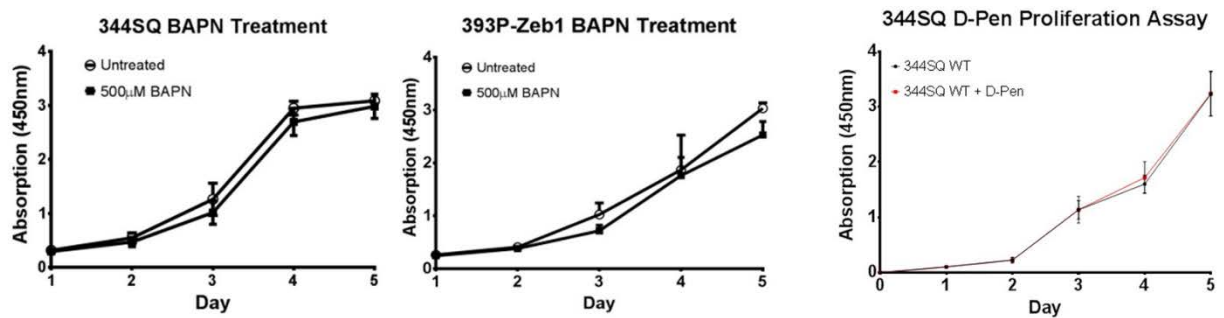


Figure 32. Left: WST-1 cell proliferation and viability assay for 344SQ and 393P-Zeb1 cells treated with 500 μ M BAPN. Right: WST-1 cell proliferation and viability assay for 344SQ cells treated with 300 μ M D-Pen.

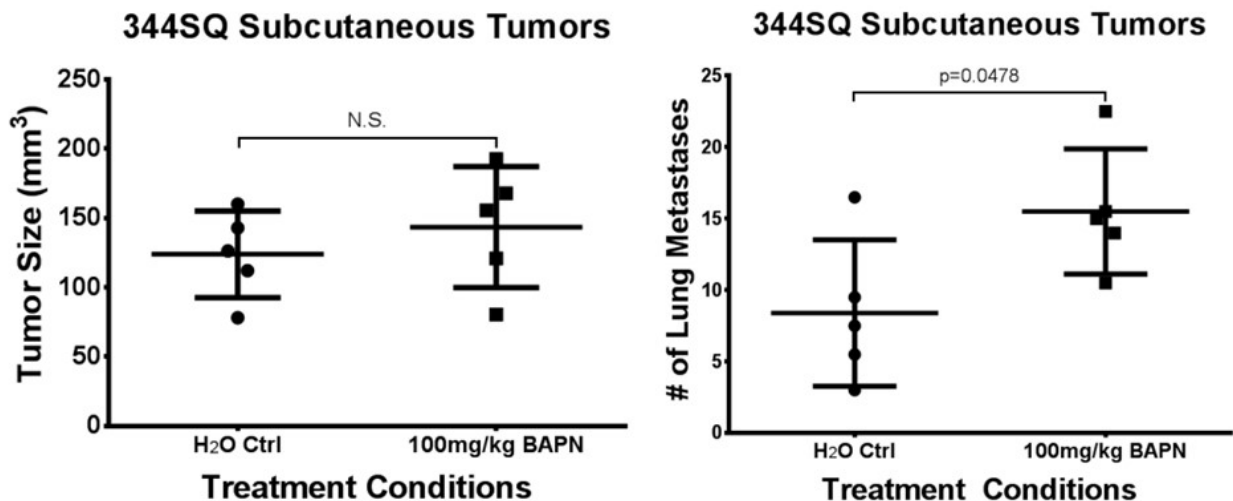


Figure 33. Left: Primary subcutaneous tumor volume of 344SQ cells injected in syngeneic mice with daily intraperitoneal (I.P.) administration of BAPN. Right: Quantification of lung metastatic nodules after treatment with BAPN.

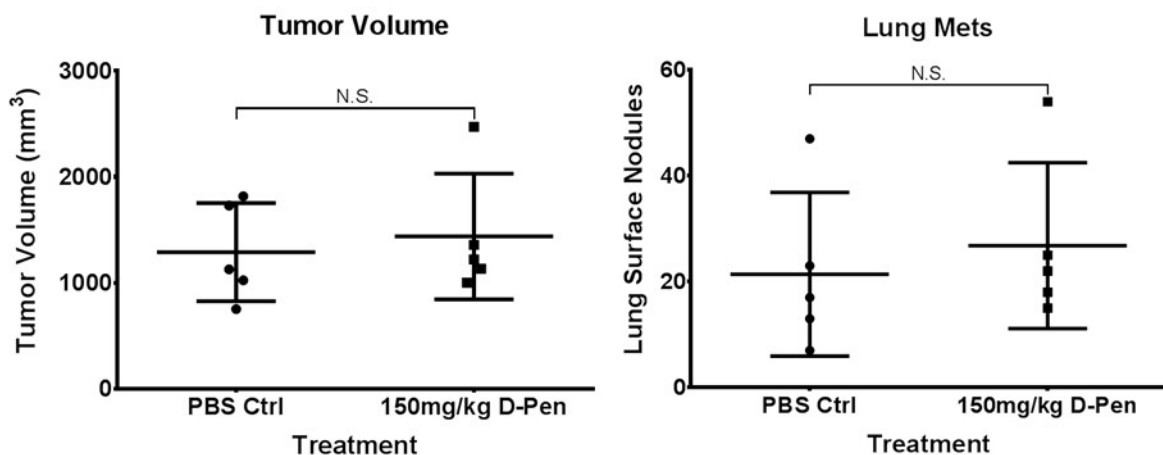


Figure 34. Left: Primary subcutaneous tumor volume of 344SQ cells injected in syngeneic mice with daily I.P. administration of D-Pen. Right: Quantification of lung metastatic nodules after treatment with D-Pen.

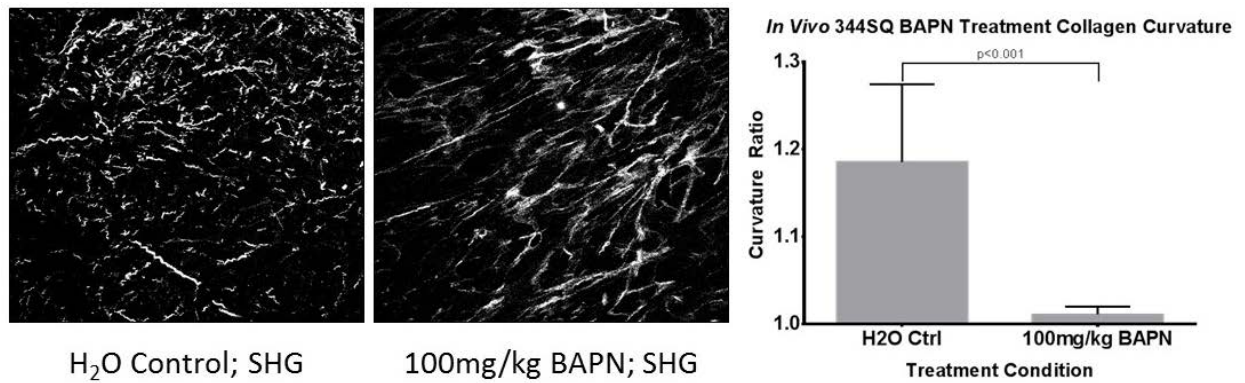


Figure 35. Left: SHG microscopy images of primary subcutaneous tumor tissues from experimental mice in Figure 33. Right: Quantification of curvature ratio for individual collagen fibers from SHG microscopy images generated on the left.

LOXL2 is necessary for collagen deposition, crosslinking and tumor cell metastasis

Given the inconsistent results with LOX chemical inhibitors *in vivo*, we next employed a genetic approach to study the role of LOX and LOXL2 in driving invasion and metastasis. Stable shRNA-mediated knockdown of LOX in metastatic 344SQ cells significantly decreased migration and invasion through Transwell Matrigel or collagen I chambers (**Figure 36**), but did not have a significant effect on primary tumor growth or metastasis *in vivo* (**Figure 37**). In contrast, LOXL2 knockdown decreased invasion only through collagen I and significantly suppressed metastasis *in vivo* (**Figure 38 – 39**). LOX and LOXL2 knockdown in a different metastatic KP cell line, 344LN, produced comparable results both *in vitro* and *in vivo*, with LOXL2 knockdown cells exhibiting diminished metastatic lung nodules that were also markedly smaller in size (**Figure 40 - 42**). Analysis of the conditioned media showed a significant decrease in enzymatic activity upon LOXL2 knockdown but an insignificant reduction when LOX was knocked down (**Figure 43**).

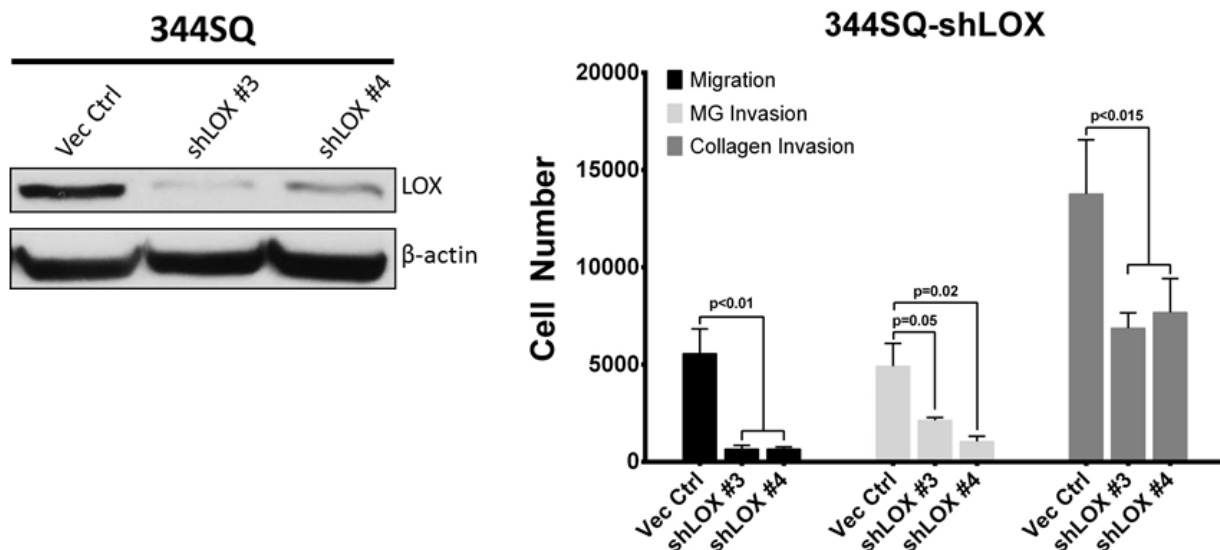


Figure 36. Left: Western blot of LOX protein levels after stable shRNA knockdown in 344SQ cells. Right: Transwell migration and invasion through Matrigel and collagen for 344SQ cells with LOX knockdown.

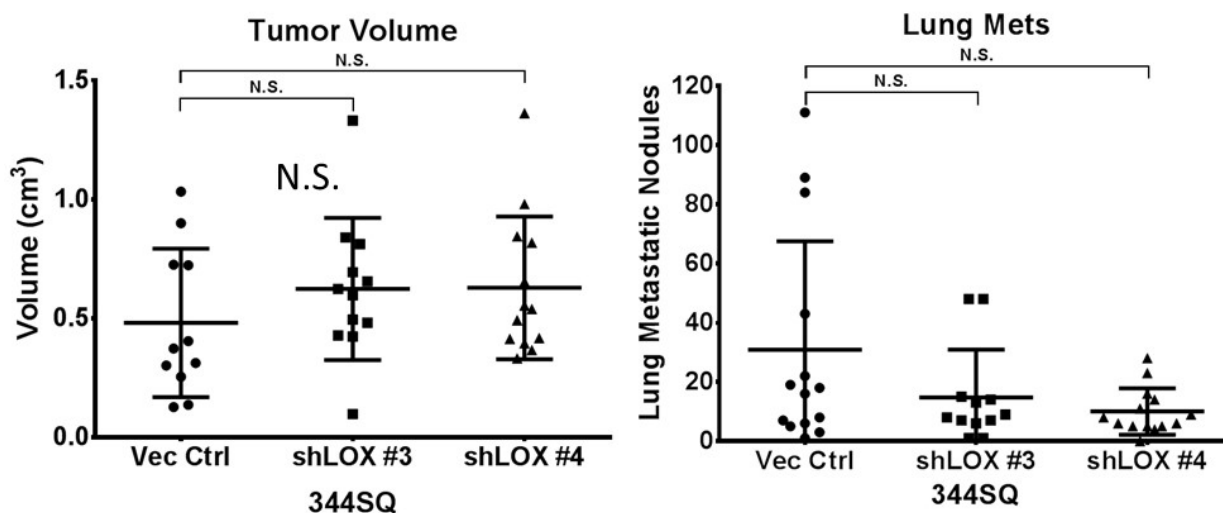


Figure 37. Left: Primary subcutaneous tumor volume of 344SQ cells with stable LOX knockdown injected into syngeneic mice. Right: Quantification of lung metastatic nodules from 344SQ cells with stable LOX knockdown.

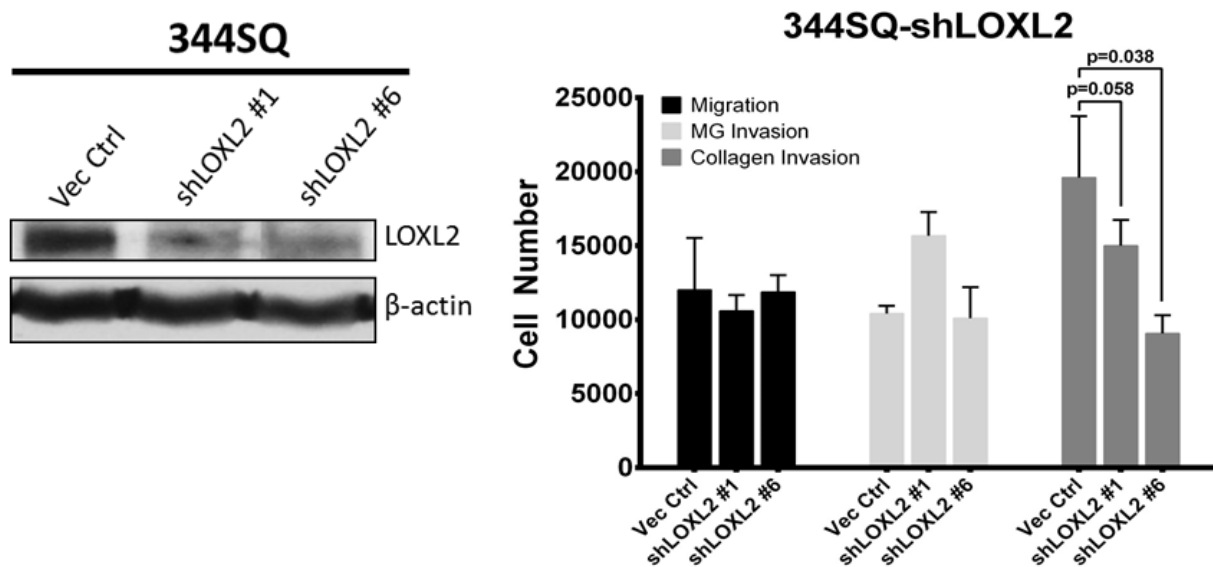


Figure 38. Left: Western blot of LOXL2 protein levels after stable shRNA knockdown in 344SQ cells. Right: Transwell migration and invasion through Matrigel and collagen for 344SQ cells with LOXL2 knockdown.

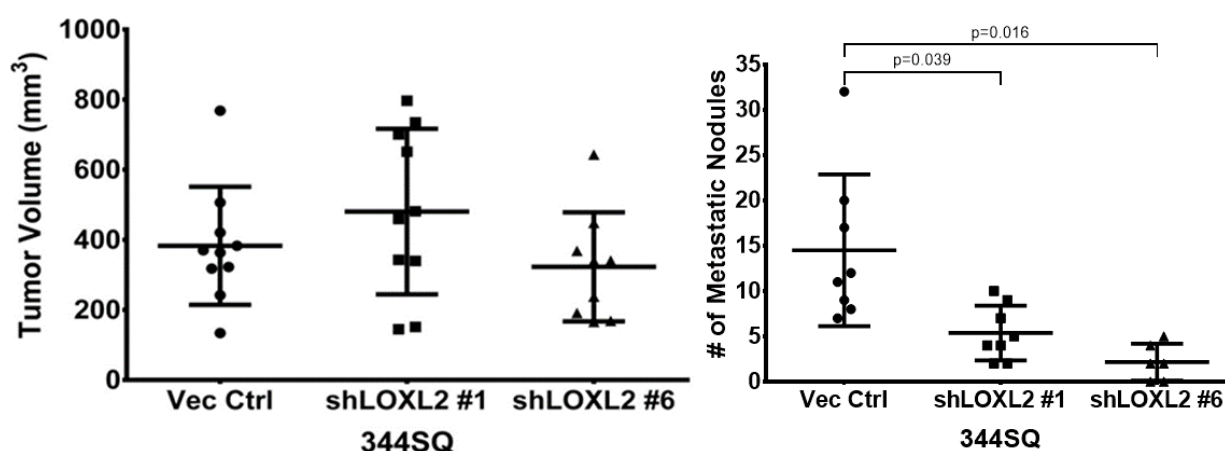


Figure 39. Left: Primary subcutaneous tumor volume of 344SQ cells with stable LOXL2 knockdown injected in syngeneic wild type mice. Right: Quantification of lung metastatic surface nodules after subcutaneous injection of 344SQ cells with stable LOXL2 knockdown in syngeneic wild type mice.

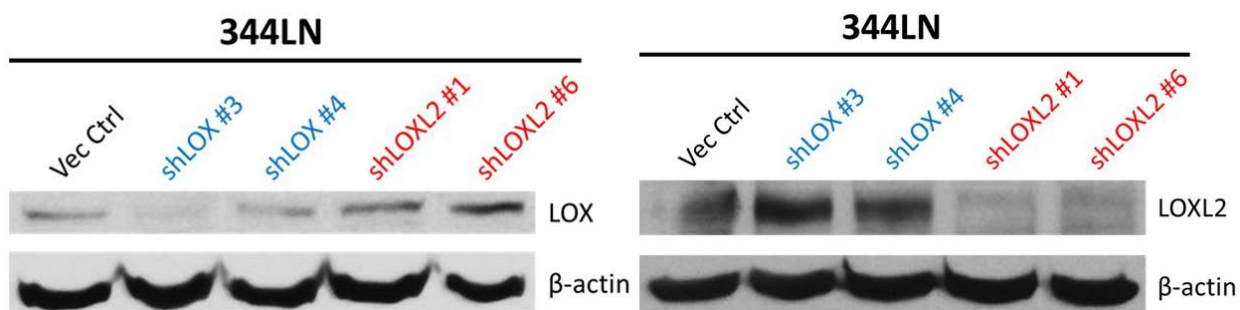


Figure 40. Western blot of LOX and LOXL2 protein levels after stable shRNA knockdown in 344LN cells.

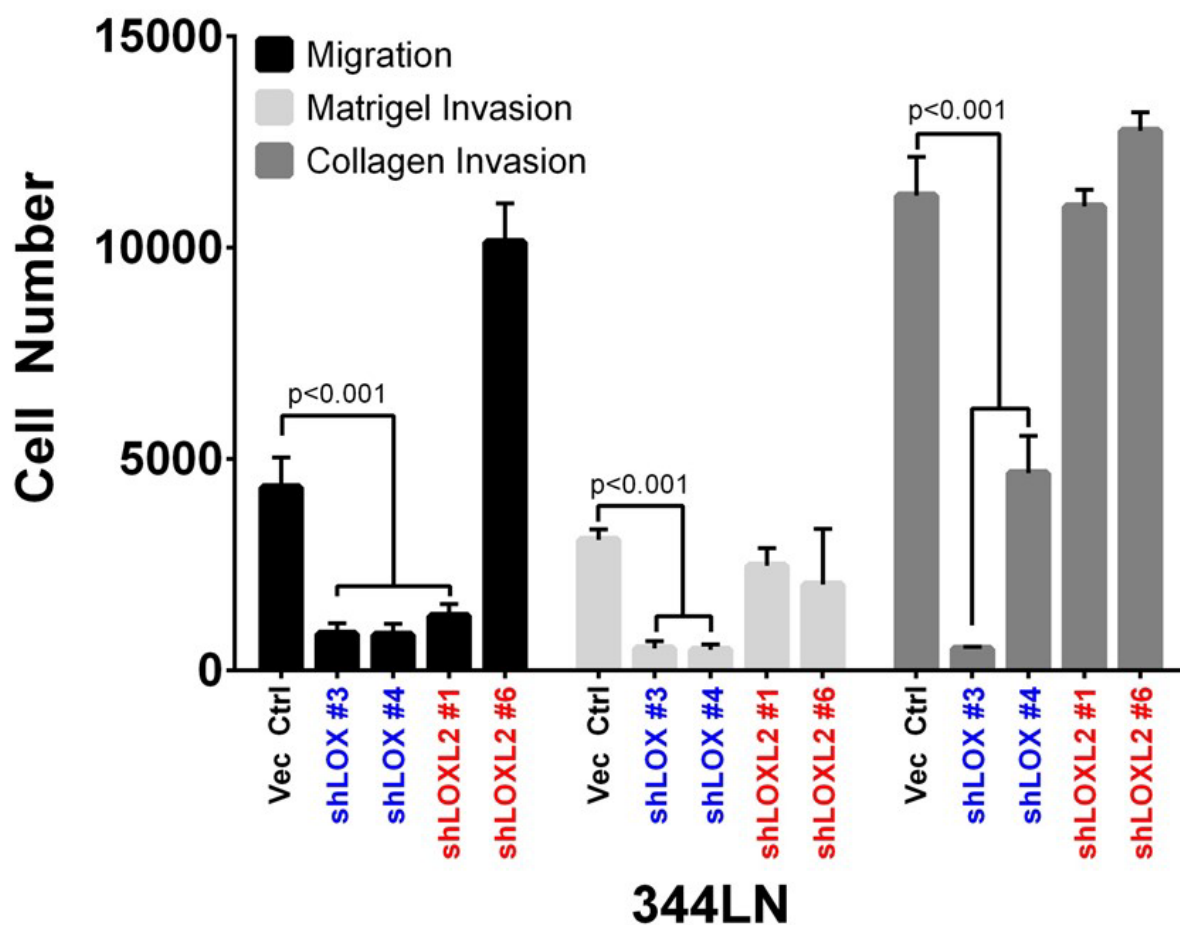


Figure 41. Migration, Matrigel invasion, and collagen invasion of 344LN cells after stable LOX and LOXL2 knockdown.

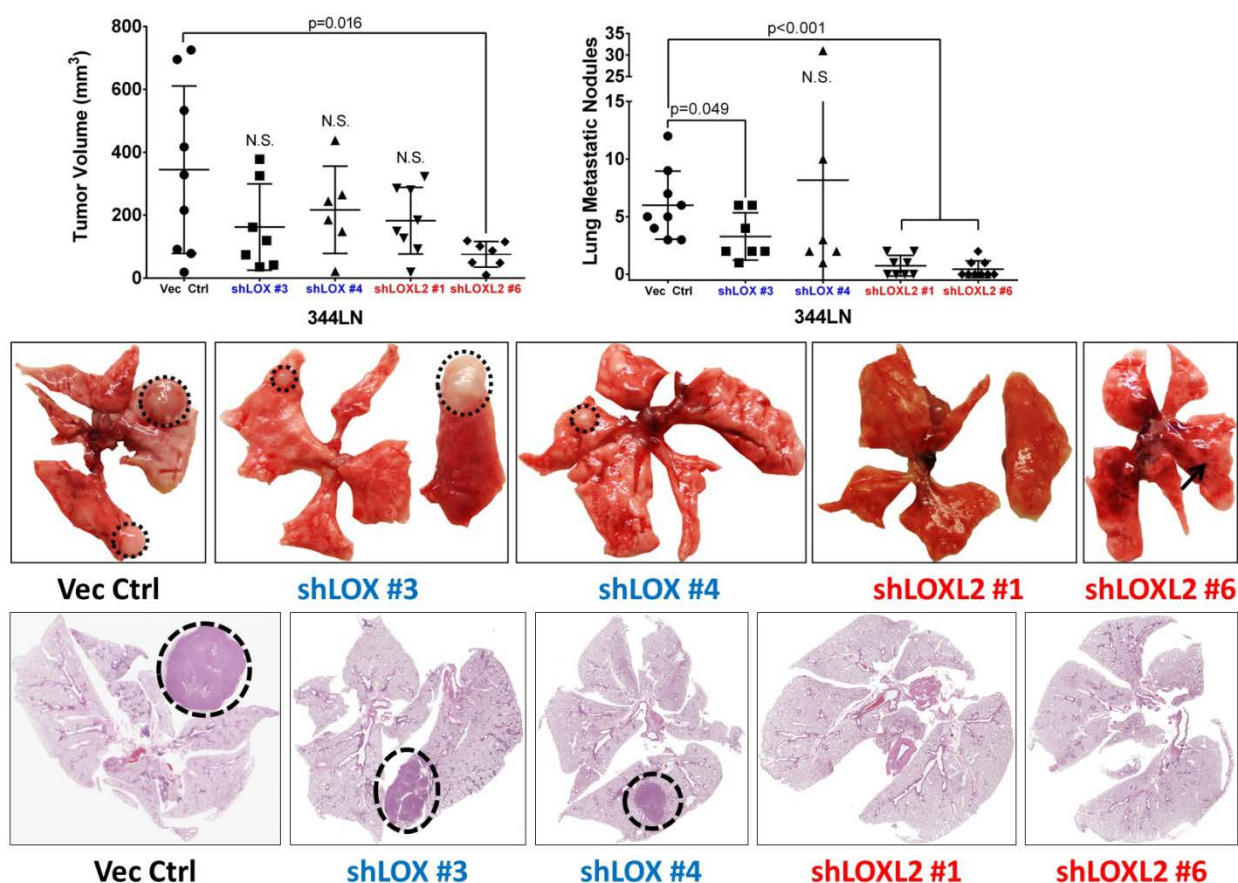


Figure 42. Left: Primary subcutaneous tumor volume of 344LN cells with stable LOX and LOXL2 knockdown injected in syngeneic wild type mice. Right: Quantification of lung metastatic nodules from 344LN cells with stable LOX and LOXL2 knockdown. Bottom: Whole tissue images and H&E sections of lungs collected from mice with subcutaneous injection of 344LN cells after stable LOX and LOXL2 knockdown.

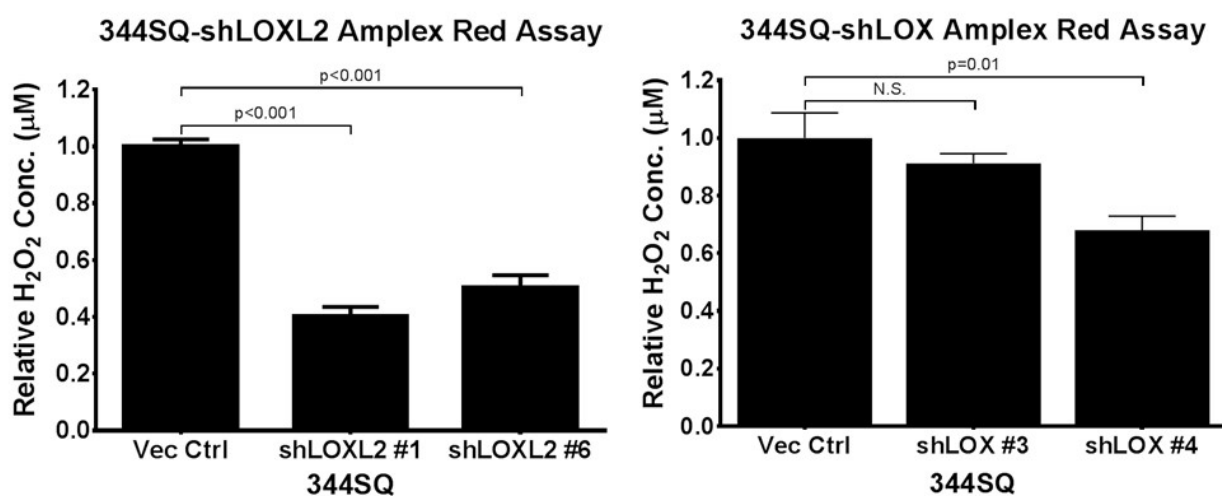


Figure 43. Amplex Red assay for H₂O₂ concentration in conditioned media of 344SQ cells with stable LOXL2 or LOX knockdown.

Developmentally, extracellular LOX enzymes are required for insoluble collagen deposition (66, 79, 108). Therefore, we analyzed the primary syngeneic tumors from our LOX and LOXL2 knockdown experiments for collagen deposition and reorganization. Upon LOXL2 knockdown, both collagen type I and type III deposition were significantly reduced, along with a significant decrease in linear collagen fibers (**Figure 44 – 45**). Consistently, the decrease in tumor collagen content and organization was followed by a decrease in tissue stiffness (**Figure 46**). In contrast, LOX knockdown had no effect on the deposition of either collagen isoform (**Figure 47**), which is consistent with results from our enzymatic activity assays. LOXL2 knockdown did not alter collagen I and III gene expression (**Figure 48**), which suggests that the decrease in collagen deposition *in vivo* is due to lack of crosslinking and maturation. To further verify that LOXL2 is involved in collagen crosslinking and linearization, we visualized collagen fibers by scanning electron microscopy after culture of 344SQ-shLOXL2 cells in collagen I gels. Fiber alignment algorithms showed a significant reduction in average linear collagen fibers when LOXL2 was knocked down compared to the vector control (**Figure 49**). To definitively confirm that LOXL2 is responsible for crosslinked collagen in the tumor tissues, we performed mass spectrometry analysis on the lysine and hydroxylysine residues of collagen (109) that form when two or three collagen molecules form covalent bonds on their lysine residues during crosslinking (DHLNL, HLNL, d-Pyr, and HHMD) (71). Knockdown of LOXL2 significantly reduced the ratio of crosslinked lysine residues in the tumor tissues compared to vector controls, directly establishing the role of LOXL2 in crosslinking collagen *in vivo* (**Figure 50**).

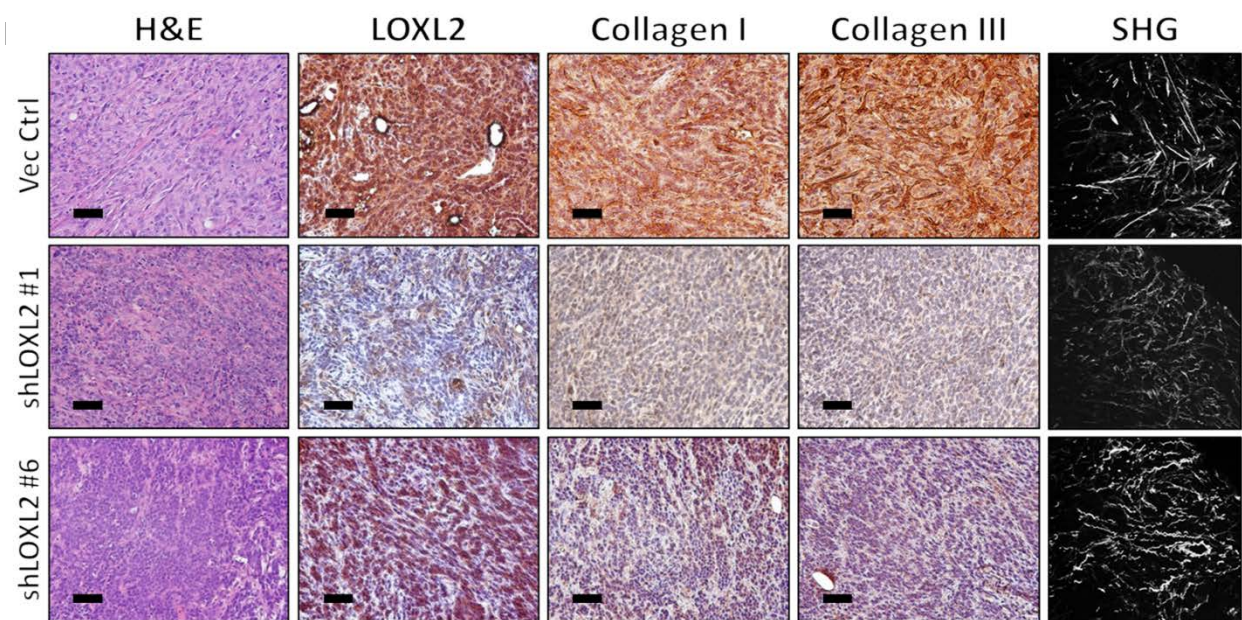


Figure 44. H&E and IHC stains of LOXL2, collagen type I, and type III along with SHG microscopy of primary syngeneic tumor tissues from 344SQ cells with either a vector control or stable LOXL2 knockdown. Microscopy images were captured at 20x magnification, scale bars represent 50 μ m.

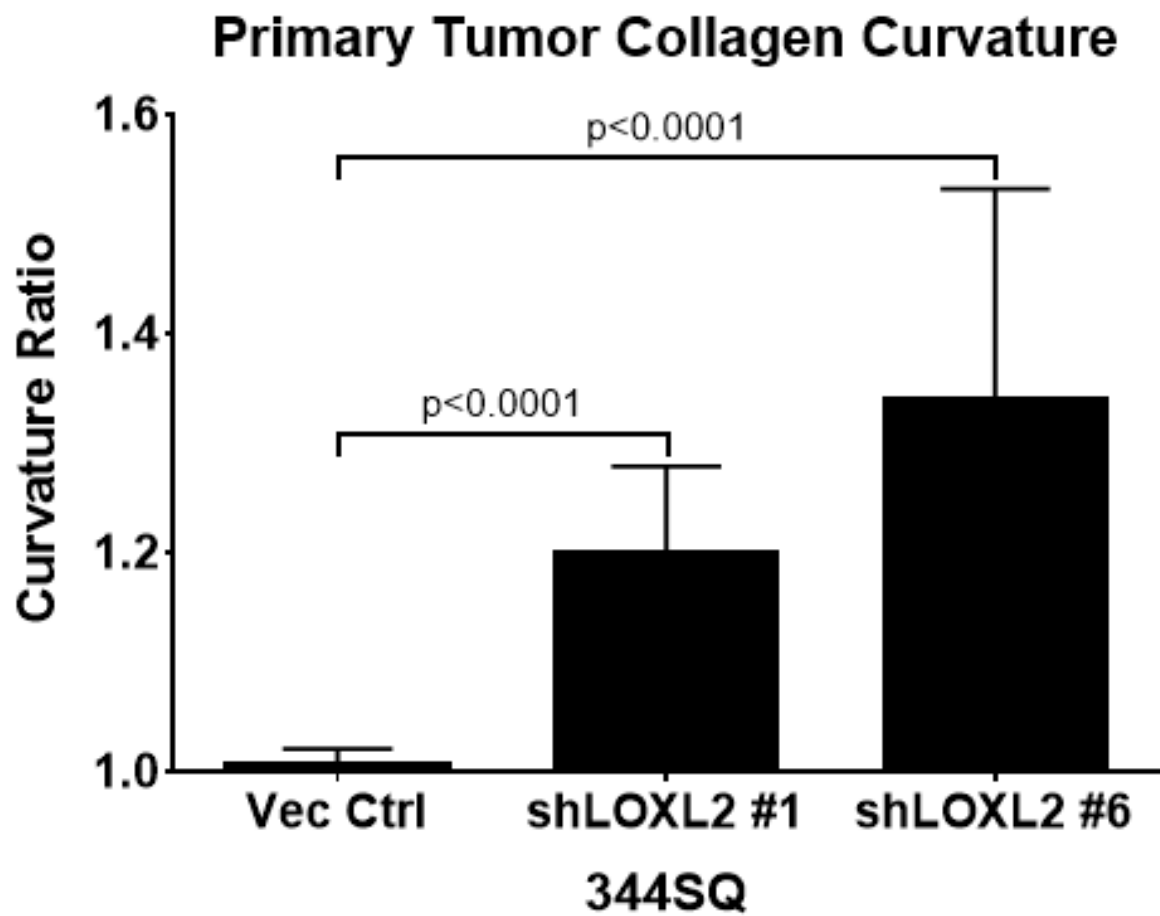


Figure 45. Quantification of curvature ratio for individual collagen fibers imaged by SHG microscopy of tumor tissues from Figure 43.

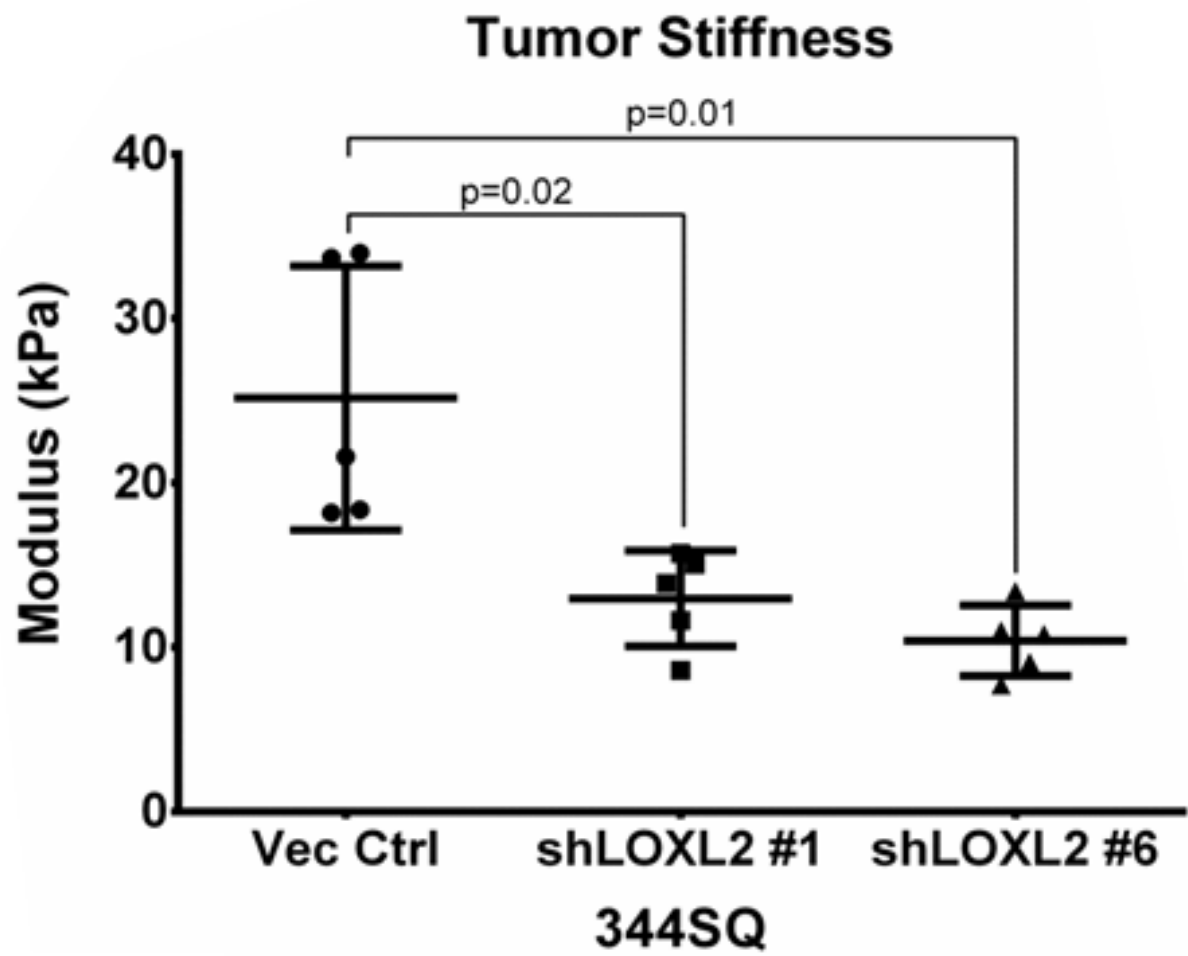


Figure 46. Mechanical stiffness measurements of tumor tissues from in Figure 43.

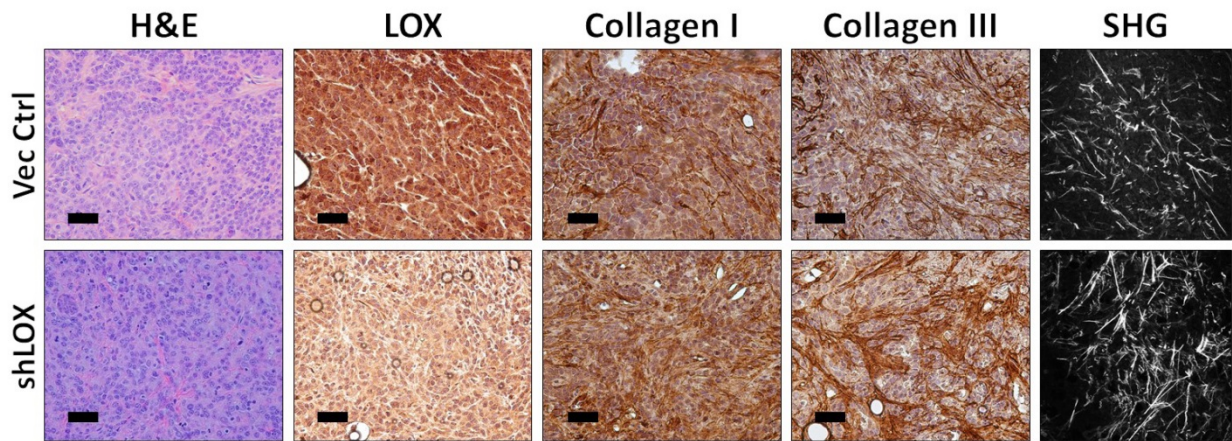


Figure 47. H&E, LOX, collagen type I/type III IHC stains, and SHG microscopy images of subcutaneous primary tumor tissues from 344SQ cells with stable LOX knockdown in syngeneic mice. Microscopy images were captured at 20x magnification, scale bars represent 50 μm.

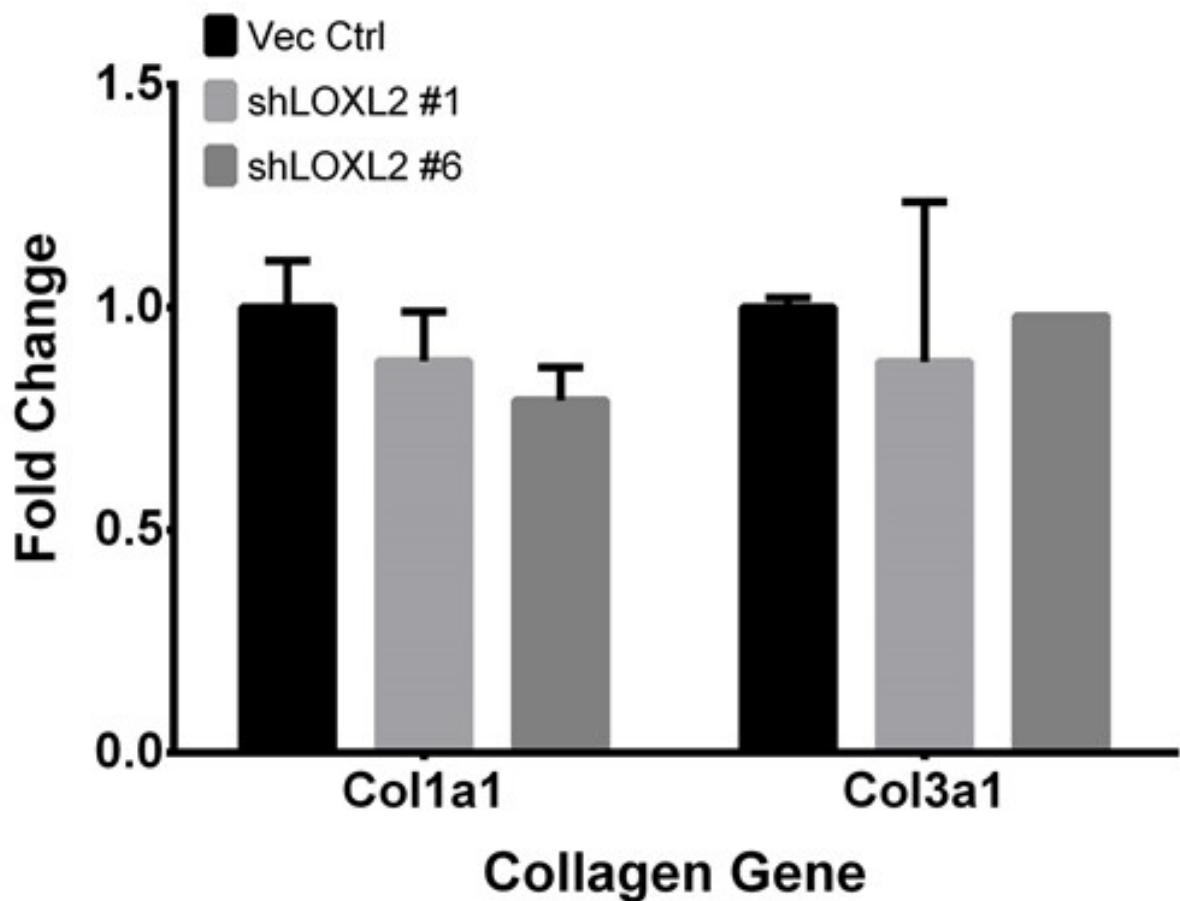


Figure 48. qPCR analysis of relative COL1A1 and COL3A1 mRNA levels after stable LOXL2 knockdown in 344SQ cells.

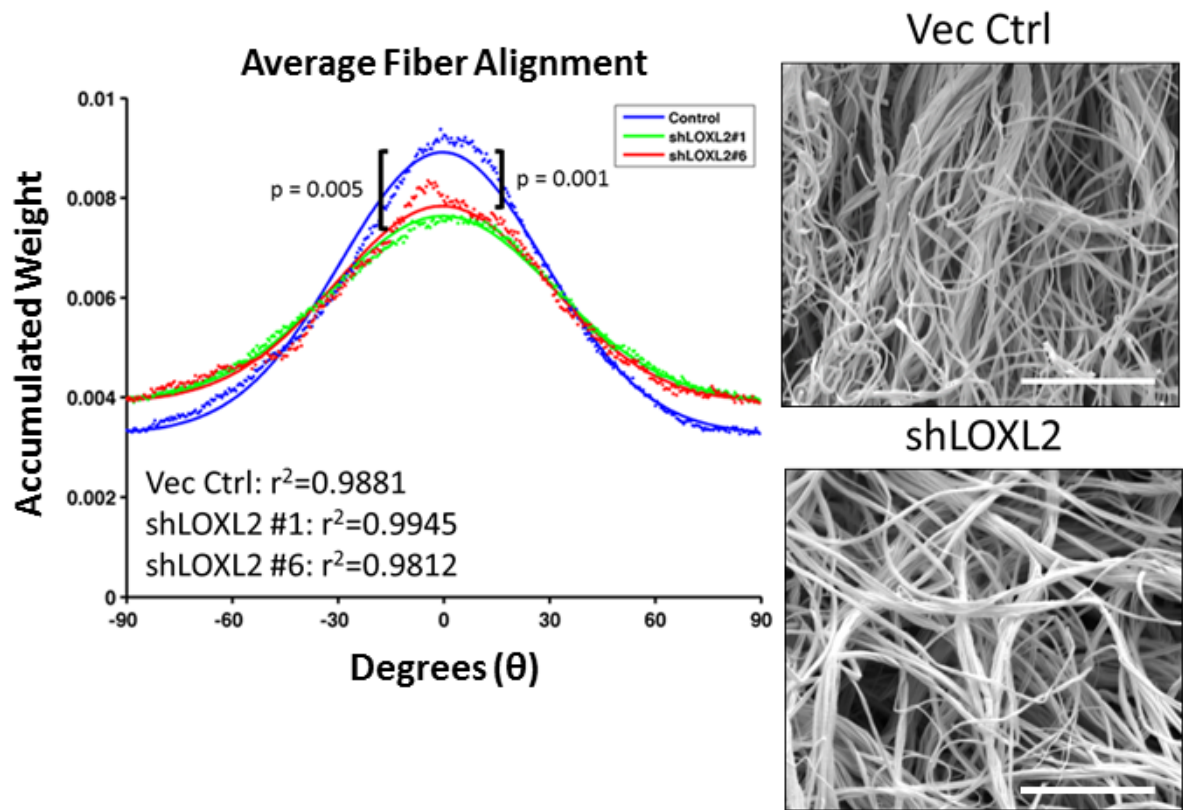


Figure 49. Right: Scanning electron microscopy (SEM) images of 2 mg/ml collagen gels after culturing 344SQ cells with or without LOXL2 knockdown. Images were viewed at 10kV and images were captured at 10kX magnification. Scale bars, 5 μ m (n = 3 collagen gel molds per cell line). Left: Alignment analysis of collagen fibers to determine linearity and organization of collagen fibers as described in Methods section. The Kuiper test was used to test for differences in alignment between the sets of decimated data with significance as indicated.

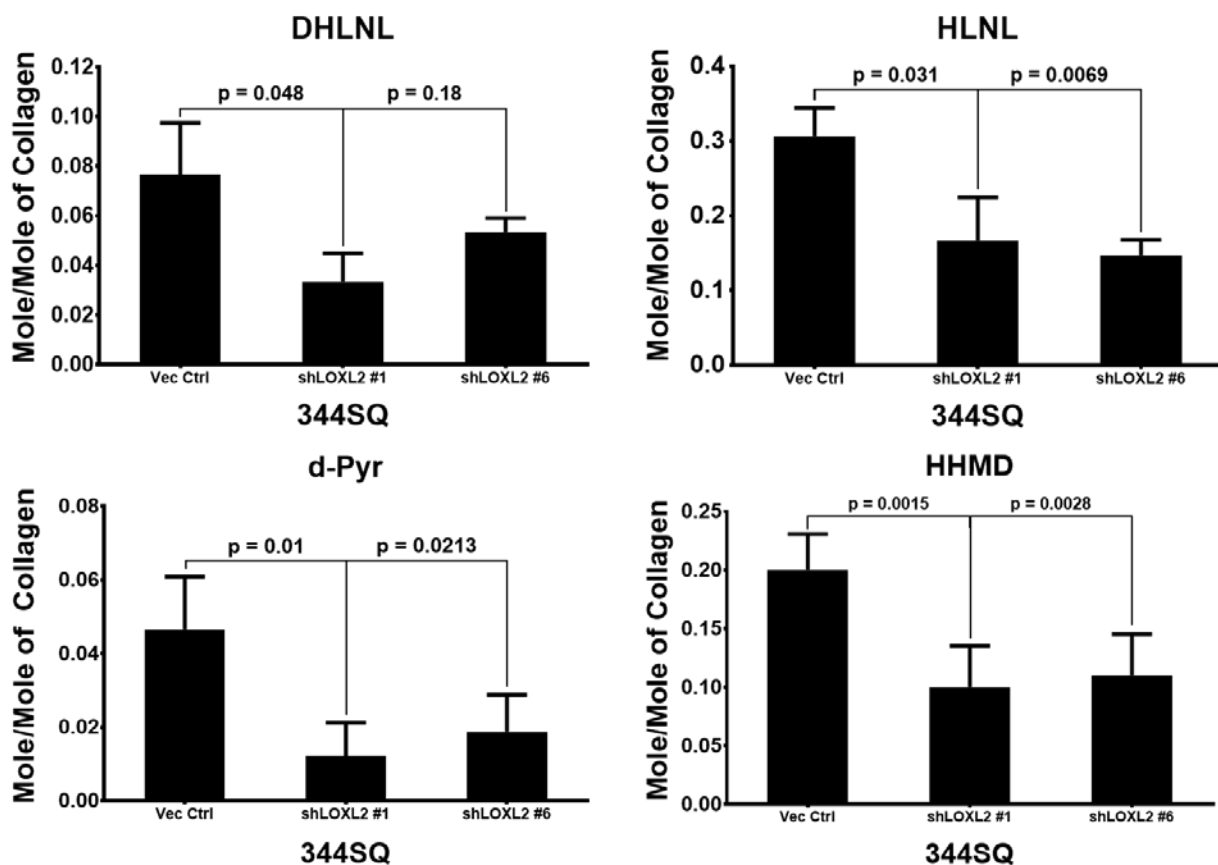


Figure 50. Ratio of the number of molecules of crosslinked lysine residues from collagen versus total collagen molecules in 344Q tumors with stable LOXL2 knockdown. Molecules of crosslinked lysine residues were analyzed by mass spec. *Mass spec analysis performed by the laboratory of Mitsuo Yamauchi from University of North Carolina.*

LOX and LOXL2 ectopic expression is not sufficient for epithelial cancer cell migration and invasion

Next, we took the converse approach and ectopically expressed LOX and LOXL2 in epithelial, non-metastatic 393P cells using a doxycycline-inducible pTRIPz vector. LOX and LOXL2 were either tagged or untagged with GFP at the N-terminus region. Western blots of LOX/LOXL2 induced cells confirmed proper expression of the desired proteins. However, only the untagged version of LOXL2 was detectable in the conditioned media, suggesting that the GFP interferes with the signaling peptide at the N-terminus region. GFP-tagged and untagged LOX was undetectable in the conditioned media (**Figure 51**). This finding was also verified by enzymatic assays of the conditioned media of the overexpression cell lines, which showed that only the LOXL2 expressing cells had extracellular enzymatic activity (**Figure 52**). There was no significant difference in Transwell migration and invasion with induced LOX expressed (**Figure 53**). However, when LOXL2 expression was induced, there was only a significant increase in invasion when extrinsic collagen was coated on the Transwell inserts (**Figure 53**). LOX and LOXL2 were also ectopically expressed in epithelial murine 307P and human H322 cells, which have low endogenous levels of LOX/LOXL2 (**Figure 13 and Figure 15**). Similar to 393P cells, we observed a significant, robust increase in invasion only through collagen coated Transwells when LOXL2 was expressed in 307P and H322 cells (**Figure 54 and 55**). Since collagen gene expression is unaltered when LOX or LOXL2 is overexpressed (**Figure 56**), this suggests that coordinate collagen expression by mesenchymal cells is also necessary to drive invasion and metastasis and that LOX or LOXL2 alone is not sufficient to promote migration and invasion.

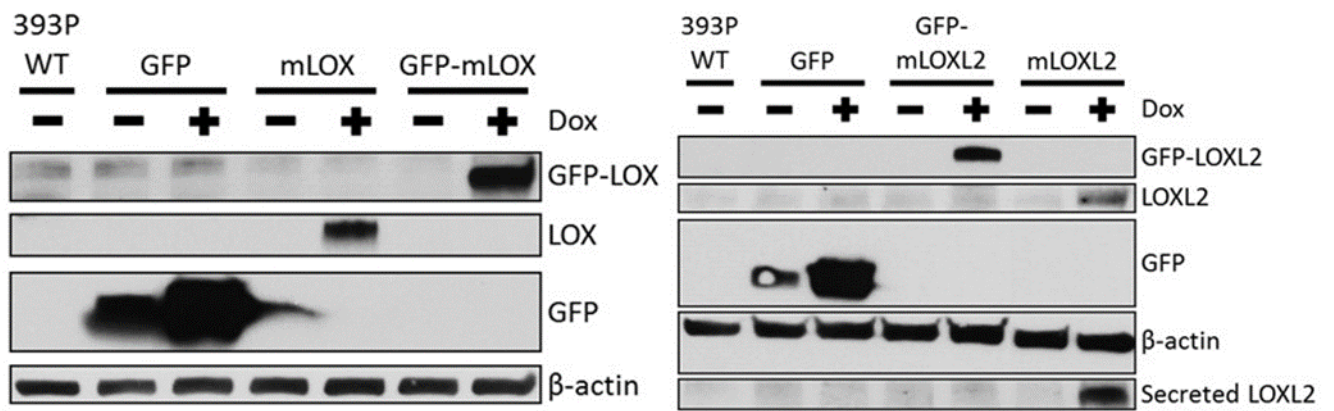


Figure 51. Left: Western blot of LOX, GFP, and β -actin in 393P cells expressing doxycycline (Dox) inducible GFP, LOX with GFP tagged to the N-terminus (GFP-LOX), or untagged LOX. Right: Western blot of LOXL2, GFP, and β -actin in 393P cells expressing Doxycycline inducible GFP, LOXL2 with GFP tagged to the N-terminus (GFP-LOXL2), or untagged LOXL2.

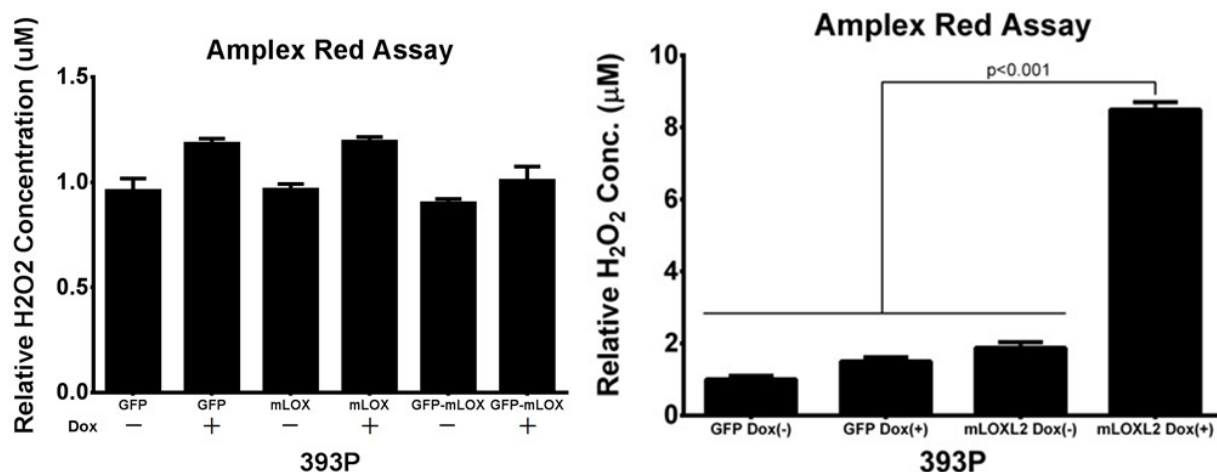


Figure 52. Left: Amplex Red assay of conditioned media from 393P cells with Dox induced GFP, GFP-LOX, or LOX. Right: Amplex Red assay of conditioned media from 393P cells with Dox induced GFP or untagged LOXL2.

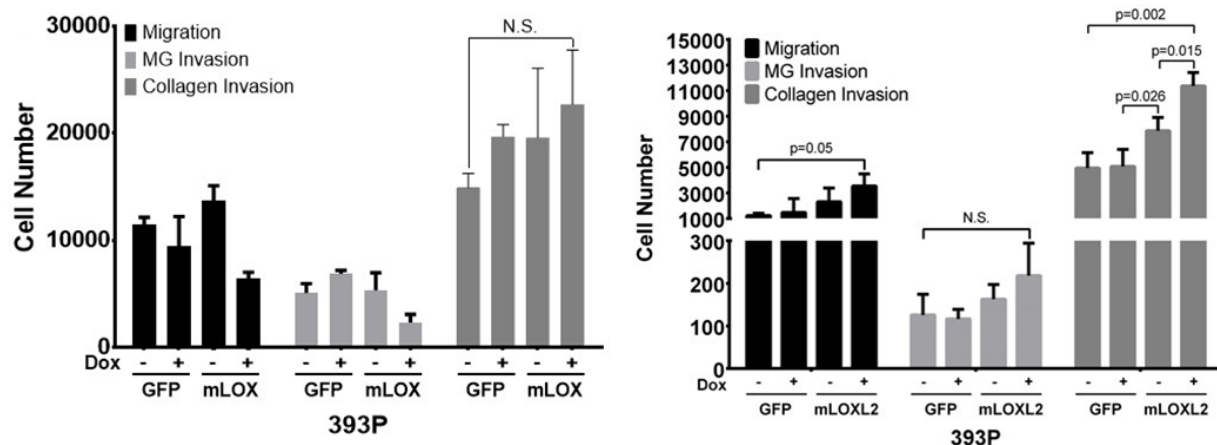


Figure 53. Left: Transwell migration and invasion through Matrigel and collagen for 393P cells expressing inducible GFP or untagged LOX. Right: Transwell migration and invasion through Matrigel and collagen for 393P cells expressing inducible GFP or untagged LOXL2.

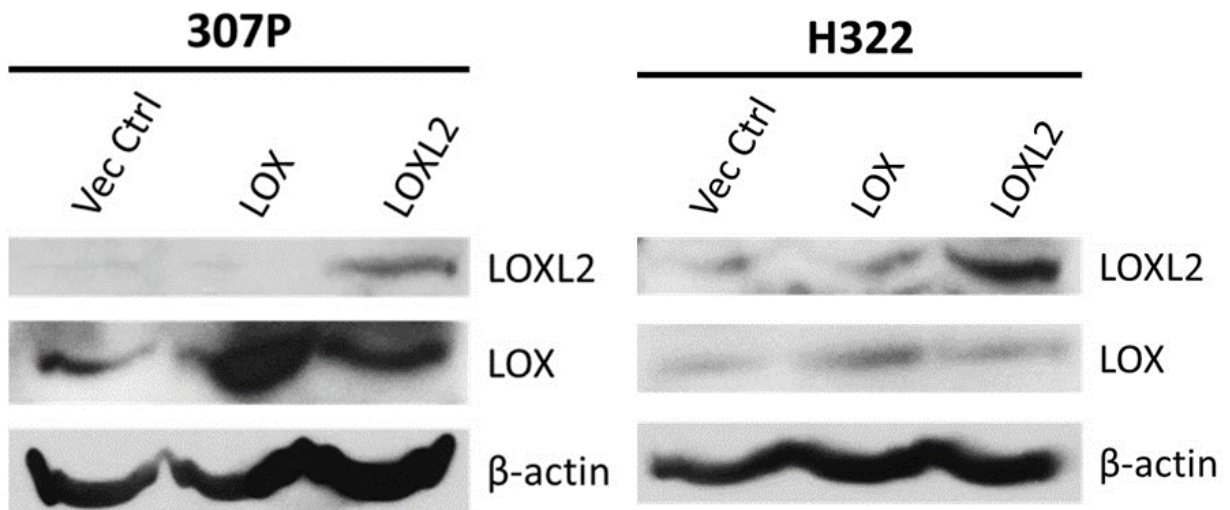


Figure 54. Left: Western blot of LOX, LOXL2, and β -actin in epithelial 307P cells transiently transfected with LOX or LOXL2. Right: Western blot of LOX, LOXL2, and β -actin in human epithelial H322 cells transiently transfected with LOX or LOXL2.

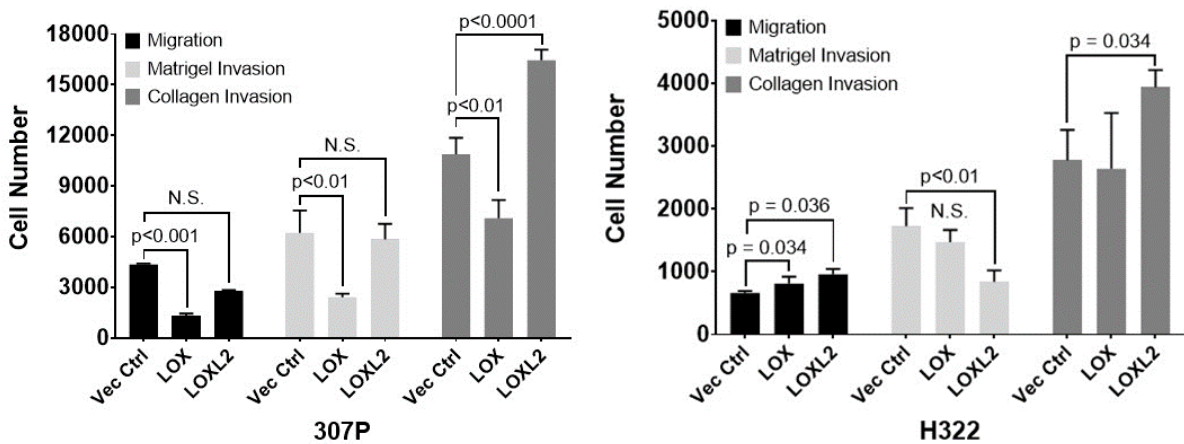


Figure 55. Left: Transwell migration, Matrigel invasion, and collagen invasion of 307P cells transiently transfected with LOX and LOXL2. Right: Transwell migration, Matrigel invasion, and collagen invasion of H322 cells transiently transfected with LOX or LOXL2.

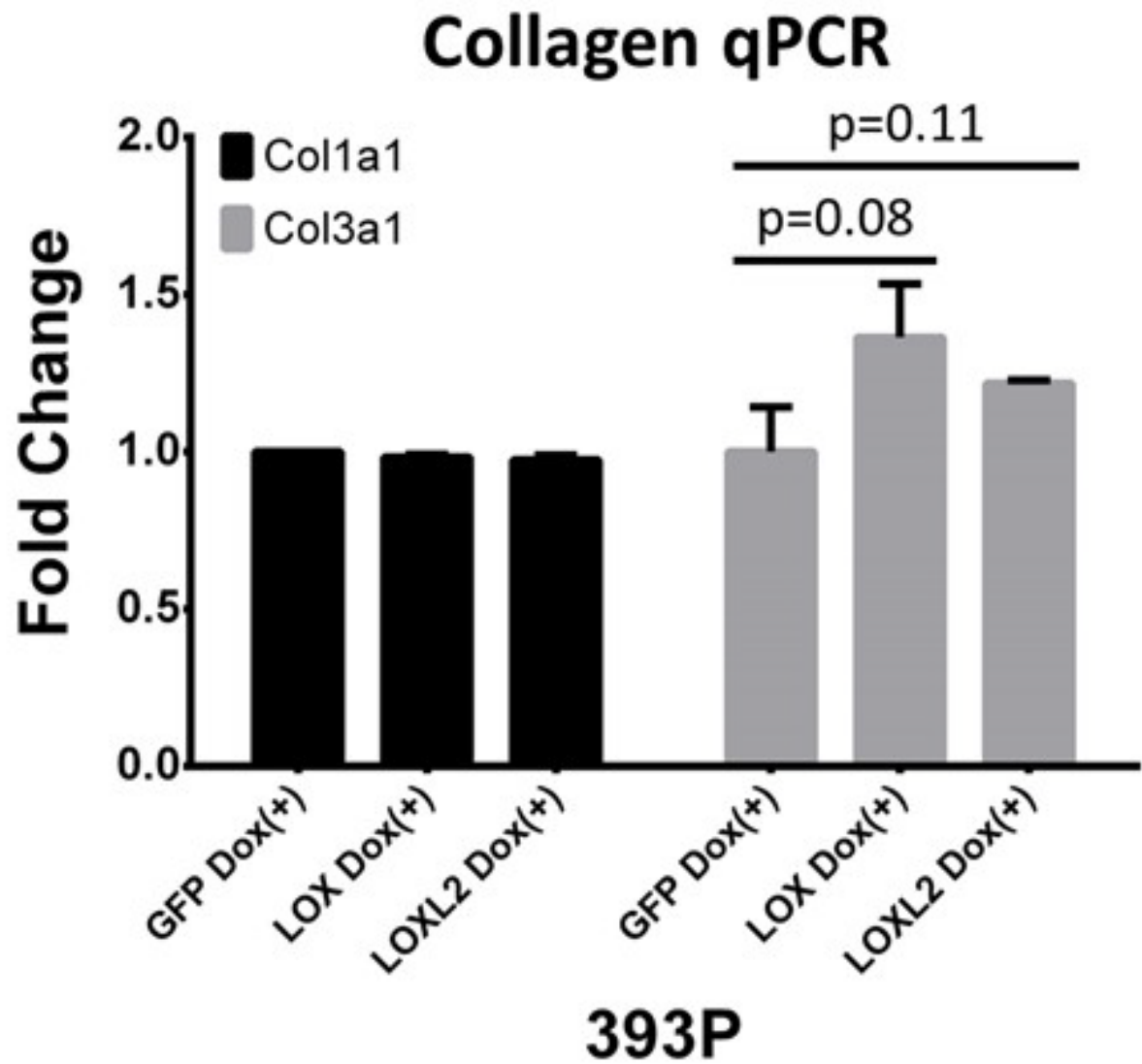


Figure 56. qPCR analysis of COL1A1 and COL3A1 in 393P cells expressing Dox induced GFP, LOX, or LOXL2.

LOXL2-mediated collagen deposition induces FAK/Src signaling *in vitro* and *in vivo*

Our group recently demonstrated that activation of the integrin β 1/FAK/Src signaling pathway through collagen type I interaction is necessary for lung cancer invasion and metastasis (58). Since EMT causes lung cancer cells to deposit insoluble collagen by LOXL2 crosslinking, we investigated the potential autocrine effect that LOXL2 has on FAK/Src signaling. Immunofluorescent staining for activated phosphorylated FAK (Y861) and Src (Y416) showed that enzymatic inhibition or knockdown of LOXL2 decreased focal adhesion formation and FAK/Src signaling after TGF- β -mediated stimulation of 344SQ cells (**Figure 57 and 58**). Western blotting confirmed the suppression of signaling by LOXL2 KD or inhibition and further emphasized that knockdown of LOX does not produce the same effect (**Figure 59**). Further analysis of primary syngeneic tumors with LOXL2 knockdown (**Figure 44**) by IHC staining revealed a decrease in activated FAK and Src versus control tumors (**Figure 60**), correlating with the decrease in collagen type I and type III deposition in the tumors (**Figure 44**). Collectively, our data supports a model in which ZEB1-driven mesenchymal lung cancer cells deposit collagen in the tumor microenvironment through LOXL2 crosslinking, which further activates the integrin/FAK/Src signaling pathway in the cancer cells, leading to invasion and metastasis (**Figure 61**).

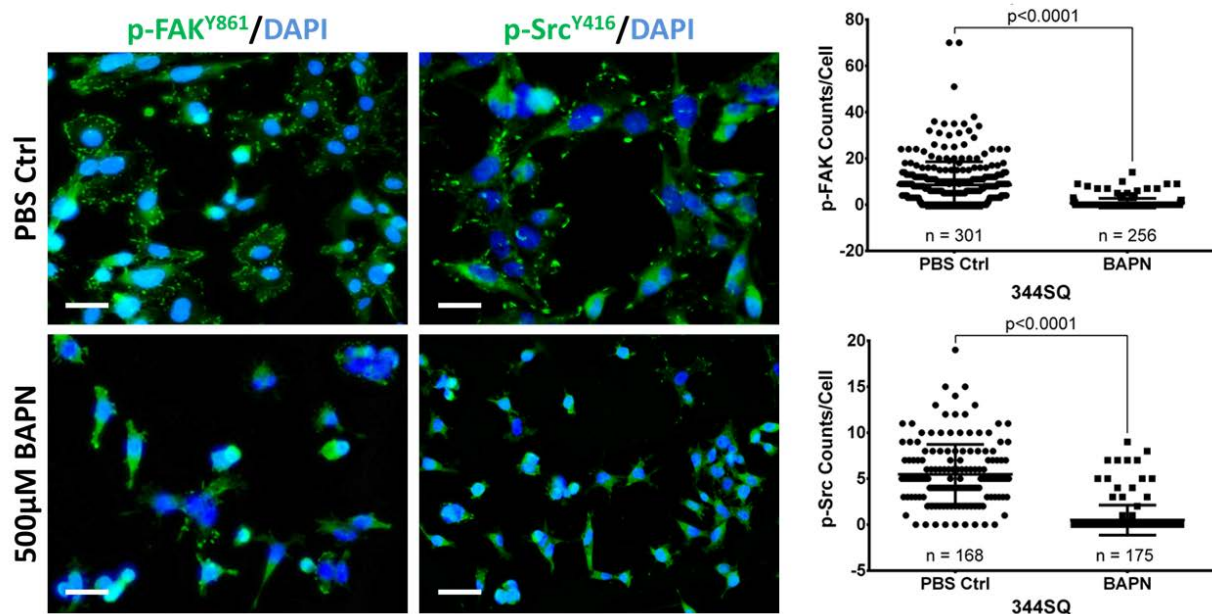


Figure 57. Left: Immunofluorescent staining of p-FAK^{Y861} and p-Src^{Y416} (green dots) in 344SQ cells treated with 5 ng/ml TGF- β for 48 hours in the presence or absence of 500 μ M BAPN. Right: Quantification of p-FAK^{Y861} and p-Src^{Y416} signal per cell from immunofluorescent stains.

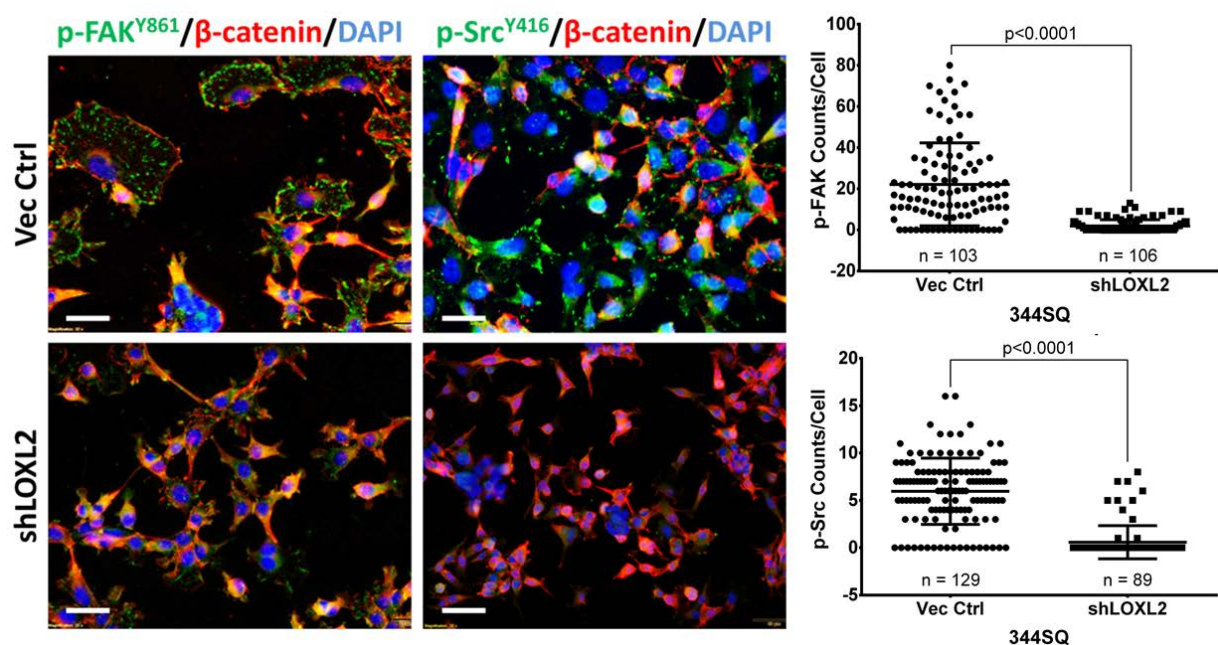


Figure 58. Left: Immunofluorescent staining of p-FAK^{Y861}, p-Src^{Y416} (green dots), and β -catenin (red) in 344SQ cells after stable shRNA knockdown of LOXL2. β -catenin used as a marker to identify cell membrane. Right: Quantification of p-FAK^{Y861} and p-Src^{Y416} signal per cell from immunofluorescent stains.

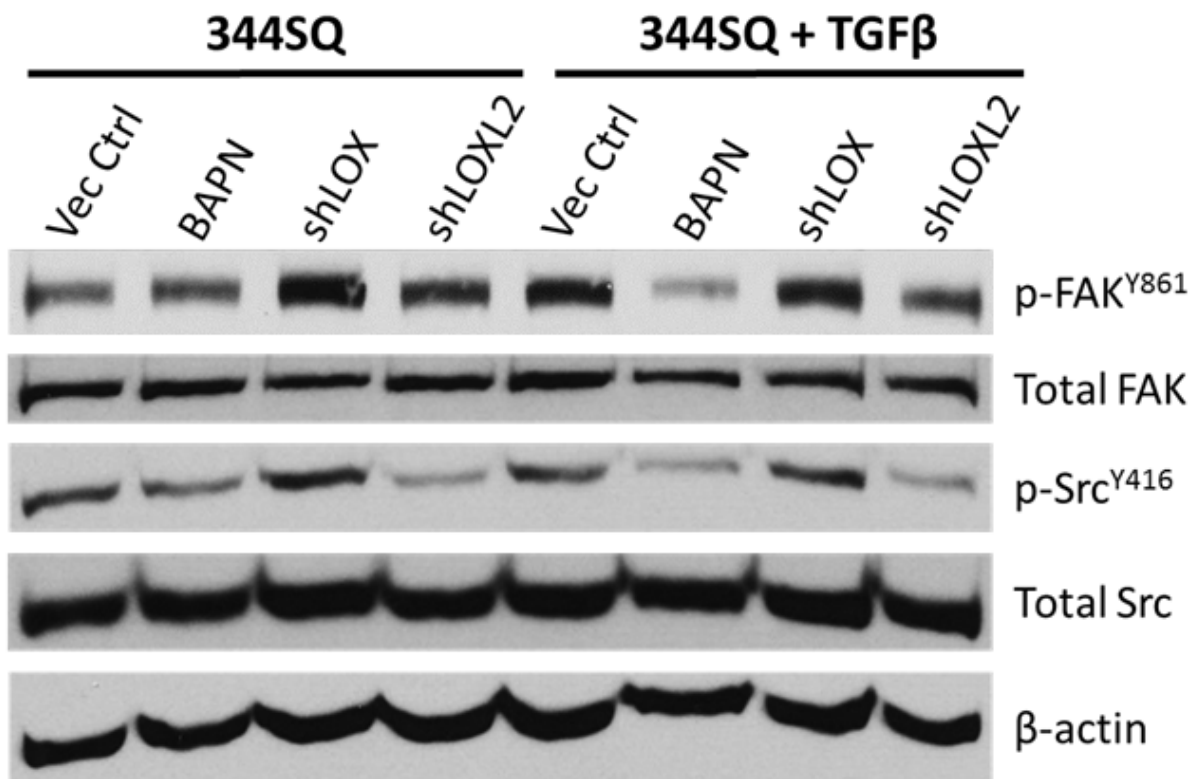


Figure 59. Western blot of p-FAK^{Y861}, total FAK, p-Src^{Y416}, and total Src in 344SQ cells \pm 5 ng/ml TGF- β treatment for 48 hours in the presence of 500 μ M BAPN, with stable LOX or LOXL2 knockdown.

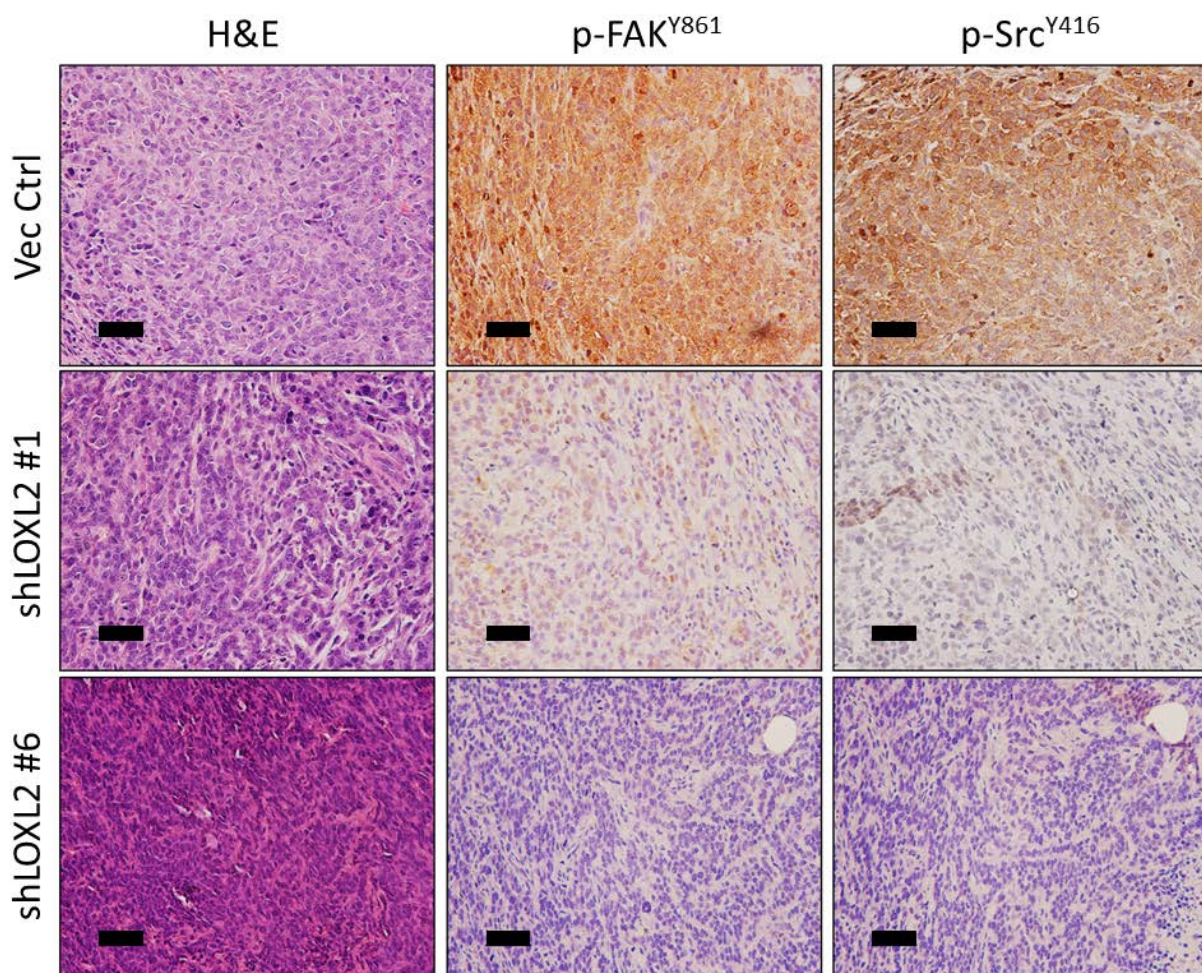


Figure 60. H&E and IHC stains of p-FAK^{Y861} and p-Src^{Y416} of primary tumor tissues from subcutaneous injection of 344SQ cells with stable LOXL2 knockdown in syngeneic wild type mice. Microscopy images captured at 20x magnification, scale bars represent 50 μ m.

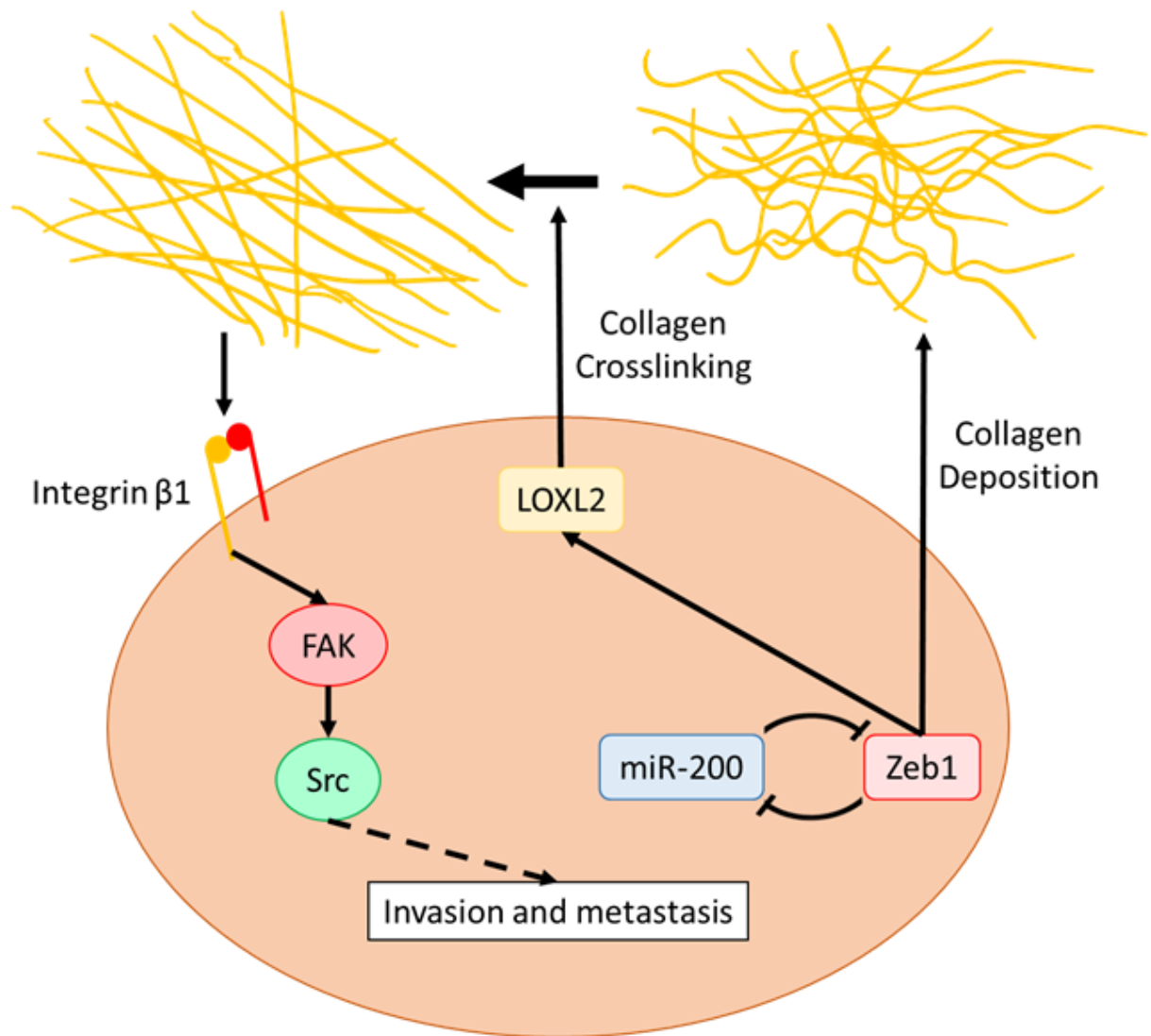


Figure 61. Proposed model demonstrating Zeb1 regulation of collagen deposition in the tumor microenvironment through LOXL2 crosslinking and stabilization, activating the Integrin $\beta 1$ /FAK/Src signaling pathway in an autocrine manner leading to invasion and metastasis.

Increased collagen, LOX, and LOXL2 expression predicts poor prognosis among patients with lung adenocarcinoma

Based upon these findings, we wanted to determine the prognostic value of the LOX and collagen proteins in predicting lung cancer patient survival and how their expression correlates with Zeb1 in human tumors. Pathologic assessment of stromal collagen I and III expression by IHC staining in a cohort of lung cancer specimens (n=490) revealed increased levels in lung adenocarcinoma (ACC) versus squamous cell carcinoma (SCC) samples (**Figure 62 – 64**), but no statistically significant correlation to pathologic stage or patient outcome (**Figure 65**). However, cytoplasmic scoring of collagen type I levels revealed greater amounts in poorly differentiated tumors of all histologic subtypes (**Figure 66**), consistent with our findings correlating collagen expression with EMT. Although we observed a trend toward higher collagen levels in late-stage adenocarcinomas and in patients with poorer outcomes (**Figure 65 and 67**), the changes were statistically insignificant due to the relatively small sample size of late-stage tumors. Collagen type III did not display strong cytoplasmic staining in tumor tissues. To determine if Zeb1 correlated with collagen expression, we scored Zeb1 IHC stains specifically in the nuclei of tumor cells from the same cohort of tissue microarray specimens (**Figure 62**). Although Zeb1 did not show a significant difference between tumor differentiation grades (**Figure 68**), there was an increase in expression in patients with SCC compared to ACC (**Figure 69**). Zeb1 expression H-scores correlated moderately, but significantly with collagen I H-scores across all tumor histologic subtypes. However, when the samples were stratified by ACC and SCC histology, we observed an increased significant correlation between Zeb1 and collagen I expression in ACC patients (**Figure 70**) but no significant correlation in patients with

SCC (**Figure 71**). Zeb1 scores did not significantly correlate with stromal collagen I or III (**Figure 72**) nor did it correlate with patient outcome or pathological stage (data not shown).

Although we tested multiple antibodies for each, we were unable to analyze LOX and LOXL2 levels in the human specimens by IHC because none of the antibodies produced staining of clinically acceptable quality for scoring. To circumvent these issues, we performed Kaplan-Meier analyses using mRNA profiling from a large compendium of lung adenocarcinoma patients (n=1,586), which revealed decreased overall survival in patients whose tumors expressed elevated levels of collagen type I, type III, LOX, or LOXL2 (**Figure 73**). This decrease in patient survival with high LOXL2 expression has also been previously observed in patients with lung SCC (110).

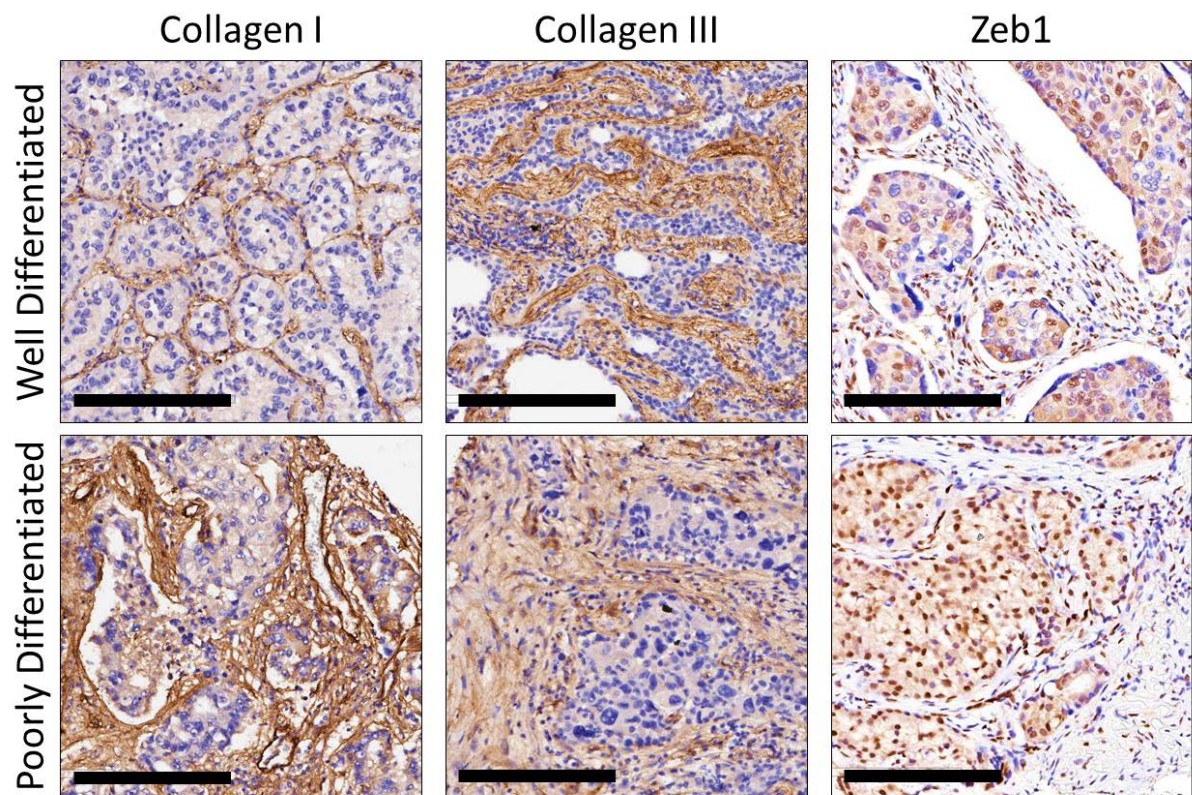


Figure 62. Well differentiated and poorly differentiated human lung adenocarcinoma tissue sections IHC stained for collagen type I, collagen type III, and Zeb1. Scale bars, 200 μ m.

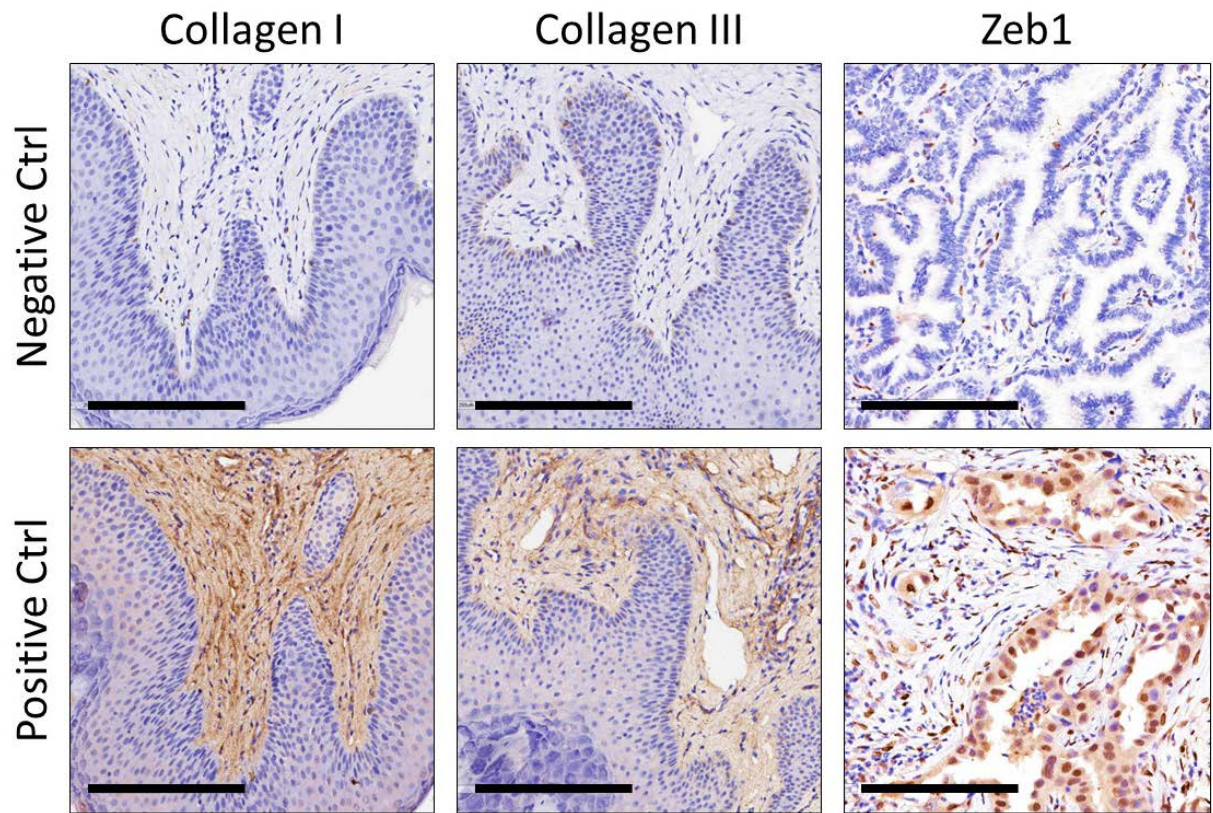


Figure 63. Positive and negative control tissues for collagen I, collagen III, and Zeb1 IHC staining. Human skin tissues were used as positive and negative controls for collagen antibodies. Scale bars, 200 μ m.

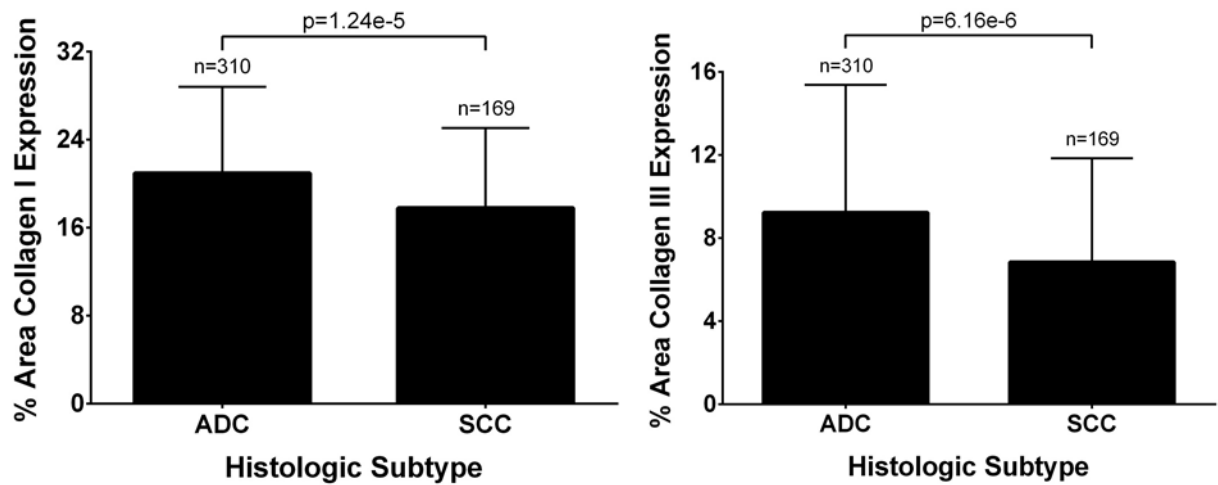


Figure 64. Percent stromal area of tumor tissues with collagen type I or type III expression in patients with lung adenocarcinoma (ACC) or squamous cell carcinoma (SCC).

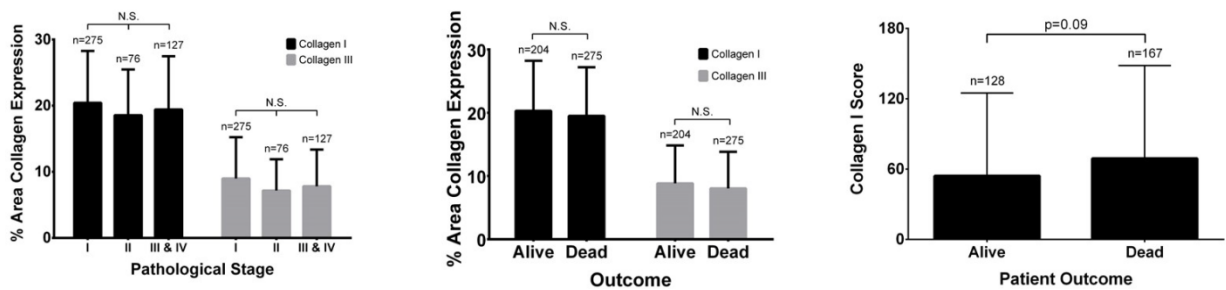


Figure 65. Left: Percent stromal area of collagen type I and type III expression in patients with lung cancer comparing different pathological stages. Middle: Percent stromal area of collagen type I and type III expression in patients with lung cancer comparing patient outcome. Right: Average final cytoplasmic H-score of collagen type I staining in patients with lung adenocarcinoma comparing patient outcome.

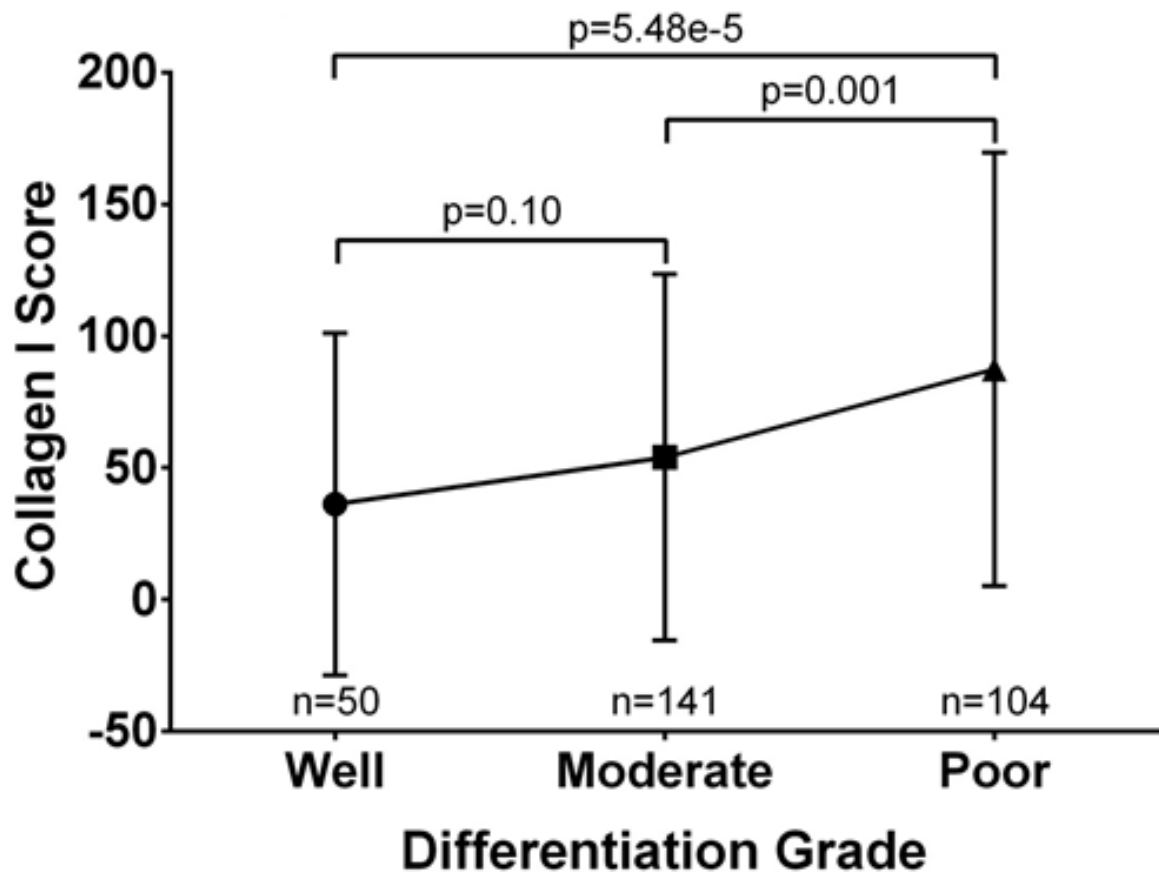


Figure 66. Average final cytoplasmic H-score of collagen type I expression in lung adenocarcinomas of different grades.

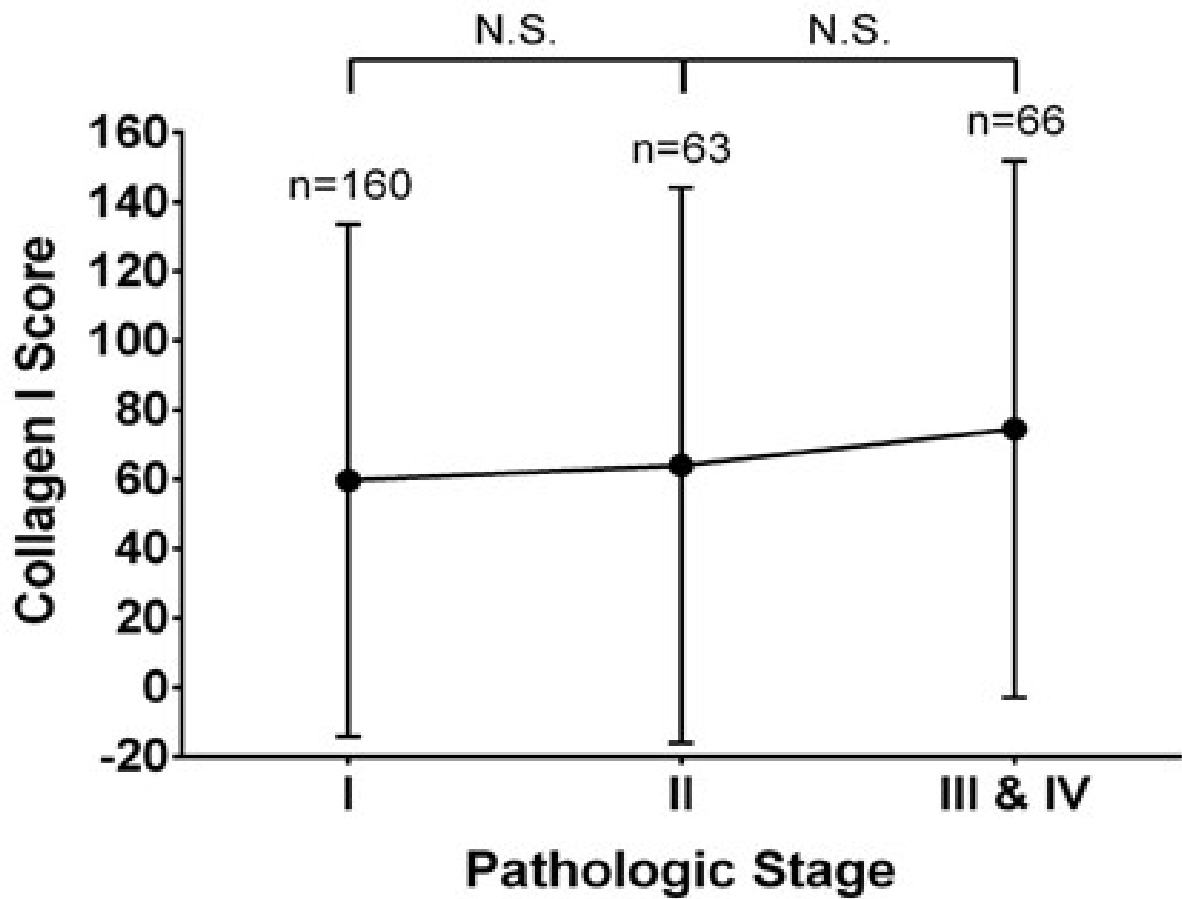


Figure 67. Average final cytoplasmic H-score of collagen type I staining in patients with lung adenocarcinomas of different pathologic stages.

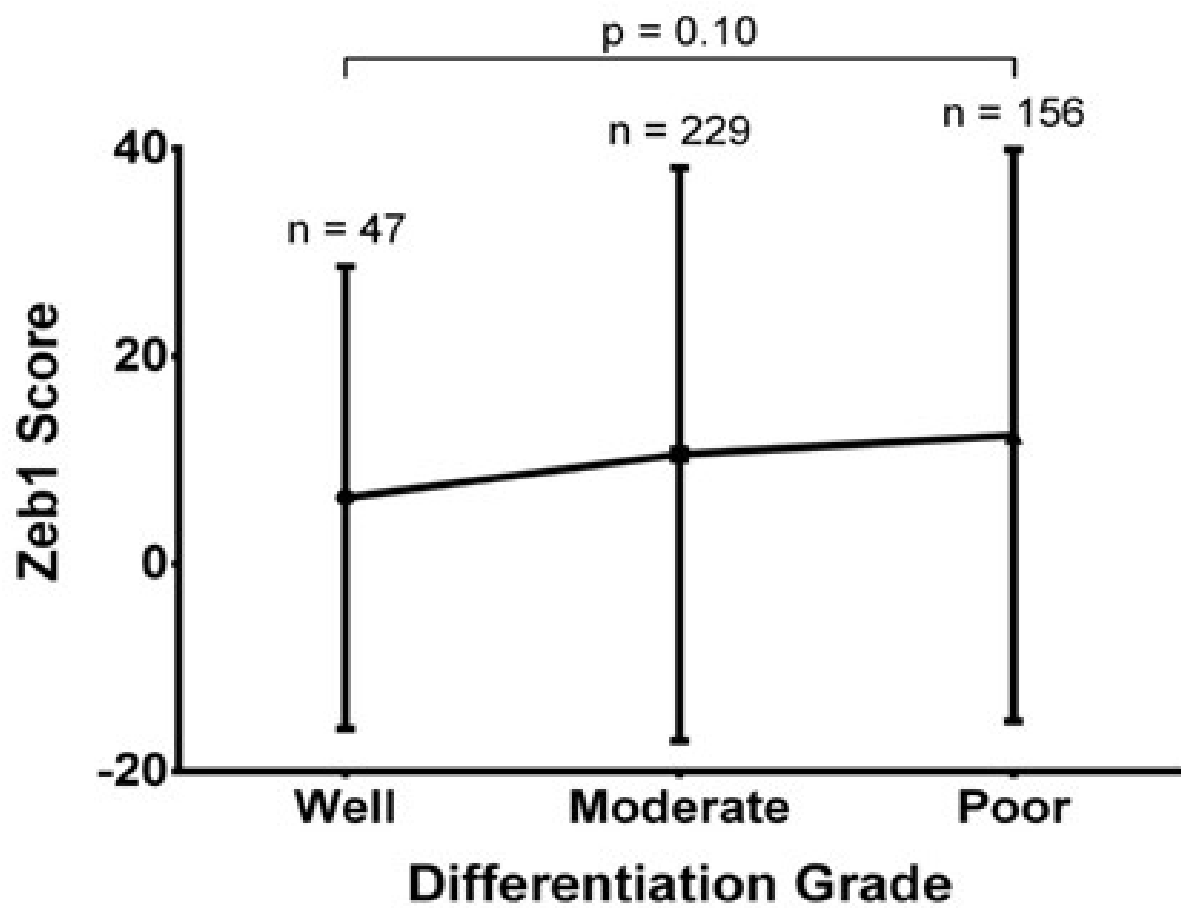


Figure 68. Average final nuclear H-score of Zeb1 staining in lung cancer patients comparing different tumor grades.

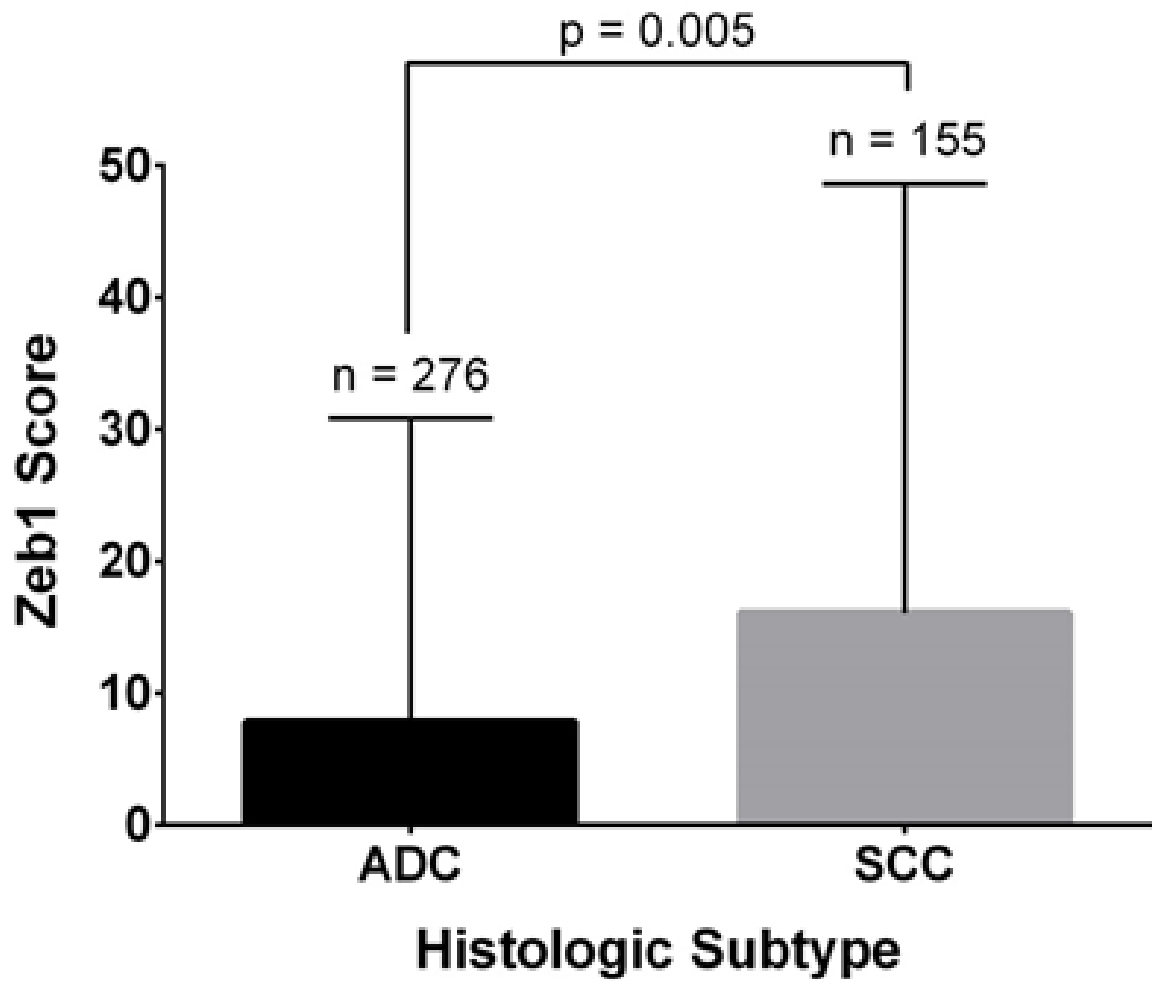


Figure 69. Average final nuclear H-score of Zeb1 in tumor cells of ADC or SCC specimens.

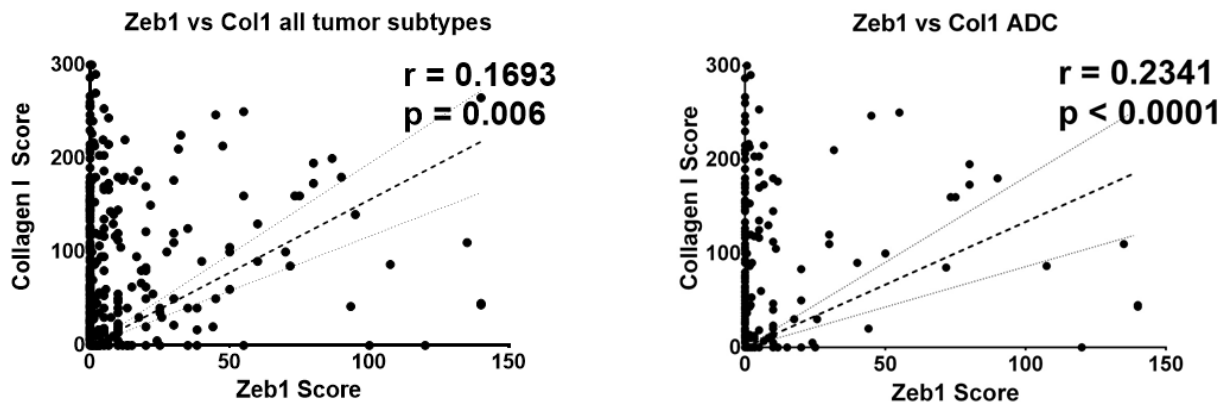


Figure 70. Left: Cluster plot analysis of Spearman's rank correlation between Zeb1 and collagen I H-score in both ADC and SCC specimens. Right: Cluster plot analysis of Spearman's rank correlation between Zeb1 and collagen I H-score in ADC samples.

Zeb1 vs Col1 SCC

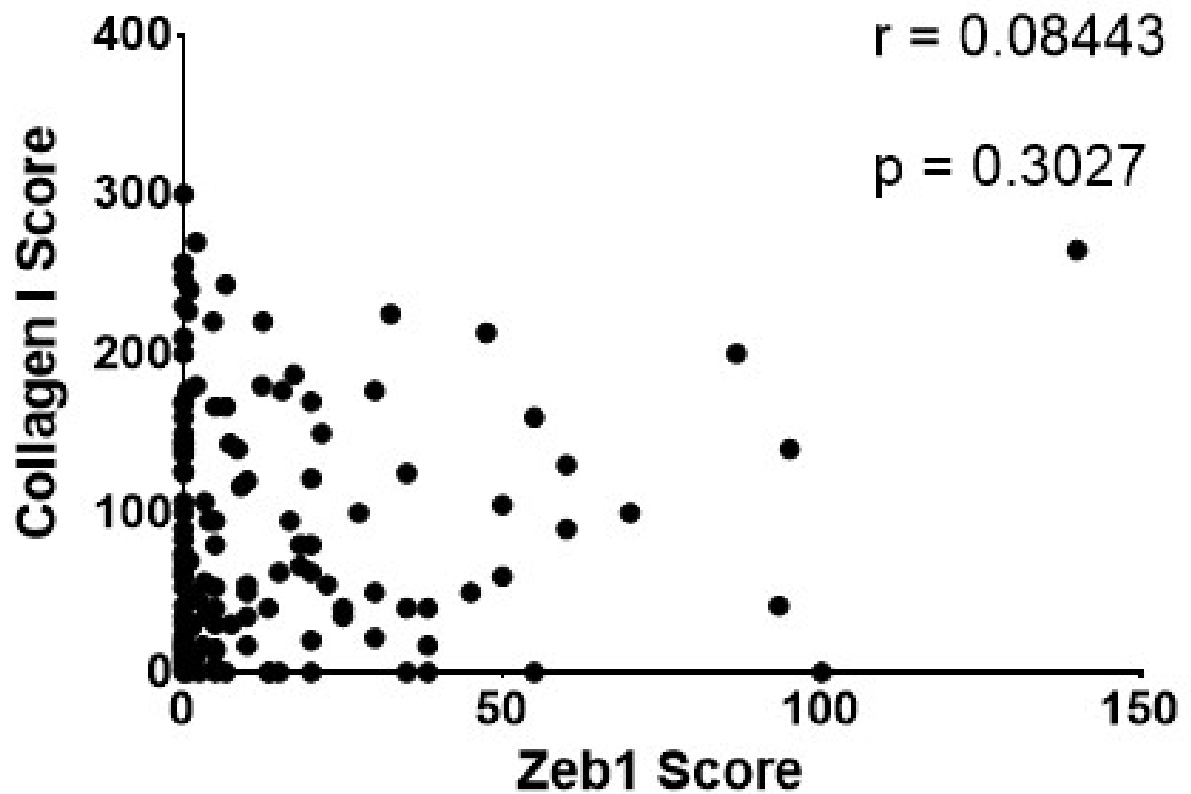


Figure 71. Cluster plot analysis of Spearman's rank correlation between Zeb1 and collagen I H-score in SCC patient tissues.

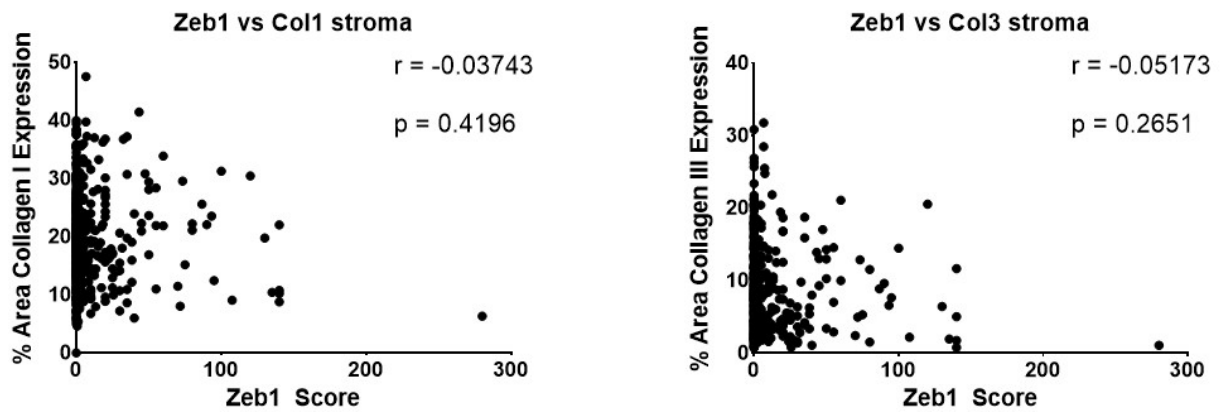


Figure 72. Left: Cluster plot analysis of Spearman's rank correlation between Zeb1 and collagen I stromal area expression. Right: Cluster plot analysis of Spearman's rank correlation between Zeb1 and collagen III stromal area expression.

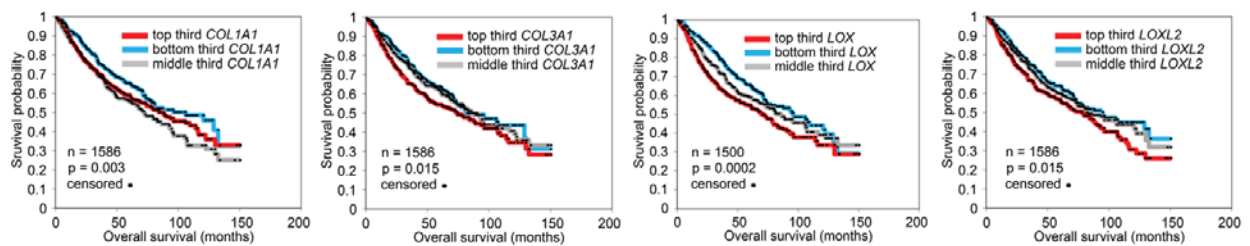


Figure 73. Kaplan-Meier survival analysis by log-rank significance test of COL1A1, COL3A1, LOX, and LOXL2 mRNA expression levels versus overall lung cancer patient survival from a compendium expression dataset of 1,586 lung adenocarcinoma cases. P-values by log-rank test.

Project 2: Epithelial-to-Mesenchymal Transition promotes MEK inhibitor resistance in KRAS mutant lung cancers through suppression of IL17rd

Epithelial lung cancer cells exhibit increased MAPK signaling and dependency for tumor growth

To identify therapeutically targetable genes essential for tumor formation and growth in epithelial and mesenchymal KRAS mutant tumors, we utilized a previously developed *in vivo* loss-of-function screen approach with barcoded, pooled shRNA libraries (97) targeting approximately 200 genes that have FDA approved pharmacological inhibitors (FDAome). The shRNA library was transduced into representative epithelial (393P) and mesenchymal (344P) Kras and p53 mutant murine lung cancer cell lines derived from the *KP* mouse model (33) and implanted subcutaneously in nude mice or cultured *in vitro* (**Figure 74**). Tumors were harvested, shRNA barcodes were quantified by deep sequencing, referenced with the respective *in vitro* cell population, and the phenotypic impact of gene knockdown was inferred by the redundant shRNA activity (RSA) algorithm (111, 112), where lower rank of the shRNA barcodes signified dropout from the population and greater dependency of the gene for tumorigenesis (**Table 2**). Comparison of the results from the two models revealed that epithelial 393P tumors were more reliant on MAPK genes for *in vitro* and *in vivo* growth, while mesenchymal 344P tumor growth was independent of MAPK signaling molecules, despite both cell lines possessing an activating *Kras*^{G12D} mutation (**Figure 75**).

Complementing the *in vivo* shRNA screen, we sought to elucidate the specific differences in signaling patterns between epithelial and mesenchymal lung cancer cells that potentially confer MEK inhibitor resistance. Using reverse phase protein array

(RPPA) to analyze changes in cell signaling proteins in a high throughput manner (113, 114), we screened a panel of previously characterized (33, 48) epithelial and mesenchymal murine/human lung cancer cell lines expressing Zeb1 or miR-200, respectively, and observed an increase in phosphorylated Mek/Erk proteins in epithelial cells (**Figure 76 and 77**). Validation of the RPPA findings by Western blotting in a representative panel of Ras mutant human NSCLC cell lines showed higher levels of endogenous MAPK activity (p-MEK & p-ERK) in epithelial cell lines as characterized by the EMT markers Zeb1, E-cadherin, and Vimentin (**Figure 78**). Additionally, modulation of the EMT status through induced miR-200 expression in mesenchymal cells increased p-Mek/p-Erk levels in a time-dependent manner, while induced Zeb1 expression in epithelial cells had the opposite effect (**Figure 78 and 79**).

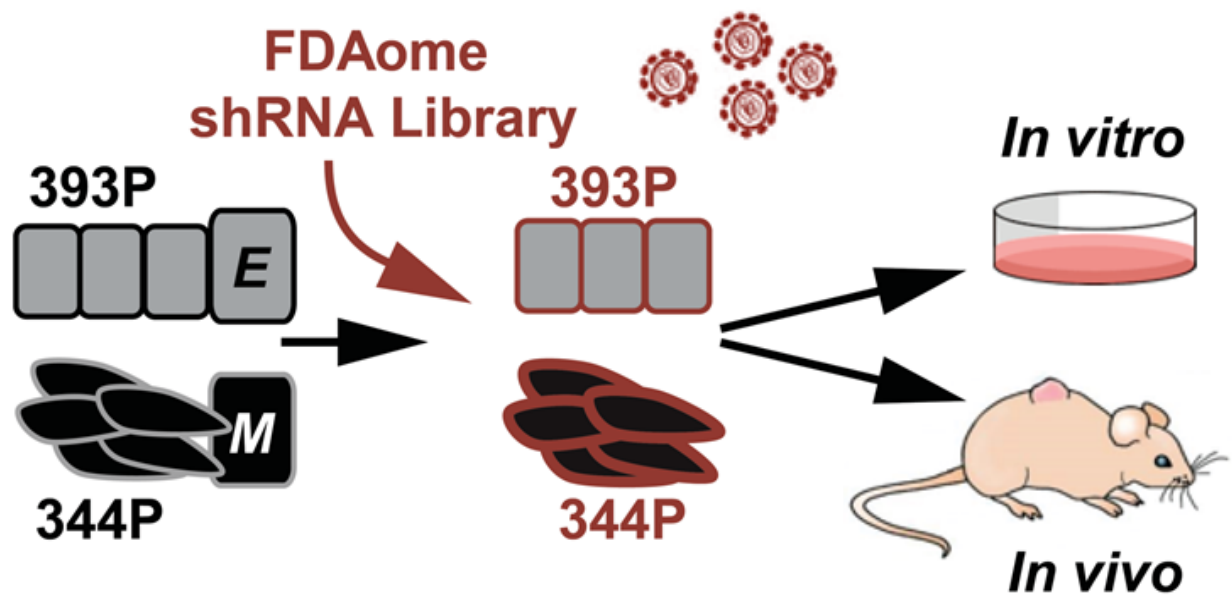


Figure 74. Experimental design for FDAome shRNA drop-out screens in epithelial (393P) and mesenchymal (344P) murine lung cancer cell lines implanted subcutaneously in vivo (nude mice) and grown in parallel in vitro (20 doublings).

Table 2. Gene level dropout scores for each of the four screens described in Figure 73. For each gene in the custom library, the log10 p-value (logP) of the RSA score is displayed, and the rank of the gene within a specific screen. The difference in ranks is also displayed for comparison of 393P and 344P.

gene	393P				344P				393P vs 344P	
	<i>in-vivo</i>		<i>in-vitro</i>		<i>in-vivo</i>		<i>in-vitro</i>		<i>in-vivo</i>	<i>in vitro</i>
	logP	rank	logP	rank	logP	rank	logP	rank	rank difference	rank difference
ErbB2	-9.5	1	-3.2	11	-3.3	11	-3.5	12	-10	-1
Psmb1	-8.8	2	-13.6	1	-2.8	19	-6.4	2	-17	-1
Raf1	-7.7	3	-7.6	3	0.0	190	-0.5	133	-187	-130
Pik3ca	-5.7	4	-2.8	17	-6.9	1	-4.3	7	3	10
Plk1	-5.4	5	-1.1	70	-6.1	3	-6.3	3	2	67
Wee1	-5.0	6	-6.3	5	-1.7	43	-3.0	15	-37	-10
Rac1	-4.3	7	-3.1	15	-2.8	17	-1.8	38	-10	-23
Mapk1	-4.1	8	-2.4	22	-0.7	107	-0.3	157	-99	-135
Cdk6	-3.9	9	-1.3	57	-3.9	8	-4.2	8	1	49
Mtor	-3.8	10	-2.0	34	-5.6	4	-1.7	40	6	-6
Prkcd	-3.7	11	-3.7	10	-4.5	6	-5.1	4	5	6
Stat3	-3.4	12	-0.8	114	-2.8	21	-2.3	27	-9	87
Bcl2	-3.2	13	-2.3	28	-5.1	5	-1.3	52	8	-24
Pim1	-3.1	14	-0.7	126	-2.1	36	-1.3	56	-22	70
Rrm1	-3.1	15	-4.2	9	-1.1	79	-2.2	29	-64	-20
Myc	-3.0	16	-6.9	4	-4.5	7	-4.8	5	9	-1
Xpo1	-3.0	17	-0.7	115	-0.7	113	-1.2	61	-96	54
Met	-2.8	18	-0.7	123	-1.6	47	-1.1	70	-29	53
Esr1	-2.8	19	-2.4	24	-2.3	31	-2.8	17	-12	7
Mapk8	-2.8	20	-1.2	62	-1.4	61	-0.9	82	-41	-20
Mapk7	-2.7	21	-0.7	119	-2.8	20	-0.7	105	1	14
Rarg	-2.7	22	-2.5	21	-2.2	35	-4.1	10	-13	11
Jak2	-2.7	23	-2.2	29	-0.8	103	-2.6	20	-80	9
Insr	-2.7	24	-1.3	58	-1.1	78	-1.1	69	-54	-11
Top2a	-2.6	25	-3.1	14	-1.6	46	-1.9	36	-21	-22
Psmd1	-2.6	26	-4.5	7	-3.6	9	-2.0	31	17	-24
Ikbke	-2.5	27	-1.8	41	-2.5	25	-0.8	92	2	-51
Egfr	-2.4	28	-0.7	117	-1.6	51	-0.8	95	-23	22
Birc5	-2.4	29	-5.9	6	-3.2	15	-2.9	16	14	-10
Blk	-2.4	30	-1.1	79	-0.3	155	-0.2	174	-125	-95
Pdgfrb	-2.3	31	-0.8	104	-0.7	112	-0.6	118	-81	-14
Src	-2.3	32	-1.1	73	-0.7	119	-1.7	41	-87	32
Mcl1	-2.2	33	-0.1	181	-1.3	71	-0.9	80	-38	101
Prkch	-2.2	34	-2.0	38	-1.0	87	-0.9	90	-53	-52
Top1	-2.1	35	-3.1	13	-2.3	29	-2.5	22	6	-9
Cdk7	-2.1	36	-0.4	144	-2.4	27	-1.1	64	9	80
Cdk9	-2.1	37	-1.2	68	-1.4	63	-0.9	88	-26	-20
Nfkb1	-1.9	38	-1.4	54	-1.3	67	-0.2	169	-29	-115
Aurkb	-1.9	39	-3.2	12	-2.8	18	-2.0	35	21	-23
Dot1l	-1.9	40	-0.6	129	-1.9	41	-0.2	180	-1	-51
Chek1	-1.9	41	-3.0	16	-1.5	52	-2.7	18	-11	-2
Prkdc	-1.8	42	-1.0	82	-1.5	55	-1.6	44	-13	38
Flt4	-1.8	43	-2.5	20	-3.2	14	-4.1	9	29	11
Parp2	-1.8	44	-0.4	140	-1.1	82	-0.8	96	-38	44
Pgd	-1.8	45	-1.9	40	-1.0	85	-1.3	57	-40	-17
Notch1	-1.8	46	-2.4	25	-1.1	81	-0.4	142	-35	-117
Atr	-1.7	47	-7.9	2	-1.9	40	-3.8	11	7	-9
Ehmt2	-1.7	48	-1.7	44	-1.2	72	-0.6	127	-24	-83
Lap3	-1.7	49	-0.4	143	-0.4	138	-0.4	151	-89	-8
Esr2	-1.6	50	-1.1	69	-2.4	28	-0.6	123	22	-54

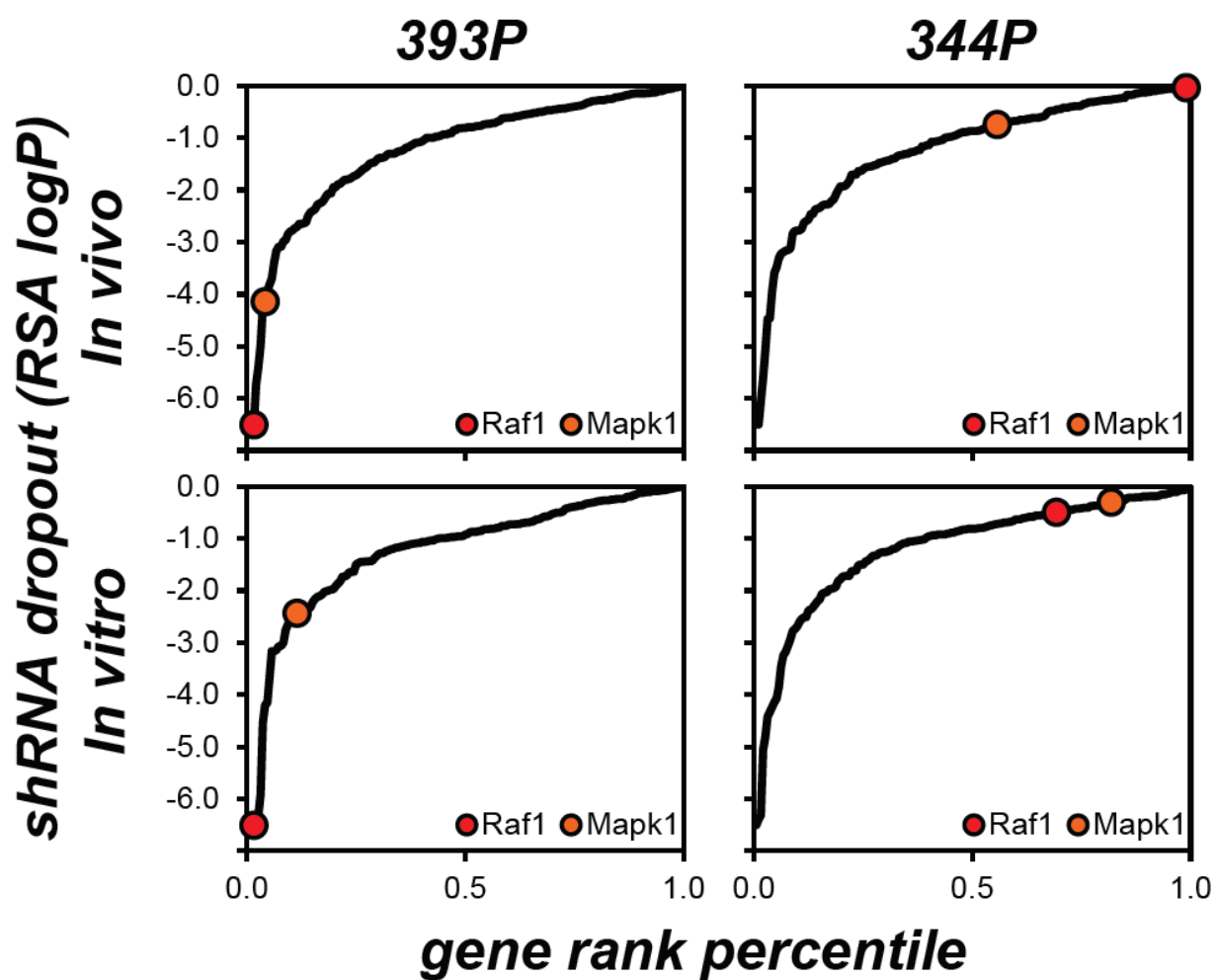


Figure 75. Gene rank analysis highlighting the behavior of Raf1 and Mapk1 genes in the FDAome *in vivo* and *in vitro* screens executed in epithelial (393P) and mesenchymal (344P) murine lung cancer cell lines (shRNA dropout score = RSA logP).

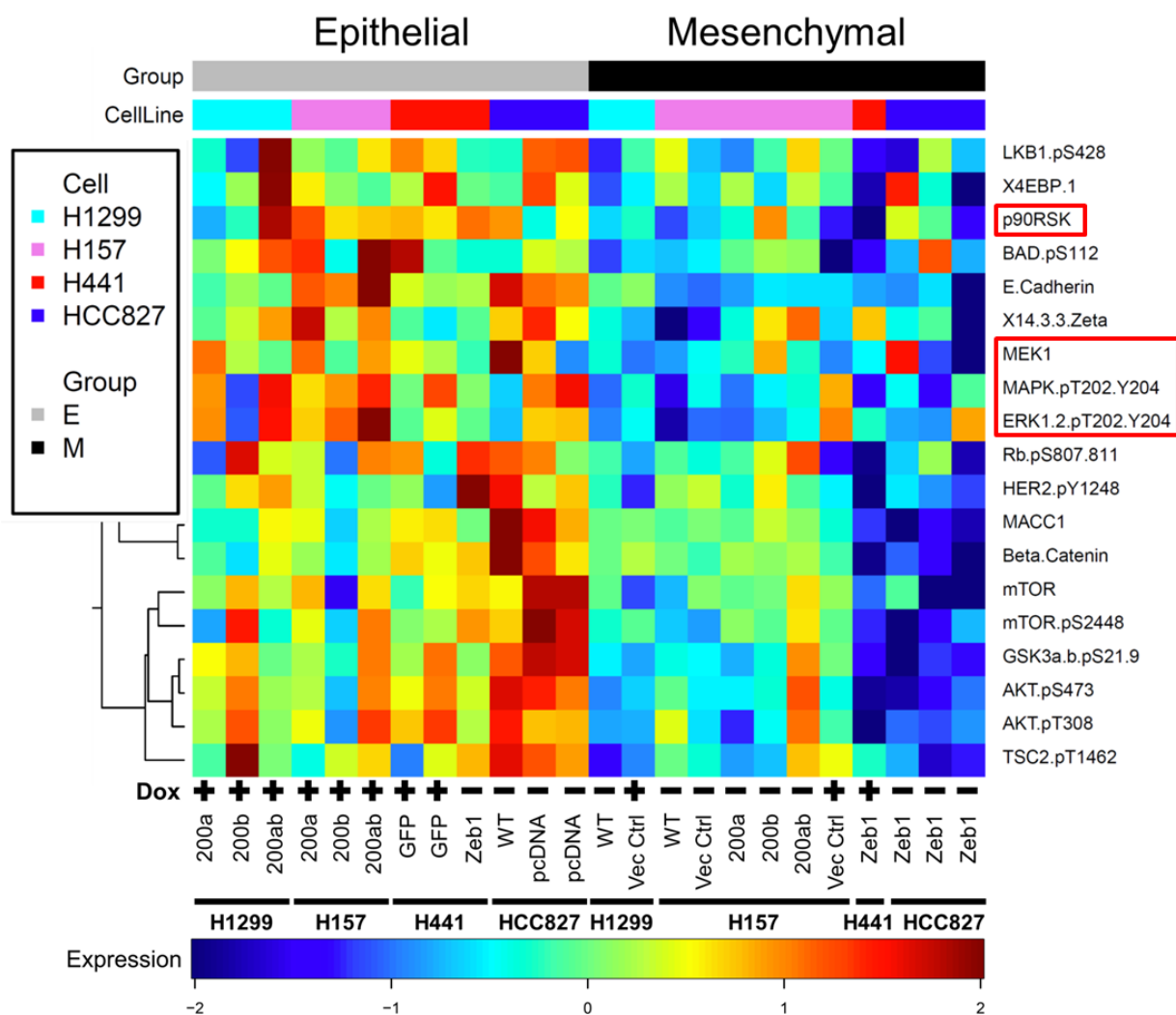


Figure 76. Heatmap showing significantly upregulated signaling proteins in isogenically-matched epithelial and mesenchymal human lung cancer cell lines. Cell lines expressed Doxycycline (Dox) inducible miR-200 or Zeb1 where indicated. Zeb1 was constitutively expressed in HCC827 cells.

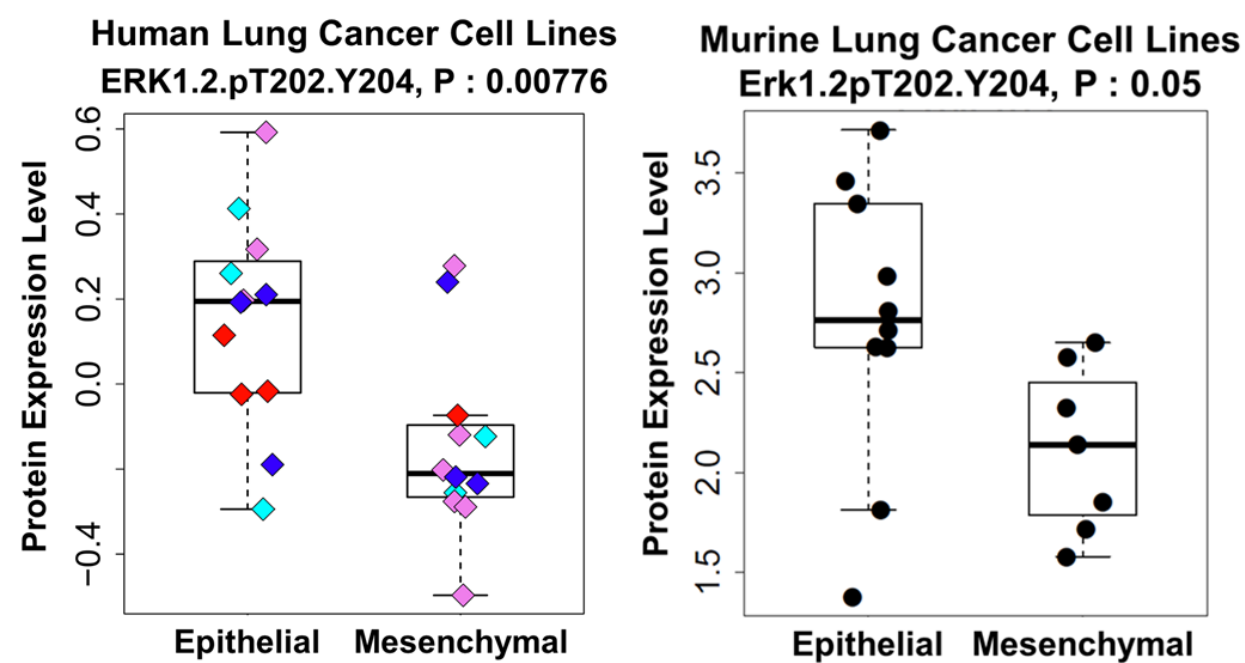


Figure 77. Dot plot of p-Erk expression levels from RPPA dataset in a panel of mesenchymal and epithelial human and murine lung cancer cells.

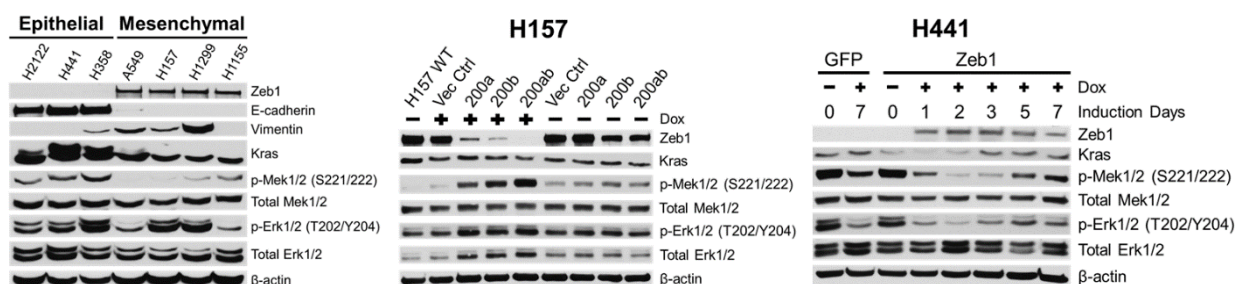


Figure 78. Left: Western blot of the EMT markers Zeb1, E-cadherin, Vimentin and MAPK signaling molecules in a panel of human KRAS mutant lung cancer cell lines. Western blot of indicated proteins in (Middle) H157 cells after Dox-induced miR-200 expression for 7 days and (Right) H441 cells after Dox-induced Zeb1 expression at indicated time points.

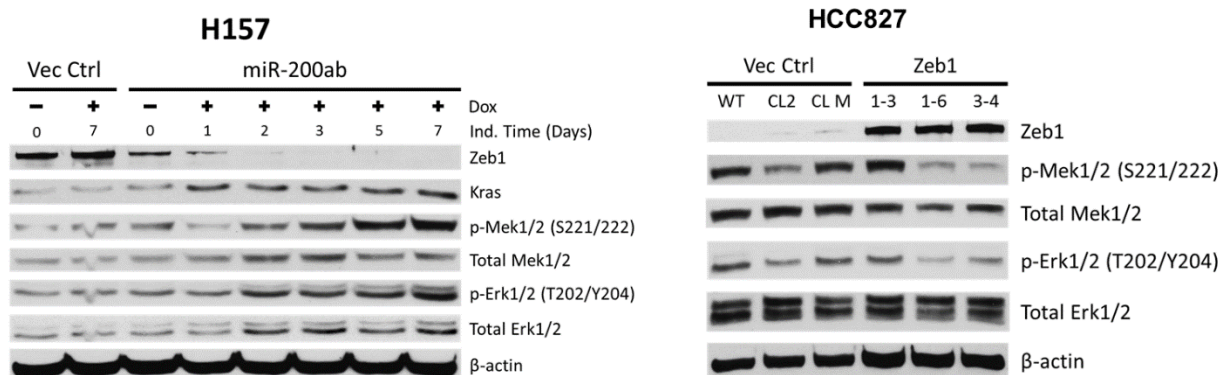


Figure 79. Left: Time course western blot of indicated proteins in H157 cells with Dox induction of miR-200. Right: Western blot of indicated proteins in HCC827 cells with stable, constitutive expression of Zeb1.

Activation of Mek/Erk signaling in epithelial cells is driven by the Ras-Raf-Mek-Erk signaling cascade

Since Mek and Erk are activated by various signaling molecules, we next sought to establish the pathway responsible for differential MAPK activation. Analysis of the canonical Ras-Raf-Mek-Erk signaling cascade (**Figure 80**) after reversion of the mesenchymal H157 and H1155 *KRAS* mutant cells to an epithelial state through induced, stable, or transient expression of miR-200 showed an increase in Kras binding to the Ras binding domain (RBD) of Raf1 (CRaf) followed by activation of MAPK signaling (**Figure 80 and 81**). The observation that MAPK signaling is dependent on the EMT status of the cells was noted despite the driver mutation present, as miR-200 expression activated MAPK signaling in *EGFR* mutant (HCC827), *NRAS* mutant (H1299), *EGFR/RAS* wild-type (WT) (H2882), and murine *Kras*^{LA1-G12D};*p53*^{R172HΔG/+} (KP) lung cancer cells (**Figure 82 and 83**). Moreover, miR-200 expression upregulated MAPK signaling in epithelial, non-transformed BEAS2B cells with constitutive expression of mutant *KRAS*^{G12D} or *EGFR*^{Δ722-726} (59) (**Figure 84**), demonstrating that this process is independent of oncogenic and co-mutational events.

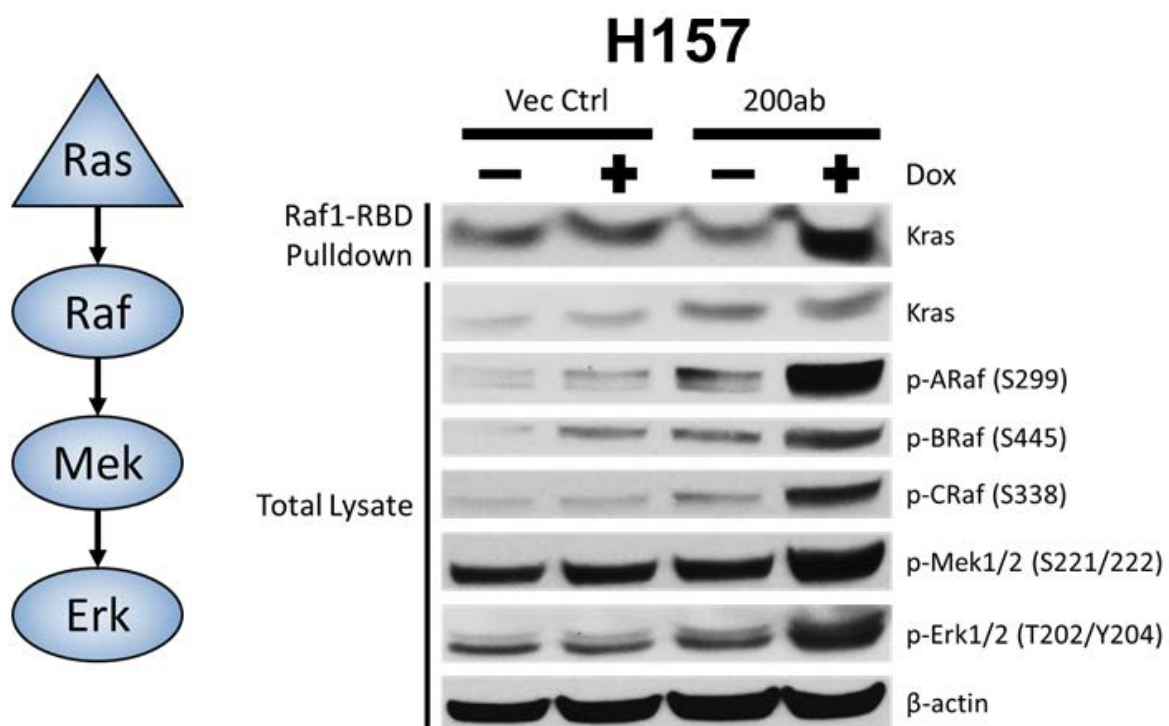


Figure 80. Left: Schematic of Ras-Raf-Mek-Erk MAPK pathway. Top Right: Western blot of Kras from Ras-GTP pulldown with the Ras binding domain (RBD) of Raf1 following miR-200 induction in mesenchymal H157 lung cancer cell line. Bottom Right: Western blots of whole cell lysates of MAPK signaling molecules in H157 cells with induced miR-200 expression.

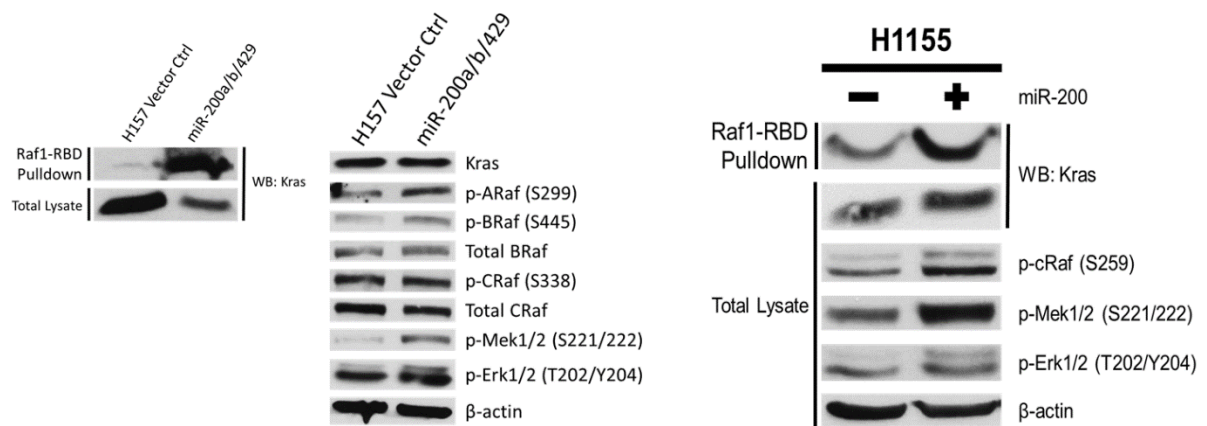


Figure 81. Left: Western blot of Kras after Ras-GTP pulldown with Raf1-RBD as well as total Kras levels in whole cell lysates of H157 cells with stable miR-200 expression. Middle: Western blot of MAPK signaling proteins in H157 cell lysates after with miR-200 expression. Right: Western blot of Kras after Ras-GTP pulldown with Raf1-RBD in mesenchymal H1155 cells with transient miR-200 expression. Total cell lysates were immunoblotted for MAPK signaling proteins.

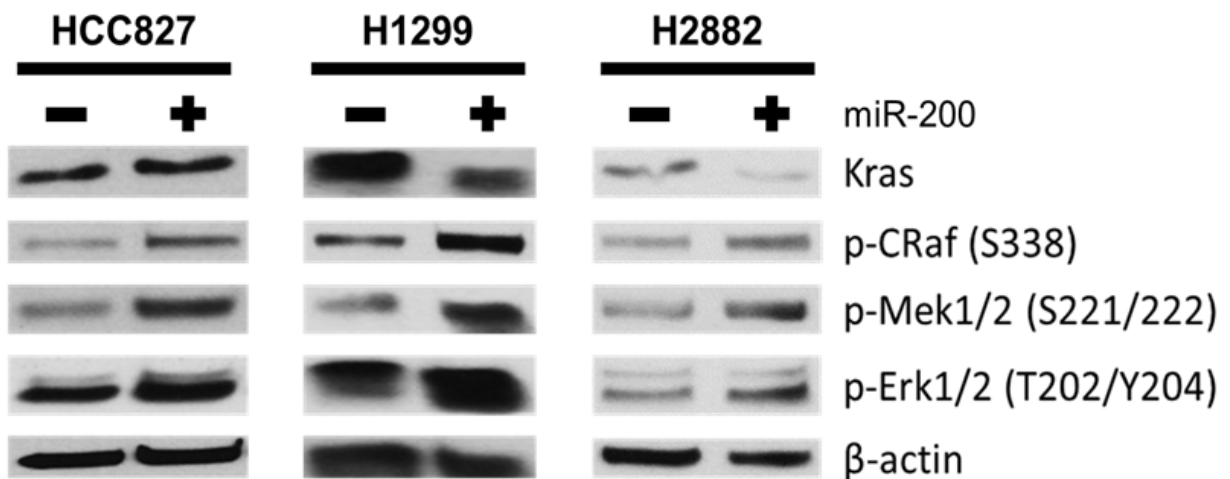


Figure 82. Western blots of MAPK signaling proteins in HCC827 (EGFR mutant), H1299 (NRAS mutant), and H2882 (EGFR and NRAS WT) human lung cancer cell lines after transient expression of miR-200a/b/c.

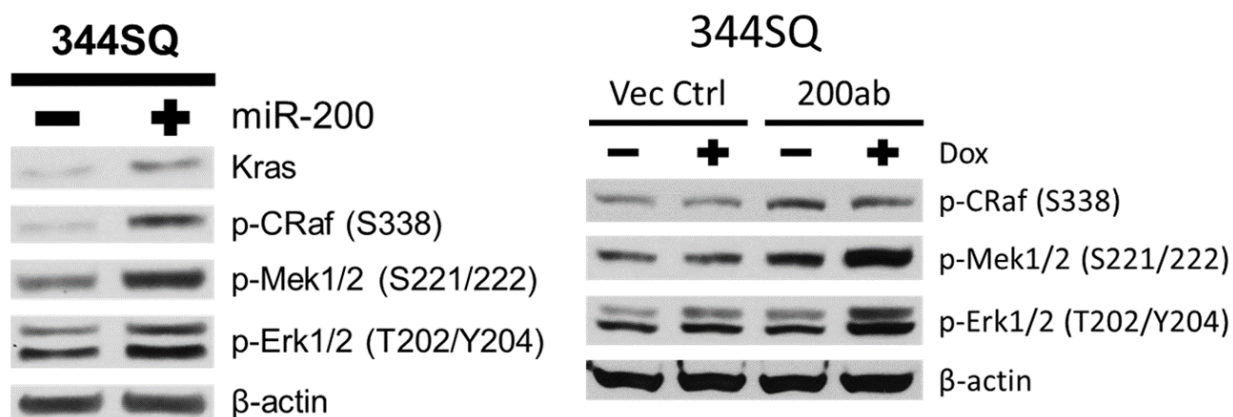


Figure 83. Western blot MAPK signaling proteins in mesenchymal 344SQ murine lung cancer cell line with (Left) transient or (Right) Dox inducible miR-200 expression.

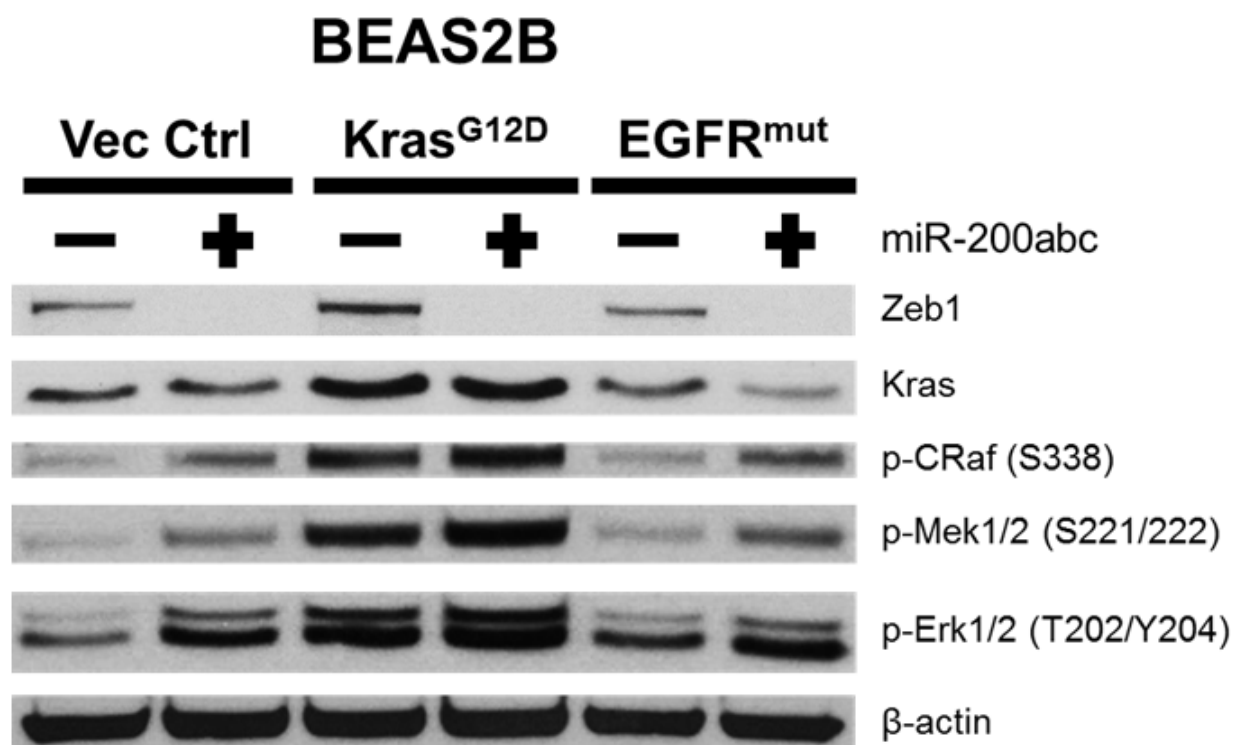


Figure 84. Western blots of MAPK signaling proteins in non-transformed BEAS2B epithelial human lung cell line expressing mutant KRAS or mutant EGFR in conjunction with transient expression of miR-200a/b/c.

To verify that the Ras-Raf-Mek pathway is necessary to activate p-Erk, we transiently knocked down *KRAS* by shRNA after miR-200 induction and observed a significant reduction in MAPK signaling in both epithelial and mesenchymal cells (**Figure 85**). Interestingly, *KRAS* knockdown caused activation of cleaved caspase-3, indicating that Kras is still necessary for cell survival despite the EMT status and suppression of MAPK signaling. Similarly, chemical inhibition of pan-Raf enzymatic activity and siRNA knockdown of Raf isoforms individually or in combination demonstrated that MAPK activation was predominantly dependent on the enzymatic function of the CRaf isoform (**Figure 86 and 87**). Knockdown of all three Raf isoforms most significantly reduced p-Mek/p-Erk in miR-200 expressing cells, but not in mesenchymal control cells, suggesting that miR-200 potentially aids Raf heterodimerization and activation by Kras to drive MAPK signaling (**Figure 87**).

In addition to the Ras-Raf pathway, we also examined the alternative Fak-Rac-Pak signaling pathway for p-Mek/p-Erk activation (**Figure 88**). Stable or induced miR-200 expression in H157 cells decreased p-Fak levels, consistent with our previous work (58), but increased levels of p-Pak2 (**Figure 88 and 89**). Small molecule inhibition of Fak had no effect on MAPK signaling, while siRNA mediated knockdown of *PAK1* and/or *PAK2* showed only partial contribution of Pak2 in activating MAPK signaling, but to a much lower degree than Ras-Raf (**Figure 89 and 90**).

H157

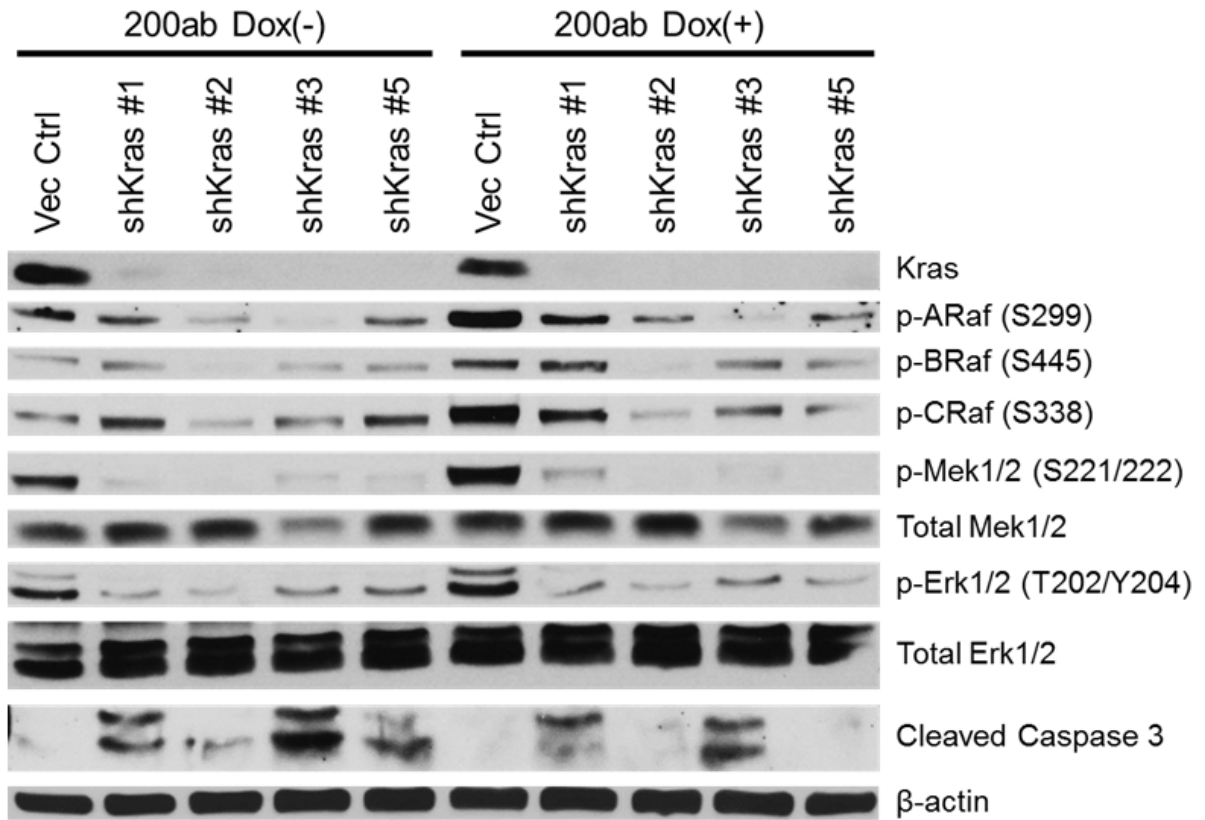


Figure 85. Western blots of MAPK signaling proteins in H157 cells with induced miR-200 expression after KRAS knockdown by shRNA.

H157

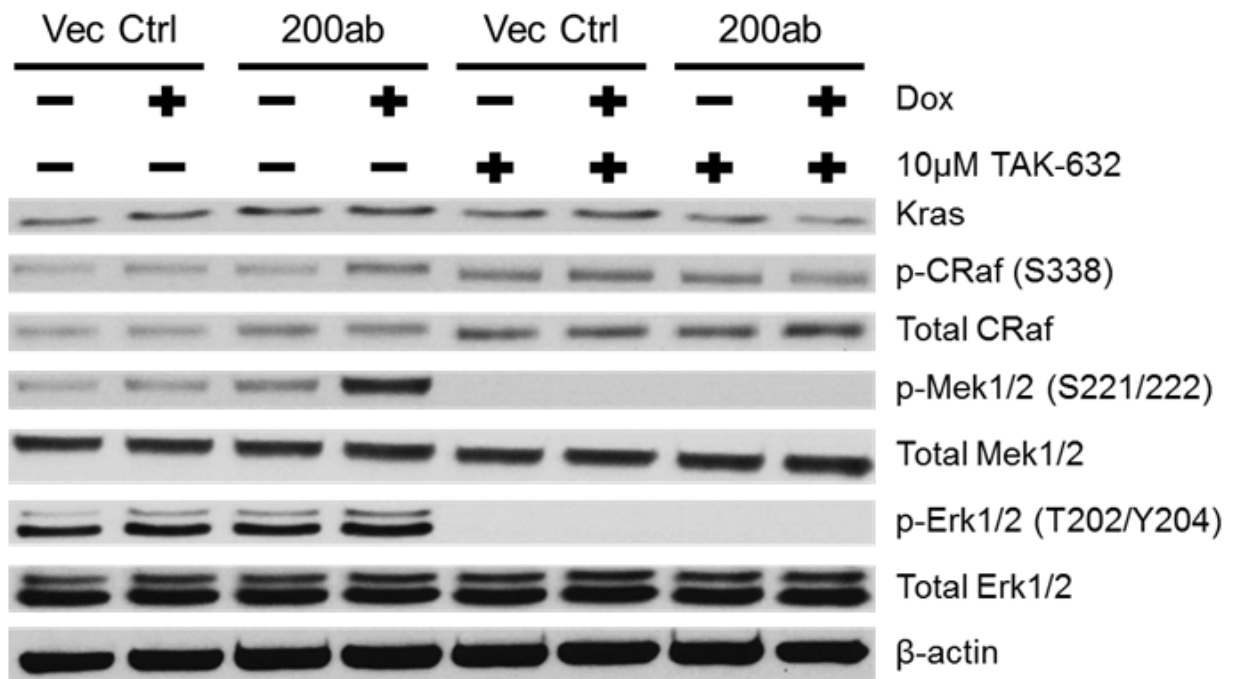


Figure 86. Western blots of MAPK signaling proteins in H157 cells with induced miR-200 expression after inhibition of pan-Raf enzymatic activity for 24 hours with TAK-632.

H157

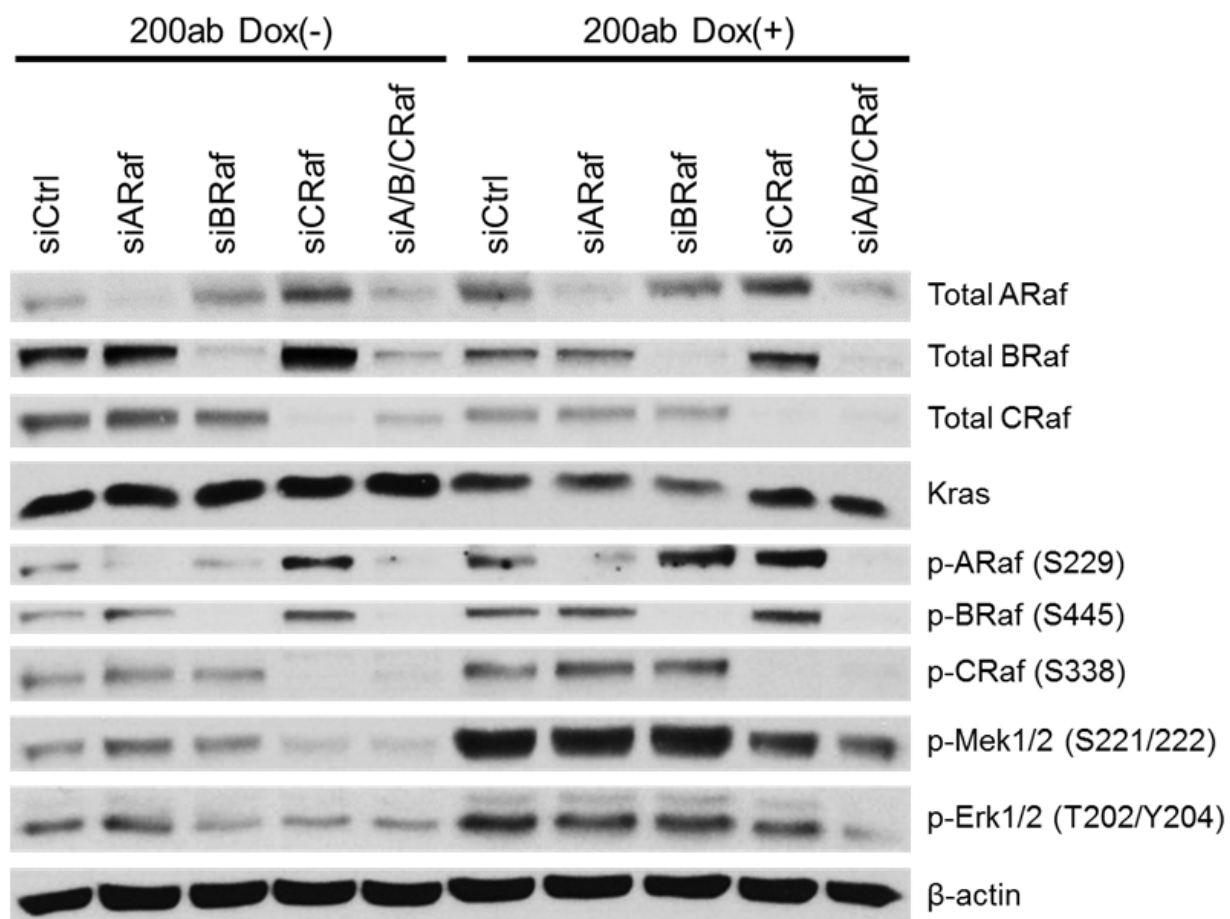


Figure 87. Western blots of MAPK signaling proteins in H157 cells with induced miR-200 expression after 48hr siRNA-mediated knockdown of Raf isoforms individually or in combination.

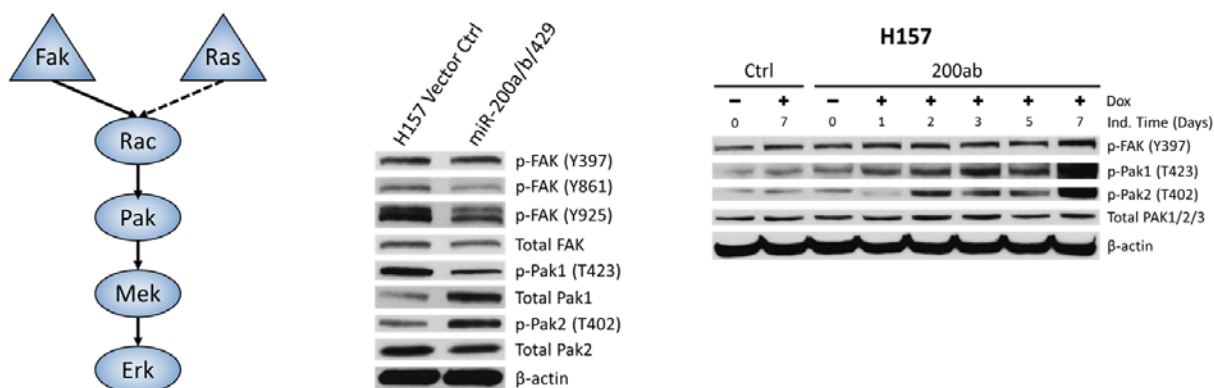


Figure 88. Left: Schematic of Fak-Rac-Pak-Mek-Erk signaling pathway. Middle: Western blot of activated p-Fak and p-Pak in H157 cells with stable miR-200 expression. Right: Time course western blot of activated p-Pak in H157 cells with Dox inducible miR-200 expression.

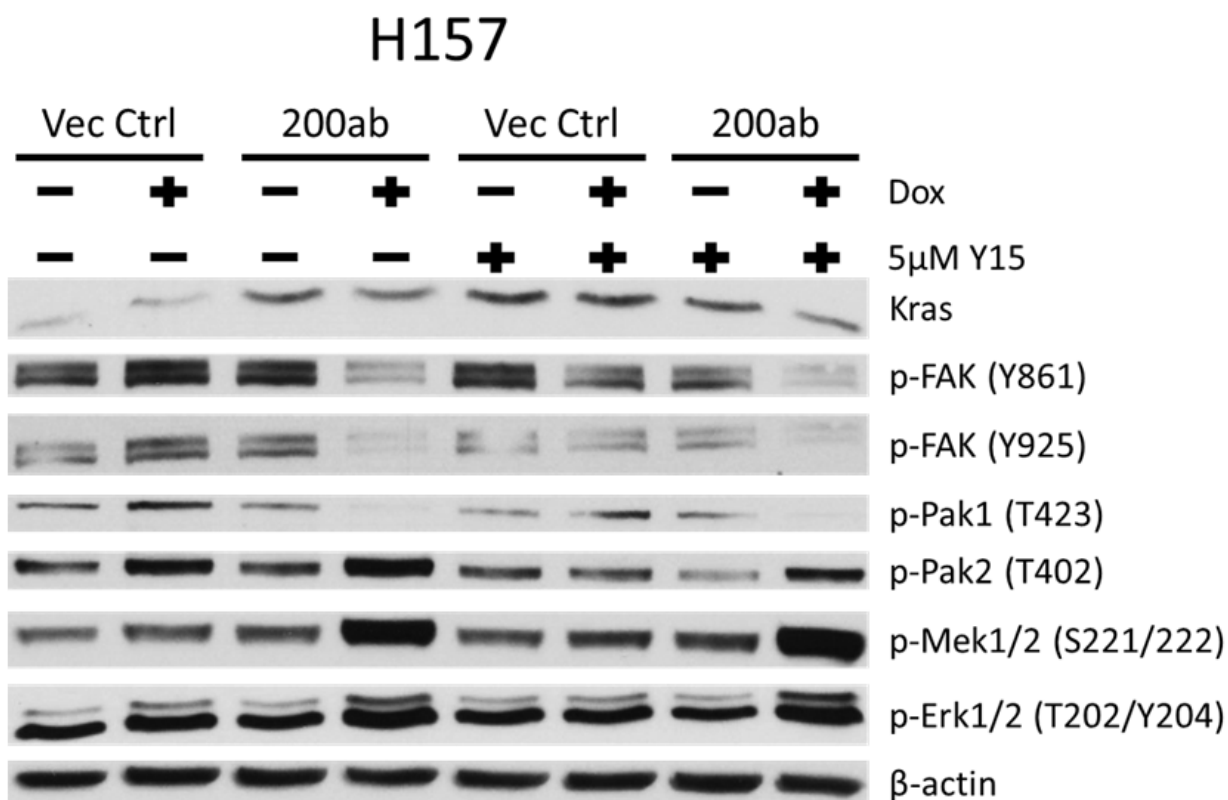


Figure 89. Western blot of indicated proteins after chemical inhibition of Fak enzymatic activity in H157 cells with 7-day Dox induced miR-200 expression.

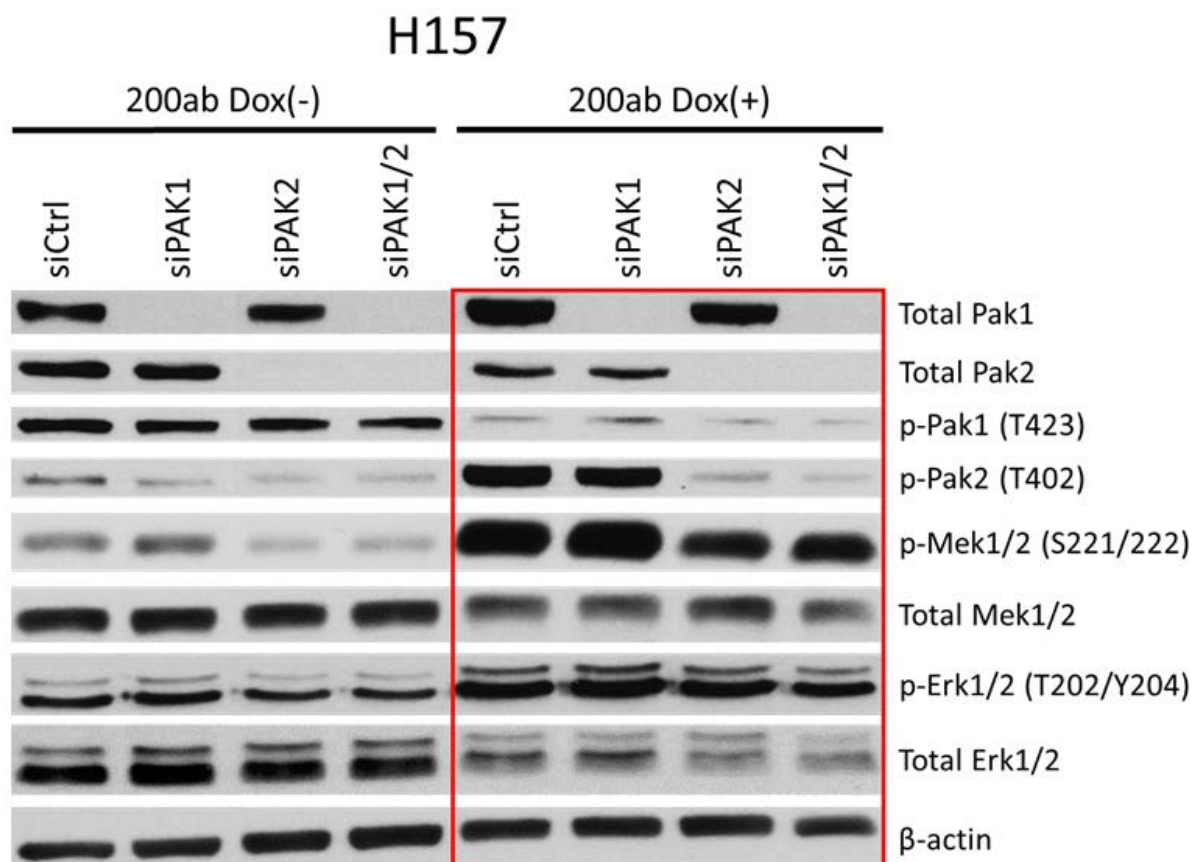


Figure 90. Western blot of indicated proteins after individual or combinatorial siRNA-mediated knockdown of Pak1 and Pak2 in H157 cells with 7-day Dox induced miR-200 expression.

Regulation of MAPK pathway signaling is linked to the EMT state by differential expression of the scaffold protein I17rd

We next sought to ascertain the mechanism of MAPK activation in epithelial cells expressing miR-200. To determine if signaling was due to upstream growth factor stimulation of receptor tyrosine kinases or other mitogen activated receptors, the KRAS mutant H157 cells in the presence or absence of miR-200 expression were cultured in serum-free media for 24 hrs and stimulated with either media containing fetal bovine serum (FBS), continued serum-free conditions, or epithelial growth factor (EGF) for 4 hrs. In mesenchymal cells, there was a significant reduction in MAPK signaling under serum-free conditions compared to FBS stimulation, while EGF only marginally activated signaling (**Figure 91**). However, cells with miR-200 induction continued to have increased MAPK signaling regardless of culture conditions (**Figure 91**), which suggests that miR-200-dependent activation of the MAPK pathway in KRAS mutant cells occurs through an intracellular component independent of extrinsic factors.

H157

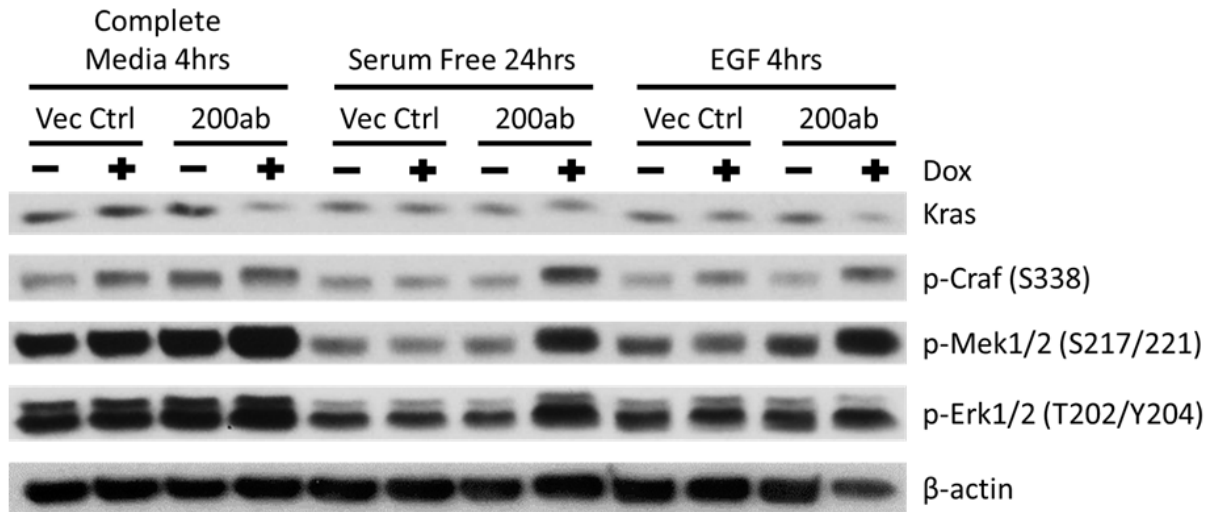


Figure 91. Western blot of MAPK signaling molecules in H157 cells +/- miR-200 expression after 24hr serum-free starvation, followed by stimulation with complete serum media, serum-free media, or EGF for 4 hours.

Since miR-200-mediated activation of Mek/Erk signaling occurs predominantly through the Ras-Raf signaling junction, is dependent on multiple Raf isoforms, and is intracellularly regulated, our data implied that MAPK regulation by EMT was dependent on changes in inhibitory or scaffolding proteins. We performed qPCR analysis for expression of MAPK inhibitory and scaffold genes reported to interact with Raf (15), with and without miR-200 induction (**Figure 92 and 93**). Inhibitory genes with at least 50% decrease or scaffold genes with at least 2-fold increase in expression after miR-200 induction were selected for further analysis (**Figure 92**). Increased expression of SPRY4 and the various DUSP genes (**Figure 93**) after miR-200 induction is consistent with feedback inhibition responses due to upstream activation of the MAPK pathway (16-18, 21, 22). As SPRY1 was the only inhibitory gene significantly downregulated by over 50% with miR-200 expression, we proceeded to knockdown SPRY1 by siRNA in H157 cells or transiently express SPRY1 in miR-200 expressing H157 cells and observed no significant effect on MAPK signaling in either case (**Figure 94**). QPCR analysis of various Raf-associated scaffolding genes (**Figure 92 and 93**) identified KSR2, SFN (14-3-3 σ), CNK2, SHOC2, and I17RD as potential targets that were significantly upregulated at least 2-fold with miR-200 expression (**Figure 92**). Western blot validation of the qPCR data showed no significant differences in SHOC2 or CNK2 protein levels (**Figure 95**). Although miR-200 expression significantly increased 14-3-3 σ protein and KSR2 mRNA levels, respectively, knockdown of either gene after miR-200 induction had no effect on MAPK signaling (**Figure 96**).

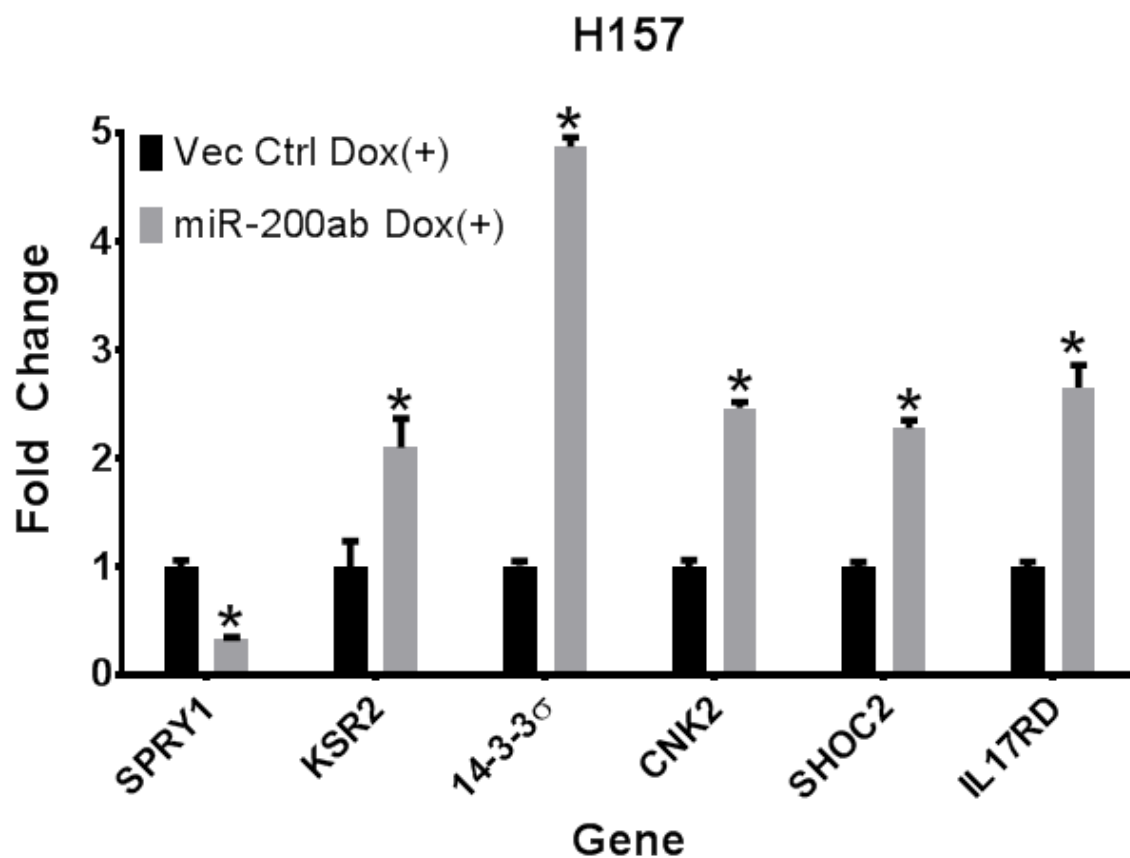


Figure 92. QPCR analysis for relative expression of SPRY1, KSR2, 14-3-3 σ /SFN, CNK2, SHOC2, and IL17RD in H157 cells with inducible miR-200 expression. Asterisks (*) represent significance value of $p < 0.01$.

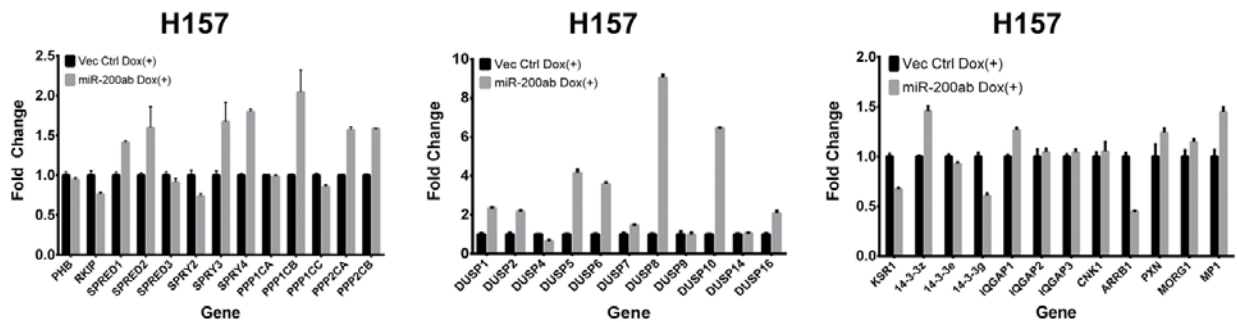


Figure 93. QPCR analysis of (Left) MAPK inhibitory genes, (Middle) DUSP gene family, and (Right) MAPK scaffold genes in H157 cells with inducible miR-200 expression.

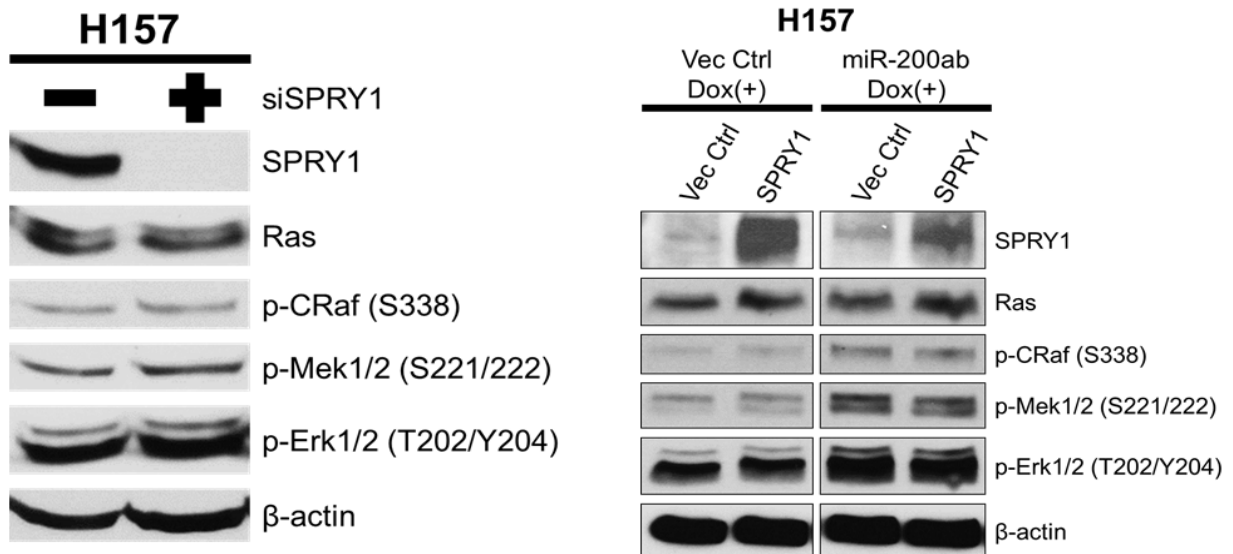


Figure 94. Left: Western blot of Spry1 and MAPK signaling molecules after 96hr siRNA knockdown of SPRY1 in mesenchymal H157 cells. Right: Western blot of Spry1 and MAPK signaling molecules in H157 cells with inducible miR-200 after 96hr SPRY1 transient overexpression.

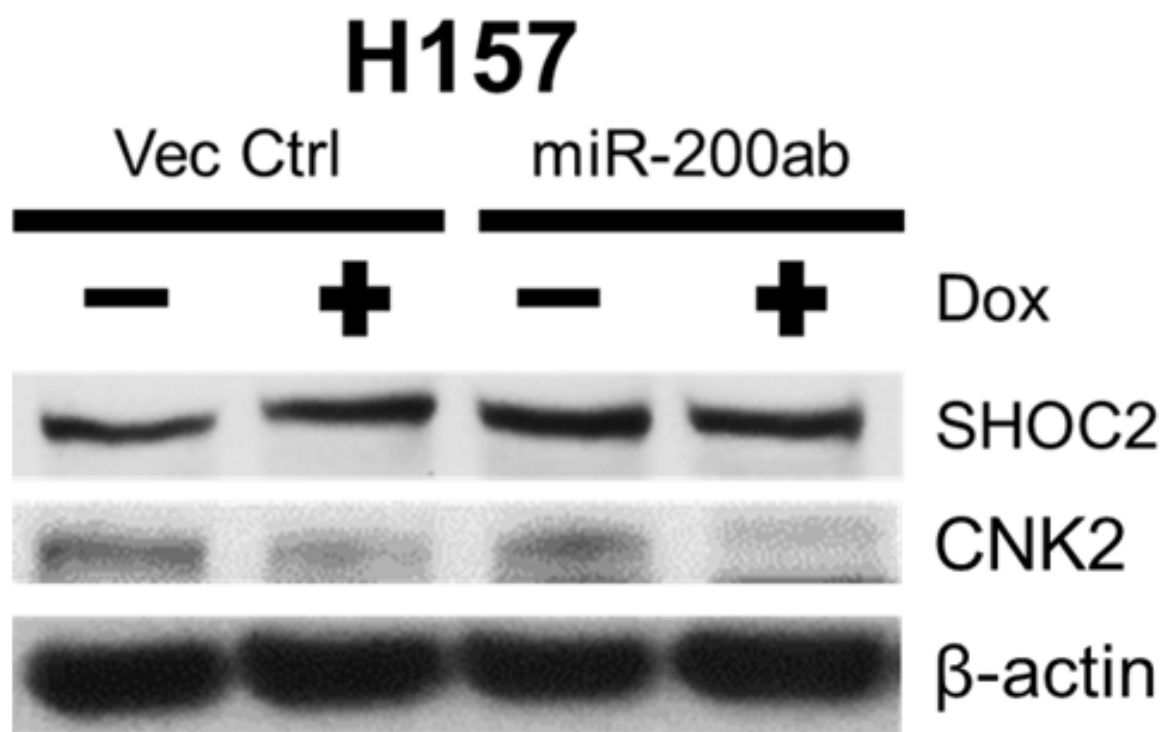


Figure 95. Western blot of Shoc2 and Cnk2 in H157 cells with inducible miR-200 expression.

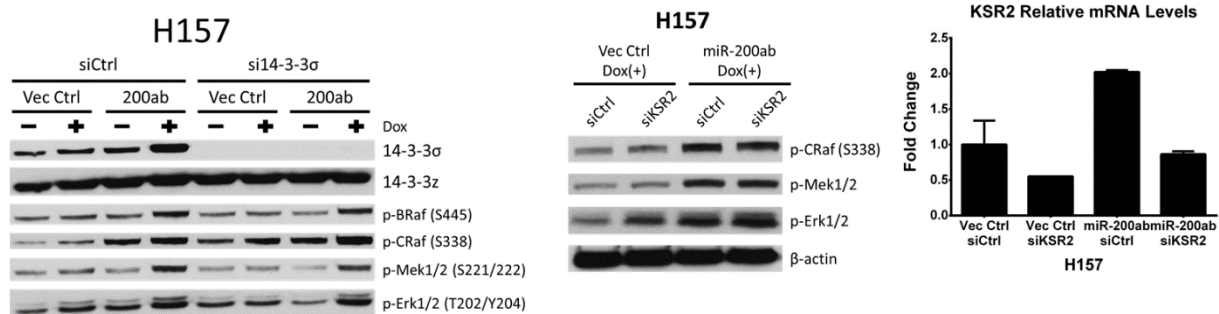


Figure 96. Left: Western blot of indicated proteins after 96hr siRNA knockdown of 14-3-3σ in H157 cells with inducible miR-200 expression. Middle: Western blot of MAPK signaling molecules after 96hr siRNA knockdown of KSR2 in H157 cells with inducible miR-200 expression. Right: qPCR analysis of KSR2 mRNA levels after 96hr siRNA knockdown of KSR2.

We next focused our analysis on the regulatory role of IL17rd on MAPK signaling. Correlation analysis of IL17RD mRNA expression to our previously reported 76-gene EMT signature score (40) in a panel of 77 human lung cancer cell lines showed a statistically significant, strong inverse correlation between IL17RD and EMT (**Figure 97**). Validation of the correlation analysis and IL17RD qPCR by Western blotting in a panel of epithelial and mesenchymal Ras mutant human lung cancer cell lines confirmed higher basal IL17rd expression in epithelial cells (**Figure 98**). Additionally, IL17rd levels were induced in mesenchymal H157 cells upon miR-200 expression and suppressed by Zeb1 expression in epithelial H441 cells (**Figure 98**). Knockdown of IL17RD by shRNA in miR-200 expressing H157 cells significantly reduced MAPK signaling (**Figure 99**), while overexpression of IL17RD in mesenchymal H157 and A549 cells increased MAPK signaling (**Figure 99**). Although IL17RD was initially implicated in inhibiting fibroblast growth factor (FGF)-induced MAPK signaling (115), in FGF-independent contexts, IL17RD has been shown to promote MAPK signaling (116, 117). Consistent with these reports, analysis of Fgfr1 protein levels revealed a reciprocal expression to IL17rd, in which mesenchymal cells have greater expression of Fgfr1 compared to epithelial cells (**Figure 100**), and transient IL17RD overexpression led to a decrease in Fgfr1 protein levels (**Figure 100**).

Lung Cancer Cell Line Panel

Overall $r=-0.302$; $p=0.0075$

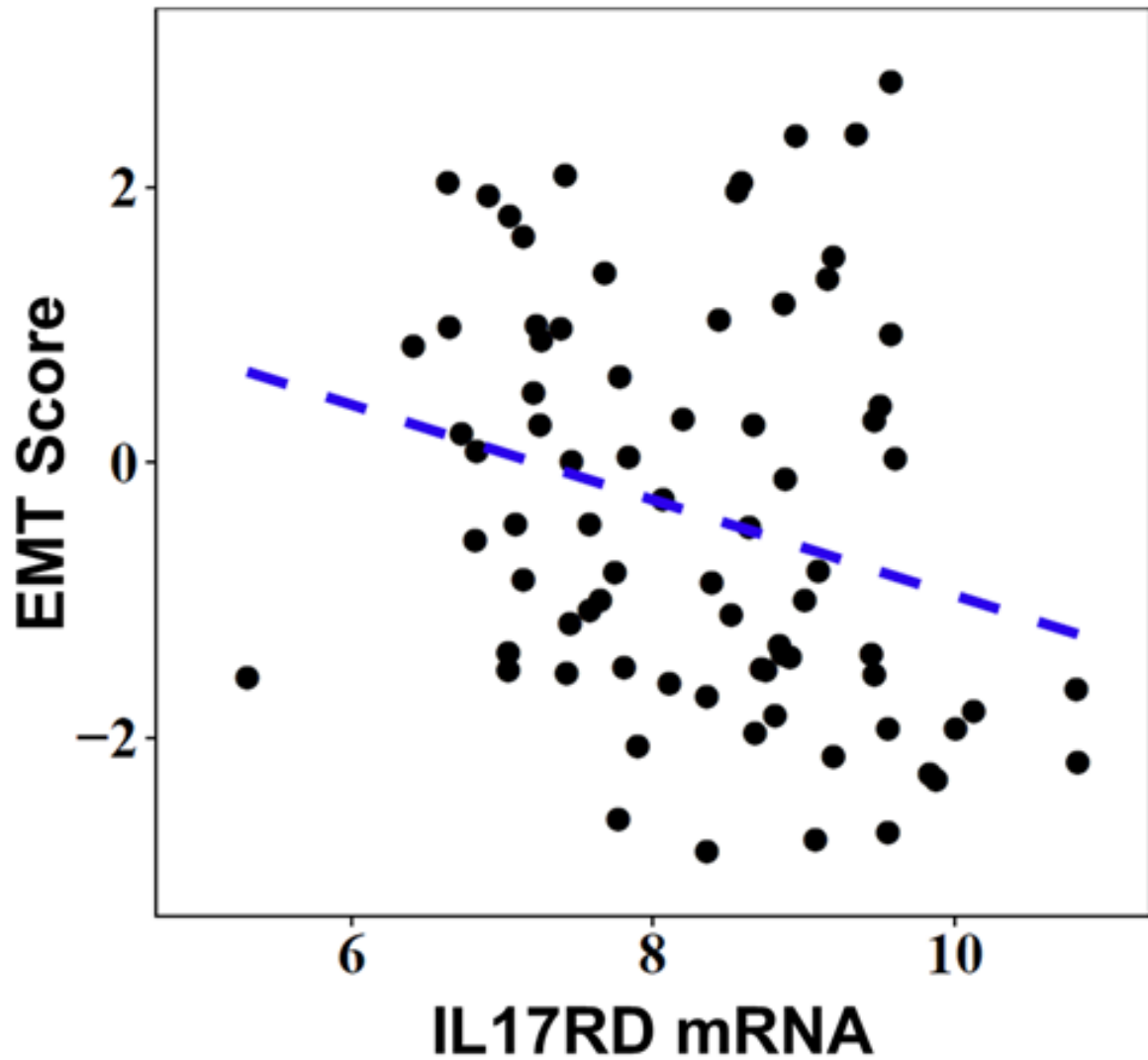


Figure 97. Correlation plot of IL17RD gene expression and EMT scores of 77 human lung cancer cell lines.

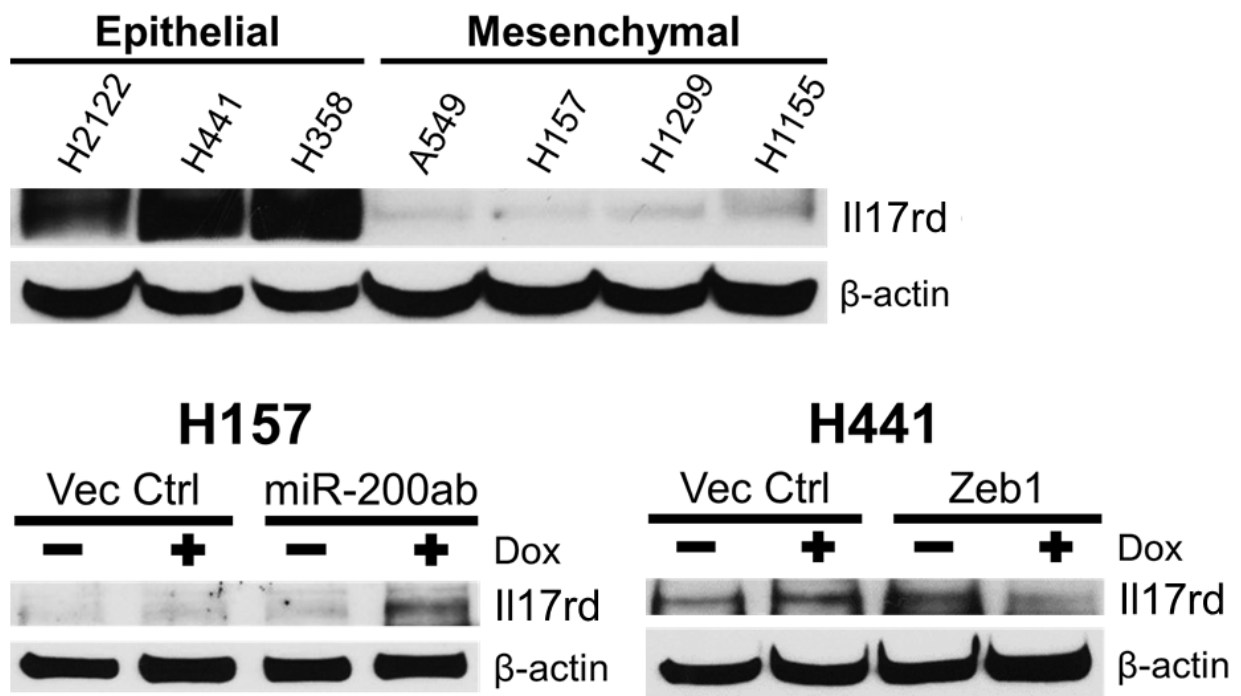


Figure 98. Western blots of IL17rd in (Top) a panel of human epithelial and mesenchymal KRAS mutant lung cancer cell lines and (Bottom) H157 or H441 cells with induced miR-200 or Zeb1 expression, respectively.

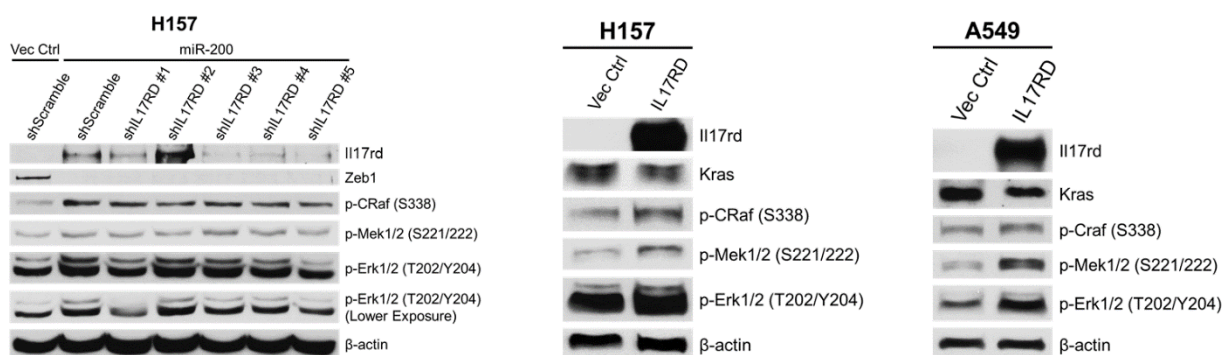


Figure 99. Left: Western blot of IL17rd and MAPK signaling molecules after transient shRNA knockdown of IL17RD in H157 cells with induced miR-200 expression. Middle and Right: Western blot of IL17rd and MAPK signaling molecules after 48hr constitutive expression of IL17RD in (Middle) H157 and (Right) A549 cells.

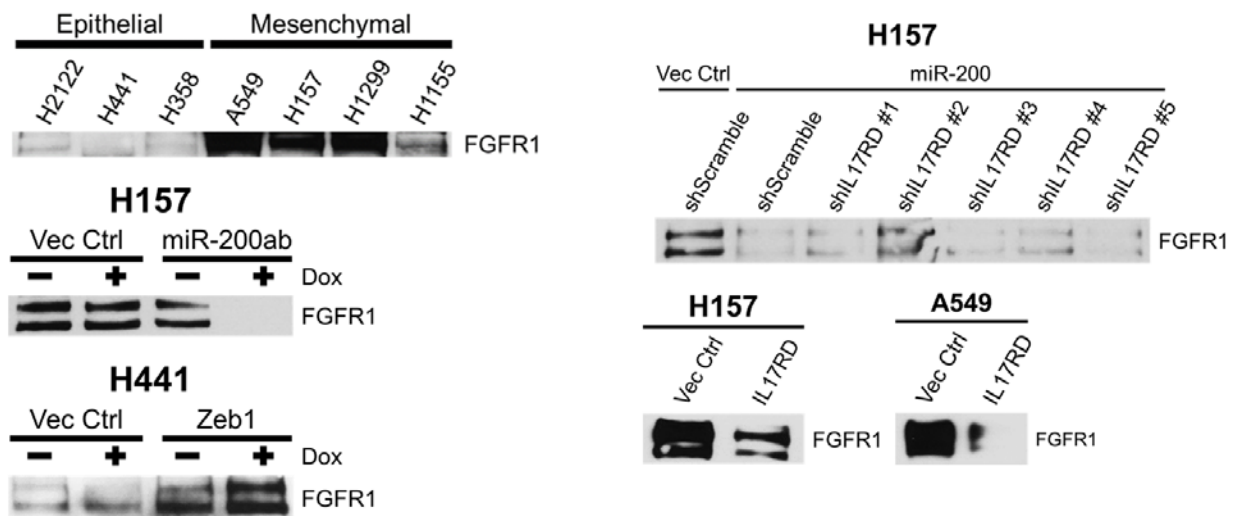


Figure 100. Left: Western blot of Fgfr1 in a panel of epithelial and mesenchymal Ras mutant human lung cancer cell lines (top), in mesenchymal H157 cells after Dox inducible miR-200 expression (middle), and in epithelial H441 cells after Dox inducible Zeb1 expression (bottom). Top Right: Western blot of Fgfr1 in H157 cells with inducible miR-200 or vector control after transient shRNA knockdown of IL17RD. Bottom Right: Western blot of Fgfr1 in H157 and A549 cells after 48hr transient overexpression of IL17RD.

Due to the strong correlation of IL17RD to EMT, we next sought to understand the regulatory mechanism of Zeb1 or miR-200 on IL17RD gene expression. Analysis of the human IL17RD promoter region using the JASPAR transcription factor database (<http://jaspar.genereg.net/>) predicted multiple potential Zeb1 E-box recognition sites (**Figure 101**) responsible for transcriptional repression of gene expression (45, 48, 57, 118). Zeb1 chromatin immunoprecipitation (ChIP) qPCR assays of the endogenous IL17RD promoter in mesenchymal H157 cells with or without miR-200 expression confirmed direct binding of Zeb1 to the IL17RD promoter with the strongest signal occurring 195 and 680 base pairs upstream of IL17RD transcriptional start site (**Figure 101**). Luciferase reporter assays with the wild-type IL17RD promoter region confirmed transcriptional repression by ZEB1, which was abrogated by introduction of mutations into the two main ZEB1 binding sites (as assessed by ChIP) individually and in combination (**Figure 101**).

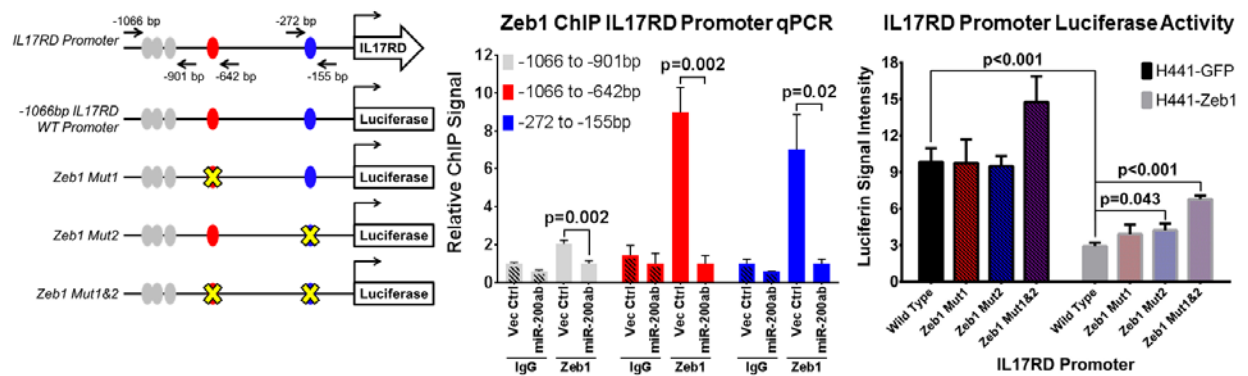


Figure 101. Left: Schematic of human IL17RD promoter region containing predicted Zeb1 binding sites represented by color-coded ellipses. Black arrows indicate location of qPCR primers used to amplify genomic region containing potential Zeb1 binding sites in IL17RD promoter after Zeb1 chromatin immunoprecipitation (ChIP). The IL17RD promoter was cloned 1,066 base pairs upstream of the transcriptional start site and inserted into a luciferase reporter vector. Mutations of potential Zeb1 binding sites indicated with yellow X. Middle: Fold enrichment by qPCR analysis of IL17RD promoter segments containing potential Zeb1 binding sites after endogenous Zeb1 ChIP in H157 cells with inducible vector control or miR-200 expression, using Zeb1 antibody or mock IgG control antibody. Primers used for qPCR amplification labeled in graph legend corresponding to numbers on black arrows (left). Right: Relative luciferase activity of IL17RD promoter reporter constructs (left) transfected into epithelial H441 cells with induced GFP control or Zeb1 expression. Relative luciferin signal was normalized to promoter-less vector control signal.

Mesenchymal lung cancer cells and tumors are resistant to MEK inhibition

The increase in MAPK levels in epithelial cells concomitant with the decrease in various other signaling pathways involved in drug resistance and invasion/metastasis such as p-Fak, p110 α , p-Stat3, p-PKC α , and Axl (40, 58, 89, 100, 119-123) (**Table 2 and Figure 89**), suggested that epithelial lung cancer cells were more dependent on MAPK signaling for growth and survival. Treatment of a panel of human and murine KRAS mutant lung cancer cell lines, stratified as either epithelial or mesenchymal based on previous profiling (33, 48, 56) (**Figure 78**), confirmed that epithelial cells were more sensitive to the MEK inhibitor Selumetinib (AZD6244) (**Figure 102**). Furthermore, resistant cell lines were re-sensitized to MEK inhibition upon miR-200 induction (**Figure 102**) while epithelial cells became more resistant to MEK inhibition with Zeb1 expression (**Figure 102**). Interestingly, constitutive expression of Il17rd in mesenchymal H157 and 344SQ cells reactivated MAPK signaling and sensitized the resistant lines to MEK inhibitor treatment (**Figure 102**).

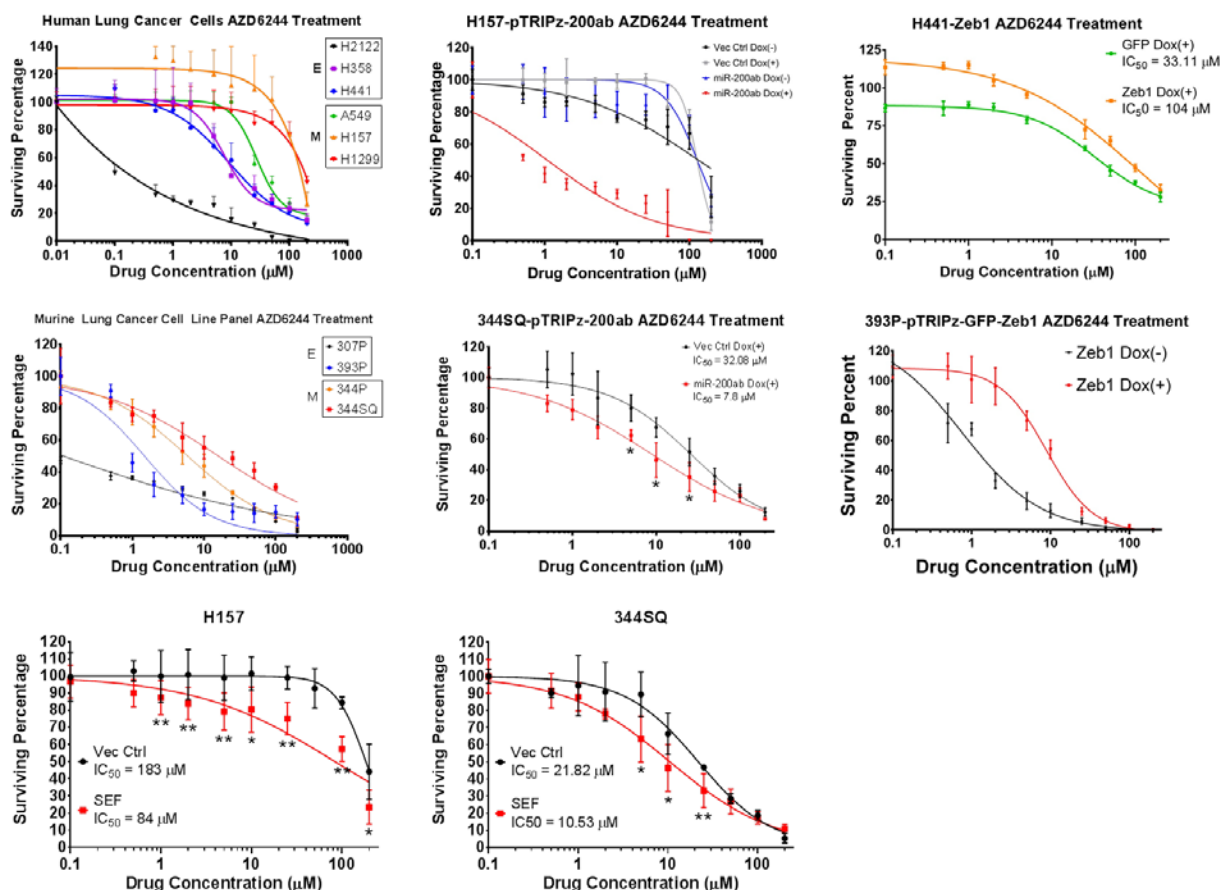


Figure 102. Growth inhibition response after 72hr AZD6244 MEK inhibitor treatment in:

Top left: A panel of epithelial and mesenchymal human lung cancer cell lines with Ras mutations. Top Middle: Mesenchymal H157 cells with inducible miR-200 expression. Top Right: Epithelial H441 cells with inducible Zeb1 expression. Center Left: A panel of epithelial and mesenchymal murine KP lung cancer cell lines. Center Middle: Mesenchymal murine 344SQ cells with inducible miR-200 expression. Center Right: Epithelial murine 393P cells with inducible Zeb1 expression. Bottom Left: Mesenchymal H157 cells with stable H17rd expression. Bottom Middle: Mesenchymal murine 344SQ cells with stable H17rd expression.

To validate our *in vitro* findings in an *in vivo* context, we first analyzed primary syngeneic tumors generated by subcutaneous implantation of epithelial 393P and mesenchymal 344SQ murine lung cancer cells in syngeneic WT mice (33). Immunohistochemical (IHC) staining of the tumor tissues for Il17rd, p-Erk, and EMT markers (high nuclear Zeb1, low/mislocalized E-cadherin, and high vimentin) showed a strong, positive correlation between Il17rd and p-Erk with an inverse correlation of the two markers to EMT (**Figure 103**). Consistent with these findings, *in vivo* administration of AZD6244 significantly reduced tumor growth only in epithelial 393P tumors, while mesenchymal 344SQ tumors were highly resistant to treatment. However, despite the pronounced efficacy, 80% of 393P tumors eventually developed resistance to MEK inhibition, reaching comparable sizes to control tumors by 12 weeks, and formed metastatic lung lesions, which are not usually observed in this model (**Figure 104**). IHC analysis of the vehicle control (393P Solvent) and AZD6244-sensitive (393P AZD6244) after 7 weeks, and the AZD6244-resistant (393P AZD-R) primary 393P tumors after 12 weeks confirmed the efficacy of AZD6244 in suppressing p-Erk levels and revealed that the resistant tumors had undergone EMT as assessed by high Zeb1, low E-cadherin, and high vimentin levels compared to control tissues (**Figure 105**). Interestingly, vimentin levels began to increase even in AZD6244-sensitive 393P tumors following MEK inhibition. To determine if *in vivo* sensitivity to MEK inhibition was a result of high miR-200 levels, we induced miR-200 expression in resistant 344SQ cells and treated syngeneic tumors with AZD6244. Although miR-200 expression alone significantly decreased tumor growth, combination with AZD6244 had an additive effect that reduced average tumor size by over 90% (**Figure 106**), similar to the response of epithelial 393P tumors with high basal levels of miR-200 expression.

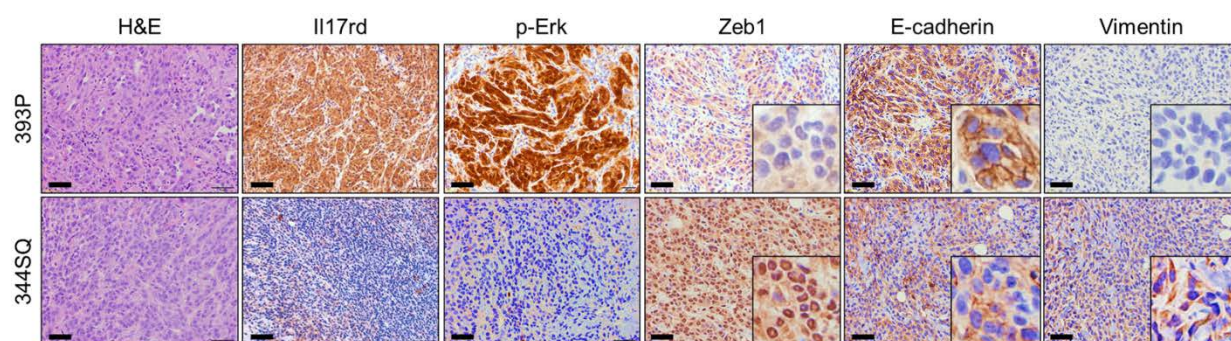


Figure 103. H&E, Il17rd, p-Erk, Zeb1, E-cadherin, and Vimentin IHC stains of primary syngeneic tumor tissues generated by subcutaneous injection of epithelial 393P and mesenchymal 344SQ murine lung cancer cell lines in syngeneic wild-type mice (n=8 tumors per group). Bright-field microscopy at 20x magnification. Scale bars, 100 μ m.

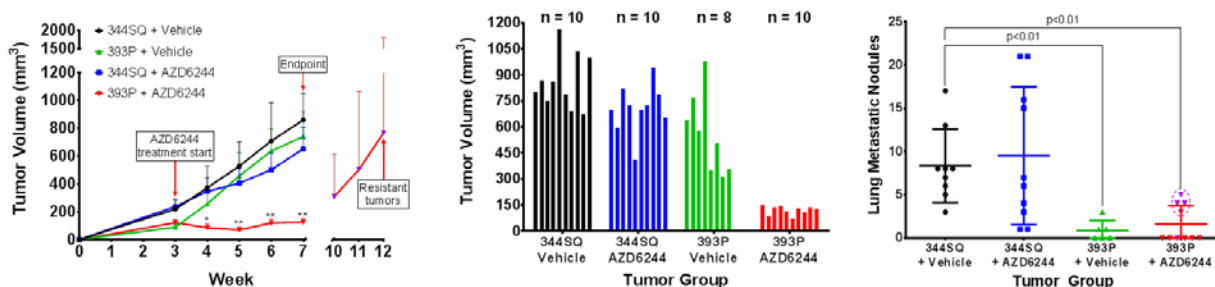


Figure 104. Left: Tumor volume measurements at indicated time points of 393P and 344SQ subcutaneous tumors in syngeneic wild-type mice after daily treatment with 25 mg/kg AZD6244 MEK inhibitor or solvent vehicle control. Treatment start time and endpoint for control mice group are denoted with red arrows. Purple data points represent 393P tumors initially responsive to MEK inhibition that developed resistance over time. Middle: Tumor volume measurements at Week 7 (4 weeks of AZD6244 treatment, endpoint). Right: Quantification of lung metastatic surface nodules of indicated experimental groups at Week 7 of experiment. Circled purple data points represent lung metastatic surface nodules at Week 12 in 393P tumors that developed resistance to AZD6244 (393P AZD-R).

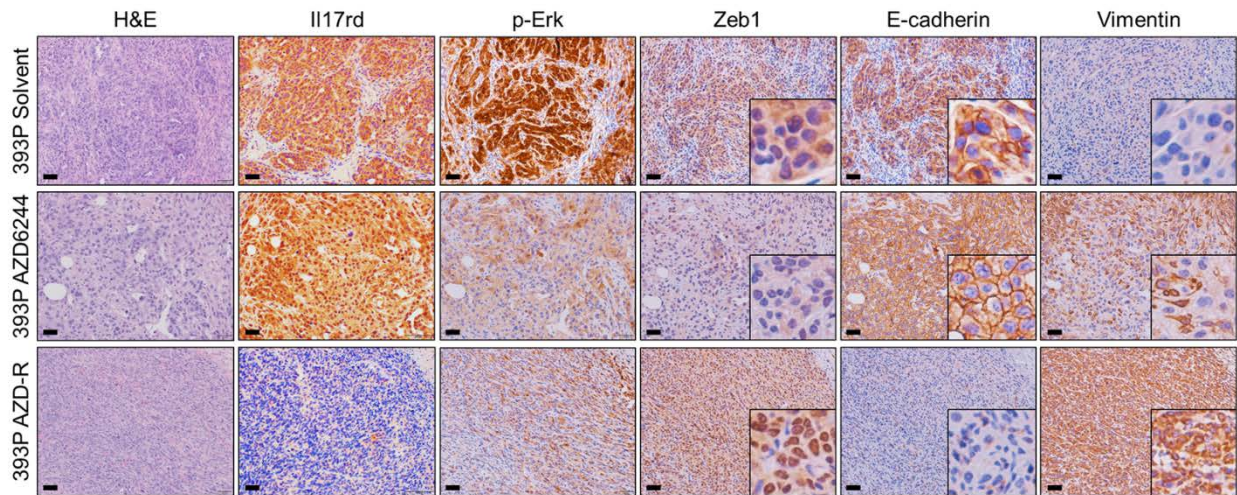


Figure 105. Stains for indicated markers of 393P tumors in mice that received solvent or AZD6244 until Week 7 of experiment in (Figure 103) (top and middle panels). Staining of 393P tumors that developed resistance to AZD6244 (393P AZD-R) at Week 12 of experiment in (Figure 103) (bottom panel). Bright- field microscopy at 20x magnification. Scale bars, 50 μ m. (n=5 tissues per group).

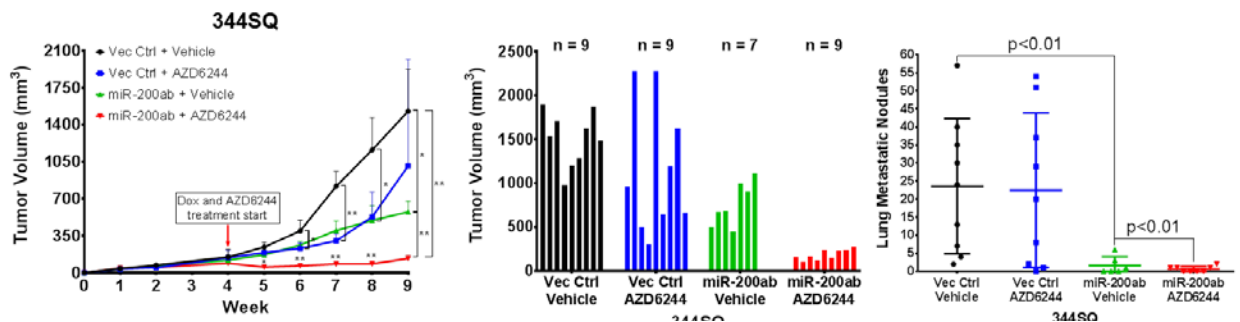


Figure 106. Left: Tumor volume measurements at indicated time points of 344SQ cells +/- inducible miR-200 expression injected subcutaneously into syngeneic wild-type mice and treated with 25 mg/kg AZD6244 or vehicle control. Starting time of treatment denoted by red arrow. Middle: Final tumor volume measurements at Week 9 (5 weeks of treatment) of experiment. Right: Quantification of lung metastatic surface nodules of indicated experimental groups at Week 9 of experiment.

Mesenchymal de-differentiation of lung tumors in *Kras* mutant mouse models is sufficient to suppress MAPK signaling and confer resistance to MEK inhibition

Murine co-clinical trials with the MEK inhibitor AZD6244 in combination with docetaxel have shown that the co-mutational status of tumors, such as loss of p53, contributed to therapy resistance (27). Previous studies by our group have reported that heterogeneous *Kras;p53* mutant lung tumors display regions of poorly differentiated tumors, as assessed by changes in expression of EMT markers, compared to mutant *Kras*^{G12D} tumors (56). These findings suggest that poorly differentiated *Kras;p53* mutant lung tumors have undergone EMT, producing drug resistance. Thus, we next analyzed lung tissues with autochthonous tumors from conditional *Kras*^{LSL-G12D} (*Kras*^{G12D}) and *Kras*^{LSL-G12D};*p53*^{fl/+} (KP^{-/+}) mice, generated through intratracheal administration of adenovirus expressing Cre recombinase (124). Histological analyses demonstrated that KP^{-/+} mice (4 – 6 months post-induction) displayed more numerous and larger tumors than *Kras*^{G12D} mice, with greater inter- and intratumoral heterogeneity, presenting a mixture of well- and poorly-differentiated tumors based on analysis of EMT markers (**Figure 107 and Figure 110**). Similar to our observations in syngeneic primary tumors (**Figure 103**), poorly-differentiated tumors exhibiting mesenchymal marker patterns had low levels of Il17rd and p-Erk, while well-differentiated, epithelial tumors had high levels of Il17rd and p-Erk (**Figure 107**).

To assess whether our findings in the KP mice were due to EMT driven by diminished miR-200 expression and not a secondary effect of p53 loss, we utilized mice with loxP sites flanking the miR-141/200c stem-loop in the *miR-141/200c* locus (95, 96) and crossed them with the *Kras*^{LSL-G12D} mice. Intratracheal delivery of adenoviral Cre recombinase produced mice with an activated *Kras*^{G12D} and loss of *miR*-

141/200c (KM). Mice expressing the targeted alleles were validated by PCR amplification of the stem-loop loxP site (**Figure 108**). Additionally, the targeting vector inserts a promoter-less lacZ gene driven by the endogenous *miR-141/200c* promoter activity after Cre-mediated removal, further validating successful locus targeting in both KM tumor tissues and in the airway epithelium of *miR-141/200c*^{-/+} (M) mice (**Figure 108**). Verification of *miR-141/200c* knockout by qPCR analysis of KM lung tumor tissues showed significant reduction in miR-141/200c levels compared to *Kras*^{G12D} tumors with no compensatory effect by other miR-200 family members (**Figure 109**). Monthly analysis of murine lung tissues at 1 to 6 months post-induction revealed greater lung tumor numbers as well as overall tumor area in KM mice compared to *Kras*^{G12D} mice as measured by micro-CT scans and H&E-stained tissues. However, overall tumor area in KM mice were smaller than KP^{-/+} tumors (**Figure 110 and 111**). No tumor growth was observed in mice harboring only the *miR-141/200c*^{-/+} mutation without an activated KRAS allele within the 6 month time course (**Figure 110**). Analysis by IHC of KM tumor tissues for EMT markers showed higher numbers of poorly-differentiated tumor regions that correlated with low levels of Il17rd and p-Erk relative to *Kras*^{G12D} tumors (**Figure 107 and Figure 110**). Interestingly, we also observed tumor heterogeneity in KM mice similar to that of the KP^{-/+} mice, with certain regions possessing well differentiated, epithelial tumors with high Il17rd and p-Erk levels.

We next sought to assess the sensitivity of the different KRAS mutant murine lung cancer models to MEK inhibition. Three months post-induction of lung tumors in K, KP and KM animals by adeno-Cre, tumor formation was confirmed by micro-CT scans and daily doses of single-agent AZD6244 were administered to mice. Micro-CT image analysis of changes in overall lung tumor area demonstrated that the predominantly

epithelial lung tumors from mice with the single *Kras*^{G12D} mutation were sensitive to MEK inhibition, while KP^{-/+} and KM lung tumors were more resistant after 4 weeks of treatment (**Figure 112**). Taken overall, these data demonstrate that EMT is sufficient to regulate IL17rd levels and MAPK signaling in autochthonous KRAS mutant lung cancers, thereby mediating resistance to MEK inhibitors.

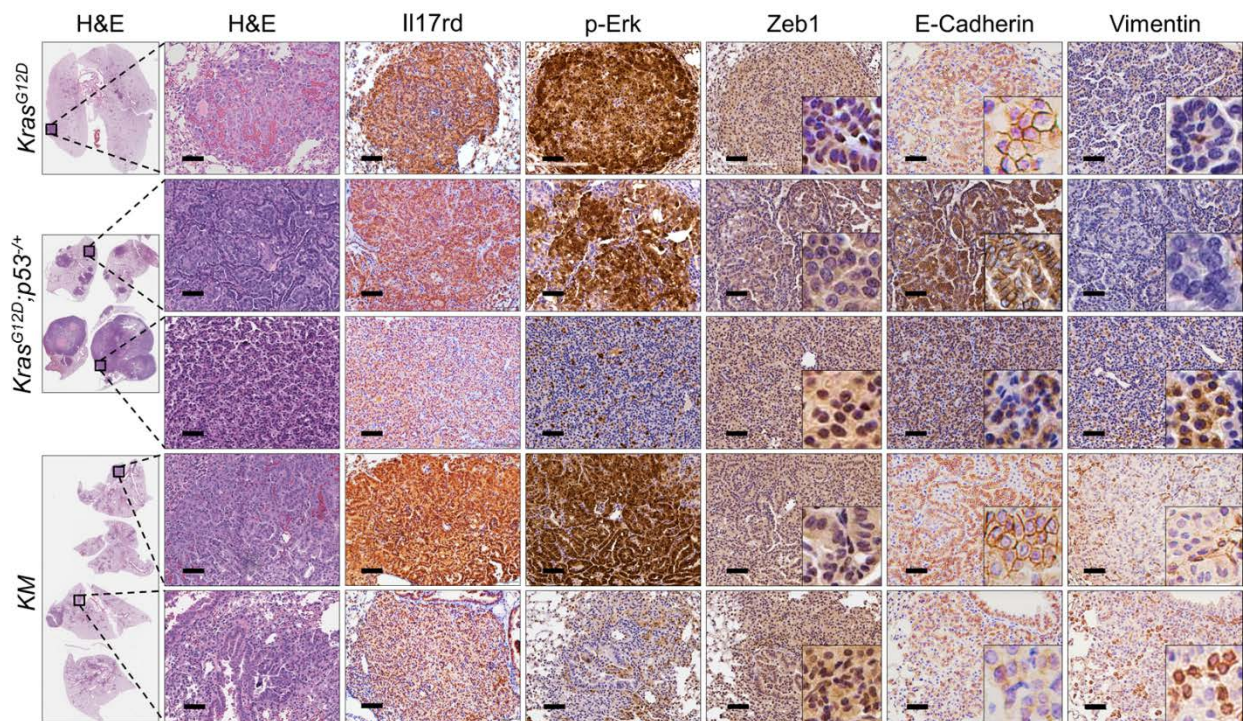


Figure 107. H&E, IL17rd, p-Erk, Zeb1, E-cadherin, and Vimentin IHC stains of different lung tumor tissue regions as denoted by zoomed-in sections of *Kras*^{G12D}, KP^{-/+}, and KM mice (n=6 tissues per group). Bright-field microscopy at 20x magnification. Scale bars, 100 μ m.

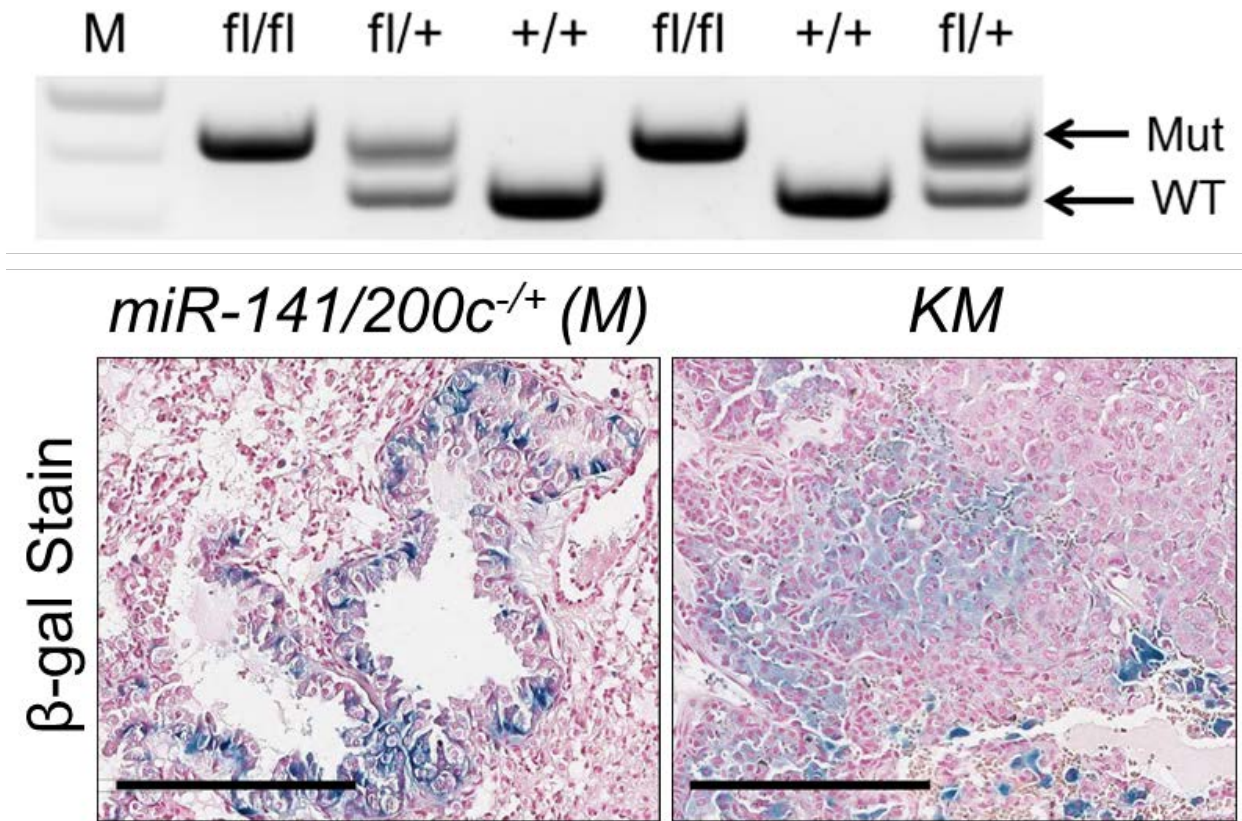


Figure 108. Top: Agarose gel image of PCR product genotyping the murine *miR-141/200c* locus flanked by loxP sites (fl). Higher band indicates floxed locus that will be deleted upon adeno-Cre induction (mut) while lower band is wild-type (WT) locus. Bottom: Lung airway epithelium of *miR-200c*^{-/+} mice and lung tumor tissues of KM mice stained with β-gal. Scale bars, 200μm.

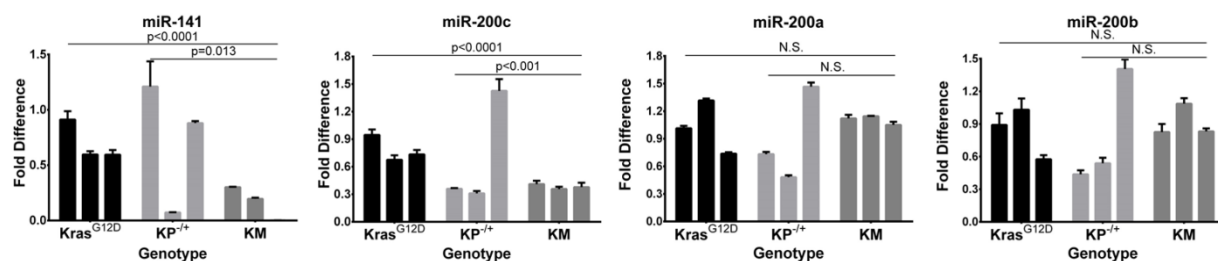


Figure 109. QPCR analysis of miR-200 family expression in lung tumors from *Kras*^{G12D}, *KP*^{-/-}, and KM mice.

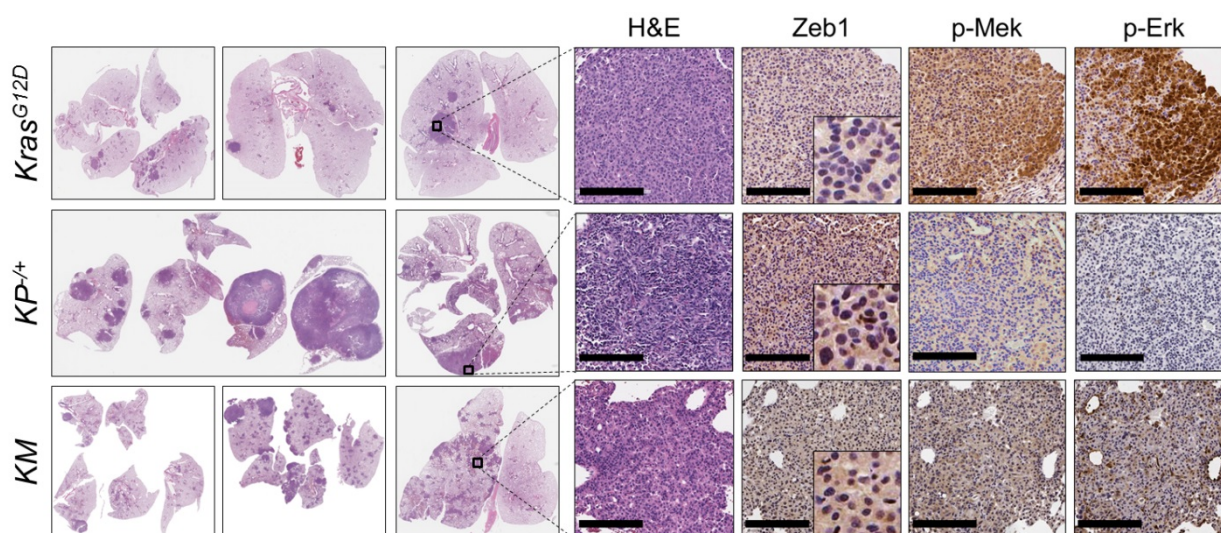


Figure 110. Left: H&E stains of lung tissue sections from various *Kras*^{G12D}, *KP*^{-/-}, and KM mice. Right: Additional H&E, Zeb1, p-Mek, and p-Erk IHC stains of different lung tumor tissue regions as denoted by black zoom box in *Kras*^{G12D}, *KP*^{-/-}, and KM mice (n=6 tissues per group). Bright field microscopy at 20x magnification. Scale bars, 200µm.

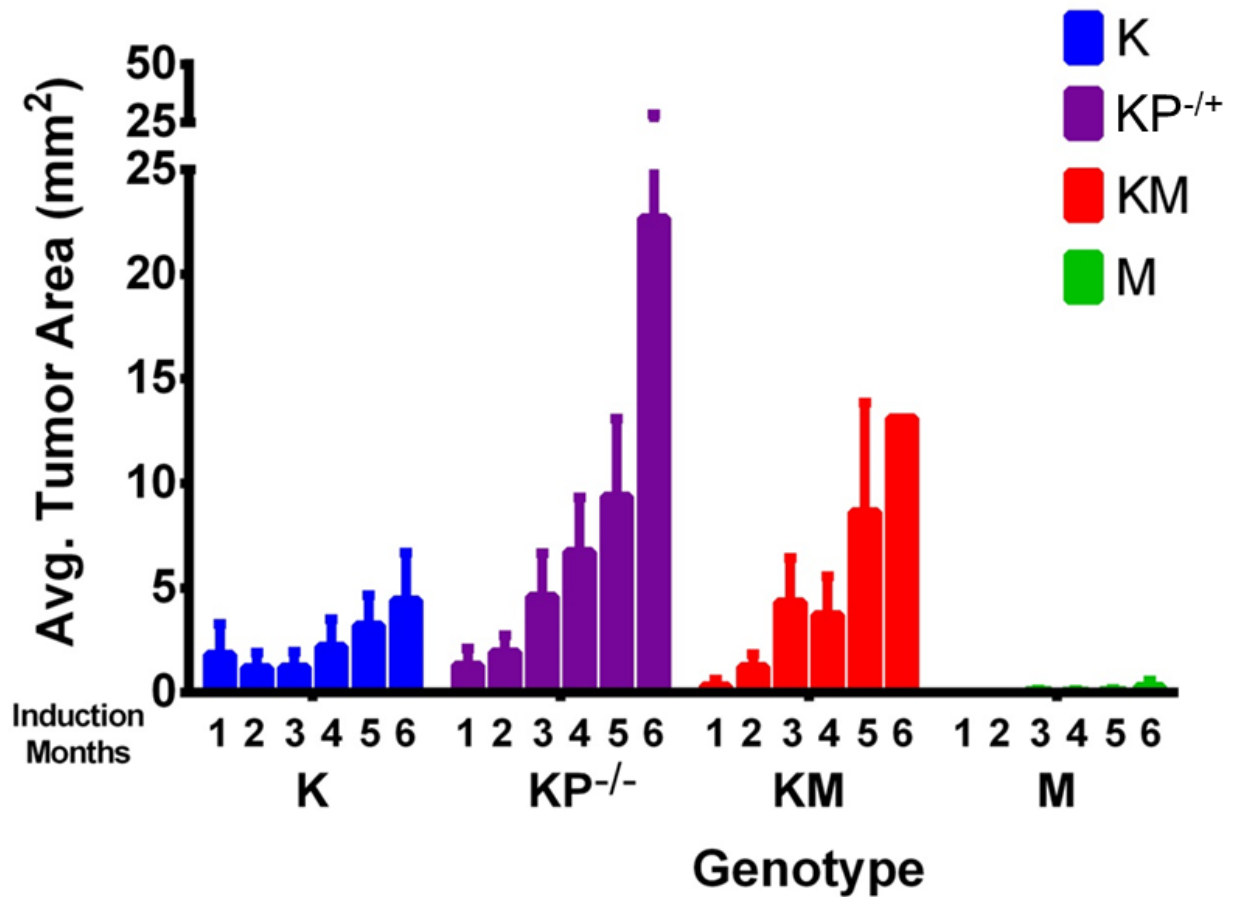


Figure 111. Average lung tumor areas of *Kras*^{G12D}, KP^{-/-}, and KM mice as assessed by micro-CT imaging of mice lungs over a course of 6 months post-induction with adeno-Cre. Mice with *miR-200c/141*^{-/-} (M) only showed no tumor formation.

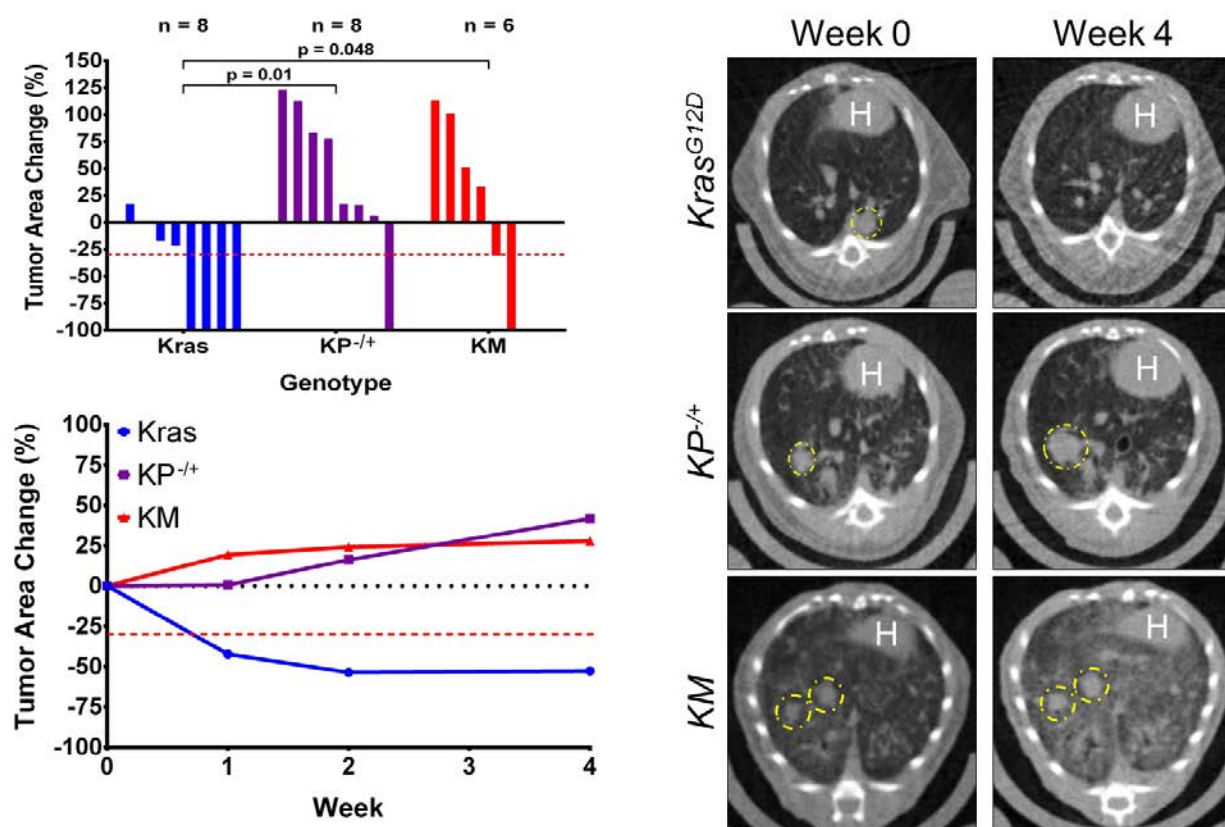


Figure 112. Top Left: Percent change in overall lung tumor area of age-matched *Kras^{G12D}*, *KP^{-/-}*, and *KM* mice after 4 weeks of daily treatment with 25 mg/kg AZD6244, as assessed by micro-CT imaging of mice lungs. Bottom Left: Trendline of percent change in overall tumor area at indicated time points of *Kras^{G12D}*, *KP^{-/-}*, and *KM* mice over 4 weeks of daily treatment with AZD6244. Right: Representative cross-sectional micro-CT images of *Kras^{G12D}*, *KP^{-/-}*, and *KM* mice lungs prior to AZD6244 administration (Week 0) and at the treatment endpoint (Week 4). Yellow circles outline representative target lesions.

Mocetinostat reverts EMT, derepresses IL17rd expression, and sensitizes resistant cancer cells to MEK inhibition

Identifying combinatorial treatment strategies with MEK inhibitors to reduce tumor growth and progression is vital for improving patient survival. Previous studies have shown that the class I histone deacetylase (HDAC) inhibitor mocetinostat reverts the EMT phenotype through restoration of epithelial microRNAs, including the miR-200 family (50). Treatment of mesenchymal H157 cells with mocetinostat induced miR-200 expression and reversed EMT at the molecular level resulting in increased IL17rd expression, increased MAPK signaling, and decreased FGFR1 levels (**Figure 113 and 114**). To verify that the observed changes were independent of secondary effects due to histone acetylation, H157 cells were treated with the pan-HDAC inhibitor Trichostatin A (TSA) and showed no significant changes in either EMT markers or MAPK signaling molecules (**Figure 115**). Mocetinostat treatment of 344SQ syngeneic tumors produced an increase in IL17rd and p-Erk levels by IHC analysis, concomitant with an increase in cell-cell adherence junctions as characterized by increased E-cadherin localization to the cell membrane (**Figure 116**). Although we did not observe a significant change in Zeb1 or vimentin levels by IHC after mocetinostat treatment (**Figure 117**), qPCR analysis of the mocetinostat-treated 344SQ tumors showed a significant upregulation of both miR-200c and IL17RD, along with a significant decrease in N-cadherin, demonstrating functional suppression of Zeb1 (**Figure 117 and 118**). As previously reported, these findings suggest that in addition to direct promoter binding, Zeb1 can functionally repress expression of epithelial-associated genes through recruitment of histone deacetylases (50, 51, 125-127).

Since epithelial cancer cells are sensitive to MEK inhibition, reversion of EMT in mesenchymal human and murine lung cancer cells *in vitro* with mocetinostat increased sensitivity to AZD6244 treatment (**Figure 119**). *In vivo* combinatorial administration of mocetinostat and selumetinib in mice bearing syngeneic 344SQ mesenchymal tumors had an additive effect on reducing average tumor size compared to single agent AZD6244 treatment (**Figure 120**). Mocetinostat alone significantly reduced tumor growth rate, with no observed decrease in the number and size of lung metastatic nodules. However, lung metastatic nodules were drastically reduced in both number and size with dual HDAC and MEK inhibition (**Figure 120**). To simulate the genetic alterations and tumor heterogeneity observed in lung adenocarcinoma patients, we treated the spontaneous $Kras^{LA1-G12D};p53^{R172H\Delta G/+}$ (KP) mice between 7 to 8 months of age with AZD6244 alone or in combination with mocetinostat. Comparable with the adeno-Cre conditional lung tumor mouse models, $Kras^{LA1-G12D}$ (Kras) tumors were sensitive to MEK inhibition while KP tumors were resistant (**Figure 121**). However, micro-CT image analysis demonstrated that combinatorial treatments of KP mice with mocetinostat and AZD6244 significantly reduced overall tumor area (**Figure 121**).

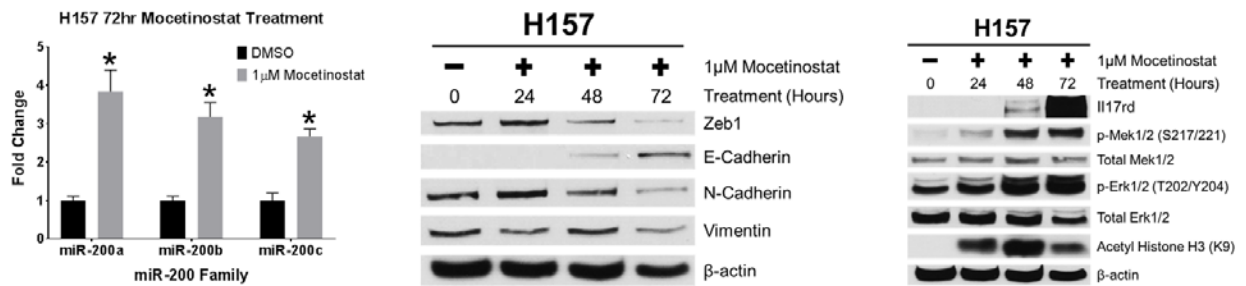


Figure 113. Left: QPCR analysis for relative expression of miR-200a, miR-200b, and miR-200c in H157 cells after 72 hr treatment with mocetinostat. Asterisks (*) indicate significance value of $p < 0.01$. Middle: Western blots of EMT markers in H157 cells after time course treatment with mocetinostat. Right: Western blots of Il17rd and MAPK signaling proteins in H157 cells after time course treatment with mocetinostat. Acetylated histone (H3K9) is included to confirm HDAC inhibition by mocetinostat.

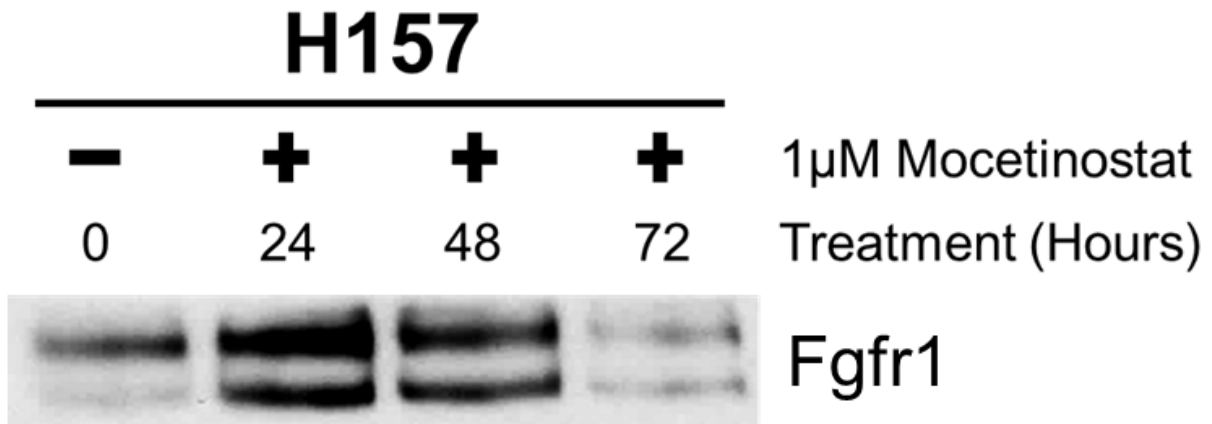


Figure 114. Western blots of Fgfr1 in H157 cells after time course treatment with mocetinostat.

H157

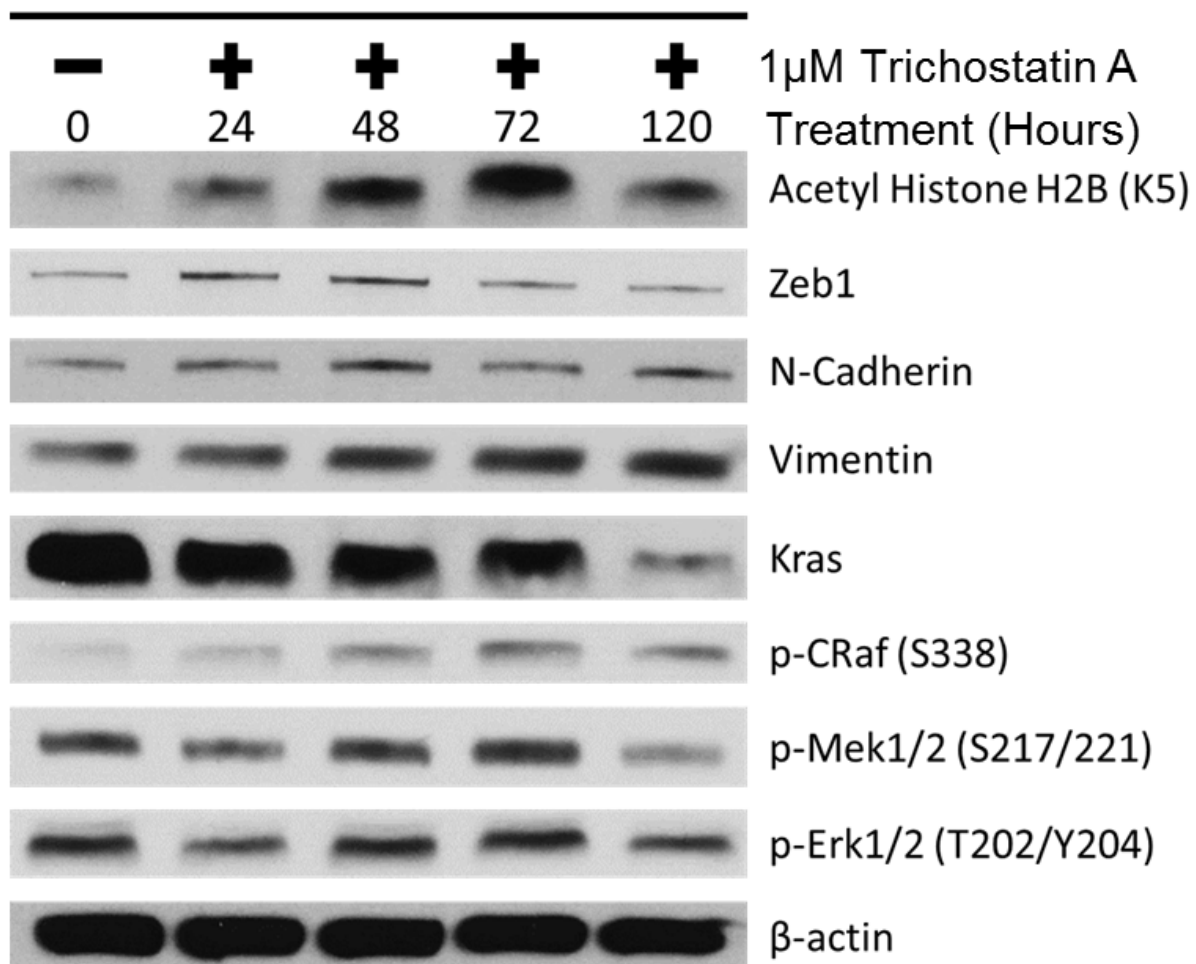


Figure 115. Western blot of indicated proteins in H157 cells treated with trichostatin A (TSA) for indicated time course. Acetyl histone H2B lysine residue 5 used as verification for HDAC inhibition.

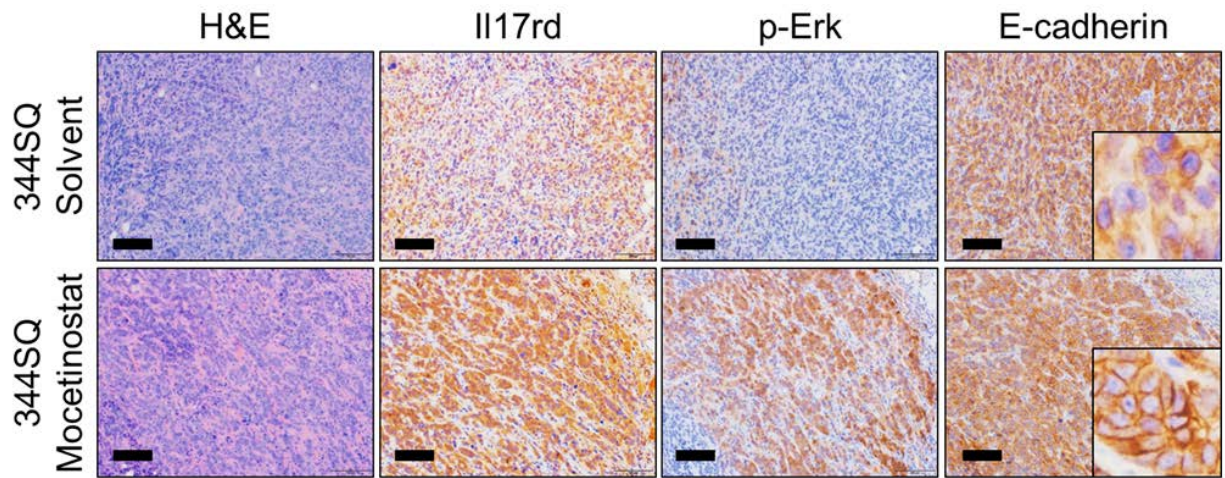


Figure 116. H&E, Il17rd, p-Erk, and E-cadherin IHC stains of primary 344SQ tumor tissues in syngeneic wild-type mice after 3 week treatment with 80 mg/kg mocetinostat or solvent control daily (n=5 tumors per group). Bright-field microscopy at 20x magnification. Scale bars, 100 μ m.

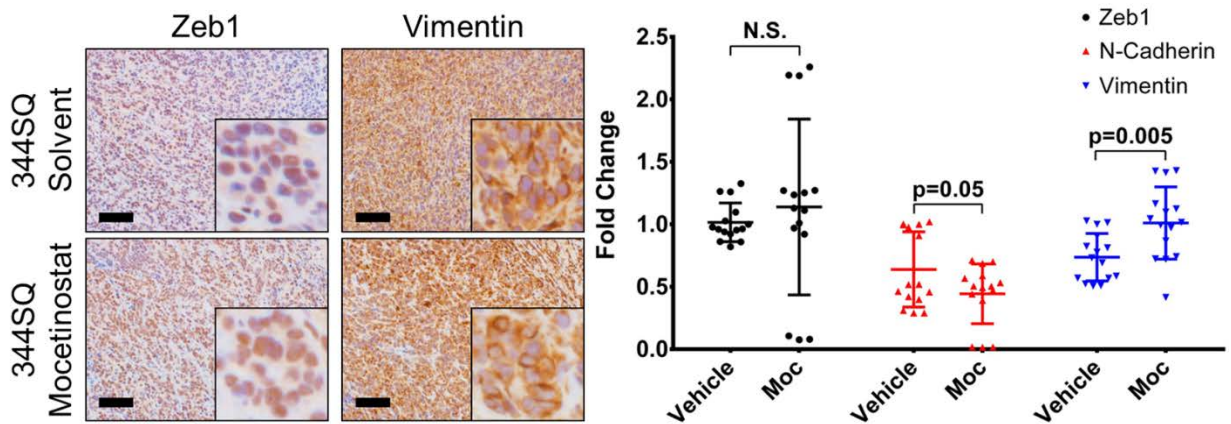


Figure 117. Left: Zeb1 and vimentin IHC stains of primary 344SQ tumor tissues in syngeneic wild-type mice after 3 week treatment with 80 mg/kg mocetinostat or solvent control daily (n=5 tumors per group). Bright-field microscopy at 20x magnification. Scale bars, 100 μ m. Right: QPCR analysis of Zeb1, N-cadherin, and Vimentin expression in 344SQ tumor tissues treated with mocetinostat or solvent control from samples above. Technical triplicates of 5 tumor tissue samples from each treatment group were analyzed for each qPCR.

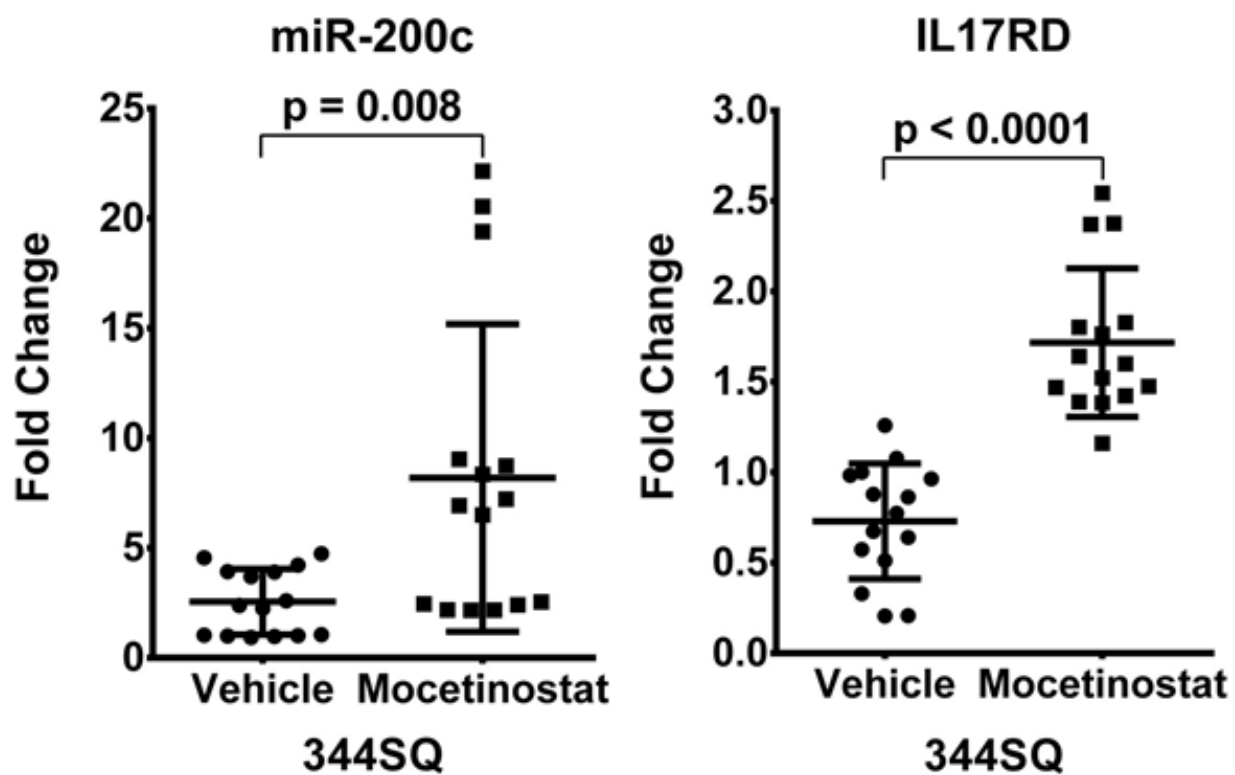


Figure 118. QPCR analysis of miR-200c and IL17RD expression in 344SQ tumor tissues treated with mocetinostat or solvent control from Figure 115. Technical triplicates of 5 tumor tissue samples from each treatment group were analyzed for each qPCR.

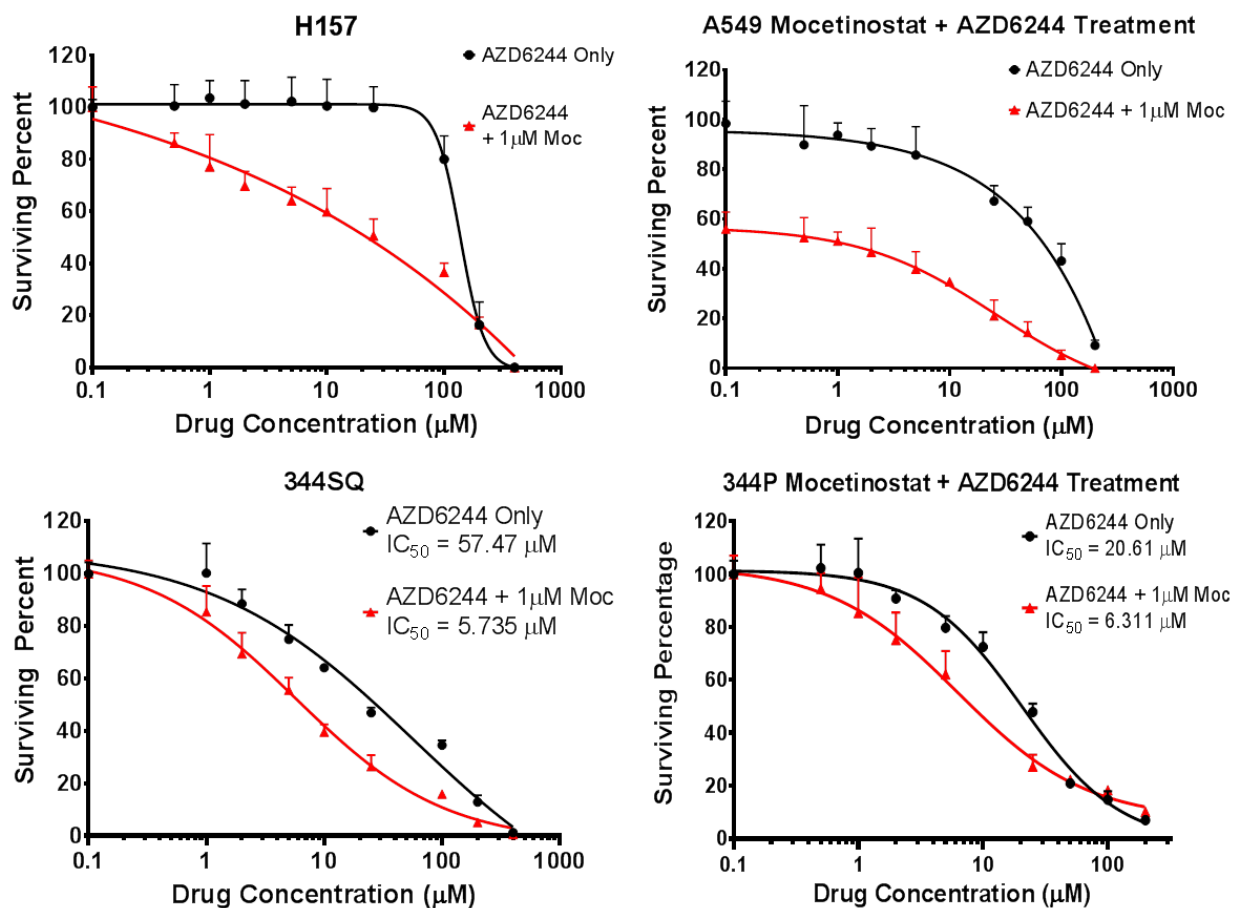


Figure 119. Growth inhibition response of mesenchymal H157, A549, 344SQ, and 344P human and murine lung cancer cell lines after 72hr treatment with single agent AZD6244 or in combination with mocetinostat.

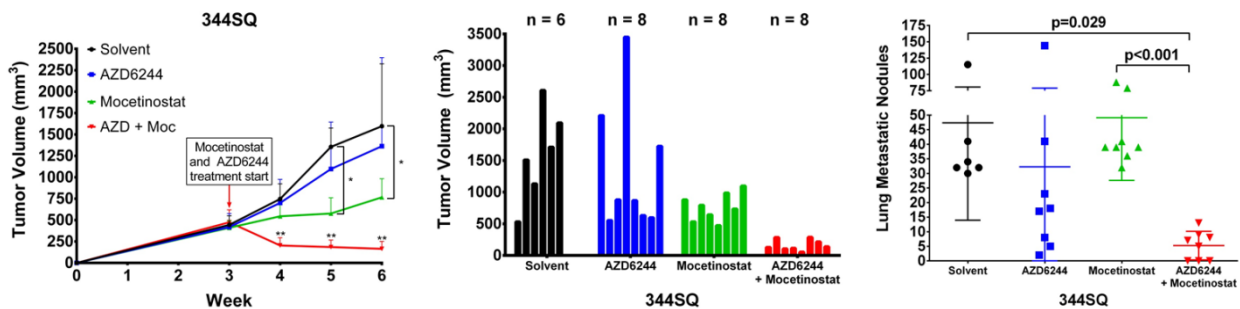


Figure 120. Left: Tumor volume measurements at indicated time points of 344SQ subcutaneous syngeneic tumors treated daily with single agent 25 mg/kg AZD6244, single agent 80 mg/kg mocetinostat, or both drugs in combination. Starting time of treatment denoted by red arrow. Middle: Final tumor volume measurements at Week 6 (3 weeks of treatment) of experiment. Right: Quantification of lung metastatic surface nodules of indicated treatment groups at Week 6 of experiment.

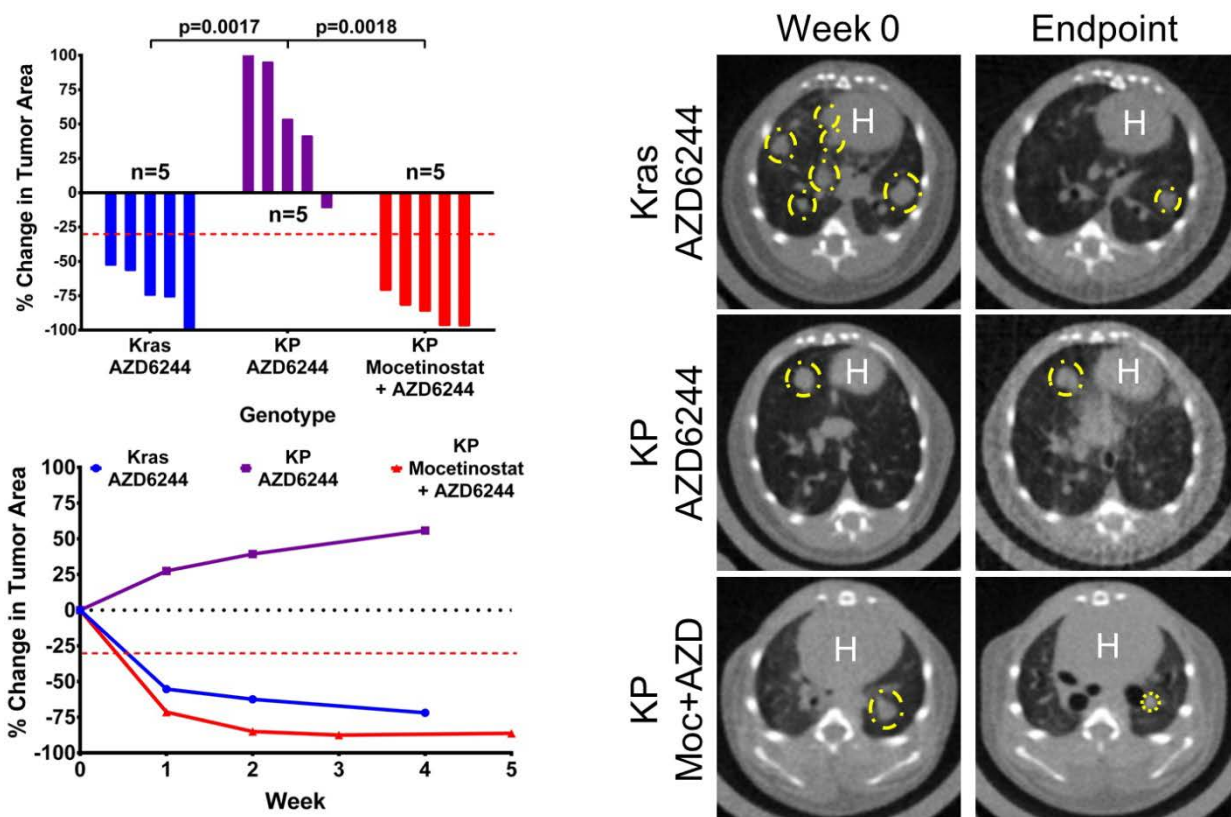


Figure 121. Top Left: Percent change in overall tumor area of *Kras*^{LA1-G12D} (Kras) and *Kras*^{LA1-G12D};p53^{R172HΔG/+} (KP) mice after 4 weeks of daily treatment with single agent 25 mg/kg AZD6244 or 5 weeks of daily combinatorial treatment with AZD6244 and 80 mg/kg mocetinostat in KP mice. Bottom Left: Trendline of percent change in overall tumor area at indicated time points of Kras and KP mice with single agent AZD6244 treatment or combinatorial treatment with AZD6244 and mocetinostat. Right: Representative micro-CT images of *Kras*^{G12D} and KP mice prior to treatment (Week 0) and at treatment endpoint.

Patients with poorly differentiated lung adenocarcinomas display lower levels of phosphorylated Erk, inversely correlating with Zeb1 expression

Finally, we wanted to determine the correlation between p-Erk, Il17rd, and EMT in human lung cancer patient samples to evaluate the clinical relevance of our findings. Pathological assessment of cytoplasmic and nuclear p-Erk H-scores by IHC staining in a cohort of patient lung tumor tissues (n = 451) showed significantly higher expression of p-Erk in patients with lung adenocarcinomas (ADC) versus patients with squamous cell carcinoma (SCC) (**Figure 122 and 123**). Pathological analyses also revealed that poorly differentiated ADC tumors have significantly lower levels of nuclear p-Erk when compared to moderately differentiated ADC tumors (**Figure 124**). We were unable to compare p-Erk expression to differentiation grade in SCC patients due to the lack of well differentiated tumors as well as a low sample number of moderate grade tissues (data not shown). Although cytoplasmic p-Erk levels showed a decreasing trend in poorly differentiated tumors, these changes were not statistically significant (**Figure 124**).

Since previous studies have demonstrated that Zeb1 is a major driver of EMT in lung adenocarcinomas, we next wanted to determine the correlation between Zeb1 and p-Erk expression in patient lung tumors. Utilizing data from Zeb1 IHC stains performed in a previous study (56) on the same patient tissue cohorts here, we compared H-score values of Zeb1 and p-Erk in each patient tumor sample and observed a moderate but significant negative correlation between Zeb1 and nuclear/cytoplasmic p-Erk in ADC histologic subtypes but not SCC samples (**Figure 125 and 126**). Due to the lack of optimized Il17rd antibodies that produced IHC stains of clinically acceptable quality for scoring, we analyzed gene expression profiles in patient lung tumor samples from the

PROSPECT dataset and observed a significant inverse correlation between IL17RD and ZEB1 mRNA levels (**Figure 127**). IL17RD expression is not prognostic of overall patient survival (**Figure 127**), suggesting that high IL17rd levels do not confer tumor growth reduction but are only predictive of sensitivity or response to MEK inhibitors, which none of the patients received. Collectively, our data demonstrate a model by which a Zeb1-driven EMT in mesenchymal lung cancers directly suppresses Mek/Erk signaling through transcriptional repression of IL17RD, resulting in upregulation of alternative signaling pathways that promote MEK inhibitor resistance and invasion/metastasis. Induction of miR-200 suppresses Zeb1 function and increases MAPK signaling/dependency, thereby sensitizing *KRAS* mutant lung cancers to MEK inhibition (**Figure 128**).

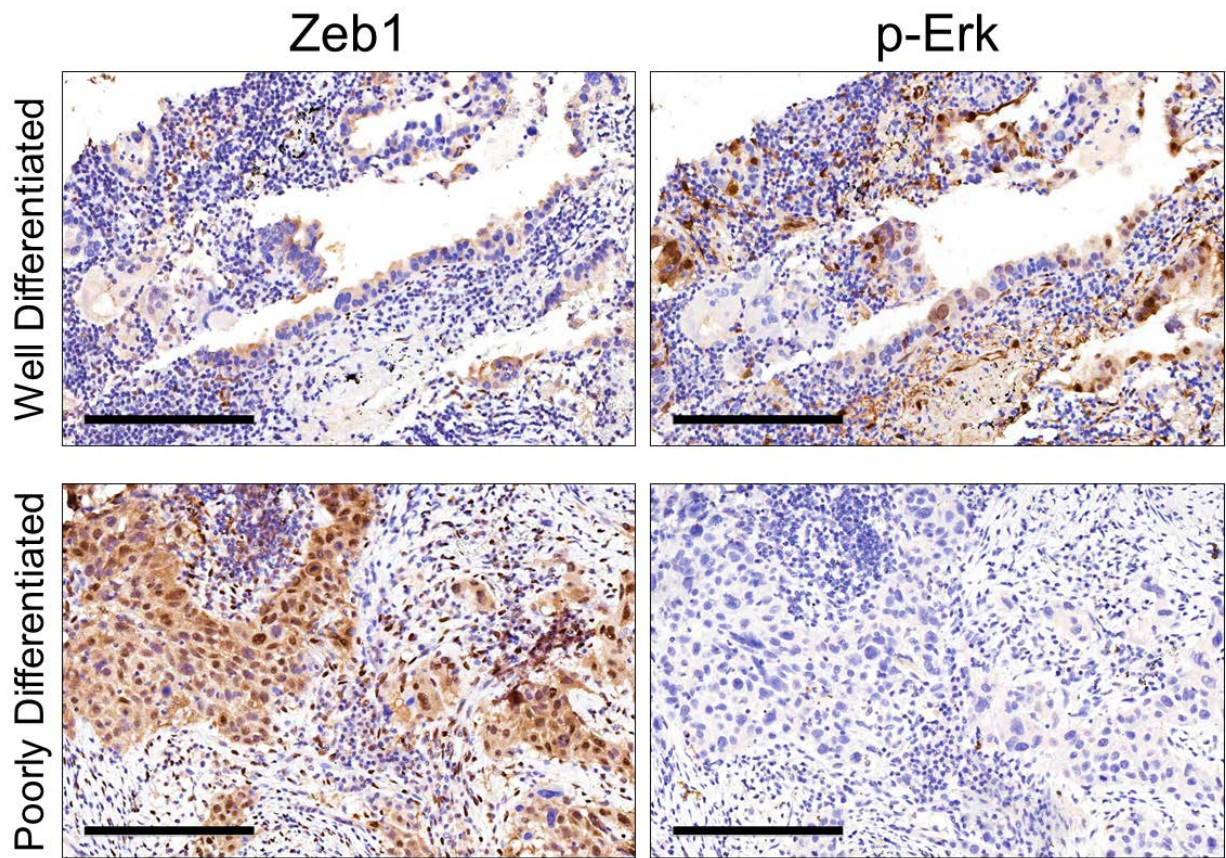


Figure 122. Examples of well- and poorly-differentiated human lung ADC tissue sections stained by IHC for Zeb1 and p-Erk. Scale bars, 200 μ m.

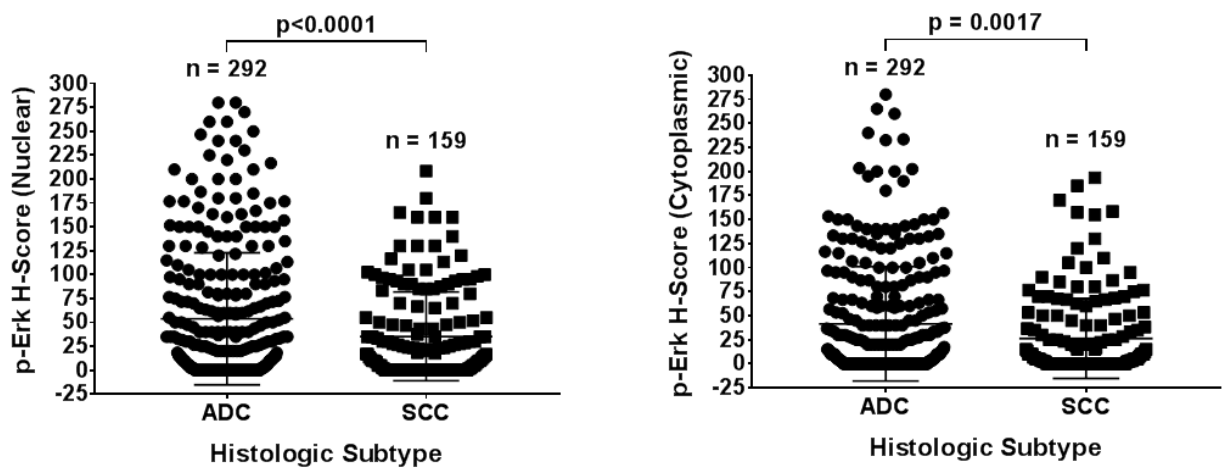


Figure 123. Left: Average final nuclear H-score of p-Erk in tumor cells of ADC or SCC specimens. Right: Average final cytoplasmic H-score of p-Erk in tumor cells of ADC or SCC specimens.

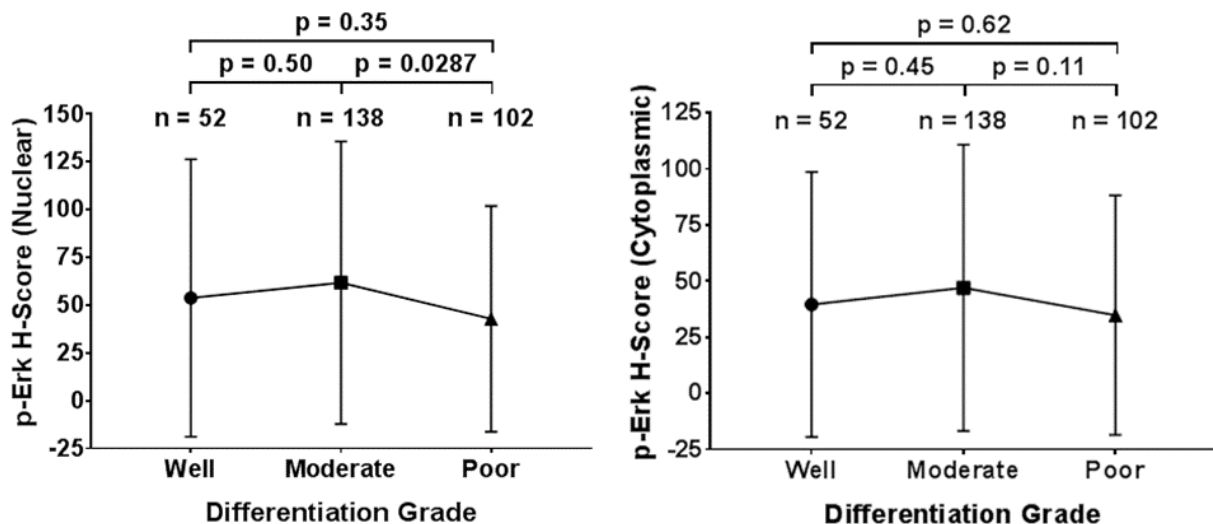


Figure 124. Left: Average final nuclear H-score of p-Erk in ADC specimens of different differentiation grades. Right: Average final cytoplasmic H-score of p-Erk in ADC specimens of different grades.

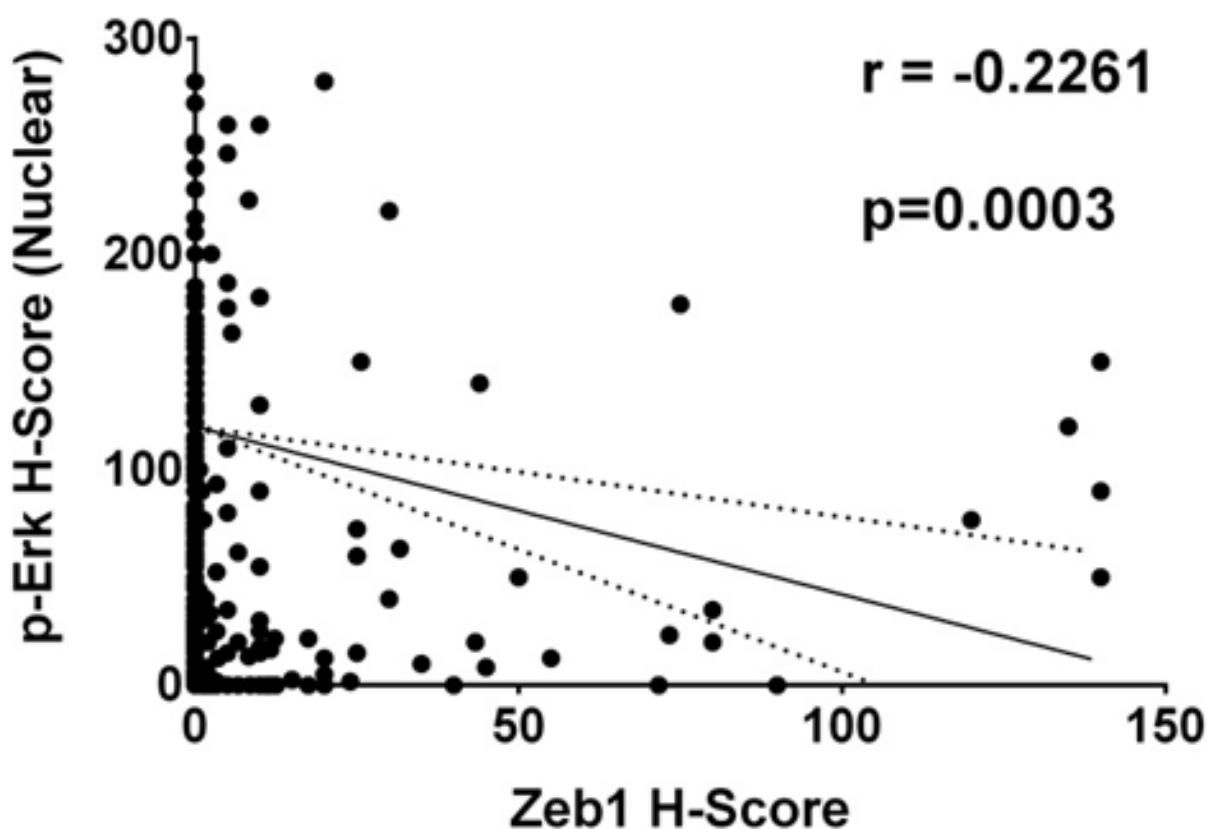


Figure 125. Cluster plot analysis of Spearman's rank correlation between Zeb1 and nuclear p-Erk H-score in ADC specimens.

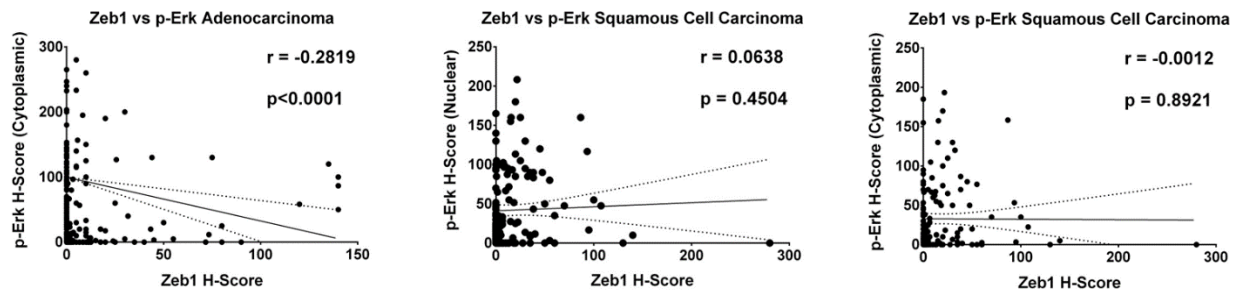


Figure 126. Left: Cluster plot analysis of Spearman's rank correlation between Zeb1 and cytoplasmic p-Erk H-score in ADC specimens. Middle and Right: Cluster plot analysis of Spearman's rank correlation between Zeb1 and (Middle) cytoplasmic and (Right) nuclear p-Erk H-score in SCC specimens.

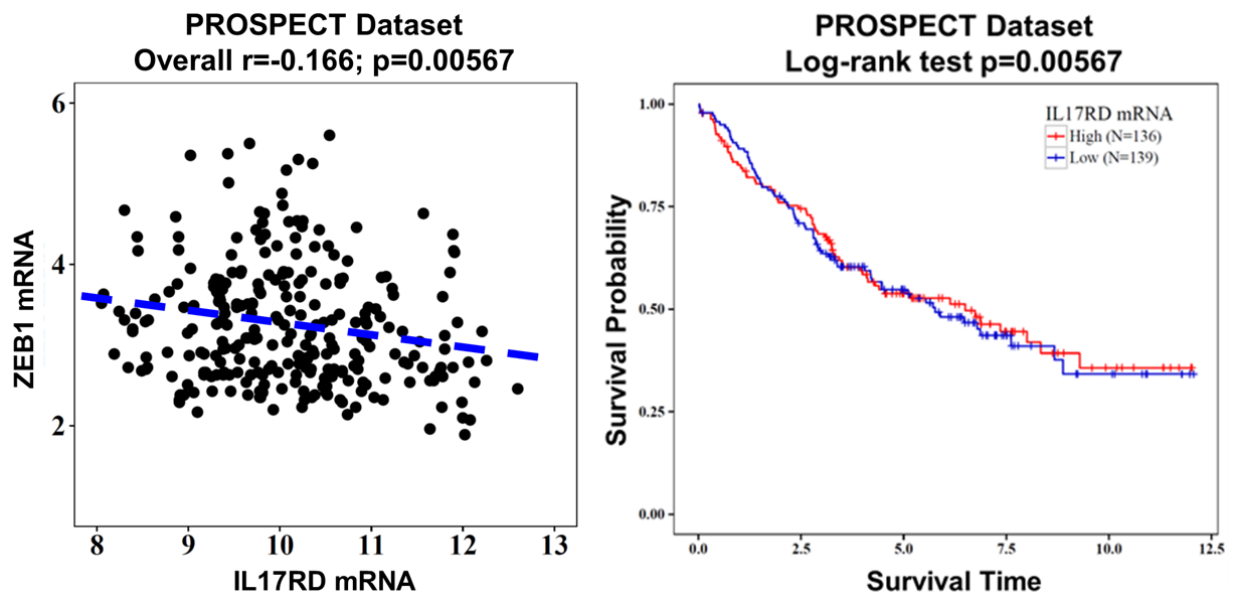


Figure 127. Left: Cluster plot analysis of Spearman's rank correlation between ZEB1 and IL17RD mRNA levels in human lung cancer patient tumor samples from PROSPECT dataset. Right: Kaplan–Meier survival analysis by log-rank significance test of IL17RD mRNA expression levels versus overall lung cancer patient survival from PROSPECT dataset.

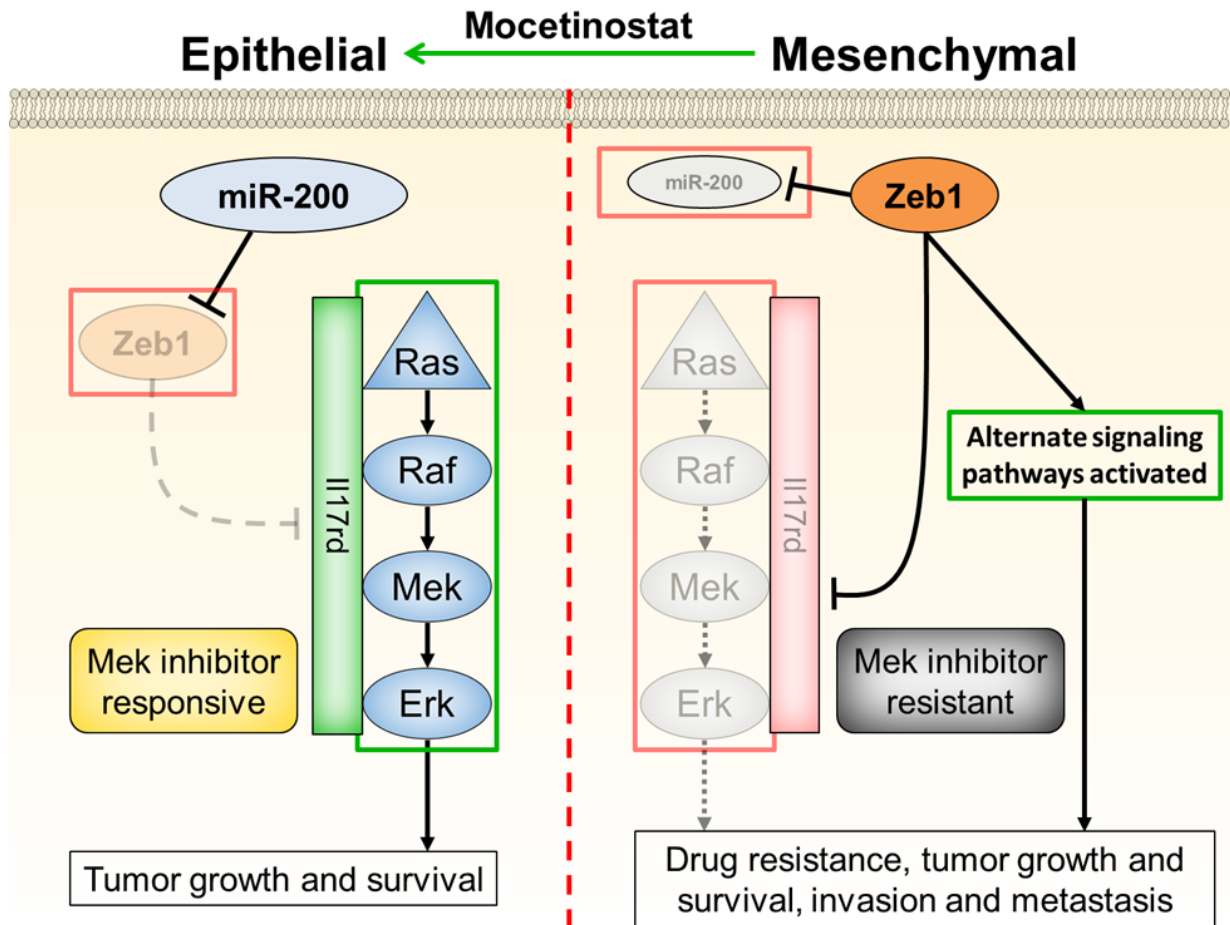


Figure 128. Proposed model demonstrating differential MAPK signaling pathway activation and sensitivity to MEK inhibitor treatment between epithelial and mesenchymal lung cancer cells due to Zeb1 regulation of Il17rd expression.

CHAPTER 4: DISCUSSION

Project 1: ZEB1 Induces LOXL2-Mediated Collagen Stabilization and Deposition in the Extracellular Matrix to Drive Lung Cancer Invasion and Metastasis

The high mortality rate of lung cancer, especially histologic subtypes with KRAS mutations, is attributed to the rapid development of therapy resistance and the propensity of the disease to metastasize to vital organs. Exacerbating matters, patients who receive first-line chemotherapies or targeted drug treatments often relapse and acquire distant metastatic lesions. Thus, we sought to investigate the underlying biological functions responsible for drug resistance and metastasis to identify potential biomarkers and therapeutic targets to improve overall patient survival. Utilizing the KP mouse model which possesses the two most commonly mutated genes in lung adenocarcinoma, initial work by our group revealed that Zeb1 suppression of miR-200 and induction EMT is crucial for lung cancer invasion and metastasis (32, 33, 48, 53, 55, 56, 58, 59, 89, 91, 128). Additionally, our finding that Zeb1-driven EMT is necessary for metastasis also presented a potential lead to study drug resistance since several studies have suggested that EMT is a potential mechanism of radiation and chemotherapy resistance (38, 39). However, inhibition of Zeb1 or rescued expression of miR-200 is therapeutically infeasible due to the non-specific, pleiotropic nature of both genes as well as the challenges in delivering mature microRNAs clinically. Therefore we were interested in greater in-depth research into the precise mechanisms of Zeb1 and miR-200 to ultimately identify potential biomarkers and therapeutic target against lung cancer progression.

From our work that identified Zeb1/miR-200 as master regulators of EMT and metastasis in lung cancer (33), we made a significant observation that the invasiveness of metastatic lung cancer cells was dependent on their interaction with the surrounding extracellular matrix. When cultured in laminin-rich Matrigel, the mesenchymal cells displayed highly epithelial morphologies and phenotypes and only formed invasive structures upon stimulation with TGF- β . This suggested that the cell-intrinsic alterations of EMT is insufficient to drive an *in vivo* invasive and metastatic phenotype and that the reciprocal and dynamic interaction between lung cancer cells and the extracellular matrix is critical for the dissemination process. The use of TGF- β simulates an *in vivo* condition and is a known inducer of EMT and stimulates collagen deposition (67, 69, 129), which we have demonstrated through *in vitro* 3D culture experiments to be necessary for the invasive phenotype (58). As there are numerous different types of collagen isoforms – each with variations in structural and biochemical properties that confer different biological consequences – the exact role of collagen on metastasis is not yet well-defined. Our bioinformatics analyses of the TCGA dataset, validated by qPCR, demonstrated that collagen type I and type III were upregulated in mesenchymal lung tumors and cancer cells. Collagen I and III are fibrillar collagens that are two of the most abundant collagen isoforms found in the body. Although our findings are consistent with breast cancer models that demonstrate that the presence of fibrillar collagen I is necessary for invasion and metastasis (62, 63), our findings here, in concordance with previous related work by our group (58), suggest that collagen-associated invasion/metastasis is due to ligand-based interaction with the Integrin β 1/Fak/Src signaling pathway but not due to mechanical stiffening of the matrix (62, 65, 130-133). Although our data does show that the presence of crosslinked

collagen stiffens the tumor tissue, this is a consequence of increased collagen matrix content that can be mimicked by other matrices such as Matrigel or an ECM-deficient PEG hydrogel (134). In fact, when we cultured our invasive/metastatic 344SQ or 393P-Zeb1 overexpressing cells in 3D *in vitro* PEG hydrogels of varying densities and stiffness, the cells always formed epithelial, spherical structures in high stiffness gels with no invasive protrusions even with the treatment of TGF- β (65), suggesting that collagen ligand is necessary for invasion and metastasis. Further emphasizing this point, when we cultured our mesenchymal cells in collagen mixed with ribose – a method of collagen stiffening by glycation (135) – we observed no difference, or a decrease, in the invasiveness of the lung cancer cells (**Figure 129**).

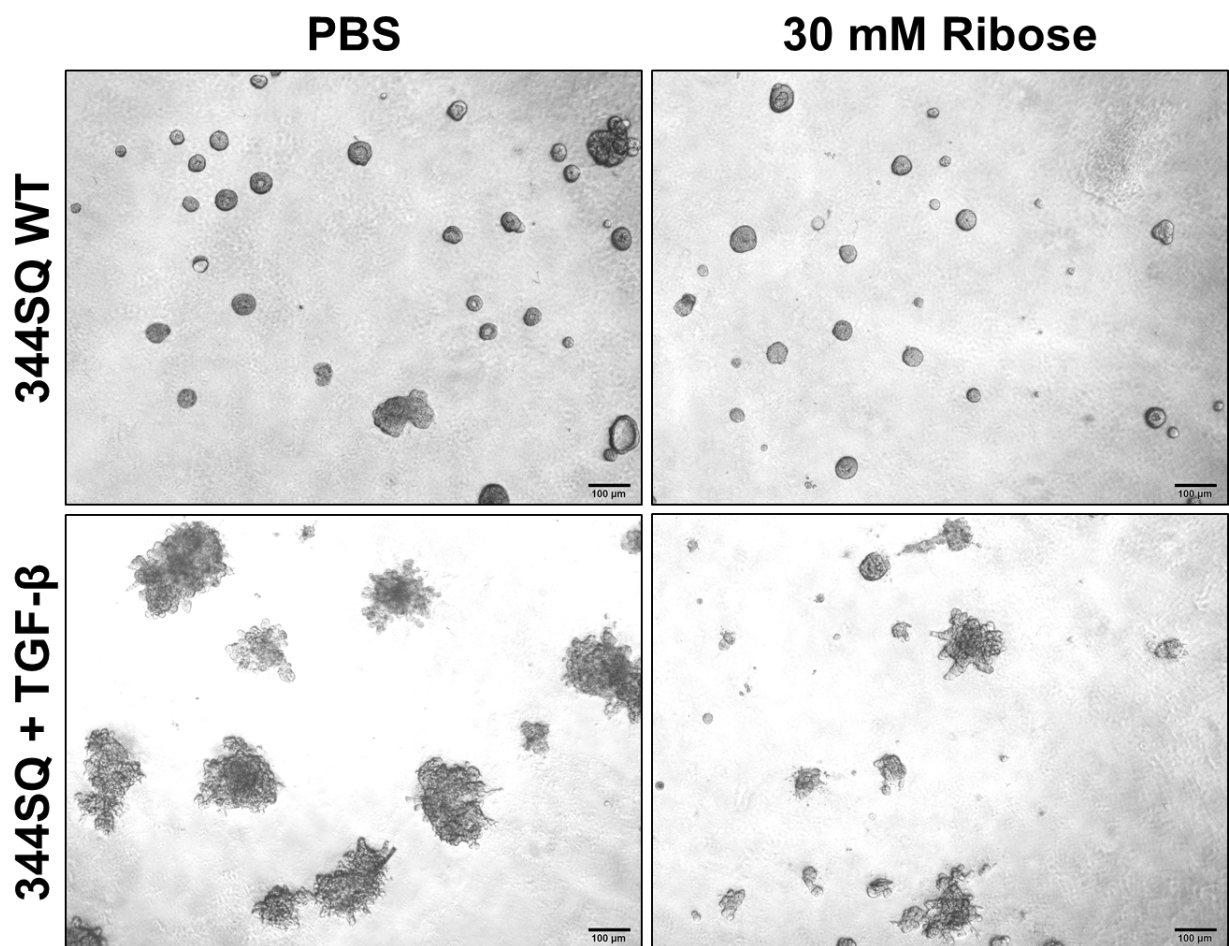


Figure 129. 344SQ cells cultured in 1.5 mg/mL collagen:Matrigel mix in the presence of PBS control, ribose, TGF- β , or TGF- β +ribose in combination. Bright field microscopy images at 4x magnification.

These conflicting reports demonstrate the complexities regarding the effects of collagen on cancer cell biology. In addition to individual collagen molecule ligand binding, the copious post-translational modifications of collagen also have a profound impact on how cells respond to the matrix protein. Moreover, manipulating collagen in an *in vitro* setting is also challenging due to collagen acquiring different properties depending on how the gel is prepared. For instance, we and others have demonstrated that collagen will spontaneously form covalent crosslinks during polymerization that is observable by SHG microscopy (56, 136). The longer the collagen remains as a liquid solution on ice, the more crosslinks will form. Furthermore, the compositional properties of the collagen gel also have an impact on the collagen crosslinks, resulting in different cancer cell response in 3D culture. For example, when we mixed a low concentration of collagen with Matrigel, we did not observe collagen crosslinks by SHG (**Figure 9**) compared to high concentrations of collagen. This increase in collagen crosslinks increases the invasiveness of the mesenchymal lung cancer cells which is consistent with previous reports (**Figure 130**) (136, 137).

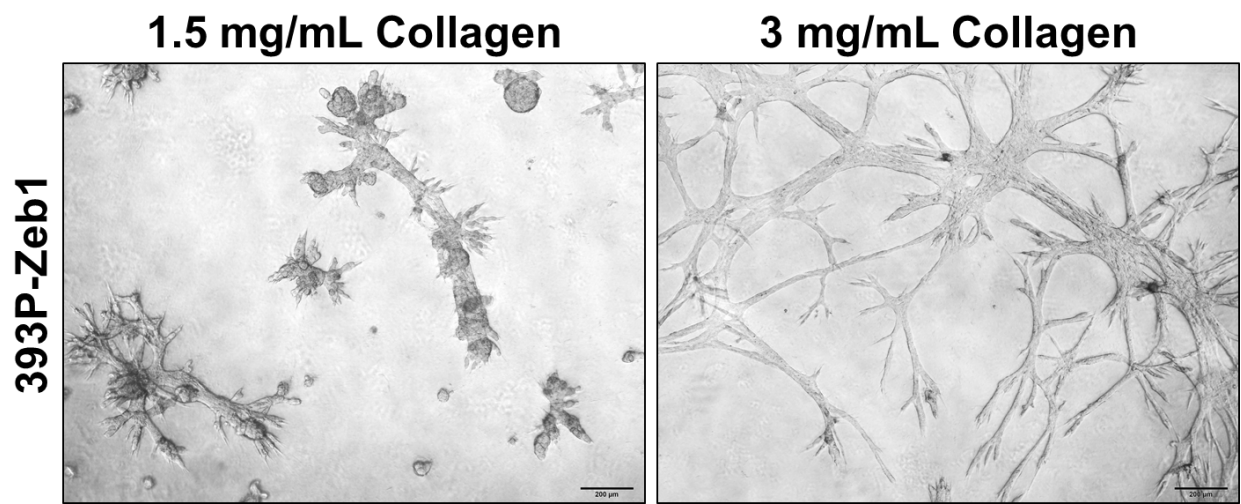


Figure 130. 393P-Zeb1 mesenchymal cells cultured in 1.5 mg/mL or 3 mg/mL final concentration of collagen mixed at a 1:1 ratio with Matrigel. Bright field microscopy images at 4x magnification.

Although higher concentrations of collagen and crosslinks increase matrix stiffness, the mesenchymal lung cancer cells still formed invasive protrusions at low collagen concentrations despite the unobservable crosslinks by SHG microscopy. This denotes that the ligand property of collagen is important for invasion. However, as seen in Figure 8 and our previous studies, only mesenchymal lung cancer cells form the invasive structures when cultured at low collagen concentrations while epithelial cells do not. This supports the statement that there is a dynamic interplay between the mesenchymal lung cancer cells and their surrounding ECM. Previous studies have demonstrated that collagen interaction with lung cancer cells promotes EMT through TGF- β signaling (69). Interestingly, we previously demonstrated that only mesenchymal lung cancer cells lines are sensitive to TGF- β stimulation (33). Furthermore, our mesenchymal lung cancer cells not only basally express high levels of collagen, but when treated with TGF- β the collagen expression levels dramatically increase. This suggests that in an *in vivo* environment collagen deposition by lung cancer cells acts in a feed-forward loop that further promotes EMT. Additionally, we previously demonstrated that lung cancer cell interaction with collagen stimulates Integrin/Fak/Src signaling through an EMT-dependent manner. Taken together, our results present a novel mechanism by which EMT-induced collagen deposition activates invasive cell signaling pathways in an autocrine fashion to drive lung cancer metastasis.

Our clinical data demonstrate that increased collagen expression correlates with EMT and is associated with poorer overall survival in lung adenocarcinoma patients, validating collagen as a promising biomarker of metastasis and survival. However, it is not therapeutically or pharmacologically feasible to target collagen directly. Fortunately, our bioinformatics analyses as well as qPCR data revealed that LOX and LOXL2 were

concurrently upregulated with collagen expression patterns in mesenchymal cells. LOX and LOXL2 are promising therapeutic targets since they are extracellular enzymes with a conserved catalytic region with reported inhibitors. The LOX family of enzymes has been shown in several tumor types – most notably in breast cancer – to promote tumor progression through various intracellular and extracellular mechanisms, including collagen crosslinking (62, 77, 78, 80, 83, 99, 100, 138-143). Functional studies revealed that LOXL2 was the primary isoform responsible for collagen crosslinking, deposition, and metastasis while LOX only had an *in vitro* effect on cell migration/invasion. This finding contrasts that of other tumor types which predominantly identify LOX as the primary isoform driving metastasis and collagen crosslinking. However, our histological data, bolstered by biochemical analyses, confirms LOXL2 crosslinking of collagen. Although LOXL2 has been implicated to be involved in collagen crosslinking due to its conserved catalytic region, our study is the first to directly validate this function. As mentioned throughout the dissertation, collagen processing and biology is very complicated. A common misconception amongst investigators that perform 3D culture experiments with collagen gels is that the collagen solutions, typically purchased from a vendor, are uncrosslinked. However, most processed and purchased collagen type I gels are derived from rat tail collagen and dissolved in an acid solution. The collagen from the rat tails are already fully mature, deaminated collagen fibers and will readily form the spontaneous covalent crosslinks resulting from LOX/LOXL2 deamination of the lysine residues. This is consistent with our *in vitro* data which demonstrate no changes in invasiveness when LOXL2 levels are manipulated without introduction of additional collagen. Overexpression of LOXL2 in epithelial lung cancer cells will have no effect on the invasiveness of the cells since the

collagen is already crosslinked and the cells have to co-express collagen, which is basally low in epithelial cells. Furthermore, epithelial cancer cells have low affinity for collagen binding which results in low activation of signaling pathways that lead to invasion and metastasis. LOXL2 is the necessary final step in collagen maturation *in vivo* and is necessary for deposition of insoluble collagen in the tissue architecture. If individual collagen fibers are not deaminated by LOXL2, there would be no intermolecular covalent bonds and collagen will remain as a soluble protein. In fact, if rat tail collagen type I gels are treated with sodium borohydride – which reverses the covalent bonds formed by the deaminated lysine residues – the gels liquefy and can be dissolved readily in solution. More importantly, the covalent crosslinks between collagen fibers must be formed with one deaminated lysine residue and one aminated lysine residue (ϵ -amine) that has not been processed by LOXL2. Hence, if LOXL2 is overexpressed at super-physiological levels, we would expect there to be no metastatic disease even in mesenchymal tumors since the overexpression of LOXL2 will go overboard with the deamination of lysine residues and no covalent bonds will form since there are no more ϵ -amine groups. Therefore, any studies on LOX or LOXL2 crosslinking of collagen and its role in metastasis must be performed with *in vivo* systems and cannot be done using overexpression systems. As a matter of fact if there are any studies that overexpress LOX or LOXL2 in cancer cells and observe deficient collagen crosslinking or diminished collagen-associated metastases, then the mechanisms reported must be re-evaluated. The findings from our study confirm that LOXL2 stabilizes insoluble collagen deposition responsible for metastasis but does not have an effect on primary tumor growth. Taking all of our mechanistic, functional, and clinical data into consideration, inhibition of LOXL2 in a clinical context must be done in

combination with other therapies that directly target the primary tumor to prevent metastatic disease often associated with first-line therapies. This study delineates a novel mechanism of KRAS mutant lung cancer metastasis whereby EMT-induced LOXL2 crosslinking, linearization, and deposition of collagen results in the activation of the Fak/Src signaling pathway to promote invasion and metastasis.

Project 2: Epithelial-to-Mesenchymal Transition promotes MEK inhibitor resistance in KRAS mutant lung cancers through suppression of IL17rd

It is imperative to understand drug resistance mechanisms because KRAS mutant lung cancer patients who receive MEK inhibitors respond very poorly to targeted therapies and even chemotherapies (25, 26). The *in vivo* FDAome shRNA dropout screen in conjunction with RPPA proteomic profiling identified differential reliance on MAPK molecules for tumor maintenance between epithelial and mesenchymal lung cancer cells and identified decreased MAPK signaling during EMT. Consistent with our prior work (40, 56, 58, 120), the RPPA dataset confirmed decreased signaling proteins involved in metastasis and certain types of drug resistance in epithelial lung cancer cells, while data from the shRNA library screen provided numerous additional drug targets for future investigations to optimize combination therapies. More importantly, though, a significant advantage in applying the shRNA screen to our immunocompetent syngeneic model is the ability to detect target genes that may synergize with immunotherapies. This study demonstrates the advantages of combining a functional hairpin screen with high-throughput proteomic profiles to characterize tumor progression and drug resistance.

Utilizing our syngeneic and genetically engineered mutant mouse models, we showed that the epithelial subpopulation of lung cancer cells within the heterogeneous tumor tissue was responsive to MEK inhibition while mesenchymal cells were resistant. These results provide an explanation to the development of therapy resistance due to co-mutations with mutant *KRAS* (27). Our *in vitro* cell line and *in vivo* tumor growth assays demonstrate that MEK inhibitor resistance is a result of both innate and acquired EMT. Translation of our histologic observations from murine tumor tissues to human specimens displayed an inverse correlation between MAPK signaling and Zeb1, presenting EMT-related molecules as prospective biomarkers to predict for MEK inhibitor response in patients.

Thorough investigation into the mechanism of MAPK stimulation by miR-200 in epithelial cells identified IL17RD as the primary activating factor and revealed direct Zeb1 repression of the IL17RD promoter. Our results directly link EMT to MAPK signaling regulation and dependency. Since re-expression of IL17RD alone activated MEK/ERK signaling and was sufficient to induce response to MEK inhibitors in mesenchymal lung cancer cells, these results suggest that IL17RD is potentially altering cell signaling patterns in a broader intracellular scope besides MAPK activation/inhibition. Analyses of human patient datasets inversely correlated IL17RD with ZEB1 mRNA expression which potentially defines IL17RD as an additional biomarker to predict MEK inhibitor sensitivity.

Since IL17RD inhibits FGFR1-associated MAPK signaling, we looked at FGFR1 expression levels in our system and saw a positive correlation between EMT and FGFR1, which is consistent with previous work exploring the role of FGFR1 in MEK inhibitor resistance through feedback reactivation of MAPK signaling (24, 144).

Conversely, IL17RD levels were high in epithelial cells and inversely correlated with FGFR1 levels. Although the published reports demonstrate that a combination of MEK inhibitors with RTK or FGFR1-specific inhibitors is able to reduce primary lung tumor growth, the studies do not address potential metastatic events following treatment, which is a major cause of lung cancer patient deaths (5, 145). Here, we validate that the class I HDAC inhibitor mocetinostat – currently undergoing multiple clinical trials (<https://clinicaltrials.gov/ct2/results?term=mocetinostat>) – is able to induce miR-200, revert EMT, and dramatically increase IL17rd expression resulting in an upregulation of MAPK signaling. Using our syngeneic tumor model to study drug response is superior to human cell line xenografts because we are able to capture the metastatic events following treatments as well as address the heterogeneity observed clinically in isogenic tumors. The *in vivo* drug treatment assays of the syngeneic tumors demonstrate that the combination of selumetinib with mocetinostat not only decreases primary tumor growth, but significantly reduces metastatic disease as well, providing pre-clinical rationale for a promising combinatorial treatment strategy in patients. This study establishes the mechanism of MAPK signaling regulation by EMT, utilizes murine models and human lung cancer specimens to predict response to MEK inhibitors, and validates a novel treatment strategy for lung cancer.

CHAPTER 5: FUTURE DIRECTIONS

Project 1: ZEB1 Induces LOXL2-Mediated Collagen Stabilization and Deposition in the Extracellular Matrix to Drive Lung Cancer Invasion and Metastasis

The importance of the extracellular function of LOXL2 in promoting metastasis makes the enzyme a promising therapeutic target against lung cancer metastasis. Although BAPN is a small molecule inhibitor of *in vitro* LOXL2 enzymatic activity, our data – consistent with numerous other studies and a failed clinical trial – shows that BAPN is a poor drug to use clinically and alternative inhibitors are necessary to target this enzyme. Currently, there exists a monoclonal antibody that neutralizes LOXL2 and is in phase II clinical trials. However, the design of the clinical trial aims to treat patients with advanced, metastatic solid tumors with the LOXL2 inhibiting antibody. Based on our data, this is the incorrect way to approach this study because the tumors are already in an advanced stage and are metastatic therefore it is no longer useful to target the collagen crosslinking enzyme. Furthermore, we also demonstrate that LOXL2 inhibition does nothing to the primary tumor growth therefore only treating these patients with LOXL2 will have no effect on primary or metastatic tumor size. Furthermore, LOXL2 also has a reported intracellular function in metastasis (83) and an antibody therapy will not be able to target the intracellular isoform of the enzyme. Therefore future studies will aim to develop novel small molecule inhibitors of LOXL2 enzymatic activity to prevent metastasis. Besides only targeting metastasis, we will aim at studying the effects of combinatorial treatments with LOXL2 inhibitors and first-line radiation or chemotherapies in pre-clinical models of lung cancer because targeting

LOXL2 alone has no effect on the growth of the primary tumor which is still important for patient survival. Our *in vitro* 3D culture data shows that mechanical stiffening of the surrounding matrix reduces invasiveness even in collagen. This suggests that the cancer cells themselves are reorganizing and remodeling mature, crosslinked collagen when they come in contact with the ECM to facilitate invasion and metastasis. Future studies will aim at understanding how the cancer cells are reshaping their milieu to drive the malignant phenotype. Lastly, since overexpression of LOX in epithelial cells did not have the opposing effect as LOX knockdown in mesenchymal cells, this means that there are other intracellular factors that operate in tandem with LOX to drive the *in vitro* migratory phenotype. Additional research to identify LOX co-factors of cell motility will be important to understand fundamental cellular functions.

Project 2: Epithelial-to-Mesenchymal Transition promotes MEK inhibitor resistance in KRAS mutant lung cancers through suppression of IL17rd

As miR-200 activation of MAPK signaling is independent of mutational status, this suggests that this process is necessary for development. Further research into the developmental role of miR-200 activation of MAPK signaling through IL17RD will help elucidate this complex biological process. Further studies with our newly generated conditional *miR-141/200c* and *KM* mutant mice will not only elucidate the role of miR-200 on tumor progression, but also provide us the means to understand various biological and developmental processes. Because IL17RD is critical during development (115, 146) and is a negative regulator of EMT (147, 148), future investigations will aim to delineate the role of IL17RD on lung cancer progression,

identify changes in global cell signaling patterns that may confer sensitivity to targeted therapies after rescued expression in mesenchymal lung cancer cells, and establish the role of IL17RD on mammalian development. Additionally, we would like to optimize IL17RD antibodies for IHC staining in human patient tumor samples and be able to predict response to MEK inhibitors. Lastly, the ability to predict sensitivity to MEK inhibition based upon EMT status will allow for the establishment of other drug combinations that target the resistant mesenchymal subpopulation of cancer cells such as immune checkpoint blockade. With regards to immune therapies, using the *in vivo* shRNA screen to identify differential dependencies between epithelial and mesenchymal lung cancer cells in nude or immunocompetent mice will also identify targeted therapies that synergize with immune checkpoint blockade.

BIBLIOGRAPHY

1. Siegel, R. L., K. D. Miller, and A. Jemal. 2017. Cancer Statistics, 2017. *CA Cancer J Clin* 67: 7-30.
2. Fossella, F. V., R. DeVore, R. N. Kerr, J. Crawford, R. R. Natale, F. Dunphy, L. Kalman, V. Miller, J. S. Lee, M. Moore, D. Gandara, D. Karp, E. Vokes, M. Kris, Y. Kim, F. Gamza, and L. Hammershaimb. 2000. Randomized phase III trial of docetaxel versus vinorelbine or ifosfamide in patients with advanced non-small-cell lung cancer previously treated with platinum-containing chemotherapy regimens. The TAX 320 Non-Small Cell Lung Cancer Study Group. *Journal of clinical oncology : official journal of the American Society of Clinical Oncology* 18: 2354-2362.
3. Kim, E. S. 2016. Chemotherapy Resistance in Lung Cancer. *Adv Exp Med Biol* 893: 189-209.
4. Kim, H. R., J. C. Lee, Y. C. Kim, K. S. Kim, I. J. Oh, S. Y. Lee, T. W. Jang, M. K. Lee, K. C. Shin, G. H. Lee, J. S. Ryu, S. H. Jang, J. W. Son, J. E. Lee, S. Y. Kim, H. J. Kim, and K. Y. Lee. 2014. Clinical characteristics of non-small cell lung cancer patients who experienced acquired resistance during gefitinib treatment. *Lung Cancer* 83: 252-258.
5. Cataldo, V. D., D. L. Gibbons, R. Pérez-Soler, and A. Quintás-Cardama. 2011. Treatment of Non–Small-Cell Lung Cancer with Erlotinib or Gefitinib. *New England Journal of Medicine* 364: 947-955.
6. Herbst, R. S., J. V. Heymach, and S. M. Lippman. 2008. Lung cancer. *N Engl J Med* 359: 1367-1380.

7. Berndt, N., A. D. Hamilton, and S. M. Sebti. 2011. Targeting protein prenylation for cancer therapy. *Nature Reviews Cancer* 11: 775-791.
8. Chan, B., and B. Hughes. 2015. Targeted therapy for non-small cell lung cancer: current standards and the promise of the future. *Transl Lung Cancer Res* 4: 36-54.
9. McGrath, J. P., D. J. Capon, D. H. Smith, E. Y. Chen, P. H. Seeburg, D. V. Goeddel, and A. D. Levinson. 1983. Structure and organization of the human K-ras proto-oncogene and a related processed pseudogene. *Nature* 304: 501-506.
10. Lavoie, H., and M. Therrien. 2015. Regulation of RAF protein kinases in ERK signalling. *Nat Rev Mol Cell Biol* 16: 281-298.
11. Gilmartin, A. G., M. R. Bleam, A. Groy, K. G. Moss, E. A. Minthorn, S. G. Kulkarni, C. M. Rominger, S. Erskine, K. E. Fisher, J. Yang, F. Zappacosta, R. Annan, D. Sutton, and S. G. Laquerre. 2011. GSK1120212 (JTP-74057) Is an Inhibitor of MEK Activity and Activation with Favorable Pharmacokinetic Properties for Sustained In Vivo Pathway Inhibition. *Clinical Cancer Research* 17: 989-1000.
12. Yeh, T. C., V. Marsh, B. A. Bernat, J. Ballard, H. Colwell, R. J. Evans, J. Parry, D. Smith, B. J. Brandhuber, S. Gross, A. Marlow, B. Hurley, J. Lyssikatos, P. A. Lee, J. D. Winkler, K. Koch, and E. Wallace. 2007. Biological Characterization of ARRY-142886 (AZD6244), a Potent, Highly Selective Mitogen-Activated Protein Kinase Kinase 1/2 Inhibitor. *Clinical Cancer Research* 13: 1576-1583.
13. Hoshino, R., Y. Chatani, T. Yamori, T. Tsuruo, H. Oka, O. Yoshida, Y. Shimada, S. Ari-i, H. Wada, J. Fujimoto, and M. Kohno. 1999. Constitutive activation of the

- 41-/43-kDa mitogen-activated protein kinase signaling pathway in human tumors. *Oncogene* 18: 813-822.
14. Blume-Jensen, P., and T. Hunter. 2001. Oncogenic kinase signalling. *Nature* 411: 355-365.
 15. An, S., Y. Yang, R. Ward, Y. Liu, X. X. Guo, and T. R. Xu. 2015. Raf-interactome in tuning the complexity and diversity of Raf function. *FEBS J* 282: 32-53.
 16. Bluthgen, N., S. Legewie, S. M. Kielbasa, A. Schramme, O. Tchernitsa, J. Keil, A. Solf, M. Vingron, R. Schafer, H. Herzelt, and C. Sers. 2009. A systems biological approach suggests that transcriptional feedback regulation by dual-specificity phosphatase 6 shapes extracellular signal-related kinase activity in RAS-transformed fibroblasts. *Febs Journal* 276: 1024-1035.
 17. Karreth, F. A., and D. A. Tuveson. 2009. Modelling oncogenic Ras/Raf signalling in the mouse. *Curr Opin Genet Dev* 19: 4-11.
 18. Owens, D. M., and S. M. Keyse. 2007. Differential regulation of MAP kinase signalling by dual-specificity protein phosphatases. *Oncogene* 26: 3203-3213.
 19. Rebocho, A. P., and R. Marais. 2013. ARAF acts as a scaffold to stabilize BRAF:CRAF heterodimers. *Oncogene* 32: 3207-3212.
 20. Sacks, D. B. 2006. The role of scaffold proteins in MEK/ERK signalling. *Biochem Soc Trans* 34: 833-836.
 21. Courtois-Cox, S., S. M. Genter Williams, E. E. Reczek, B. W. Johnson, L. T. McGillicuddy, C. M. Johannessen, P. E. Hollstein, M. MacCollin, and K. Cichowski. 2006. A negative feedback signaling network underlies oncogene-induced senescence. *Cancer Cell* 10: 459-472.

22. Zhao, Z., C. C. Chen, C. D. Rillahan, R. L. Shen, T. Kitzing, M. E. McNerney, E. Diaz-Flores, J. Zuber, K. Shannon, M. M. Le Beau, M. S. Spector, S. C. Kogan, and S. W. Lowe. 2015. Cooperative loss of RAS feedback regulation drives myeloid leukemogenesis. *Nat Genet* 47: 539-U150.
23. Zhao, Y., and A. A. Adjei. 2014. The clinical development of MEK inhibitors. *Nature Reviews Clinical Oncology* 11: 385-400.
24. Kitai, H., H. Ebi, S. Tomida, K. V. Floros, H. Kotani, Y. Adachi, S. Oizumi, M. Nishimura, A. C. Faber, and S. Yano. 2016. Epithelial-to-Mesenchymal Transition Defines Feedback Activation of Receptor Tyrosine Kinase Signaling Induced by MEK Inhibition in KRAS-Mutant Lung Cancer. *Cancer Discov* 6: 754-769.
25. Blumenschein, G. R., Jr., E. F. Smit, D. Planchard, D. W. Kim, J. Cadranel, T. De Pas, F. Dunphy, K. Udud, M. J. Ahn, N. H. Hanna, J. H. Kim, J. Mazieres, S. W. Kim, P. Baas, E. Rappold, S. Redhu, A. Puski, F. S. Wu, and P. A. Janne. 2015. A randomized phase II study of the MEK1/MEK2 inhibitor trametinib (GSK1120212) compared with docetaxel in KRAS-mutant advanced non-small-cell lung cancer (NSCLC)dagger. *Ann Oncol* 26: 894-901.
26. Jänne, P. A., M. M. van den Heuvel, F. Barlesi, M. Cobo, J. Mazieres, L. Crinò, S. Orlov, F. Blackhall, J. Wolf, P. Garrido, A. Poltoratskiy, G. Mariani, D. Ghiorghiu, E. Kilgour, P. Smith, A. Kohlmann, D. J. Carlile, D. Lawrence, K. Bowen, and J. Vansteenkiste. 2017. Selumetinib Plus Docetaxel Compared With Docetaxel Alone and Progression-Free Survival in Patients With KRAS-Mutant Advanced Non–Small Cell Lung Cancer. *Jama* 317: 1844.

27. Chen, Z., K. Cheng, Z. Walton, Y. Wang, H. Ebi, T. Shimamura, Y. Liu, T. Tupper, J. Ouyang, J. Li, P. Gao, M. S. Woo, C. Xu, M. Yanagita, A. Altabef, S. Wang, C. Lee, Y. Nakada, C. G. Pena, Y. Sun, Y. Franchetti, C. Yao, A. Saur, M. D. Cameron, M. Nishino, D. N. Hayes, M. D. Wilkerson, P. J. Roberts, C. B. Lee, N. Bardeesy, M. Butaney, L. R. Chirieac, D. B. Costa, D. Jackman, N. E. Sharpless, D. H. Castrillon, G. D. Demetri, P. A. Janne, P. P. Pandolfi, L. C. Cantley, A. L. Kung, J. A. Engelman, and K. K. Wong. 2012. A murine lung cancer co-clinical trial identifies genetic modifiers of therapeutic response. *Nature* 483: 613-617.
28. Bourdon, J.-C., S. Surget, and M. P. Khoury. 2013. Uncovering the role of p53 splice variants in human malignancy: a clinical perspective. *OncoTargets and Therapy*: 57.
29. Steels, E., B. Paesmans, T. Berghmans, F. Branle, F. Lemaitre, C. Mascaux, A. P. Meert, F. Vallot, J. J. Lafitte, and J. P. Sculier. 2001. Role of p53 as a prognostic factor for survival in lung cancer: a systematic review of the literature with a meta-analysis. *Eur Respir J* 18: 705-719.
30. Gao, J., B. A. Aksoy, U. Dogrusoz, G. Dresdner, B. Gross, S. O. Sumer, Y. Sun, A. Jacobsen, R. Sinha, E. Larsson, E. Cerami, C. Sander, and N. Schultz. 2013. Integrative Analysis of Complex Cancer Genomics and Clinical Profiles Using the cBioPortal. *Science Signaling* 6: pl1-pl1.
31. Cerami, E., J. Gao, U. Dogrusoz, B. E. Gross, S. O. Sumer, B. A. Aksoy, A. Jacobsen, C. J. Byrne, M. L. Heuer, E. Larsson, Y. Antipin, B. Reva, A. P. Goldberg, C. Sander, and N. Schultz. 2012. The cBio Cancer Genomics Portal:

- An Open Platform for Exploring Multidimensional Cancer Genomics Data: Figure 1. *Cancer Discovery* 2: 401-404.
32. Zheng, S., A. K. El-Naggar, E. S. Kim, J. M. Kurie, and G. Lozano. 2007. A genetic mouse model for metastatic lung cancer with gender differences in survival. *Oncogene* 26: 6896-6904.
 33. Gibbons, D. L., W. Lin, C. J. Creighton, Z. H. Rizvi, P. A. Gregory, G. J. Goodall, N. Thilaganathan, L. Du, Y. Zhang, A. Pertsemlidis, and J. M. Kurie. 2009. Contextual extracellular cues promote tumor cell EMT and metastasis by regulating miR-200 family expression. *Genes Dev* 23: 2140-2151.
 34. Kalluri, R., and R. A. Weinberg. 2009. The basics of epithelial-mesenchymal transition. *J Clin Invest* 119: 1420-1428.
 35. Ma, L., and R. A. Weinberg. 2008. Micromanagers of malignancy: role of microRNAs in regulating metastasis. *Trends Genet* 24: 448-456.
 36. Yang, J., and R. A. Weinberg. 2008. Epithelial-mesenchymal transition: at the crossroads of development and tumor metastasis. *Developmental cell* 14: 818-829.
 37. Tsai, J. H., and J. Yang. 2013. Epithelial-mesenchymal plasticity in carcinoma metastasis. *Genes Dev* 27: 2192-2206.
 38. Zhang, P., Y. Wei, L. Wang, B. G. Debeb, Y. Yuan, J. Zhang, J. Yuan, M. Wang, D. Chen, Y. Sun, W. A. Woodward, Y. Liu, D. C. Dean, H. Liang, Y. Hu, K. K. Ang, M. C. Hung, J. Chen, and L. Ma. 2014. ATM-mediated stabilization of ZEB1 promotes DNA damage response and radioresistance through CHK1. *Nat Cell Biol* 16: 864-875.

39. Zheng, X., J. L. Carstens, J. Kim, M. Scheible, J. Kaye, H. Sugimoto, C. C. Wu, V. S. LeBleu, and R. Kalluri. 2015. Epithelial-to-mesenchymal transition is dispensable for metastasis but induces chemoresistance in pancreatic cancer. *Nature* 527: 525-530.
40. Byers, L. A., L. Diao, J. Wang, P. Saintigny, L. Girard, M. Peyton, L. Shen, Y. Fan, U. Giri, P. K. Tumula, M. B. Nilsson, J. Gudikote, H. Tran, R. J. Cardnell, D. J. Bearss, S. L. Warner, J. M. Foulks, S. B. Kanner, V. Gandhi, N. Krett, S. T. Rosen, E. S. Kim, R. S. Herbst, G. R. Blumenschein, J. J. Lee, S. M. Lippman, K. K. Ang, G. B. Mills, W. K. Hong, J. N. Weinstein, Wistuba, II, K. R. Coombes, J. D. Minna, and J. V. Heymach. 2013. An epithelial-mesenchymal transition gene signature predicts resistance to EGFR and PI3K inhibitors and identifies Axl as a therapeutic target for overcoming EGFR inhibitor resistance. *Clin Cancer Res* 19: 279-290.
41. Ferrarotto, R., R. Goonatilake, S. Young Yoo, P. Tong, U. Giri, S. Peng, J. Minna, L. Girard, Y. Wang, L. Wang, L. Li, L. Diao, D. H. Peng, D. L. Gibbons, B. S. Glisson, J. V. Heymach, J. Wang, L. A. Byers, and F. M. Johnson. 2016. Epithelial-Mesenchymal Transition Predicts Polo-Like Kinase 1 Inhibitor-Mediated Apoptosis in Non-Small Cell Lung Cancer. *Clin Cancer Res* 22: 1674-1686.
42. Shibue, T., and R. A. Weinberg. 2017. EMT, CSCs, and drug resistance: the mechanistic link and clinical implications. *Nat Rev Clin Oncol*.
43. Fischer, K. R., A. Durrans, S. Lee, J. Sheng, F. Li, S. T. C. Wong, H. Choi, T. El Rayes, S. Ryu, J. Troeger, R. F. Schwabe, L. T. Vahdat, N. K. Altorki, V. Mittal,

- and D. Gao. 2015. Epithelial-to-mesenchymal transition is not required for lung metastasis but contributes to chemoresistance. *Nature* 527: 472-476.
44. Larsen, J. E., V. Nathan, J. K. Osborne, R. K. Farrow, D. Deb, J. P. Sullivan, P. D. Dospoy, A. Augustyn, S. K. Hight, M. Sato, L. Girard, C. Behrens, Wistuba, II, A. F. Gazdar, N. K. Hayward, and J. D. Minna. 2016. ZEB1 drives epithelial-to-mesenchymal transition in lung cancer. *J Clin Invest* 126: 3219-3235.
 45. Wellner, U., J. Schubert, U. C. Burk, O. Schmalhofer, F. Zhu, A. Sonntag, B. Waldvogel, C. Vannier, D. Darling, A. zur Hausen, V. G. Brunton, J. Morton, O. Sansom, J. Schuler, M. P. Stemmler, C. Herzberger, U. Hopt, T. Keck, S. Brabletz, and T. Brabletz. 2009. The EMT-activator ZEB1 promotes tumorigenicity by repressing stemness-inhibiting microRNAs. *Nat Cell Biol* 11: 1487-1495.
 46. Gregory, P. A., A. G. Bert, E. L. Paterson, S. C. Barry, A. Tsykin, G. Farshid, M. A. Vadas, Y. Khew-Goodall, and G. J. Goodall. 2008. The miR-200 family and miR-205 regulate epithelial to mesenchymal transition by targeting ZEB1 and SIP1. *Nat Cell Biol* 10: 593-601.
 47. Gregory, P. A., C. P. Bracken, E. Smith, A. G. Bert, J. A. Wright, S. Roslan, M. Morris, L. Wyatt, G. Farshid, Y. Y. Lim, G. J. Lindeman, M. F. Shannon, P. A. Drew, Y. Khew-Goodall, and G. J. Goodall. 2011. An autocrine TGF-beta/ZEB/miR-200 signaling network regulates establishment and maintenance of epithelial-mesenchymal transition. *Mol Biol Cell* 22: 1686-1698.
 48. Ahn, Y. H., D. L. Gibbons, D. Chakravarti, C. J. Creighton, Z. H. Rizvi, H. P. Adams, A. Pertsemlidis, P. A. Gregory, J. A. Wright, G. J. Goodall, E. R. Flores,

- and J. M. Kurie. 2012. ZEB1 drives prometastatic actin cytoskeletal remodeling by downregulating miR-34a expression. *J Clin Invest* 122: 3170-3183.
49. Burk, U., J. Schubert, U. Wellner, O. Schmalhofer, E. Vincan, S. Spaderna, and T. Brabletz. 2008. A reciprocal repression between ZEB1 and members of the miR-200 family promotes EMT and invasion in cancer cells. *EMBO reports* 9: 582-589.
 50. Meidhof, S., S. Brabletz, W. Lehmann, B. T. Preca, K. Mock, M. Ruh, J. Schuler, M. Berthold, A. Weber, U. Burk, M. Lubbert, M. Pühr, Z. Culig, U. Wellner, T. Keck, P. Bronsert, S. Kusters, U. T. Hopt, M. P. Stemmler, and T. Brabletz. 2015. ZEB1-associated drug resistance in cancer cells is reversed by the class I HDAC inhibitor mocetinostat. *EMBO Mol Med* 7: 831-847.
 51. Aghdassi, A., M. Sendler, A. Guenther, J. Mayerle, C. O. Behn, C. D. Heidecke, H. Friess, M. Buchler, M. Evert, M. M. Lerch, and F. U. Weiss. 2012. Recruitment of histone deacetylases HDAC1 and HDAC2 by the transcriptional repressor ZEB1 downregulates E-cadherin expression in pancreatic cancer. *Gut* 61: 439-448.
 52. Argast, G. M., J. S. Krueger, S. Thomson, I. Sujka-Kwok, K. Carey, S. Silva, M. O'Connor, P. Mercado, I. J. Mulford, G. D. Young, R. Sennello, R. Wild, J. A. Pachter, J. L. Kan, J. Haley, M. Rosenfeld-Franklin, and D. M. Epstein. 2011. Inducible expression of TGFbeta, snail and Zeb1 recapitulates EMT in vitro and in vivo in a NSCLC model. *Clin Exp Metastasis* 28: 593-614.
 53. Chen, L., D. L. Gibbons, S. Goswami, M. A. Cortez, Y. H. Ahn, L. A. Byers, X. Zhang, X. Yi, D. Dwyer, W. Lin, L. Diao, J. Wang, J. D. Roybal, M. Patel, C. Ungewiss, D. Peng, S. Antonia, M. Mediavilla-Varela, G. Robertson, S. Jones,

- M. Suraokar, J. W. Welsh, B. Erez, Wistuba, II, L. Chen, D. Peng, S. Wang, S. E. Ullrich, J. V. Heymach, J. M. Kurie, and F. X. Qin. 2014. Metastasis is regulated via microRNA-200/ZEB1 axis control of tumour cell PD-L1 expression and intratumoral immunosuppression. *Nat Commun* 5: 5241.
54. Gemmill, R. M., J. Roche, V. A. Potiron, P. Nasarre, M. Mitas, C. D. Coldren, B. A. Helfrich, E. Garrett-Mayer, P. A. Bunn, and H. A. Drabkin. 2011. ZEB1-responsive genes in non-small cell lung cancer. *Cancer Lett* 300: 66-78.
 55. Kundu, S. T., L. A. Byers, D. H. Peng, J. D. Roybal, L. Diao, J. Wang, P. Tong, C. J. Creighton, and D. L. Gibbons. 2015. The miR-200 family and the miR-183~96~182 cluster target Foxf2 to inhibit invasion and metastasis in lung cancers. *Oncogene*.
 56. Peng, D. H., C. Ungewiss, P. Tong, L. A. Byers, J. Wang, J. R. Canales, P. A. Villalobos, N. Uraoka, B. Mino, C. Behrens, Wistuba, II, R. I. Han, C. A. Wanna, M. Fahrenholtz, K. J. Grande-Allen, C. J. Creighton, and D. L. Gibbons. 2016. ZEB1 induces LOXL2-mediated collagen stabilization and deposition in the extracellular matrix to drive lung cancer invasion and metastasis. *Oncogene*.
 57. Spaderna, S., O. Schmalhofer, M. Wahlbuhl, A. Dimmler, K. Bauer, A. Sultan, F. Hlubek, A. Jung, D. Strand, A. Eger, T. Kirchner, J. Behrens, and T. Brabletz. 2008. The transcriptional repressor ZEB1 promotes metastasis and loss of cell polarity in cancer. *Cancer Res* 68: 537-544.
 58. Ungewiss, C., Z. H. Rizvi, J. D. Roybal, D. H. Peng, K. A. Gold, D. H. Shin, C. J. Creighton, and D. L. Gibbons. 2016. The microRNA-200/Zeb1 axis regulates ECM-dependent beta1-integrin/FAK signaling, cancer cell invasion and metastasis through CRKL. *Sci Rep* 6: 18652.

59. Zhang, T., L. Guo, C. J. Creighton, Q. Lu, D. L. Gibbons, E. S. Yi, B. Deng, J. R. Molina, Z. Sun, P. Yang, and Y. Yang. 2016. A genetic cell context-dependent role for ZEB1 in lung cancer. *Nat Commun* 7: 12231.
60. Lehmann, W., D. Mossmann, J. Kleemann, K. Mock, C. Meisinger, T. Brummer, R. Herr, S. Brabletz, M. P. Stemmler, and T. Brabletz. 2016. ZEB1 turns into a transcriptional activator by interacting with YAP1 in aggressive cancer types. *Nat Commun* 7: 10498.
61. Nieto, M. A., R. Y. Huang, R. A. Jackson, and J. P. Thiery. 2016. Emt: 2016. *Cell* 166: 21-45.
62. Levental, K. R., H. Yu, L. Kass, J. N. Lakins, M. Egeblad, J. T. Erler, S. F. Fong, K. Csiszar, A. Giaccia, W. Weninger, M. Yamauchi, D. L. Gasser, and V. M. Weaver. 2009. Matrix crosslinking forces tumor progression by enhancing integrin signaling. *Cell* 139: 891-906.
63. Egeblad, M., M. G. Rasch, and V. M. Weaver. 2010. Dynamic interplay between the collagen scaffold and tumor evolution. *Curr Opin Cell Biol* 22: 697-706.
64. Streuli, C. H., N. Bailey, and M. J. Bissell. 1991. Control of Mammary Epithelial Differentiation - Basement-Membrane Induces Tissue-Specific Gene-Expression in the Absence of Cell Cell-Interaction and Morphological Polarity. *J Cell Biol* 115: 1383-1395.
65. Gill, B. J., D. L. Gibbons, L. C. Roudsari, J. E. Saik, Z. H. Rizvi, J. D. Roybal, J. M. Kurie, and J. L. West. 2012. A synthetic matrix with independently tunable biochemistry and mechanical properties to study epithelial morphogenesis and EMT in a lung adenocarcinoma model. *Cancer Res* 72: 6013-6023.

66. Gilkes, D. M., G. L. Semenza, and D. Wirtz. 2014. Hypoxia and the extracellular matrix: drivers of tumour metastasis. *Nat Rev Cancer* 14: 430-439.
67. Jung, H. Y., L. Fattet, and J. Yang. 2015. Molecular pathways: linking tumor microenvironment to epithelial-mesenchymal transition in metastasis. *Clin Cancer Res* 21: 962-968.
68. Schliekelman, M. J., D. L. Gibbons, V. M. Faca, C. J. Creighton, Z. H. Rizvi, Q. Zhang, C. H. Wong, H. Wang, C. Ungewiss, Y. H. Ahn, D. H. Shin, J. M. Kurie, and S. M. Hanash. 2011. Targets of the tumor suppressor miR-200 in regulation of the epithelial-mesenchymal transition in cancer. *Cancer Res* 71: 7670-7682.
69. Shintani, Y., M. Maeda, N. Chaika, K. R. Johnson, and M. J. Wheelock. 2008. Collagen I promotes epithelial-to-mesenchymal transition in lung cancer cells via transforming growth factor-beta signaling. *American journal of respiratory cell and molecular biology* 38: 95-104.
70. Carter, E. M., and C. L. Raggio. 2009. Genetic and orthopedic aspects of collagen disorders. *Curr Opin Pediatr* 21: 46-54.
71. Yamauchi, M., and M. Sricholpech. 2012. Lysine post-translational modifications of collagen. *Essays Biochem* 52: 113-133.
72. Huijbers, I. J., M. Iravani, S. Popov, D. Robertson, S. Al-Sarraj, C. Jones, and C. M. Isacke. 2010. A role for fibrillar collagen deposition and the collagen internalization receptor endo180 in glioma invasion. *PLoS One* 5: e9808.
73. Zhu, G. G., L. Risteli, M. Makinen, J. Risteli, A. Kauppila, and F. Stenback. 1995. Immunohistochemical study of type I collagen and type I pN-collagen in benign and malignant ovarian neoplasms. *Cancer* 75: 1010-1017.

74. Kauppila, S., F. Stenback, J. Risteli, A. Jukkola, and L. Risteli. 1998. Aberrant type I and type III collagen gene expression in human breast cancer in vivo. *J Pathol* 186: 262-268.
75. Leight, J. L., M. A. Wozniak, S. Chen, M. L. Lynch, and C. S. Chen. 2012. Matrix rigidity regulates a switch between TGF-beta1-induced apoptosis and epithelial-mesenchymal transition. *Mol Biol Cell* 23: 781-791.
76. Paszek, M. J., N. Zahir, K. R. Johnson, J. N. Lakins, G. I. Rozenberg, A. Gefen, C. A. Reinhart-King, S. S. Margulies, M. Dembo, D. Boettiger, D. A. Hammer, and V. M. Weaver. 2005. Tensional homeostasis and the malignant phenotype. *Cancer Cell* 8: 241-254.
77. Erler, J. T., K. L. Bennewith, M. Nicolau, N. Dornhofer, C. Kong, Q. T. Le, J. T. Chi, S. S. Jeffrey, and A. J. Giaccia. 2006. Lysyl oxidase is essential for hypoxia-induced metastasis. *Nature* 440: 1222-1226.
78. Cox, T. R., D. Bird, A. M. Baker, H. E. Barker, M. W. Ho, G. Lang, and J. T. Erler. 2013. LOX-mediated collagen crosslinking is responsible for fibrosis-enhanced metastasis. *Cancer Res* 73: 1721-1732.
79. Kagan, H. M., and W. Li. 2003. Lysyl oxidase: properties, specificity, and biological roles inside and outside of the cell. *J Cell Biochem* 88: 660-672.
80. Barker, H. E., T. R. Cox, and J. T. Erler. 2012. The rationale for targeting the LOX family in cancer. *Nat Rev Cancer* 12: 540-552.
81. Herranz, N., N. Dave, A. Millanes-Romero, L. Morey, V. M. Diaz, V. Lorenz-Fonfria, R. Gutierrez-Gallego, C. Jeronimo, L. Di Croce, A. Garcia de Herreros, and S. Peiro. 2012. Lysyl oxidase-like 2 deaminates lysine 4 in histone H3. *Mol Cell* 46: 369-376.

82. Millanes-Romero, A., N. Herranz, V. Perrera, A. Iturbide, J. Loubat-Casanovas, J. Gil, T. Jenuwein, A. Garcia de Herreros, and S. Peiro. 2013. Regulation of heterochromatin transcription by Snail1/LOXL2 during epithelial-to-mesenchymal transition. *Mol Cell* 52: 746-757.
83. Canesin, G., E. P. Cuevas, V. Santos, C. Lopez-Menendez, G. Moreno-Bueno, Y. Huang, K. Csiszar, F. Portillo, H. Peinado, D. Lyden, and A. Cano. 2015. Lysyl oxidase-like 2 (LOXL2) and E47 EMT factor: novel partners in E-cadherin repression and early metastasis colonization. *Oncogene* 34: 951-964.
84. Sanchez-Morgan, N., K. H. Kirsch, P. C. Trackman, and G. E. Sonenshein. 2011. The lysyl oxidase propeptide interacts with the receptor-type protein tyrosine phosphatase kappa and inhibits beta-catenin transcriptional activity in lung cancer cells. *Mol Cell Biol* 31: 3286-3297.
85. Liu, N., T. R. Cox, W. Cui, G. Adell, B. Holmlund, J. Ping, I. Jarlsfelt, J. T. Erler, and X.-F. Sun. 2014. Nuclear expression of lysyl oxidase enzyme is an independent prognostic factor in rectal cancer patients. *Oncotarget*.
86. Iturbide, A., A. García de Herreros, and S. Peiró. 2015. A new role for LOX and LOXL2 proteins in transcription regulation. *FEBS Journal* 282: 1768-1773.
87. Akbani, R., P. K. Ng, H. M. Werner, M. Shahmoradgoli, F. Zhang, Z. Ju, W. Liu, J. Y. Yang, K. Yoshihara, J. Li, S. Ling, E. G. Seviour, P. T. Ram, J. D. Minna, L. Diao, P. Tong, J. V. Heymach, S. M. Hill, F. Dondelinger, N. Stadler, L. A. Byers, F. Meric-Bernstam, J. N. Weinstein, B. M. Broom, R. G. Verhaak, H. Liang, S. Mukherjee, Y. Lu, and G. B. Mills. 2014. A pan-cancer proteomic perspective on The Cancer Genome Atlas. *Nat Commun* 5: 3887.

88. Hoadley, K. A., C. Yau, D. M. Wolf, A. D. Cherniack, D. Tamborero, S. Ng, M. D. Leiserson, B. Niu, M. D. McLellan, V. Uzunangelov, J. Zhang, C. Kandoth, R. Akbani, H. Shen, L. Omberg, A. Chu, A. A. Margolin, L. J. Van't Veer, N. Lopez-Bigas, P. W. Laird, B. J. Raphael, L. Ding, A. G. Robertson, L. A. Byers, G. B. Mills, J. N. Weinstein, C. Van Waes, Z. Chen, E. A. Collisson, N. Cancer Genome Atlas Research, C. C. Benz, C. M. Perou, and J. M. Stuart. 2014. Multiplatform analysis of 12 cancer types reveals molecular classification within and across tissues of origin. *Cell* 158: 929-944.
89. Yang, Y., Y. H. Ahn, Y. Chen, X. Tan, L. Guo, D. L. Gibbons, C. Ungewiss, D. H. Peng, X. Liu, S. H. Lin, N. Thilaganathan, Wistuba, II, J. Rodriguez-Canales, G. McLendon, C. J. Creighton, and J. M. Kurie. 2014. ZEB1 sensitizes lung adenocarcinoma to metastasis suppression by PI3K antagonism. *J Clin Invest* 124: 2696-2708.
90. Sato, M., J. E. Larsen, W. Lee, H. Sun, D. S. Shames, M. P. Dalvi, R. D. Ramirez, H. Tang, J. M. DiMaio, B. Gao, Y. Xie, Wistuba, II, A. F. Gazdar, J. W. Shay, and J. D. Minna. 2013. Human lung epithelial cells progressed to malignancy through specific oncogenic manipulations. *Mol Cancer Res* 11: 638-650.
91. Yang, Y., Y. H. Ahn, D. L. Gibbons, Y. Zang, W. Lin, N. Thilaganathan, C. A. Alvarez, D. C. Moreira, C. J. Creighton, P. A. Gregory, G. J. Goodall, and J. M. Kurie. 2011. The Notch ligand Jagged2 promotes lung adenocarcinoma metastasis through a miR-200-dependent pathway in mice. *J Clin Invest* 121: 1373-1385.

92. Oliver, W. C., and G. M. Pharr. 1992. An Improved Technique for Determining Hardness and Elastic-Modulus Using Load and Displacement Sensing Indentation Experiments. *J Mater Res* 7: 1564-1583.
93. Rossi, M. A., M. A. Abreu, and L. B. Santoro. 1998. Connective Tissue Skeleton of the Human Heart : A Demonstration by Cell-Maceration Scanning Electron Microscope Method. *Circulation* 97: 934-935.
94. Chaudhuri, B. B., P. Kundu, and N. Sarkar. 1993. Detection and Gradation of Oriented Texture. *Pattern Recogn Lett* 14: 147-153.
95. Cao, H., A. Jheon, X. Li, Z. Sun, J. Wang, S. Florez, Z. Zhang, M. T. McManus, O. D. Klein, and B. A. Amendt. 2013. The Pitx2:miR-200c/141:noggin pathway regulates Bmp signaling and ameloblast differentiation. *Development* 140: 3348-3359.
96. Park, C. Y., L. T. Jeker, K. Carver-Moore, A. Oh, H. J. Liu, R. Cameron, H. Richards, Z. Li, D. Adler, Y. Yoshinaga, M. Martinez, M. Nefadov, A. K. Abbas, A. Weiss, L. L. Lanier, P. J. de Jong, J. A. Bluestone, D. Srivastava, and M. T. McManus. 2012. A resource for the conditional ablation of microRNAs in the mouse. *Cell reports* 1: 385-391.
97. Carugo, A., G. Genovese, S. Seth, L. Nezi, J. L. Rose, D. Bossi, A. Cicalese, P. K. Shah, A. Viale, P. F. Pettazzoni, K. C. Akdemir, C. A. Bristow, F. S. Robinson, J. Tepper, N. Sanchez, S. Gupta, M. R. Estecio, V. Giuliani, G. I. Dellino, L. Riva, W. Yao, M. E. Di Francesco, T. Green, C. D'Alesio, D. Corti, Y. Kang, P. Jones, H. Wang, J. B. Fleming, A. Maitra, P. G. Pelicci, L. Chin, R. A. DePinho, L. Lanfrancone, T. P. Heffernan, and G. F. Draetta. 2016. In Vivo Functional

- Platform Targeting Patient-Derived Xenografts Identifies WDR5-Myc Association as a Critical Determinant of Pancreatic Cancer. *Cell reports* 16: 133-147.
98. Barry-Hamilton, V., R. Spangler, D. Marshall, S. McCauley, H. M. Rodriguez, M. Oyasu, A. Mikels, M. Vaysberg, H. Ghermazien, C. Wai, C. A. Garcia, A. C. Velayo, B. Jorgensen, D. Biermann, D. Tsai, J. Green, S. Zaffryar-Eilot, A. Holzer, S. Ogg, D. Thai, G. Neufeld, P. Van Vlasselaer, and V. Smith. 2010. Allosteric inhibition of lysyl oxidase-like-2 impedes the development of a pathologic microenvironment. *Nat Med* 16: 1009-1017.
99. Pickup, M. W., H. Laklai, I. Acerbi, P. Owens, A. E. Gorska, A. Chytil, M. Aakre, V. M. Weaver, and H. L. Moses. 2013. Stromally derived lysyl oxidase promotes metastasis of transforming growth factor-beta-deficient mouse mammary carcinomas. *Cancer Res* 73: 5336-5346.
100. Peng, L., Y. L. Ran, H. Hu, L. Yu, Q. Liu, Z. Zhou, Y. M. Sun, L. C. Sun, J. Pan, L. X. Sun, P. Zhao, and Z. H. Yang. 2009. Secreted LOXL2 is a novel therapeutic target that promotes gastric cancer metastasis via the Src/FAK pathway. *Carcinogenesis* 30: 1660-1669.
101. Palamakumbura, A. H., and P. C. Trackman. 2002. A fluorometric assay for detection of lysyl oxidase enzyme activity in biological samples. *Anal Biochem* 300: 245-251.
102. Fuxe, J., T. Vincent, and A. G. de Herreros. 2010. Transcriptional crosstalk between TGF beta and stem cell pathways in tumor cell invasion Role of EMT promoting Smad complexes. *Cell Cycle* 9: 2363-2374.
103. Lindemann, R. K., P. Ballsehmieter, A. Nordheim, and J. Dittmer. 2001. Transforming growth factor beta regulates parathyroid hormone-related protein

- expression in MDA-MB-231 breast cancer cells through a novel Smad/Ets synergism. *Journal of Biological Chemistry* 276: 46661-46670.
104. Vadasz, Z., O. Kessler, G. Akiri, S. Gengrinovitch, H. M. Kagan, Y. Baruch, O. B. Izhak, and G. Neufeld. 2005. Abnormal deposition of collagen around hepatocytes in Wilson's disease is associated with hepatocyte specific expression of lysyl oxidase and lysyl oxidase like protein-2. *J Hepatol* 43: 499-507.
 105. Hollosi, P., J. K. Yakushiji, K. S. Fong, K. Csiszar, and S. F. Fong. 2009. Lysyl oxidase-like 2 promotes migration in noninvasive breast cancer cells but not in normal breast epithelial cells. *Int J Cancer* 125: 318-327.
 106. Zhan, P., X. K. Shen, Q. Qian, J. P. Zhu, Y. Zhang, H. Y. Xie, C. H. Xu, K. K. Hao, W. Hu, N. Xia, G. J. Lu, and L. K. Yu. 2012. Down-regulation of lysyl oxidase-like 2 (LOXL2) is associated with disease progression in lung adenocarcinomas. *Med Oncol* 29: 648-655.
 107. Payne, S. L., M. J. Hendrix, and D. A. Kirschmann. 2007. Paradoxical roles for lysyl oxidases in cancer--a prospect. *J Cell Biochem* 101: 1338-1354.
 108. Hong, H. H., N. Pischon, R. B. Santana, A. H. Palamakumbura, H. B. Chase, D. Gantz, Y. Guo, M. I. Uzel, D. Ma, and P. C. Trackman. 2004. A role for lysyl oxidase regulation in the control of normal collagen deposition in differentiating osteoblast cultures. *J Cell Physiol* 200: 53-62.
 109. Chen, Y., M. Terajima, Y. Yang, L. Sun, Y. H. Ahn, D. Pankova, D. S. Puperi, T. Watanabe, M. P. Kim, S. H. Blackmon, J. Rodriguez, H. Liu, C. Behrens, Wistuba, II, R. Minelli, K. L. Scott, J. Sanchez-Adams, F. Guilak, D. Pati, N. Thilaganathan, A. R. Burns, C. J. Creighton, E. D. Martinez, T. Zal, K. J.

- Grande-Allen, M. Yamauchi, and J. M. Kurie. 2015. Lysyl hydroxylase 2 induces a collagen cross-link switch in tumor stroma. *J Clin Invest* 125: 1147-1162.
110. Peinado, H., G. Moreno-Bueno, D. Hardisson, E. Perez-Gomez, V. Santos, M. Mendiola, J. I. de Diego, M. Nistal, M. Quintanilla, F. Portillo, and A. Cano. 2008. Lysyl oxidase-like 2 as a new poor prognosis marker of squamous cell carcinomas. *Cancer Res* 68: 4541-4550.
 111. Konig, R., C. Y. Chiang, B. P. Tu, S. F. Yan, P. D. DeJesus, A. Romero, T. Bergauer, A. Orth, U. Krueger, Y. Zhou, and S. K. Chanda. 2007. A probability-based approach for the analysis of large-scale RNAi screens. *Nat Methods* 4: 847-849.
 112. Birmingham, A., L. M. Selfors, T. Forster, D. Wrobel, C. J. Kennedy, E. Shanks, J. Santoyo-Lopez, D. J. Dunican, A. Long, D. Kelleher, Q. Smith, R. L. Beijersbergen, P. Ghazal, and C. E. Shamu. 2009. Statistical methods for analysis of high-throughput RNA interference screens. *Nat Methods* 6: 569-575.
 113. Cardnell, R. J., C. Behrens, L. Diao, Y. Fan, X. Tang, P. Tong, J. D. Minna, G. B. Mills, J. V. Heymach, Wistuba, II, J. Wang, and L. A. Byers. 2015. An Integrated Molecular Analysis of Lung Adenocarcinomas Identifies Potential Therapeutic Targets among TTF1-Negative Tumors, Including DNA Repair Proteins and Nrf2. *Clin Cancer Res* 21: 3480-3491.
 114. Hennessy, B. T., Y. Lu, A. M. Gonzalez-Angulo, M. S. Carey, S. Myhre, Z. Ju, M. A. Davies, W. Liu, K. Coombes, F. Meric-Bernstam, I. Bedrosian, M. McGahren, R. Agarwal, F. Zhang, J. Overgaard, J. Alsner, R. M. Neve, W. L. Kuo, J. W. Gray, A. L. Borresen-Dale, and G. B. Mills. 2010. A Technical Assessment of the

- Utility of Reverse Phase Protein Arrays for the Study of the Functional Proteome in Non-microdissected Human Breast Cancers. *Clin Proteomics* 6: 129-151.
115. Furthauer, M., W. Lin, S. L. Ang, B. Thisse, and C. Thisse. 2002. Sef is a feedback-induced antagonist of Ras/MAPK-mediated FGF signalling. *Nat Cell Biol* 4: 170-174.
116. Ren, Y., L. Cheng, Z. Rong, Z. Li, Y. Li, X. Zhang, S. Xiong, J. Hu, X. Y. Fu, and Z. Chang. 2008. hSef potentiates EGF-mediated MAPK signaling through affecting EGFR trafficking and degradation. *Cell Signal* 20: 518-533.
117. Kovalenko, D., X. Yang, R. J. Nadeau, L. K. Harkins, and R. Friesel. 2003. Sef inhibits fibroblast growth factor signaling by inhibiting FGFR1 tyrosine phosphorylation and subsequent ERK activation. *J Biol Chem* 278: 14087-14091.
118. Thiery, J. P. 2002. Epithelial-mesenchymal transitions in tumour progression. *Nat Rev Cancer* 2: 442-454.
119. Wee, S., Z. Jagani, K. X. Xiang, A. Loo, M. Dorsch, Y. M. Yao, W. R. Sellers, C. Lengauer, and F. Stegmeier. 2009. PI3K pathway activation mediates resistance to MEK inhibitors in KRAS mutant cancers. *Cancer Res* 69: 4286-4293.
120. Lee, H. J., G. Zhuang, Y. Cao, P. Du, H. J. Kim, and J. Settleman. 2014. Drug resistance via feedback activation of Stat3 in oncogene-addicted cancer cells. *Cancer Cell* 26: 207-221.
121. Xiong, H., J. Hong, W. Du, Y. W. Lin, L. L. Ren, Y. C. Wang, W. Y. Su, J. L. Wang, Y. Cui, Z. H. Wang, and J. Y. Fang. 2012. Roles of STAT3 and ZEB1 proteins in E-cadherin down-regulation and human colorectal cancer epithelial-mesenchymal transition. *J Biol Chem* 287: 5819-5832.

122. Cheng, X., J. Gu, M. Zhang, J. Yuan, B. Zhao, J. Jiang, and X. Jia. 2014. Astragaloside IV inhibits migration and invasion in human lung cancer A549 cells via regulating PKC- α -ERK1/2-NF- κ B pathway. *Int Immunopharmacol* 23: 304-313.
123. Tan, M., P. Li, M. Sun, G. Yin, and D. Yu. 2006. Upregulation and activation of PKC α by ErbB2 through Src promotes breast cancer cell invasion that can be blocked by combined treatment with PKC α and Src inhibitors. *Oncogene* 25: 3286-3295.
124. DuPage, M., A. L. Dooley, and T. Jacks. 2009. Conditional mouse lung cancer models using adenoviral or lentiviral delivery of Cre recombinase. *Nat Protoc* 4: 1064-1072.
125. Kakihana, M., T. Ohira, D. Chan, R. B. Webster, H. Kato, H. A. Drabkin, and R. M. Gemmill. 2009. Induction of E-cadherin in lung cancer and interaction with growth suppression by histone deacetylase inhibition. *J Thorac Oncol* 4: 1455-1465.
126. Witta, S. E., R. M. Gemmill, F. R. Hirsch, C. D. Coldren, K. Hedman, L. Ravdel, B. Helfrich, R. Dziadziuszko, D. C. Chan, M. Sugita, Z. Chan, A. Baron, W. Franklin, H. A. Drabkin, L. Girard, A. F. Gazdar, J. D. Minna, and P. A. Bunn, Jr. 2006. Restoring E-cadherin expression increases sensitivity to epidermal growth factor receptor inhibitors in lung cancer cell lines. *Cancer Res* 66: 944-950.
127. Lin, X., B. Sun, M. Liang, Y.-Y. Liang, A. Gast, J. Hildebrand, F. C. Brunicardi, F. Melchior, and X.-H. Feng. 2003. Opposed Regulation of Corepressor CtBP by SUMOylation and PDZ Binding. *Molecular Cell* 11: 1389-1396.

128. Roybal, J. D., Y. Zang, Y. H. Ahn, Y. Yang, D. L. Gibbons, B. N. Baird, C. Alvarez, N. Thilaganathan, D. D. Liu, P. Saintigny, J. V. Heymach, C. J. Creighton, and J. M. Kurie. 2011. miR-200 Inhibits lung adenocarcinoma cell invasion and metastasis by targeting Flt1/VEGFR1. *Mol Cancer Res* 9: 25-35.
129. Hosper, N. A., P. P. van den Berg, S. de Rond, E. R. Popa, M. J. Wilmer, R. Masereeuw, and R. A. Bank. 2013. Epithelial-to-mesenchymal transition in fibrosis: collagen type I expression is highly upregulated after EMT, but does not contribute to collagen deposition. *Experimental cell research* 319: 3000-3009.
130. Barcus, C. E., P. J. Keely, K. W. Eliceiri, and L. A. Schuler. 2013. Stiff collagen matrices increase tumorigenic prolactin signaling in breast cancer cells. *J Biol Chem* 288: 12722-12732.
131. Erler, J. T., and V. M. Weaver. 2009. Three-dimensional context regulation of metastasis. *Clin Exp Metastasis* 26: 35-49.
132. Seewaldt, V. 2014. ECM stiffness paves the way for tumor cells. *Nat Med* 20: 332-333.
133. Stanisavljevic, J., J. Loubat-Casanovas, M. Herrera, T. Luque, R. Pena, A. Lluch, J. Albanell, F. Bonilla, A. Rovira, C. Pena, D. Navajas, F. Rojo, A. Garcia de Herreros, and J. Baulida. 2015. Snail1-expressing fibroblasts in the tumor microenvironment display mechanical properties that support metastasis. *Cancer Res* 75: 284-295.
134. Beck, J. N., A. Singh, A. R. Rothenberg, J. H. Elisseeff, and A. J. Ewald. 2013. The independent roles of mechanical, structural and adhesion characteristics of 3D hydrogels on the regulation of cancer invasion and dissemination. *Biomaterials* 34: 9486-9495.

135. Roy, R., A. Boskey, and L. J. Bonassar. 2009. Processing of type I collagen gels using nonenzymatic glycation. *Journal of Biomedical Materials Research Part A* 9999A: NA-NA.
136. Nguyen-Ngoc, K. V., and A. J. Ewald. 2013. Mammary ductal elongation and myoepithelial migration are regulated by the composition of the extracellular matrix. *J Microsc* 251: 212-223.
137. Nguyen-Ngoc, K. V., K. J. Cheung, A. Brenot, E. R. Shamir, R. S. Gray, W. C. Hines, P. Yaswen, Z. Werb, and A. J. Ewald. 2012. ECM microenvironment regulates collective migration and local dissemination in normal and malignant mammary epithelium. *Proc Natl Acad Sci U S A* 109: E2595-2604.
138. Baker, A. M., T. R. Cox, D. Bird, G. Lang, G. I. Murray, X. F. Sun, S. M. Southall, J. R. Wilson, and J. T. Erler. 2011. The role of lysyl oxidase in SRC-dependent proliferation and metastasis of colorectal cancer. *J Natl Cancer Inst* 103: 407-424.
139. Barker, H. E., D. Bird, G. Lang, and J. T. Erler. 2013. Tumor-secreted LOXL2 activates fibroblasts through FAK signaling. *Mol Cancer Res* 11: 1425-1436.
140. Barker, H. E., J. Chang, T. R. Cox, G. Lang, D. Bird, M. Nicolau, H. R. Evans, A. Gartland, and J. T. Erler. 2011. LOXL2-mediated matrix remodeling in metastasis and mammary gland involution. *Cancer Res* 71: 1561-1572.
141. Fong, S. F., E. Dietzsch, K. S. Fong, P. Hollosi, L. Asuncion, Q. He, M. I. Parker, and K. Csiszar. 2007. Lysyl oxidase-like 2 expression is increased in colon and esophageal tumors and associated with less differentiated colon tumors. *Genes Chromosomes Cancer* 46: 644-655.

142. Lucero, H. A., and H. M. Kagan. 2006. Lysyl oxidase: an oxidative enzyme and effector of cell function. *Cell Mol Life Sci* 63: 2304-2316.
143. Peinado, H., M. Del Carmen Iglesias-de la Cruz, D. Olmeda, K. Csiszar, K. S. Fong, S. Vega, M. A. Nieto, A. Cano, and F. Portillo. 2005. A molecular role for lysyl oxidase-like 2 enzyme in snail regulation and tumor progression. *EMBO J* 24: 3446-3458.
144. Manchado, E., S. Weissmueller, J. P. t. Morris, C. C. Chen, R. Wullenkord, A. Lujambio, E. de Stanchina, J. T. Poirier, J. F. Gainor, R. B. Corcoran, J. A. Engelman, C. M. Rudin, N. Rosen, and S. W. Lowe. 2016. A combinatorial strategy for treating KRAS-mutant lung cancer. *Nature* 534: 647-651.
145. Siegel, R. L., K. D. Miller, and A. Jemal. 2016. Cancer statistics, 2016. *CA Cancer J Clin* 66: 7-30.
146. Tsang, M., R. Friesel, T. Kudoh, and I. B. Dawid. 2002. Identification of Sef, a novel modulator of FGF signalling. *Nat Cell Biol* 4: 165-169.
147. He, Q., Y. Gong, L. Gower, X. Yang, and R. E. Friesel. 2016. Sef Regulates Epithelial-Mesenchymal Transition in Breast Cancer Cells. *J Cell Biochem* 117: 2346-2356.
148. Hori, S., K. Wadhwa, V. Pisupati, V. Zecchini, A. Ramos-Montoya, A. Y. Warren, D. E. Neal, and V. J. Gnanapragasam. 2017. Loss of hSef promotes metastasis through upregulation of EMT in prostate cancer. *Int J Cancer* 140: 1881-1887.

VITA

David Hwa Peng was born in Houston, Texas on March 6th, 1985, the son of Pei-Feng Chen and Cheng Peng. After completing his studies at Bellaire High School, Houston, Texas in 2003, he entered Cornell University in Ithaca, New York. He received the degree of Bachelor of Science with a major in Biological Engineering from Cornell in May, 2008. He then received the degree of Masters of Engineering with a major in Biomedical Engineering from Cornell in December, 2009. For the next two years he worked as a research technician in the Department of Immunology at Cornell University and in the Institute of Cellular and System Medicine at the National Health Research Institutes in Taiwan. In August of 2011 he entered the University Of Texas MD Anderson Cancer Center UTHHealth Graduate School Of Biomedical Sciences. As a graduate student, David was supported by the Graduate Scholar Training Grant awarded by the Cancer Prevention and Research Institute of Texas (CPRIT RP140106). He was also the recipient of the Investing in Student Futures Scholarship and placed first in the MD Anderson Trainee Research Day Oral Competition.

Permanent Address:

145 Whipple Dr.

Bellaire, TX 77401